Simulation of sensory-evoked signal flow in anatomically realistic models of neural networks

Dissertation

zur Erlangung des Grades eines

Doktors der Naturwissenschaften

der Mathematisch-Naturwissenschaftlichen Fakultät

und

der Medizinischen Fakultät

der Eberhard-Karls-Universität Tübingen

vorgelegt

von

Robert Egger

aus Wiesbaden, Deutschland

Dezember 2015

Tag der mündlichen Prüfung: 17. Juni 2016

Dekan der Math.-Nat. Fakultät: Prof. Dr. W. Rosenstiel
Dekan der Medizinischen Fakultät: Prof. Dr. I. B. Autenrieth

1. Berichterstatter: Dr. M. Oberländer
2. Berichterstatter: Prof. Dr. M. Bethge

Prüfungskommission: Prof. Dr. C. Schwarz
Prof. Dr. M. Bethge
Dr. M. Oberländer
Dr. A. Burgalossi

Erklärung:

Ich erkläre, dass ich die zur Promotion eingereichte Arbeit mit dem Titel:
"Simulation of sensory-evoked signal flow in anatomically realistic models of neural networks"
selbständig verfasst, nur die angegebenen Quellen und Hilfsmittel benutzt und wörtlich oder inhaltlich übernommene Stellen als solche gekennzeichnet habe. Ich versichere an Eides statt, dass diese Angaben wahr sind und dass ich nichts verschwiegen habe. Mir ist bekannt, dass die falsche Abgabe einer Versicherung an Eides statt mit Freiheitsstrafe bis zu drei Jahren oder mit Geldstrafe bestraft wird.

Tübingen, den ....

Datum Unterschrift

Zusammenfassung

Diese Dissertation beschreibt einen neuartigen Ansatz zur Entwicklung und Simulation von Modellen des Signalflusses in neuronalen Netzwerken unter anatomisch und funktionell realistischen Randbedingungen. Dieser Ansatz besteht aus den folgenden Methoden:

1. Ein standardisiertes anatomisches Referenzsystem der betrachteten Hirnregion und Registrierungsmethoden die es erlauben anatomische Daten aus unterschiedlichen Experimenten mit höchstmöglicher Genauigkeit zu integrieren.

2. Eine Methode zur Bestimmung morphologischer Typen von Nervenzellen um Messungen von der Morphologie und funktioneller Antworten einzelner Nervenzellen in Bezug zu setzen.

3. Eine Methode um ein mittleres dreidimensionales (3D) statistisches Modell der neuronalen Netzwerke in einer Hirnregion zu bauen, das auf einer repräsentativen Stichprobe aller Nervenzelltypen in dieser Hirnregion beruht. Dieses Modell beinhaltet 3D morphologische Modelle für jede Nervenzelle in der Hirnregion, und die Zahl und 3D Verteilung synaptischer Verknüpfungen zwischen diesen.

4. Eine Methode um dieses Netzwerk aufgrund von gemessenen Antworten unterschiedlicher Nervenzelltypen zu aktivieren, und die Antwort einzelner repräsentativer Nervenzellen bestimmten Typs innerhalb dieses Netzwerkmodells zu simulieren.

Die Machbarkeit und Gültigkeit dieses Ansatzes wird am Beispiel des Tasthaarsystems im Kortex der Ratte demonstriert. Das 3D Modell dieses primären sensorischen Kortex enthält $\sim$ 530000 Nervenzellen von 16 unterschiedlichen Typen und $\sim 6 \times 10^9$ thalamokortikale und intrakortikale Synapsen. Aktivierung dieses Modells mit gemessen funktionellen Antworten auf passive Berührung eines Schnurrhaares und Simulation der Antworten unterschiedlicher Nervenzelltypen zeigt dass die simulierten Antworten mit experimentellen Messungen übereinstimmen. Dies erlaubt es mit Hilfe von Computersimulationen zu untersuchen wie robuste Antworten auf unterschiedliche Sinnesreize in unterschiedlichen Nervenzelltypen entstehen, und experimentell überprüfbare Vorhersagen zu machen.

Abstract English

In this thesis, a new concept for development and simulation of anatomically and functionally constrained models of signal flow in neural networks is described. This approach consists of the following tools:

1. A standardized anatomical reference frame of the brain region studied and registration methods to integrate anatomical data from different experiments with the highest precision possible.

2. A method for determining morphological neuron types to allow correlation between measurements of the morphology and functional responses of individual neurons.

3. A tool to build an average three-dimensional (3D) statistical model of the neural networks in a brain region based on a representative sparse sample of all neuron types present in the brain region. This model contains 3D morphological models for every neuron in the brain region, as well as the total number and 3D distribution of synaptic contacts between them.

4. A method to activate the network based on measured responses of different neuron types, and to simulate the response of individual neurons representative of different cell types within this network model.

The feasibility and validity of this process is demonstrated on the example of rat vibrissal cortex. The 3D model of this primary sensory area in cortex contains $\sim 530,000$ neurons of 16 different types and $\sim 6 \times 10^9$ thalamocortical and intracortical synapses. Activation of this model with functional responses measured after whisker touch and simulation of the responses of different neuron types shows that the simulated model responses match experimental measurements. This allowed investigating how robust sensory-evoked responses after different sensory stimuli are formed in different neuron types using computer simulations, and to make predictions to experimentally test these hypotheses.

Acknowledgements

Special thanks go to:

- My supervisor Dr. Marcel Oberlaender, for the great teamwork, support and trust, and for the opportunity to finish all these projects.
- My advisory commitee, Prof. Dr. Cornelius Schwarz and Prof. Dr. Matthias Bethge, for helpful comments and discussions.
- My collaborators (in alphabetical order): Dr. Vincent Dercksen, Mike Guest, Dr. Andrew Johnson, Dr. Hanno Sebastian Meyer, Dr. Rajeev Narayanan, Dr. Gerardo Rojas Piloni, Dr. Arno Schmitt and Daniel Udvary. Without your great teamwork, this thesis would have been impossible.
- Dr. Marcel Oberlaender, Dr. Jason Kerr, Dr. Christiaan de Kock and Prof. Dr. Bert Sakmann, for giving me the opportunity to work on these amazing projects.
- All students in the Computational Neuroanatomy Group: Alison, Chris, David, Max and Simon.
- Chris Roome and Joachim Werner - for technical support anywhere, any time.

Most importantly:

My wife Aya: For her support during the last years. This would not have been possible without you.

Contents

List of Tables

List of Figures

Chapter 1

Introduction

1.1 Simulating sensory-evoked signal flow in neural networks

One fundamental question in neuroscience is how sensory input gives rise to perception, and ultimately behavior. This question is usually studied by presenting an animal with a sensory stimulus, and measuring the resulting flow of sensory-evoked signals in different brain networks, for example by measuring the electrical activity of nerve cells (neurons). The responses of neurons to sensory stimuli have been characterized depending on different parameters of the stimulus, giving rise to the concept of receptive fields. While an experimentally controlled parameter of the stimulus (for example, the frequency of a sound) is varied, the response of the same neuron to repeated demonstrations of the same stimulus (i.e., trials) is measured. This revealed that individual neurons can display responses to a specific subset of stimulus parameters (i.e. to specific stimulus features). For example, a neuron in primary auditory cortex may only respond to sounds with a frequency between 400-450Hz, while a neuron in primary visual cortex may respond to bars of a certain orientation, or a neuron in primary somatosensory cortex to touch of a specific part of the body.

On the other hand, over the past 100 years, the anatomical, biophysical and synaptic properties of individual neurons, and their relations, have been studied extensively. For example, neurons are commonly grouped into different cell types based on the shape of

their dendrites (i.e. the processes that receive signals) and axon (i.e. the process that transmits the output signal of a neuron) morphologies. Often, these cell types defined by structural parameters display specific functional properties. For example, neurons in cortex that have spines on their dendrites in general release excitatory neurotransmitters at their synapses (i.e., they may serve to increase the activity of other neurons), while neurons without spines usually release inhibitory neurotransmitters (i.e., they may decrease the activity of other neurons). The biophysical properties of neurons are dependent on the presence of ion channels in the cell membrane, which determine the response of a neuron to changes of the membrane potential. The detailed dendrite morphology and the spatial distribution of different types of ion channels within the neuron can further influence integration of electrical signals. Finally, neurons are interconnected by synapses that allow presynaptic neurons to influence the membrane potential in postsynaptic neurons. The location of these synapses on different parts of the dendrites and soma of postsynaptic neurons further influences how their signals are integrated by the postsynaptic neuron. In the living animal, all these properties of neurons interact in linear and nonlinear ways and give rise to measured responses after presentation of a sensory stimulus. However, because the basic mechanisms underlying signal flow in the brain (i.e., synaptic transmission, electrical signal propagation in dendrites and axons, and function of ion channels) have been studied and described in detail over the last 70 years, it has been suggested to develop biologically detailed and comprehensive models combining these mechanisms with data about the structural and functional organization of specific brain regions, also referred to as across-scale-models. The goal of these models is to understand principles underlying the observed signal flow in the living brain, such as the mechanisms giving rise to receptive fields of different neurons ([1, 2], Figure 1.1).

Here, I am going to describe a "network-embedded modeling" approach implementing this idea. In this approach, all model parameters are to be determined by experimental data. These model parameters are used as boundary conditions for simulations of neuron activity based on mathematical descriptions of different biophysical mechanisms, e.g. synaptic transmission. If the simulation results agree with experimental results, the model can be regarded as "functionally realistic", i.e., it is representative of the neural activity in the brain of a living animal. This allows to investigate the effect of the

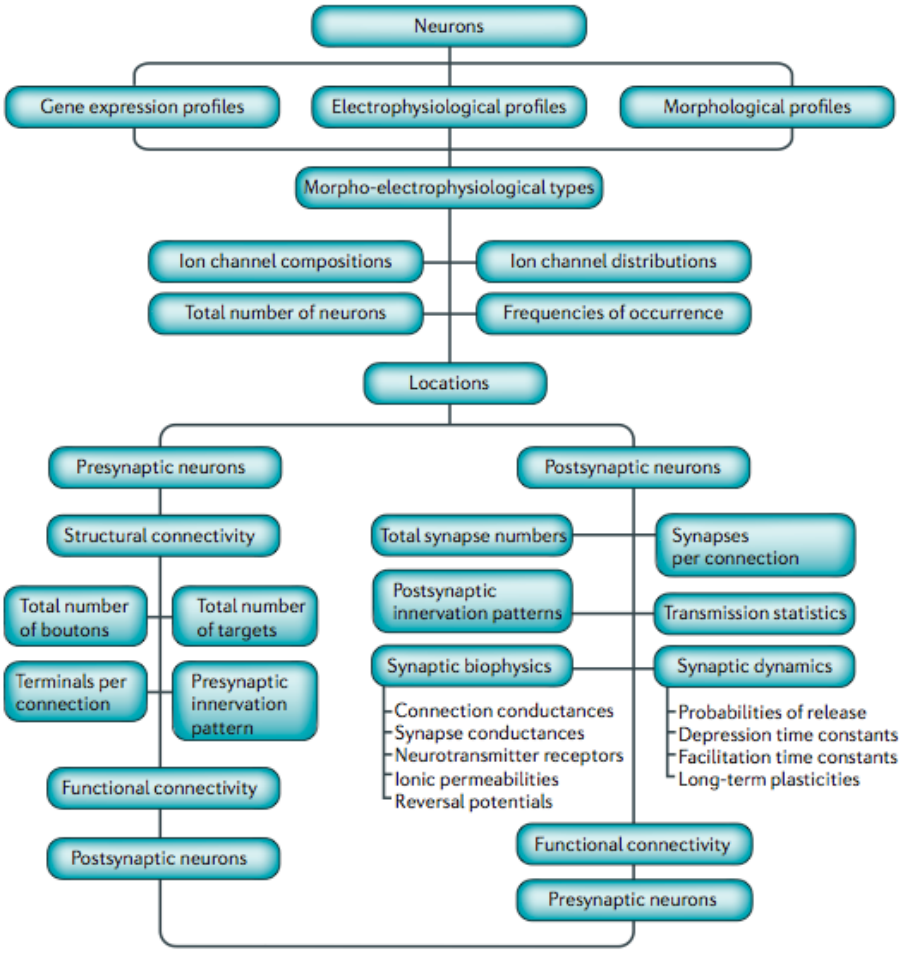

Figure 1.1: Prerequisites for predictive simulations of neural circuits. Minimal requirements to generate biophysically and anatomically realistic models of neurons and the connections between them (synapses). In this thesis, I will describe how to define morphological neuron types and correlate these with electrophysiological measurements; how to determine anatomical connectivity between these neurons based on the total number, spatial distribution and morphology of neurons of different types; and how to convert these neurons and the synapses between them into biophysically and functionally realistic average models. Figure adopted from [1].

model parameters (which are often not easy to control and manipulate experimentally) on functional responses and to identify mechanistic principles underlying these responses. In turn, the model can then be used to make predictions about the effects of specific manipulations which are experimentally testable.

The goal of this thesis is to develop the concepts and tools necessary to develop models of neural networks that allow such predictive simulations. On the example of the vibrissal part of rat primary somatosensory cortex (vS1, often referred to as barrel cortex), I will

describe how to perform network-embedded simulations of neurons of different cell types integrated into an anatomically realistic model of the neural networks in this brain region. The basic modeling concept used in this approach is to determine all synaptic inputs to a neuron that are active after a sensory stimulus, and simulate the response of the neuron to these inputs. In order to do so, the following data are necessary (see Figure 1.1):

- Measurements of action potential (AP)/spiking responses of all presynaptic neurons.
- Measurements of the synaptic connectivity between all presynaptic neurons and the postsynaptic neuron (commonly referred to as a "connectome").
- Measurements of the biophysical properties of synapses of the presynaptic neurons onto the postsynaptic neuron, and of the dendrites and axon of the postsynaptic neuron.

At present, the only experimental methods that allow simultaneous measurement of AP/spiking responses of neurons and reconstruction of the neuron morphology (required to determine synaptic connectivity) are whole-cell or cell-attached electrophysiological recordings. However, using these methods it is usually only possible to record the activity and recover the morphology of one neuron per animal. Therefore, the concept of cell types [3] (i.e., cells that have common synaptic input, common response properties and common output targets) is used to combine functional and morphological data from many different experiments. Specifically, I developed a framework that allows to go from a sparse, but representative sample of functional and morphological measurements from all cell types in rat vS1 to a dense model of the neural networks in rat vS1 (i.e., a model containing the total number of neurons found in rat vS1, as well as their cell type, morphologies and functional properties). Here, a sparse representative sample refers to the requirement that the experimental sample should contain all cell types present in rat vS1, and represent the average and biological variability of functional and morphological parameters within a cell type. Hence, the model is statistical in nature, and the modeling approach uses the resulting statistical distributions of cell type-specific connectivity patterns and response properties as constraints. During simulations, I draw samples from

these distributions, for example, the response probability of each neuron in the model to a sensory stimulus, or the probability of finding one or more synapses between two neurons. Each sample results in a possible spatiotemporal pattern of synaptic inputs to the simulated neuron, and is therefore interpreted as an individual trial. The spatiotemporal pattern of synaptic inputs in each trial is used to simulate the time course of the membrane potential of the neuron in response to these inputs. The simulation results of many trials are then used to compute quantities that are experimentally accessible, for example, the average membrane potential at the soma, or the probability and timing of AP responses at the soma after a stimulus. These quantities are then compared to experimental measurements. If the simulation results and experimental measurements match within the observed variability, the model is regarded as functionally realistic and can be used further to identify mechanisms underlying the responses of the simulated neuron, i.e., the influence of the different statistical distributions of functional and anatomical parameters on the response is investigated.
The thesis is organized as follows:

- Brief review of biopysical descriptions of single neurons and the organization of the rat vibrissal system.
- Description of the anatomical data, concepts and methods needed to build the statistical network model.
- How to combine the statistical network model with statistical distributions of the activity of different cell types and biophysical models of synapses and neurons to perform network-embedded simulations.
- Description of the properties of the anatomically realistic network model.
- Description of the results of network-embedded simulations of neurons from different cell types in response to sensory input.

1.2 Biophysical models of neurons and synapses

The membrane of a neuron is formed by a $\sim 2-4nm$ thick lipid bilayer, which is nearly impermeable to ions dissolved in the cell plasma. If there are different ionic concentrations in the cell plasma and the extracellular space, the cell membrane can therefore be electrically described as a capacitor. However, there are ion-permeable proteins in the cell membrane (ion channels). These ion channels can be permeable for a wide range of ions (unspecific) or selective for specific ions (e.g. Na^+ or Ca^{2+} channels). Ion flow (i.e., the current) through these channels can be described by Ohm's law:

$$I(t) = g(V,t) \cdot (V_m(t) - E_{rev})$$

Here, I is the total current through the ion channel, g is the channel conductance, V_m is the potential across the cell membrane and E_{rev} is the reversal potential of the ion channel. If the ion channel is selective for a single ion species, the reversal potential is determined by the concentration difference of this ion species across the cell membrane and can be calculated by the Nernst equation [4]. If the channel is permeable for multiple ion species, the reversal potential depends on the concentration difference of all permitted ion species. Some ion channels always permit ion flow (i.e., they are open), and are called leak or passive channels. These channels are mostly responsible for the resting membrane potential of a neuron, which is usually around $-80mV$. The conductance of other ion channels is voltage- and/or time-dependent (i.e., active channels). This leads to nonlinear depolarization of the membrane potential in response to changes, for example giving rise to the action potential as described by Hodgkin and Huxley [5]. The action potential is thought to be the fundamental unit of information processing in the brain. Briefly, sufficient depolarization of the membrane potential opens voltage-dependent Na^+ channels. Because the concentration of Na^+ in the intracellular plasma is lower than in the extracellular space, this results in influx of Na^+ ions, leading to further depolarization of the membrane potential. This nonlinear amplification leads to rapid (within $\sim 1ms$) depolarization of the membrane potential towards the reversal potential of Na^+ ions. After a short time, the Na^+ channels become inactivated. At the same time, more slowly reacting voltage-dependent K^+ channels open. The concentration of K^+ ions is reversed

compared to Na^+; hence this leads to an outward K^+ current, that hyperpolarizes the cell again towards the resting membrane potential.

In addition to various voltage- and time-dependent ion channels present in the cell membrane, the morphology of the dendrites and the axon of a neuron leads to a non-uniform membrane potential distribution. To describe this quantitatively, the dendrites and axon are modeled as cylinders with specific membrane resistance and capacitance r_m and c_m (i.e. normalized to membrane surface area), and with specific axial resistance r_a (i.e. normalized to length and cross-sectional area of the dendrite/axon). Because the diameter of dendrites/axon is much smaller than their length, the membrane potential is assumed to be uniform along the radial dimension. Then, the membrane potential can be described by the cable equation as introduced by Rall [6]:

$$\tau \frac{\partial V}{\partial t} = -V + \lambda^2 \frac{\partial^2 V}{\partial x^2}$$

Here, $\tau = r_m c_m$ is the characteristic time constant, and $\lambda = \sqrt{\frac{d r_m}{4 r_a}}$, where d is the diameter of the dendrite/axon, is the characteristic length. τ is the time scale during which the membrane potential adjusts to changes, and λ is the length scale across which changes in the membrane potential spread along the dendrites and axon.

Finally, neurons are interconnected through chemical and/or electrical synapses [7]. Electrical synapses (gap junctions) are formed by specialized ion channels that permeate the membrane of both connected neurons and thus allow ion flow, usually in both directions; however, they are rarely found in cortex. In contrast, chemical synapses transmit signals in one direction. Upon depolarization of the presynaptic axon during an action potential, neurotransmitters are released and chemically bind to receptors on the postsynaptic side. These receptors open ion channels in the postsynaptic membrane, leading to current flow across the postsynaptic membrane. Depending on the reversal potential of the ion channels, the effect of the synapse can either be inhibitory (i.e. hyperpolarization of the membrane potential) or excitatory (i.e. depolarization of the membrane potential).

Thus, electrical activity in a single neuron is determined by the activity of all its presynaptic neurons, the morphology and biophysical properties of its dendrites/axon integrating this activity, and in turn it influences the activity of all its postsynaptic neurons.

Mathematically, this can be describe by a large system of coupled non-linear differential equations, which in general cannot be solved analytically. Instead, neuron morphologies are spatially discretized into isopotential compartments, and the cable equation and Hodgkin-Huxley-type equations are solved numerically for all compartments and ion channels present within them [8].

1.3 The rat vibrissal system

The vibrissal system of rodents is a widely used model system for studying sensory-evoked signal flow and behavior. For example, sensory-evoked input to a single facial whisker is sufficient to trigger decision making in rats [9]. A unique property of the vibrissal system is that there exists a corresponce between structural and functional units processing whisker touch, which provide an anchor point for the present approach to integrated anatomical and functional data from different experiments. In cortical layer (L) 4 of vS1, neuron-dense regions, termed "barrels", exist. These barrels are arranged horizontally into rows and arcs, mirroring the layout of the facial whiskers (i.e., somatotopic layout). Neurons located within, above and below a barrel respond to deflections of the whisker that is somatotopically aligned to this barrel. Vertical arrangement of neurons responding to the same sensory input is observed across sensory modalities and species [10, 11, 12], and gave rise to the concept of "cortical columns" as elementary functional units of sensory cortices. Extrapolation of barrels throughout the entire cortical depth gives rise to cylindrical structures called barrel columns, which are regarded as the structural correlates of cortical columns in vS1, each representing a single whisker (Figure 1.2).

The following description of the structural and functional organization of the rat vibrissal system is adapted from Feldmeyer et al. 2013 [14].
The sensory signal flow towards the barrel column starts in the primary afferent fibers that innervate the whisker follicle using a variety of specialized end organs. The primary sensory neurons with somata in the trigeminal ganglion (TG) carry strictly mono-whisker signals to the brainstem trigeminal nuclei (TN), which in turn relay whisker-specific and unspecific signals to different thalamic nuclei, which in turn innervate sensory and motor cortical areas. These cortical areas display interconnections, as well as feedback

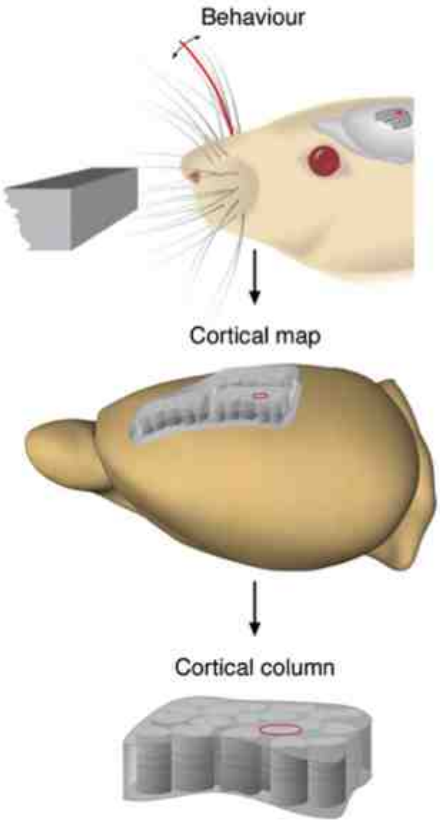

Figure 1.2: Functional organization of rat vibrissal cortex. Sensory input to individual whiskers is sufficient to trigger decision-making in rats. The specific arrangement of the facial whiskers is mirrored in the organization of rat vS1. There, adjacent facial whiskers are represented by adjacent functional cortical columns. These functional columns have an anatomical correlate in L4, called barrel. Figure adopted from [13].

connections to the vibrissae-related thalamic and brainstem nuclei, thus forming a large sensory-motor loop (Figure 1.3). Here, I am going to focus on the lemniscal pathway providing whisker-specific signals from the ventral posterior medial nucleus of the thalamus (VPM) to vS1, and on intrinsic cortical circuits within vS1.

The lemniscal pathway originating in brainstem principal nucleus of the trigeminal complex is relayed via VPM thalamus and terminates in L4. Thalamocortical inputs are met with strongly interconnected L4 circuitry which in terms of synaptic numbers and strengths is affected much more by internal cortical circuitry than the thalamic input. L4 then projects the bulk of its output fibers to L2/3 which in turn send a major pathway down to L5 (Figure 1.4; for a review see [15]).

Extracellular recordings of action potential firing and intracellular recordings of membrane potential have provided rich information about barrel cortex function. Extracel-

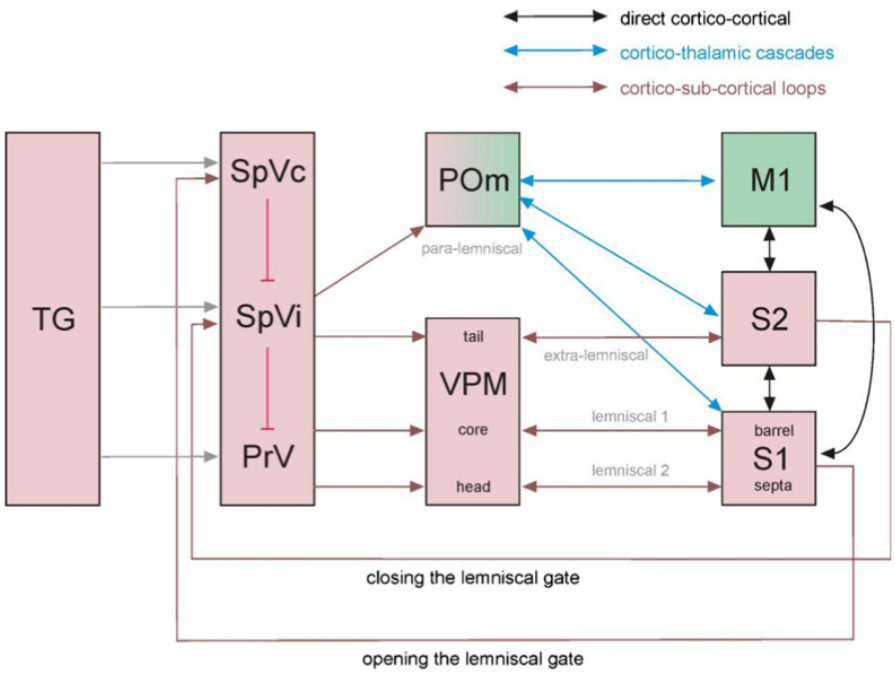

Figure 1.3: Functional organization of the rat vibrissal system. TG: trigeminal ganglion. SpVc: spinal trigeminal nucleus pars caudalis. SpVi: spinal trigeminal nucleus pars interpolaris. PrV: principal trigeminal nucleus. POm: posterior medial subdivision of the thalamus. VPM: ventral posterior medial nucleus of the thalamus. M1: primary motor cortex. S2: secondary somatosensory cortex. S1: primary somatosensory cortex. In this study, I will focus on the lemniscal pathway from VPM to vS1, and on circuits within vS1. Figure adopted from [14].

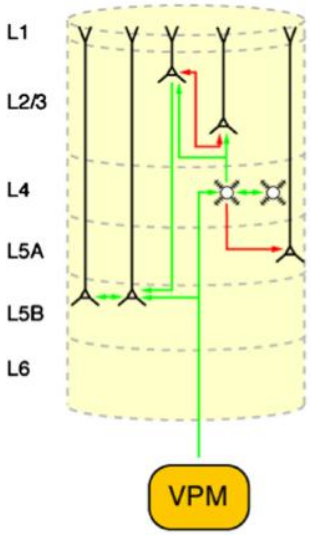

Figure 1.4: The 'canonical' microcircuit of rat vibrissal cortex. The 'canonical' microcircuits receiving lemniscal thalamic input from the ventroposterior medial nucleus (VPM) predominantly in L4 (and to lesser degree in L5B). Figure adopted from [14].

lular microelectrode recordings in anaesthetized, awake and behaving rats revealed the typical cortical response in the main receiving column ('the principal column', PC) to precise single-whisker deflections, which is a short lasting excitatory response typically followed by strong inhibition. The inhibitory period suppresses tactile inputs following at a short interval fitting the notion of a fine balance between excitatory and inhibitory signal flows [16, 17, 18, 19, 20, 21, 22]. Activation of barrel cortex follows a laminar pattern [23, 24, 25]. However, relating response patterns to the neuron type by juxtacellular recordings and subsequent neuronal reconstruction [26, 27] confirmed layer-specific delays of transient responses but showed clear deviation from what would be expected from the known anatomically defined sequence of intracolumnar projections discussed before. The shortest latencies were found in L4, and L6, the thalamus-recipient layers, as expected by available anatomical data. However, L5B thick tufted cells, which appear as an endpoint of cortical processing, show similar short latency responses. It has been shown that L5 neurons receive significant thalamic input, via their apical dendrites in L4 and their basal dendrites in L5 and L6, and therefore bypass processing in L4 and L2/3 [28, 29, 30, 31, 32].

The best-studied properties of barrel cortex receptive fields are multi-whisker integration and directionality. It is important to point out that these properties already exist on the ascending pathway but are transformed at the entry to the barrel cortex [33]. Therefore, it is an ongoing experimental effort to find out which aspect of the multi-whisker response is due to integration on the ascending pathway and which one is generated by trans-columnar processing [23, 34, 35, 36, 37, 38, 39]. A current consensus is that trans-columnar processing plays generally a leading role in shaping excitatory and inhibitory parts of receptive fields [40, 35].

However, current models of how receptive fields are generated at the synaptic level disagree with recent experimental findings. For example, a popular model of generating responses in cortical neurons is to assume that functionally specific excitatory synaptic inputs are spatially clustered on dendritic branches [41]. When activated by the same stimulus, the effect of these synapses is nonlinearly amplified by voltage-dependent NMDA receptors, leading to a response of the postsynaptic neuron. However, two-photon imaging of putative excitatory synaptic inputs in cortical neurons revealed that these

inputs are not spatially clustered, but rather randomly distributed (i.e. in a salt-and-pepper-like pattern) across the dendrites of the postsynaptic neuron [42, 43]. A different model suggests that instead of spatial clustering of synaptic input, synchronous activation of synapses (i.e., within a few milliseconds) may underlie sensory-evoked responses of cortical neurons [44]. However, this has only been demonstrated experimentally for thalamic input giving rise to sensory-evoked responses after deflection of the principal whisker (PW, i.e., somatotopically aligned to the barrel column where the neuron is located) [45]. In contrast, responses to surrounding whiskers (SuW), as mentioned above, are assumed to be shaped by intracortical connections. However, to date it has remained unclear what the underlying pathways are.

This problem is often studied on the example of two cell types in rat vS1: L2 pyramidal neurons in the superficial layers, which are easily accessible experimentally, and L5 thick-tufted pyramidal neurons, which provide output from cortex to various subcortical regions. The receptive field properties of both cell types in response to PW and SuW deflections have been widely studied at the sub- and suprathreshold level [46, 47, 26, 48]. Here, I will show which pathways are underlying the broad subthreshold responses of L2 pyramidal neurons to SuW deflections, which have been observed to be highly heterogeneous [43], and how the interaction of excitatory and inhibitory synapses results in a robust representation of the sensory stimulus. Further, I will identify the specific pathways underlying the sub- and suprathreshold responses of L5 thick-tufted pyramidal neurons. Here, synchronous thalamocortical and intracortical synaptic inputs give rise to PW responses of this cell type, while the response to SuW deflections is mediated by a specific cell type in cortical L6.

Chapter 2

Methods

Anatomical data required to determine cell type-specific synaptic input distributions of neurons in rat vibrissal cortex span many orders of magnitude in spatial scale. For example, individual boutons (swellings along axons and presynaptic part of a synapse) and spines (protrusions from dendrites and postsynaptic part of a synapse) have a size in the order of micrometers [49], while the total length of axons of individual neurons can reach up to tens of centimeters [50]. Further, anatomical data are acquired in many different experiments and using different histological protocols to visualize different parts of neurons and the brain. For example, to reconstruct the morphology of dendrites, soma and axon of single neurons, usually only one neuron is labeled in an individual experiment [51, 52]. In other experiments, neuron-specific proteins expressed in the soma are labeled immunohistochemically to determine the total number of neurons in a brain region [53, 30]. Therefore, I first developed a method to register anatomical data from different experiments to an average 3D model of rat vS1 using anatomical landmarks (i.e. the barrels in L4, the pia and white matter surfaces) as references [54]. The goal of this registration method was to minimize systematic errors of morphological and anatomical measurements due to tissue processing in order to determine the biological variability of morphological and anatomical parameters between different animals. Second, I determined the total number and 3D distribution of all excitatory and inhibitory neuron somata in rat vS1 and VPM thalamus and their variability across animals (collaboration with Hanno Meyer at the Max Planck Florida Institute for Neuroscience). Third, I determined the number and spatial distribution of different morphological (i.e. dendrite and

axon patterns) types of excitatory and inhibitory neurons after registration to the average vS1 model (collaboration with Rajeevan Narayanan and Daniel Udvary at the Max Planck Institute for Biological Cybernetics). Based on these data, I developed a new concept and a statistical framework to determine anatomical synaptic connectivity between all neurons in vS1 using overlap of presynaptic bouton and postsynaptic spine distributions (collaboration with Vincent Dercksen at the Zuse Institut Berlin). This statistical model contains $\sim 6 \times 10^9$ synapses between $\sim 530,000$ neurons and allows statistical measurements of the average connectivity and its variability based on cell type identity, soma location and detailed 3D dendrite/axon morphology. Finally, I used the morphology of neurons reconstructed after physiological measurements to associate functional properties of these neurons, such as response probabilities or synaptic input strength, with the corresponding morphological cell types. These data and tools allowed me to embed individual neuron models into the network model of vS1 and statistically measure the distribution of synaptic inputs at subcellular resolution, as well as the response probabilities of presynaptic neurons based on their cell type identity. Monte Carlo sampling from the distribution of these model constraints, where each sample determines a possible pattern of active synaptic inputs impinging onto the neuron model after whisker deflection (i.e., a trial), was then used to simulate the response of these neurons to many trials of sensory-evoked synaptic input patterns.

2.1 Acquisition of anatomical and functional data

Experiments to acquire functional and/or morphological data in the present thesis were performed by Arno Schmitt and Damian Wallace (Max Planck Institute for Biological Cybernetics, Tuebingen, and caesar institute, Bonn), Christiaan de Kock (VU University, Amsterdam), Rajeev Narayanan (Max Planck Institute for Biological Cybernetics, Tuebingen), Mike Hemberger (Max Planck Institute for Medical Research, Heidelberg), Marlene Arzt and Hanno Meyer (Max Planck Florida Institute for Neuroscience).
Note: All methods have been described in detail previously and are adopted from the respective publications [54, 55, 52, 56, 57].

Animal preparation. All experiments were carried out in accordance with the Dutch law after evaluation by a local ethical committee at the VU University Amsterdam, The Netherlands, and with the animal welfare guidelines of the Max Planck Society. All procedures have been described in detail previously [26, 52]. Briefly, Wistar rats (P25-P45, m/f, Charles River) were anesthetized with isoflurane and subsequently with urethane by intraperitoneal injection. The depth of anesthesia was assessed by monitoring pinch withdrawal, eyelid reflexes and vibrissae movements. Throughout the experiment, the animal's body temperature was maintained at 37.5 ± 0.5^oC by a heating pad.

In vivo recording and labeling of single neurons. In vivo cell-attached recordings and biocytin fillings have been described in detail previously [51, 52]. Briefly, pipettes were filled with normal rat ringer supplemented with 2% biocytin. The pipette was advanced in $1\mu m$ steps to locate single neurons, which was indicated by an increase in electrode resistance (unbiased sampling, irrespective of spiking activity). Juxtasomal biocytin filling was performed by applying square pulses of positive current. Filling sessions were repeated to obtain high quality axon fillings.

Unlabeled inhibitory interneurons (INs) located in L1 and pyramidal neurons (PNs) in L2 of rat vS1 were targeted for whole-cell electrical recordings using two-photon (2p) microscopy. Recordings were targeted to the principal column (PC, i.e., the barrel column containing the neuron's soma) / surround column (SC, i.e., a barrel column different from the PC) using intrinsic optical imaging (IOI). The pipette solution contained $0.3 - 0.5\%$ biocytin, and neurons were labeled after recording sessions. Fluorescent dye was added to visualize the pipette and the patched neurons. Membrane potential was recorded using an Axoclamp 2-B amplifier or a MultiClamp 700B amplifier (Axon Instruments) and digitized using a CED power1401 data acquisition board (CED; Cambridge Electronic Design).

Whisker stimulation. A piezoelectric stimulator was attached to a whisker $\sim 10mm$ from its base, and the whisker was deflected by 3.3 to $\sim 5^o$ ($\sim 1mm$ amplitude) for 200-500ms. Stimulation was repeated at constant intervals of 2–3.5 s, was not triggered by membrane potential, and occurred randomly with respect to up- and down-states.

Histology. Animals were transcardially perfused with 0.9% saline followed by 4% paraformaldehyde (PFA). Brains were removed and post-fixed with 4% PFA for 24h,

transferred to 0.05M phosphate buffer and stored at 4^o C.

For reconstruction of neuron morphology, $100\mu m$ thick vibratome sections were cut tangential to vS1 (45^o angle) ranging from the pia surface to the boundary of the white matter. Sections 6-12 containing the granular part of cortex were processed for cytochrome-C oxidase staining in order to better visualize barrel contours [58]. All sections were treated with avidin-biotin (ABC) solution and subsequently neurons were identified using the chromogen 3,3'-diaminobenzidine tetrahydrochloride (DAB) for post-hoc reconstruction procedures [59]. Selection criteria for reconstructions were adequate labeling across all serial sections and sufficient cytochrome-C signals to reconstruct the barrel and septum pattern.

For neuron counting in cortex, 43-48 consecutive vibratome sections of $50\mu m$ thickness were cut tangentially to vibrissal cortex of 28-29 days old rats; and for neuron counting in thalamus, 15-18 $50\mu m$ thick sections were cut semi-coronally, i.e., approximately tangential to the barreloid field [60]. Sections were then double-immunolabeled for GAD67 [61, 62, 63] and NeuN [64] to reveal excitatory and inhibitory neuron somata, as described previously [53, 65].

2.2 Registration of anatomical data to an average reference frame

Note: The description of these methods is in parts adopted from Egger et al. 2012, Meyer, Egger et al. 2013 and Egger, Dercksen et al. 2014 [54], [55] and [66].

2.2.1 3D reference frame

The most important prerequisite to assemble average dense models of the neuronal circuitry is the definition of an average 3D reference frame that allows integration of anatomical data obtained from many animals. In general, the reference frame describes the 3D geometry of the brain region(s) of interest in terms of anatomical landmarks. Further, it specifies the variability of these landmarks across animals, which serves as a resolution limit of the average network model. More specifically, the 3D reference frame has to de-

scribe (i) the boundaries of the brain region(s) of interest, (ii) anatomical substructures within these regions, and (iii) a global and/or multiple local coordinate systems. The latter reflects the general scenario that brain areas have irregular and/or curved boundaries and sub-structures. In case of rat vS1, the 3D reference frame has been generated by reconstructing the pia surface of entire rat cortex, the white matter tract (WM) boundary surface and the circumferences of 24 cortical barrel columns (i.e. each representing one of the large facial whiskers on the animals' snout [67]). Using high-resolution 3D images of the left hemisphere of Wistar rats at an age of 28 days (Figure 2.1, [54, 68]), 2D outlines of barrels, the pia and WM surface were detected automatically in individual optical sections. The 3D pia and WM surfaces, as well as barrel top and bottom points and orientations were reconstructed in 3D from these 2D contours. Barrel columns were reconstructed by extrapolating the L4 barrel outlines along the vertical column axes towards the pia and WM surfaces (compensating for overlapping columns in deep layers [54]).

Repeating these reconstructions for 12 animals of the same strain and age, I superimposed all geometries using rigid transformations, minimized the distances between the respective center locations of the 24 barrel columns and calculated the average column center locations, column diameters and orientations, as well as the average 3D surfaces of the pia and WM above and below vS1, respectively (Figure 2.2).

The column centers are given with respect to a global coordinate system, where the z-axis is defined as the shortest perpendicular axis between the center of the barrel column representing the D2 whisker and the pia surface above the column. The x-axis points from the D2 center towards the center of the first adjacent rostral column (i.e. along the whisker row towards D3). The y-axis points approximately towards the first adjacent caudal column (i.e. along the whisker arc towards C2). Because the pia and WM surfaces are curved, the orientation of each barrel column is tilted with respect to the (D2) z-axis. Therefore, I determined 23 additional local coordinate systems (i.e. for each barrel column), using the same approach used to determine the global D2 coordinate system. The final average reference frame of rat vS1 thus comprises the average pia and WM surfaces, 24 column center coordinates and diameters with respect to the global D2 coordinate system and 24 z-axes, representing local coordinate systems that define the

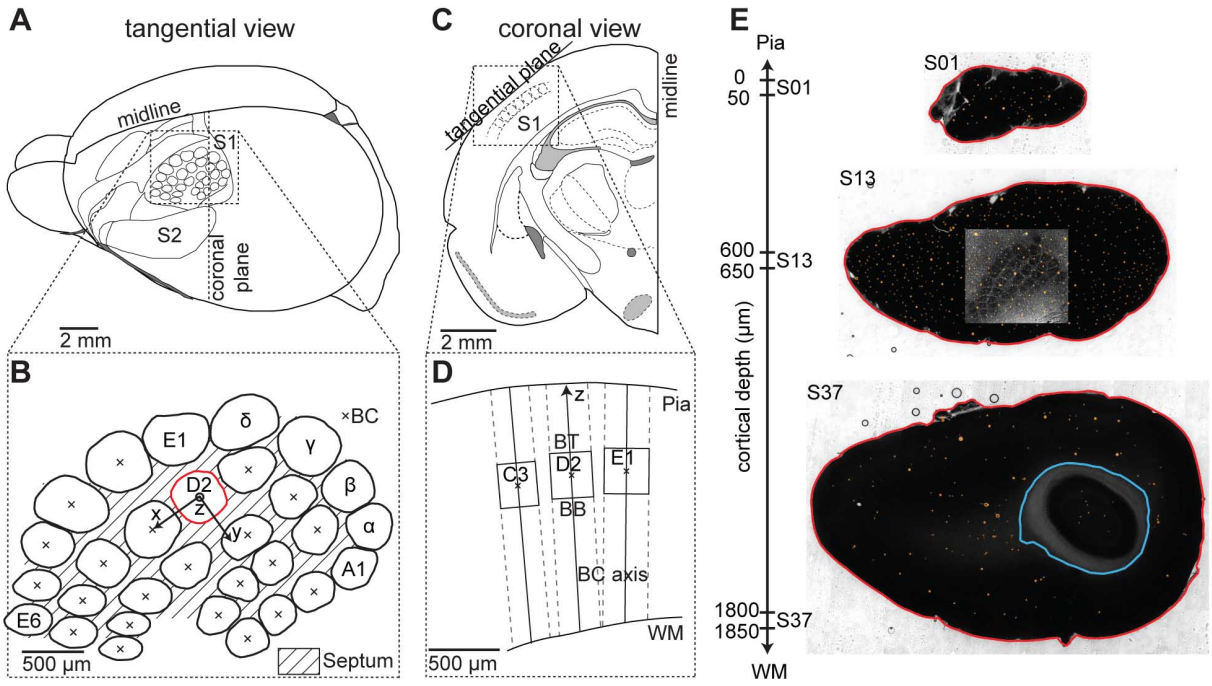

Figure 2.1: 3D reconstruction of anatomical landmarks in rat vibrissal cortex. (A) Tangential view of the left hemisphere of a rat brain. The barrel field is located in the primary somatosensory cortex (S1), adjacent to the secondary somatosensory cortex (S2). (B) The barrels are arranged in a somatotopic layout of rows (A–E) and arcs (1–6). The four barrels in front of the first arc are named by greek labels (α-δ). The barrel center (BC) is the centroid of a barrel and is used to describe the 3D location of individual barrels. The coordinate system used to describe the 3D layout of the barrel field based on the position of the BCs is centered on the D2 barrel (red), which is centrally located within the barrel field. The z axis points vertically along the D2 barrel column axis, the x axis is chosen to point towards the D3 barrel center (approximately along the row) and the y axis is perpendicular to the x and z axes and points approximately along the arc. (C) View of a coronal section of the left hemisphere (see dashed line in a). Barrels can be visualized by cutting cortical sections tangential to the barrel cortex. (D) The barrel cortex is organized into vertical barrel columns. These are obtained by cylindrical extrapolation of the barrel outlines along their respective BC axis to the pia and WM, respectively. The location of a barrel along the BC axis is described by the barrel top (BT) and barrel bottom (BB) points. (E) Tangential sections through rat cortex, indicating the relative depth below the pia, with anatomical landmarks: red – pia, blue – WM, orange – blood vessels. The inset in section S13 shows an example of a high-resolution optical section of the barrel field. Figure adopted from [54].

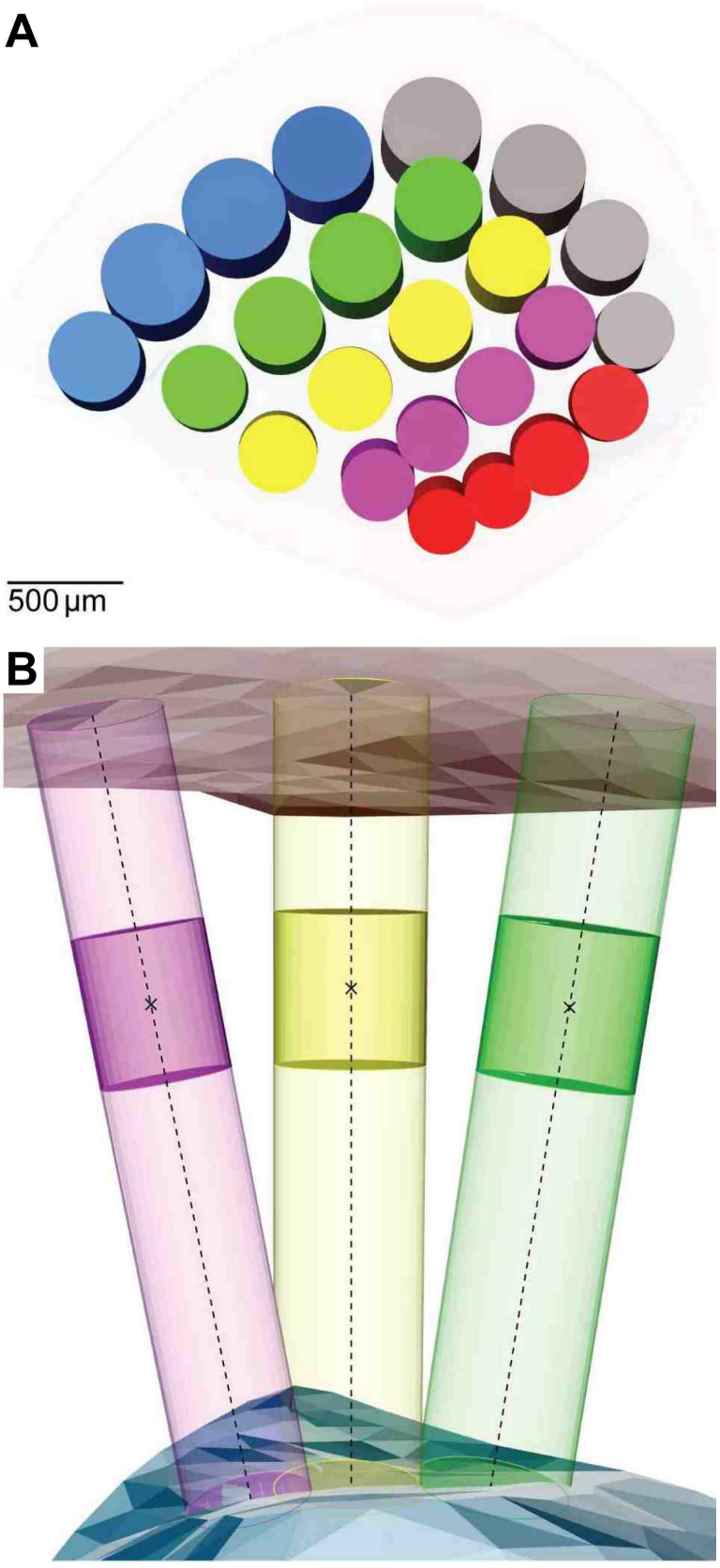

Figure 2.2: Average 3D reference frame of the barrel cortex. (A) Standardized barrels, pia and WM shown from a tangential view. (B) Three standardized barrels and barrel columns (B3, C2, D1), pia and WM shown from a (semi-coronal) side view. Figure adopted from [54].

orientation of each barrel column within the curved cortex. I further measured the variability of these anatomical landmarks across animals. The 3D standard deviations (SDs) of the column center locations were on average $89\mu m$ (i.e., equivalent to a cube with $\sim 50\mu m$ sides), of the pia-WM distances $\sim 100\mu m$ and of the column orientations 4.5^o (see section 3.1.1). Thus, I defined the resolution limit of the average reference frame accordingly as $50\mu m$. Consequently, the volume comprising the average reference frame of rat vS1 was superimposed with a grid of 50x50x50μm^3 voxels and a local z-axis was calculated for each voxel by interpolating from the respective nearest barrel column axes. The resolution limit of the average reference frame poses a lower limit for the possible precision with which anatomical data from different experiments can be registered, and determines the spatial resolution at which synaptic connectivity between different neurons in the average network model can be estimated.

2.2.2 3D registration of anatomical landmarks

All anatomical and morphological data, when acquired with respect to a 3D reconstruction of the anatomical landmarks present in the reference frame, can be registered to this reference frame. Each 3D reconstruction of the anatomical landmarks in an individual experiment is aligned to the average reference frame of rat vS1 by matching the location of corresponding anatomical landmarks using rigid 3D transformations, i.e., translation, rotation and scaling. The optimal transformations are found by minimizing the sum of squared distances between corresponding anatomical landmarks in the individual experiment and the average reference frame. The optimal translation aligns the centers of mass of the reconstruction and the average reference frame [69]. After translation to the center of mass, an optimal transformation for each 3D reconstruction is computed by minimizing the sum of squared differences S between the barrel top and barrel bottom points of corresponding barrels in the reconstruction and the average reference frame:

$$S = \sum_{i=1}^{n} (\vec{x}_{i,Avg} - T \cdot \vec{x}_{i,Recon})^2$$

Here, $i = 1, \ldots, n$ enumerates the corresponding barrel top and barrel bottom points, T is a transformation matrix, and Avg and $Recon$ refer to the average reference frame and

the reconstruction to be matched at each corresponding point i. To compute the optimal rotation, all points that are to be aligned are then written in two 3xN matrices M_{Avg} and M_{Recon}. Now, the optimal transformation matrix T_{opt} can be computed from the singular value decomposition (SVD) of:

$$M_{Recon}M_{Avg}^T = V\Sigma U^T$$

V and U are orthogonal matrices whose columns are the left and right singular vectors of $M_{Recon}M_{Avg}^T$, respectively. The matrix Σ has the singular values as entries on the diagonal. The optimal rotation can now be computed:

$$T_{opt} = UV^T$$

(see [69]). During registration of neuron somata counts to the average reference frame of vS1, scaling in the horizontal (i.e. the x-y) plane is allowed in addition to rotation. In these experiments, tissue sections are processed to allow immunohistochemical staining of neuron somata and not fixed, but prepared as free-floating sections. This can lead to anisotropic deformations in the horizontal plane. In this case, the transformation matrix is regarded as the product of a rotation matrix R and a scaling matrix $\Lambda = diag(\lambda_x, \lambda_y, 1)$. Finding the optimal transformation matrix $T_{opt} = R_{opt}\Lambda_{opt}$ is done using an iterative algorithm that alternates between solving for the optimal rotation matrix and the optimal scaling matrix. In this iterative algorithm, the optimal transformation matrix can be computed from the SVD of:

$$\begin{aligned} \Lambda M_{Recon}M_{Avg}^T &= V\Sigma U^T \\ \Rightarrow T_{opt} &= UV^T \end{aligned}$$

In the alternating step, the elements λ_k of the optimal scaling matrix Λ_{opt} can be computed as:

$$\lambda_k = \frac{\left(M_{Recon}M_{Avg}^T R_{opt}\right)_{kk}}{\left(M_{Recon}M_{Recon}^T\right)_{kk}}$$

Here, the index kk refers to the diagonal elements of the matrices in the numerator and denominator of the expression. Iteration is stopped when the relative change of the sum of squared distances between iterations is smaller than 10^{-3}.

2.2.3 3D reconstruction of neuron somata distributions

Images used for automated detection of neuron somata were acquired using a prototype confocal laser scanning system (based on LAS AF SP5, Leica Microsystems) equipped with a glycerol/oil immersion objective (HC PL APO 20x, 0.7 N.A.), a tandem scanning system (Resonance Scanner), spectral detectors with hybrid technology (GaAsP photocathode) and mosaic scanning software (Matrix Screener (beta-version), provided by Frank Sieckmann, Leica Microsystems). Mosaic image stacks of volumes up to 5mm x 3.5mm x 0.05mm (in cortex) and 3mm x 3mm x 0.05mm (in thalamus) were acquired at a resolution of $0.36075\mu m$ x $0.36075\mu m$ x $0.5\mu m$ per voxel (2.5x digital zoom, 8x line average, 8kHz scanning speed, 15x10 and 9x9 fields of view in cortex and thalamus, respectively) for each consecutive brain section.

NeuN-positive somata were detected in each confocal image stack using a previously described automated counting algorithm ([70]; Figure 2.3). Each detected soma is represented by a 3D position landmark. The accuracy and robustness of the algorithms has been validated against manual counts performed by expert users [70, 53]. The precentage of false-positive and false-negative detected NeuN-positive somata was $\sim 5\%$ each, and the mean deviation of the automatically detected 3D soma location was $\sim 6\mu m$. For detection of GAD67-positive somata, the previously reported automated algorithms were modified to allow for reliable detection independent of the density of GAD67-positive boutons. Images were subdivided into overlapping bricks of 1024x1024 pixels. Uneven background intensity within bricks due to spatially varying density of GAD67-positive boutons was removed, followed by detection and removal of individual GAD67-positive boutons. Accuracy and precision of the automated counts of GAD67-positive somata was validated by comparison with manual counts by an expert user (Hanno Meyer). At a resolution of $50\mu m$ (corresponding to the resolution of the average model of rat vS1), the percentage of false-positive and false-negative detected GAD67-positive neuron somata

was $\sim$ 12%. Hence, the inter-animal variability of neuron somata distributions can be determined with $\sim$ 5% accuracy for all neuron somata at a resolution of $50\mu m$, and with $\sim$ 12% accuracy for excitatory and inhibitory neuron somata distributions at a resolution of $50\mu m$.

Note: In 5 out of 96 columns (A1-3, B2-3), the automated routines failed to reliably separate between GAD67-positive and negative somata in some portions of supragranular and granular layers. Excitatory/inhibitory neuron numbers of A1-3 and B2-3 in vS1 are thus based on data from 3, instead of 4 animals.

After automated detection of neuron somata in each section, the 3D distribution of landmarks from each section was scaled to a section thickness of $50\mu m$ to compensate for tissue shrinkage along the slicing direction. Outlines of anatomical structures (i.e. pia, barrels and WM in cortex, and VPM, barreloids and the thalamic reticular nucleus (RT) in thalamus) were manually drawn on median projections of the GAD67 image stacks for each section for the neuron soma count experiments. Using the blood vessel patterns as reference landmarks, the contours and soma landmarks of adjacent cortical brain sections were aligned manually by rigid transformations using ZIBAmira software (VisualizationScienceGroup) [54]. Contours and soma landmarks from thalamic sections were aligned analogously using the outlines of RT and individual barreloids as reference structures. 3D reconstruction of cortex geometry was performed as described above. Barreloids in VPM were reconstructed from 2D outlines using 3D Delaunay triangulation.

After alignment of all sections and 3D reconstruction of anatomical landmarks, each neuron soma was assigned to the closest barrel column/barreloid or to septum, as well as to supragranular, granular or infragranular cortical layers (i.e., above, within or below the L4 barrels). Total neuron counts for individual columns/barreloids were obtained by counting all neuron somata assigned to the same column/barreloid. Vertical density profiles were computed in $50\mu m$ steps along the respective vertical column axes. Density profiles along the row or arc were obtained after registration of the 3D neuron somata distribution of all experiments to the average model of rat vS1, as described above (section 2.2). After registration, each counting dataset was superimposed with a $50\mu m$ voxel grid and converted into two 3D somata distributions for excitatory and inhibitory neurons, respectively (i.e. number of somata in 10^3 per mm^3). Finally, all four 3D somata density

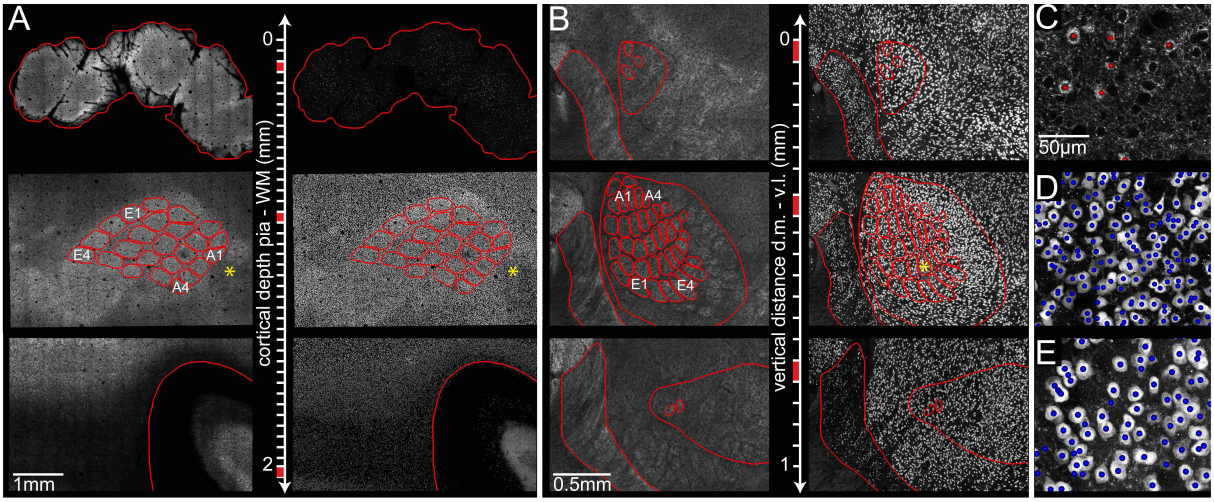

Figure 2.3: Automated detection of all excitatory and inhibitory neuron somata in the vibrissal areas of rat somatosensory cortex and thalamus. (A) Large-scale, high-resolution confocal image stacks from 50μm-thick brain sections, cut tangentially to the cortical surface from the pia to the WM. (Left) GAD67 projection images allow delineation of anatomical reference structures (red) in each section, such as pia, L4 barrels, and WM. (Right) NeuN projection images in the same sections. (B) Confocal image stacks from 50μm-thick sections of vibrissal thalamus, cut tangentially from the dorsal medial (d.m.) to the ventral lateral (v.l.) direction. (Left) GAD67 projection images allow delineation of anatomical reference structures (red), such as RT (Left), VPM (Right), and individual barreloids. (Right) NeuN projection images in the same sections. (C) Optical section of GAD67 image stack from A (*) superimposed with landmarks representing automatically detected inhibitory somata (red). (D) NeuN-positive somata were automatically detected within the same area. (E) Area from B (*) with automatically detected NeuN-positive neuron somata. Brightness has been adjusted in all panels for visualization purposes. Figure adopted from [55].

distributions were averaged separately for excitatory and inhibitory neurons.

In summary, the present approach of automated detection of all neuron somata within entire rat vS1 allowed to analyze the 3D distribution of excitatory and inhibitory neuron somata at the resolution of the average model of rat vS1. Therefore, no assumptions about organizational principles of neuron somata were necessary during development of the average model of neural networks in rat vS1, as presented later in section 2.4.

2.3 Morphological cell type assignment of neurons in vS1

Note: This description is in part adapted from Narayanan, Egger et al. 2015 [56].

The concept of cell types is used here to describe neurons that share common properties of synaptic input, sensory-evoked responses and synaptic output to other neurons. Synaptic input to neurons is largely determined by soma location and dendrite morphology, while synaptic output is related to the axon projection patterns. Hence, I used morphological parameters of neuron somata, dendrites or axons to objectively determine cell types in rat vS1. These morphological cell types serve to combine morphological, physiological and functional data from experiments performed in different animals to generate an average model of the neural networks in rat vS1, as well as network embedded simulations of single neurons with cell type-specific distributions and properties of synaptic input.

3D morphological reconstructions. The dataset used for determination of morphological cell types should reveal location-dependent differences in morphology, spatial distribution and overlap of different cell types at the resolution of the average reference frame of rat vS1, i.e., capturing the morphological variability between and within cell types. In order to obtain such a representative and unbiased sample of different cell types in rat vS1, neurons across the entire cortical depth were targeted blindly in vivo (in case of excitatory neurons) or based on their soma shape in vitro (in case of inhibitory interneurons). In total, 167 in vivo-labeled neuron morphologies of excitatory cell types and 204 in vitro-labeled neuron morphologies of inhibitory cell types were analyzed in this thesis.

Experiments to label excitatory neuron morphologies were performed by Christiaan de Kock and Rajeev Narayanan, in addition to 21 morphologies of excitatory cell types in vS1 and 14 morphologies of thalamocortical axons from VPM projecting into vS1 published previously and generously provided by Randy Bruno, Marcel Oberlaender and Bert Sakmann [71, 72, 50, 73]. Of the 153 neurons of excitatory cell types in vS1, 79 contained soma and dendrites, and 74 contained soma, dendrites and axon. Neuronal structures were traced manually using Neurolucida software (MicroBrightfield, Williston, VT; 78 re-

constructions with soma and dendrites, and 11 reconstructions with soma, dendrites and axon), or automatically extracted (n=64) from image stacks using a previously reported and validated automated tracing software [74]. 3D image stacks of up to 5mm x 5mm x 0.1mm were acquired in vS1 at a resolution of $0.092\mu m$ x $0.092\mu m$ x $0.5\mu m$ per voxel (i.e. at 100x magnification, numerical aperture 1.4). Manual proof-editing of individual sections and automated alignment across sections were performed using custom-designed software [75]. For registration of single neuron morphologies to the average reference frame of rat vS1, outlines of pia, barrels and WM in cortex were manually drawn on low resolution images (4x) of each section.

Experiments to label inhibitory neuron morphologies in acute brain slices were performed by Hanno Meyer, Marlene Arzt and Mike Hemberger (MPI Heidelberg and MPI Florida). In addition, 91 neuron morphologies of inhibitory cell types (also labeled in vitro) that have previously been published [76, 77] were kindly provided by Moritz Helmstaedter, Dirk Feldmeyer and Bert Sakmann. Neuronal structures were traced manually using Neurolucida software (MicroBrightfield, Williston, VT). The pia outline was drawn on a high-resolution (40x) image, while outlines of WM and the barrel bottom border were drawn onto a low-resolution image (4x) of the tissue section containing the neuron. These outlines were then used as landmarks for registration of the neuron morphologies to the average reference frame of rat vS1.

Excitatory morphological cell types. Dendritic cell types were determined based on 22 morphological, topological and reference frame-dependent features that were determined for each dendrite reconstruction after registration to the D2 column [54]. In the first step, all cells were grouped under manual supervision with the help of the OPTICS algorithm [78]. Briefly, this algorithm results in a sorting of all data points based on the density of data points in the 22-dimensional feature space, and their respective distances to each other in this feature space. Neurons that are located closely in feature space are located closely in the resulting sorting. However, this sorting does not result in assignment of neurons to different groups. Instead, groups are assigned manually based on the sorted results of the OPTICS algorithm, i.e., neurons that are located closely in the OPTICS sorting and have small mutual distance values are assigned to the same group. This revealed a clear separation between supragranular/granular (in the following

refered to as [supra-]granular) and infragranular neurons, except for one neuron, which was subsequently grouped with the [supra-]granular neurons based on its laminar soma location. Next, [supra-]granular neurons were sorted using OPTICS in 3D feature spaces that have previously been shown to separate supragranular and granular cell types, respectively [31]. Neurons that could be unambiguously assigned to the supragranular or granular feature spaces were not considered in the other feature space anymore. This procedure was iteratively repeated until a robust set of supragranular (4 groups comprising 38 neurons) and granular (4 groups comprising 36 neurons) groups was determined, while a minority of neurons (n=16) could not be unambiguously assigned. Infragranular neurons were sorted using OPTICS in a 21-dimensional feature space which has previously been shown to separate between infragranular cell types [31]. This sorting revealed 4 infragranular neuron groups comprising 56 neurons. For 7 neurons, unambiguous manual assignment to one of these groups was not possible. In order to also assign ambiguous neurons to one of the groups in an unbiased way, I calculated their distances to each group. The distance d_k of a neuron to group k was calculated as follows:

$$d_k = \sqrt{(\vec{f} - \vec{\mu_k})^T C_k^{-1} (\vec{f} - \vec{\mu_k})}$$

Here, $\vec{f}$ is the feature vector of the neuron, $\vec{\mu_k}$ is the mean feature vector of group k, and C_k^{-1} is the inverse covariance matrix of group k in the respective feature space. Intuitively, this is the distance of the neuron to the mean of group k in the feature space in units of standard deviations of each feature of group k. Because [supra-]granular and infragranular feature spaces have different dimensions (3 vs. 21), I converted these distances into a comparable probability space. Assuming that neuron features are normally distributed around the mean of each group, I converted each distance d_k into a probability p_k using the cumulative distribution function F of the chi-squared distribution (i.e. p_k is the probability of finding a neuron at a distance equal to or more than d_k from group k):

$$p_k = 1 - F(d_k^2, DOF_k)$$

Here, DOF_k are the degrees of freedom of group k. For [supra-]granular neurons, this was equal to the dimensions of the feature space. For infragranular neurons, this was equal to the rank of the covariance matrix C_k, because infragranular groups consisted of less neurons than the dimensionality of the infragranular feature space. In these cases, C_k^{-1} was replaced by the pseudo-inverse C_k^{+}. p_k was then compared to the values computed for all other groups and the neuron was assigned to the group with the highest value of p_k, and the probability of the neuron belonging to group k was calculated as:

$$P(k) = \frac{p_k}{\sum_{groups\, i} p_i}$$

These different groups were given cell type names by comparison of the dendrite morphology with previously reported cell types in rat vS1. In supragranular layers, excitatory cell types are named L2 pyramidal neurons (L2py), L3 pyramidal neurons (L3py); in granular layers, L4 pyramidal neurons (L4py), L4 star-pyramidal neurons (L4sp), L4 spiny stellate neurons (L4ss); in infragranular layers, L5 slender-tufted pyramidal neurons (L5st), L5 thick-tufted neurons (L5tt), L6 cortico-cortical pyramidal neurons (L6cc), L6 inverted pyramidal neurons (L6inv), and L6 cortico-thalamic neurons (L6ct). Finally, three groups in supragranular layers were merged to L3py, two groups in the granular layer were merged to L4sp and one neuron group in infragranular layers was split into the L6cc and L6inv based on common dendritic/axonal vertical projection profiles.

Inhibitory morphological cell types. Morphological cell types of inhibitory interneurons (INs) were determined based on 9 morphological and reference frame-dependent features of 204 in vitro labeled axon morphologies after registration to the D2 column (described in detail in the Master thesis by Daniel Udvary [79]). In contrast to excitatory cell types, INs were grouped based on their axon projection patterns to reveal organizational principles of inhibitory pathways along the vertical column axis. Axon projection patterns of INs were analyzed with respect to zones defined by variations in the density of inhibitory neuron somata along the vertical column axis (i.e., complementary to the concept of cortical layers as defined by variations of the density of excitatory neuron somata [53]). Because INs were labeled in acute brain slices, absolute axon length values may suffer from uncontrollable cutting artifacts, hence axon projection patterns along the

vertical column axis were normalized to an integral of 1. Similarly to the assignment of excitatory cell types, INs were sorted hierarchically using a supervised grouping method. Remaining INs that could not be assigned to one group were subsequently assigned based on the probability space defined by the set of unambiguously assigned groups of INs. In the first step, INs were sorted into two groups based on the vertical extent of their axon projection patterns (i.e., local projecting INs (n=80) with axon projections remaining close to the soma, and non-local projecting INs (n=78) with additional axon projections targeting other zones along the vertical column axis). In the next steps, non-local projecting INs were subdivided into 4 different groups based on their soma location and non-local axon projection patterns. INs were manually grouped based on their respective distances in 5- or 9-dimensional feature spaces, based on how many of the 9 features were required to separate IN groups. Similar to the sorting using the OPTICS algorithm described above, INs were sorted based on their mutual distances within these feature spaces (i.e., INs with similar feature values were grouped together). The resulting cell types were named according to the region along the vertical column axis where somata of each cell type were most commonly found, and according to their non-local projection patterns (supragranular-asymmetric projecting INs (n=11), granular-symmetric (n=11) and granular-asymmetric (n=9) projecting INs, and infragranular-asymmetric projecting INs (n=47)). In the last step, the remaining INs (n=46) were grouped using the probability space defined by unambiguously assigned INs.

Correlation of functional data with morphological cell types. In order to correlate functional and physiological properties of cortical neurons in rat vS1 with the above defined morphological cell types, I only used data from experiments where neurons were labeled and reconstructed after recording their functional or physiological properties. In a subset (n=57) of the excitatory neurons used for determination of morphological cell types described above, spontaneous spiking activity as well as responses to whisker deflections in the anaesthetized rats were recorded. Properties of synaptic connections between excitatory and inhibitory neurons in rat vS1 were based on studies in which physiological characterization of synapses (e.g. measurement of unitary excitatory/inhibitory postsynaptic potential (EPSP/IPSP) amplitudes, rise and decay time constants of EPSPs/IPSPs, or measurements of synaptic facilitation and/or depression) was fol-

lowed by labeling and reconstruction of neuron morphologies. Biophysical properties of cell types simulated in detail in network-embedded models were taken from in vivo or in vitro studies measuring the response properties of neurons to current injections into the soma and/or dendrites followed by labeling and reconstruction of neuron morphology. Correspondence between morphologies described in these studies and the cell types identified in this thesis was performed based on qualitative description of morphological features, because in vitro studies suffer from uncontrollable systematic errors in quantitative descriptions of morphological parameters of neurons [31, 56].

2.4 Generation of a dense statistical connectome from sparse morphological data

Note: The description in the following sections has been adapted from Egger, Dercksen et al. 2014 [66].

Here, I present a novel approach to statistically measure connectivity between neurons, implemented within an interactive software environment called NeuroNet, which formulates a coherent framework to measure structural overlap between two neurons, yielding connection probabilities with respect to all neurons present in the overlapping volume. Estimating synaptic connectivity based on structural overlap is commonly referred to as "Peters' rule" [80]. So far, no consistent quantitative framework for estimating connectivity between pairs of neurons based on this concept has been developed, leading to controversy about the validity and limits of Peters' rule [81, 82, 83, 84]. I developed a quantitative version of Peters' rule that requires generation of an average dense model of the neuronal circuitry; dense referring to the fact that every neuron within the model of the brain structure of interest (i) has to be distributed according to measured 3D soma distributions, (ii) is represented by a complete 3D reconstruction of soma, dendrites and axon found at the respective location and (iii) contains information of cell type, as well as subcellular distributions of dendritic spines, diameters and axonal boutons (Figure 2.4 A). NeuroNet allows integrating such anatomical data into a common reference frame

that describes the average geometry, as well as its variability across animals, of the brain region(s) of interest (Figure 2.4 B). Within the resolution of the reference frame, NeuroNet further allows calculating synaptic innervation between any two neurons in the model, always taking all other neurons within the respective overlap volumes into account (Figure 2.4 C). The resultant dense "statistical" connectome yields pairwise connection probabilities, statistical distribution of numbers of putative synaptic contacts between connected neurons and subcellular synapse distributions for all neurons within an entire brain region. Structural connectivity underlying network-embedded simulations is determined by sampling from these distributions.

NeuroNet has been implemented as an extension package for the Amira visualization software (VisualizationScienceGroup) by Vincent Dercksen (Zuse Institut Berlin), allowing for 3D visualization of anatomical input data, dense neuronal networks and synaptic connectivity measurements [85].

2.4.1 Anatomical input data

Mandatory anatomical input data to NeuroNet comprise: 1. an average 3D reference frame, 2. 3D distributions of excitatory and inhibitory neuron somata, 3. representative samples of cell type-specific complete 3D morphological reconstructions and 4. measurements of cell type-specific subcellular distributions of soma/dendrite surface areas, dendritic spines and axonal boutons. In the following I introduce the formats for presenting the respective data to NeuroNet at the example of anatomical data from rat vS1 (Figure 2.5).

1. Average 3D reference frame. The 3D reference frame of rat vS1 is presented to NeuroNet as follows:

1. A spreadsheet (csv file) contains information about the barrel column geometries with respect to the global coordinate system, i.e. the 3D center locations, column radii and a unit vector pointing along the respective orientation. Each column is further assigned a unique identifier (substructure) label.

2. A 3D vector field (AmiraMesh vector field) containing unit vectors at $50\mu m$ resolution pointing towards the curved pia surface. In general, such vector fields should

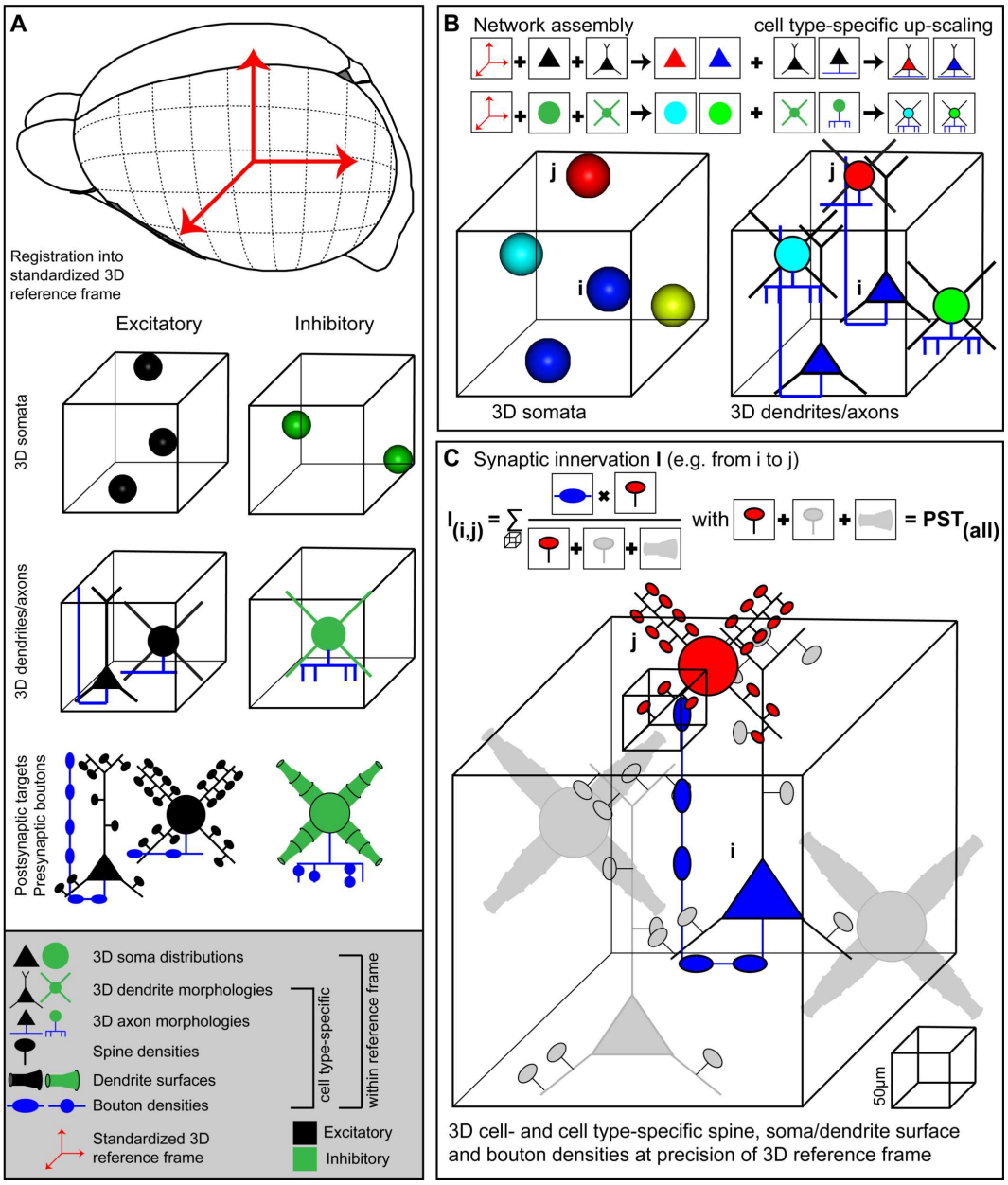

be sampled at the resolution of the 3D reference frame.

3. 3D boundary surfaces (AmiraSurface format) describing the 3D volume of the brain region (here: pia and WM surfaces). Additional boundary surfaces of anatomical substructures can be provided, e.g. borders of cytoarchitectonic cortical layers.

2. 3D soma distributions. The second anatomical prerequisite to generate an average dense model of the neuronal circuitry are measurements of the number and 3D distribu-

Figure 2.4 *(previous page)*: Generating dense statistical connectomes. (A) Generating a dense statistical connectome of a brain or brain region requires an average 3D reference frame of this brain region. The reference frame is used to register all anatomical data obtained from different experiments to a common coordinate system. Anatomical data to be collected from the brain region of interest: Number and 3D distribution of excitatory and inhibitory neuron somata; 3D reconstructions of representative samples of dendrites and axons of excitatory and inhibitory neuron cell types; determination of postsynaptic target sites, e.g., spine densities and dendrite surfaces, and presynaptic bouton densities for excitatory and inhibitory neuron cell types. (B) Anatomical data are assembled into a complete 3D network model. First, based on their 3D location, excitatory and inhibitory neuron somata are assigned to different anatomical substructures of the brain regions and to cell types. Next, somata of all cell types are replaced with dendrite and axon morphologies of the respective cell types. (C) Innervation from neuron i to neuron j is computed in 3D at a resolution determined by the anatomical variability of the 3D reference frame. This computation takes all possible postsynaptic targets of neuron i in addition to neuron j into account. Figure adopted from [66].

tion of excitatory and inhibitory neuron somata for the entire brain region(s) of interest (Figure 2.5 B). These distributions have to be obtained with respect to, and at the resolution of, the average reference frame. The average density fields of excitatory/inhibitory neuron somata for entire rat vS1 are provided to NeuroNet as 3D images (AmiraMesh format). I further determined the number of neurons per thalamic barreloid [86, 55], which provide whisker-specific input to the respective barrel column [87].

3. Cell type-specific 3D morphologies. The third prerequisite to generate an average dense model of the neuronal circuitry are reconstructions of complete 3D soma/-dendrite/axon morphologies of all cell types present in rat vS1 (Figure 2.5 C). For each cell type, a number of properties is defined using a spreadsheet:

1. whether the cell type is excitatory or inhibitory,

2. whether the morphology should be rotated during network assembly, i.e. if dendrites/axon display asymmetric projections, such as polar dendrites pointing towards the center of a barrel column (e.g. L4ss [71]),

3. whether the reconstructions contain only axon or dendrites/axon,

4. whether the cell type has somata within and/or outside barrel columns (e.g. L4ss/L4sp

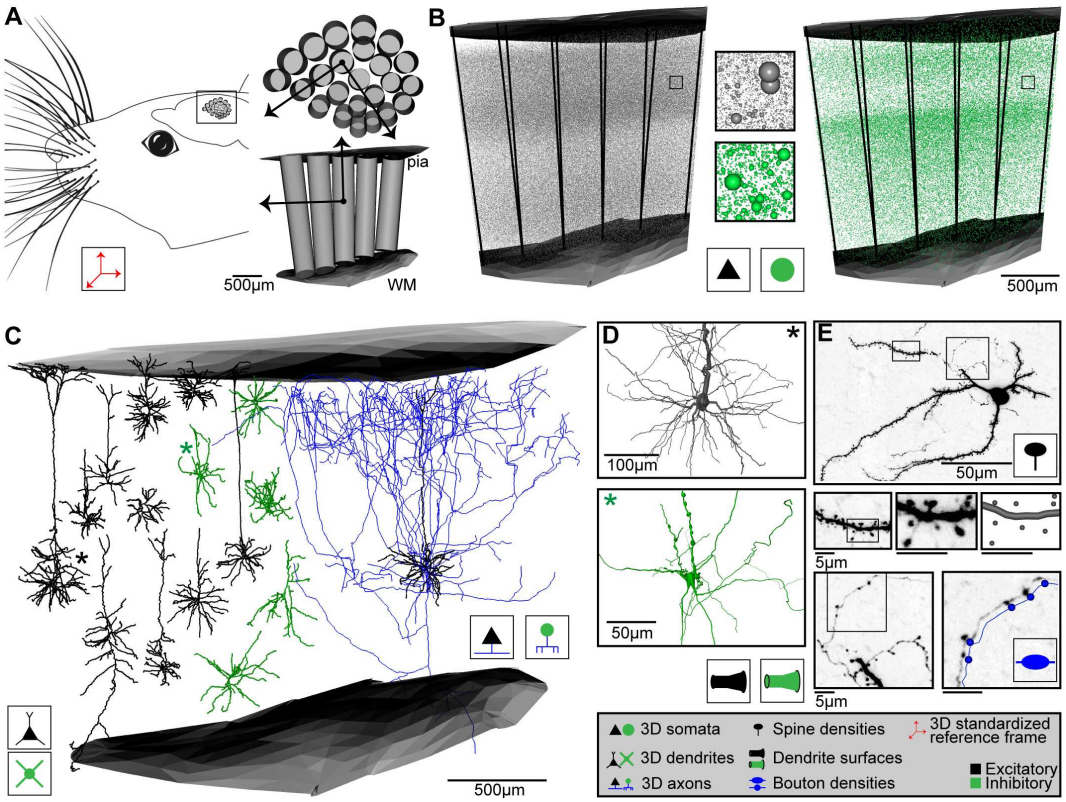

Figure 2.5: Anatomical data used for generating dense statistical connectomes of rat vibrissal cortex (vS1). (A) Left: Rat vS1 contains segregated anatomical structures, called barrels, which are arranged somatotopically to the pattern of the large facial whiskers. Right top: Tangential view of barrels in the average reference frame of rat vS1 cortex (see inset on left). These barrels provide natural landmarks for registration of anatomical data into the average reference frame. Bottom: Semi-coronal view of barrel columns in 3D. Pia and WM surfaces delineate the vertical cortical boundaries in 3D. (B) 3D distribution of excitatory (left) and inhibitory (right) neuron somata with respect to cortical barrel columns in rat vS1. Center: Close-up view of neuron somata in insets in left and right panels. (C) Left: 3D dendrite reconstructions of 10 excitatory (black) and 5 inhibitory (green) cell types. Right: 3D dendrite (black) and axon (blue) reconstruction of an excitatory L5 slender-tufted pyramidal neuron. (D) Close-up views of the soma and dendrite surface reconstructions of an excitatory (black, top) and an inhibitory (green, bottom) neuron, corresponding to the dendrite morphologies marked with an asterisk (*) in (C). (E) Determination of dendritic spines, dendrite surface and axonal boutons of a L4 spiny stellate neuron. Top: z-projection of a $50\mu m$ thick section containing the soma, dendrites and axon branches. Center: From left to right: Close-up view of dendrite branch in left inset in top panel; close-up view of dendrite segment in inset in panel to the left; digital reconstruction of dendrite surface and spine locations of dendrite segment in panel to the left. Bottom left: Close-up view of axon branch in right inset in top panel. Bottom right: Close-up view of axon segment in inset in bottom left panel, with digital reconstruction of axon and bouton locations along the axon (shifted for visualization). Figure adopted from [66].

are only located inside the column, but not in septa between columns [88, 45, 71]),

5. the density of presynaptic contact sites (i.e. boutons) per μm axon, in particular one value for boutons in infragranular, granular and supragranular layers of vS1, respectively.

Each neuron morphology is further registered to all barrel columns in the average reference frame of rat vS1. Because column height, column diameter, as well as the barrel height vary across rat vS1 [68], each morphology is scaled along the vertical column axis, and its relative radial soma distance to the column axis is preserved. This ensures that its laminar soma location, horizontal soma location (e.g. inside barrel column or in the septum between columns), as well as layer-specific dendrite and axon projections are preserved. Finally, the spatial distribution of each cell type is determined by 3D boundary surfaces that describe the (sub)regions(s) where the cell type is found. If more than one cell type is present within such a 3D region, the relative frequency of morphologies from each cell type within the overlap region is specified using spreadsheets for excitatory and inhibitory cell types, respectively. The morphologies are specified as Amira SpatialGraphs [75], and the branches comprising the morphologies are labeled as soma, apical dendrite, basal dendrite, or axon, respectively. Each cell type is represented twice, both as an axon cell type and a dendrite cell type. This implementation allows including long-range connections such as VPM axons, where soma/dendrites are located in the thalamus. The number of these long-range axon morphologies is specified using a spreadsheet based on cell counts in thalamus (i.e. the number of neurons per whisker-specific barreloid [55]).

4. Subcellular morphological statistics. The final anatomical prerequisite to generate an average dense model of the neuronal circuitry is measurements of the density of postsynaptic target sites (PSTs), i.e. spines along dendrites of excitatory neurons and surface areas of somata and dendrites of excitatory/inhibitory neurons for all cell types present within the brain region(s) of interest. 3D reconstructions of soma and dendrite diameters of excitatory and inhibitory neurons were performed manually using NeuroLucida software (Figure 2.5 D). Dendrite morphologies obtained using the automated reconstruction pipeline did not have associated diameter values. Therefore, I developed a database of dendrite branch diameters grouped by cell type and distance of

the branch tip to the soma based on the set of reconstructions with associated dendrite diameters. Dendrite branches of all reconstructions of the same cell type were grouped into basal and apical dendrites, and assigned to distance bins in $50\mu m$ steps if the distance of the branch tip to the soma was less then $400\mu m$, and in $100\mu m$ steps if the distance was greater than $100\mu m$. Diameter values of all branches were fit with an exponential function $A + B\exp(-Cd)$, where d is the distance of the branch tip to the soma. Parameter B was normalized by the soma diameter. The values of the fit parameters of all branches belonging to the same cell type and distance bin were averaged and stored in the database. Then, dendrite morphologies without associated diameter values were assigned diameter values by an exponential function with parameter values from the corresponding cell type/ soma distance entry in the database. Parameter B was scaled by the soma diameter of the morphology.

Average bouton length densities were obtained from high-resolution image stacks (100x, NA=1.4; 0.092 x 0.092 x $0.2\mu m^3$ voxel size) in supra-, granular and infragranular layers. Horizontally projecting axons were chosen for analysis. Bouton length densities were determined by manually marking the 3D location of each bouton along the reconstructed axons and measuring the respective path lengths between the marked boutons. Boutons were assigned as en passant or terminal. En passant boutons were identified as prominent and approximately spherical swellings along axonal branches, without definition of a minimal radius. Terminal boutons were identified as prominent and approximately spherical swellings located at the end of short axonal branches. Swellings were assigned as boutons only if the swellings were visible in all three image planes. Measurements were performed for n=11,386 boutons from axonal segments in n=22 different rats (see Table 2.1).

These data are grouped by morphological cell type. Connections between cell types are specified in NeuroNet using a spreadsheet (csv file) with predefined format. For each possible connection between two cell types, the presynaptic cell type, postsynaptic cell type, as well as the normalized number of PSTs per μm^2 area, and/or per μm branch length is defined, based on measured values (using the methods stated above) for each cell type and substructure (soma, apical dendrite, or basal dendrite). This meta-connectivity list thus specifies general knowledge of whether two cell types can in principle connect to each other and at which substructures. For example, inhibitory interneurons may specif-

Cell type	Supragra.	Granular	Infragra.
L2	0.31	0.31*	0.34
L3	0.23	0.25	0.25
L4py	0.18	0.25	0.22
L4sp	0.21	0.28	0.24
L4ss	0.24	0.27	0.25
L5st	0.19	0.24	0.28
L5tt	0.20	0.25	0.19
L6cc	0.20	0.27	0.26
L6inv	0.29	0.26	0.23
L6ct	0.27*	0.27*	0.27
VPM	0.28	0.31	0.34
L1	0.48	0.48*	0.48*
Other IN	0.20	0.20	0.20

Table 2.1: Cell type-specific bouton density. Densities are given in μm^{-1}. Values were determined separately for axon branches in supragranular, granular and infragranular layers. (*) Assumed because no horizontally projecting axon branches could be found.

ically innervate somata and dendritic shafts of excitatory neurons. Thus, connections from interneuron to excitatory cell types can be specified in the meta-connectivity list such that PSTs are exclusively calculated by the surface areas of the excitatory somata and dendrites (i.e. soma/dendrite surface-specific PSTs). In contrast, connections from excitatory to excitatory cell types may be specified in the meta-connectivity list such that PSTs are calculated exclusively by the spine densities (i.e. dendrite length-specific PSTs).

2.4.2 Data integration and up-scaling to generate average dense circuit models

Upon availability of the above described anatomical data in appropriate formats, NeuroNet automatically generates an average dense representation of the neuronal circuitry of the brain region defined by the reference frame (Figure 2.6). First, the cell type-specific boundary surfaces are integrated (Figure 2.6 A shows a subsample of the cell type-boundaries) into the 3D reference frame. Next, the excitatory and inhibitory somata distributions are registered into the 3D reference frame. Excitatory and inhibitory soma positions are generated for all voxels in the soma density grid by multiplying the

respective density values within the voxel volume (e.g. $(50\mu m)^3$) and rounding to the nearest integer. 3D soma locations within a voxel are drawn from a uniform distribution. Based on the 3D location, each soma is further assigned to a unique substructure (barrel column) and cell type (Figure 2.6 B). Each soma is assigned to the barrel column (modeled as a cylinder) that contains the 3D soma position. To determine the cell type, first the region containing the soma is determined by identifying its location with respect to the cell type boundary surfaces. The cell type is then selected randomly based on the relative frequency of cell types within this region (as specified by the respective csv file). Soma/dendrite morphologies are then placed at all computed soma positions (Figure 2.6 C). For each soma, a dendrite morphology is chosen at random from all morphologies fulfilling the following criteria:

1. the cell type of the morphology is the same as the cell type assigned to the soma,

2. the morphology is registered to the barrel column that is closest to the new soma location,

3. the soma location of the morphology is not further away from the new soma location than one voxel of the resolution of the average vS1 model (i.e., the original soma location of the morphology and its location within the model are within $\pm 50\mu m$ along the z-axis of the respective column).

The latter step guarantees that potential location-specific morphological properties are preserved within the resolution limit of the reference frame. Lastly, the morphologies are transformed as follows: (i) translation of the morphology to the new soma location; (ii) rotation around the soma, such that the vertical orientation is preserved and optionally (iii) cells with asymmetric projection patterns (e.g. polar dendrites) are rotated such that their orientation is retained (e.g. L4ss are rotated around the column axis to preserve projections towards the barrel column center). Third, axon morphologies of each cell type are inserted to match the number of somata/dendrites for each cell type (Figure 2.6 D). For each soma, an axon morphology is chosen at random from all morphologies fulfilling the following criteria:

1. the cell type of the morphology is the same as the cell type assigned to the soma,

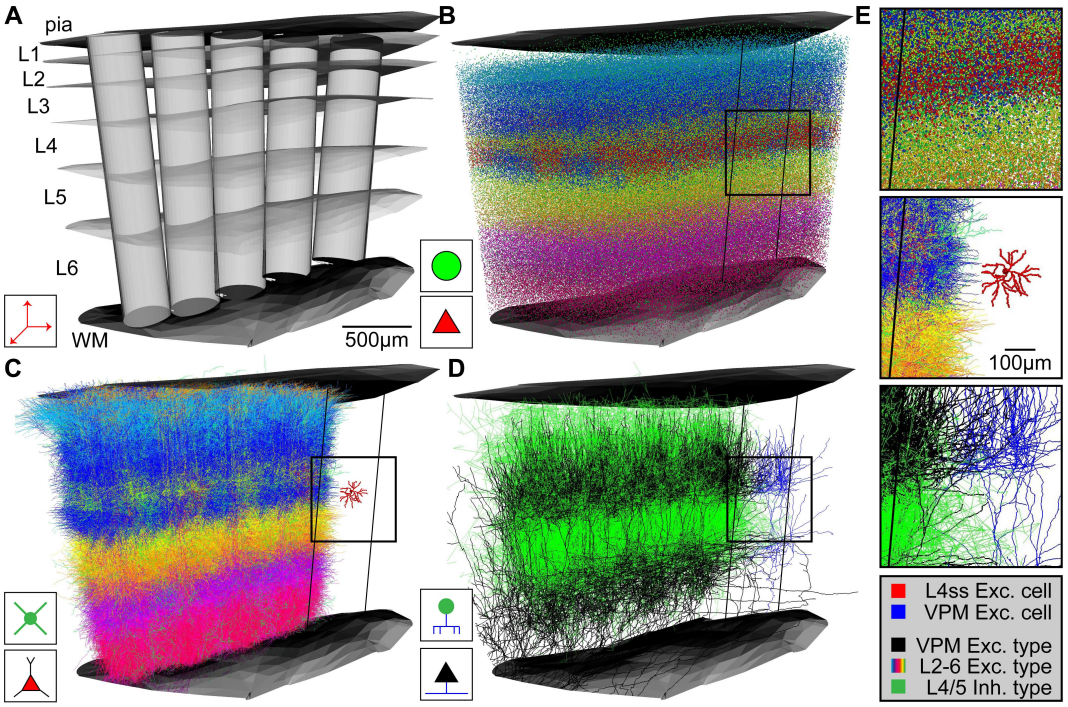

Figure 2.6: Network assembly process. (A) Average 3D reference frame of rat vibrissal cortex, with 3D organization of horizontal (i.e., barrel columns) and vertical (i.e., layers) structures. Every point in this brain region can be assigned to a barrel column and a cortical layer with $50\mu m$ precision. (B) 3D distribution of 530,000 somata of 10 excitatory and 6 inhibitory cell types. (C) Replacement of somata with cell type-specific 3D dendrite morphologies. (D) Replacement of somata with cell type-specific 3D axon morphologies. Shown here: Thalamocortical axons from VPM (black), intracortical axons of inhibitory interneurons (green). (E) Top: Close-up view of inset in (B). Center: Close-up view of inset in (C), showing the dendrites of a single L4 spiny stellate (L4ss) neuron (red) next to all dendrites from all cell types in the neighboring barrel column. Bottom: Close-up view of inset in (D), showing a single thalamocortical VPM axon (blue) next to all axons from two cell types in the neighboring barrel column. Figure adopted from [66].

2. the morphology is registered to the barrel column that is closest to the soma location.

In contrast to dendrite morphologies, axon morphologies are not transformed to new soma locations to prevent that rotation/translation results in loss of location-specific projection patterns (e.g. L4ss neuron in vS1 display axons confined to the respective barrel column containing the soma [71] and hence translations would result in innervation of septal areas, which is not observed experimentally). Long-range axons innervating the modeled brain region (i.e. their somata are located elsewhere) are registered in the same way as cell types with somata inside the brain region of interest, preserving their vertical and

horizontal projection patterns with respect to the reference frame at $50\mu m$ resolution. Then, long-range axons are up-scaled (i.e. duplicated) until the number of morphologies specified for this cell type is reached (e.g. VPM axons are up-scaled to meet the average number of somata per thalamic barreloid, e.g. 311 for the D2 whisker [55]). The result of the network assembly step is a dense representation of the neuronal circuitry of an entire brain region, where each neuron of a measured 3D soma distribution is represented by dendrite/axon morphologies of the appropriate cell type and location/orientation within the resolution of the average vS1 model (Figure 2.6 E).

2.4.3 Calculation of statistical synaptic innervation at subcellular levels

So far, the dense network model of rat vS1 does not contain synapses between neurons. The set of connections between all neurons in a network is usually referred to as a connectome [89]. The sparse morphological sample underlying the dense network model has been obtained from different animals, and hence anatomical connectivity can only be described statistically at the resolution of the average model. Here, I will describe how to obtain such a statistical connectome from the dense network model under the assumption of independent synapse formation. The statistical connectome describes the probability of finding a certain number of synapses between any two neurons in the dense network model, as well as the subcellular distribution of these synapses (i.e., their location on the dendrites/soma of the postsynaptic neuron at the resolution of the average reference frame of rat vS1).

First, for each presynaptic neuron i its axon is converted into a 3D bouton density at the resolution of the reference frame by clipping the axon of neuron i with all six faces of each voxel, summing up the length of the respective axon branches within the voxel and multiplying this value by the cell type- and substructure-specific bouton length density. Second, each postsynaptic neuron j is converted into a 3D PST density at the resolution of the reference frame by clipping the soma and dendrites of neuron j with all six faces of each voxel, summing up the length and the surface area of the respective dendrite branches and the soma and multiplying these values by the connection-specific PST length

or area density. Dendrite and soma surface area are computed from the diameter values along the branches using trapezoidal integration. 3D PST densities of each postsynaptic neuron j for connections with neurons of cell type *T(i)* of the presynaptic neuron i in the voxel centered on $\vec{x}$ are determined as the sum of two terms ($PST_{spines} + PST_{surface}$):

$$PST_j(\vec{x}, T(i)) = \sum_{labels\, L} l_{j,L}(\vec{x}) \cdot \lambda_{T(i),T(j)}(L) + \sum_{labels\, L} a_{j,L}(\vec{x}) \cdot \alpha_{T(i),T(j)}(L)$$

Here, label L refers to a subcellular structure of the postsynaptic neuron, i.e. soma, basal dendrite or apical dendrite. $l_{j,L}(\vec{x})$ is the total length of all compartments of label L of neuron j inside the voxel centered on $\vec{x}$ (in μm). $\lambda_{T(i),T(j)}(L)$ is the length PST density (e.g. 1 spine per μm basal dendrite) for connections from neurons of type *T(i)* to neurons of type *T(j)* onto target structures with label L (in μm^{-1}), as provided by spine density measurements and specified in the meta-connectivity spreadsheet. $a_{j,L}(\vec{x})$ is the total surface area of all compartments of label L of neuron j inside the voxel centered on $\vec{x}$ (in μm^2). $\alpha_{T(i),T(j)}(L)$ is the surface PST density (e.g. 0.4 PSTs per μm^2 soma surface) for connections from neurons of type *T(i)* to neurons of type *T(j)* onto target structures with label L (in μm^{-2}). Whereas bouton distributions can be measured (e.g. using the methods stated above), I derived spine and surface PST densities by assuming that the total number of boutons $B_{all}(\vec{x})$ (see Table 2.1) from all presynaptic cell types *T(i)* should match the number of total PSTs from all cell types *T(j)*:

$$\sum_{i,j} PST_{surface,j}(\vec{x}, T(i)) + PST_{spine,j}(\vec{x}, T(i)) = B_{all}(\vec{x})$$

I reduced this equation to 1 dimension (i.e. collapsing the 3D densities to the z axis), and assumed that:

1. connections from excitatory to excitatory cell types exclusively target spines (i.e. the surface PST density values were set to 0 [90])

2. connections from excitatory to inhibitory cell types exclusively target surface PSTs (including the soma), because inhibitory dendrites are usually aspiny (i.e. length PST density values were set to 0 [91])

3. connections from inhibitory to all other cell types exclusively target surface PSTs (i.e. inhibitory dendrites are usually aspiny, and inhibitory neurons target dendritic shafts and the soma of excitatory neurons [92])

4. spine density can be different in supragranular, granular and infragranular layers [93]

5. surface area PST density values are identical for all cell types and different subcellular structures (assumption, because no experimental data are available)

Then, I fit the respective PST density values $\lambda_{T(i),T(j)}$ and $\alpha_{T(i),T(j)}$ using standard least squares algorithms (see fitting result in Figure 2.7 and Table 2.2).

Pre Type	Post Type	λ_{apic}	λ_{basal}	α_{soma}	α_{apic}	α_{basal}
EXC	L2	1.68	1.68	–	–	–
EXC	L3	1.68	1.68	–	–	–
EXC	L4py	1.68	1.17	–	–	–
EXC	L4sp	1.17	1.17	–	–	–
EXC	L4ss	1.17	1.17	–	–	–
EXC	L5st	1.68	1.04	–	–	–
EXC	L5tt	1.68	1.04	–	–	–
EXC	L6cc	1.04	1.04	–	–	–
EXC	L6inv	1.04	1.04	–	–	–
EXC	L6ct	1.04	1.04	–	–	–
EXC	IN	–	–	0.74	0.74	0.74
IN	EXC	–	–	0.06	0.06	0.06
IN	IN	–	–	0.06	0.06	0.06

Table 2.2: Cell type-specific meta-connectivity list. EXC - all excitatory cell types; IN - all inhibitory cell types. Units: λ: μm^{-1}; α: μm^{-2}.

Third, the precision (across animal variability) of the average reference frame determines the voxel resolution, i.e. the smallest scale at which axo-dendritic overlap can be calculated between morphologies obtained in different animals. Thus, locations of somata/dendrites/axons within a voxel cannot be further resolved and proximity of boutons and PSTs within a voxel cannot be used to estimate synaptic innervation. Instead, I assume that all PSTs within a voxel are equally likely to receive any bouton in the same voxel (i.e. independent synapse formation at resolutions smaller than the accuracy of the reference frame). The probability that neuron j is targeted by a bouton within the voxel

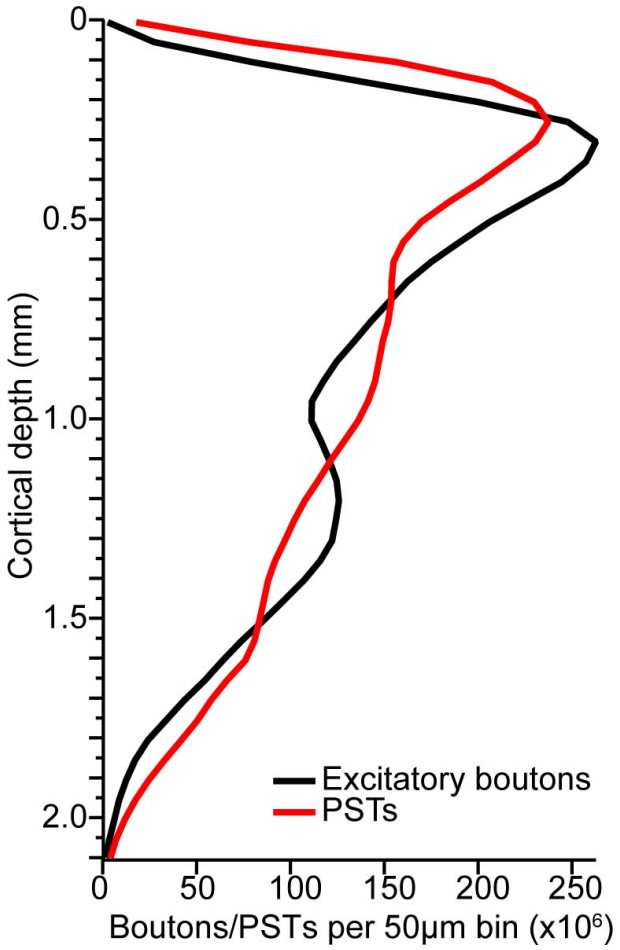

Figure 2.7: Excitatory bouton and PST distribution. Total number of excitatory boutons and corresponding PSTs in rat vS1, measured in $50\mu m$ bins along the vertical column axis. PSTs are calculated based on the distribution of dendrite lengths of excitatory neurons, and dendrite and soma surface areas of inhibitory interneurons, and the fit results in Table 2.2.

centered on $\vec{x}$ is then given by:

$$p_j(\vec{x}, T(i)) = \frac{PST_j(\vec{x}, T(i))}{PST_{all}(\vec{x}, T(i))}$$

Here, $PST_{all}(\vec{x}, T(i))$ refers to the total number of potential postsynaptic contact sites for connections with presynaptic cell of type $T(i)$ in the voxel centered on $\vec{x}$, i.e.

$$PST_{all}(\vec{x}, T(i)) = \sum_j PST_j(\vec{x}, T(i))$$

If B_i boutons from neuron i are present in the voxel at $\vec{x}$, the probability that neuron j is targeted by n of these boutons is given by the binomial distribution:

$$P(n; p_j, B_i) = \binom{B_i}{n} p_j^n (1 - p_j)^{B_i - n}$$

Average values for B_i and p_j in our networks are O(10^1)-O(10^2) and O(10^{-3}), respectively. Given the about 5 orders of magnitude differences between B_i and p_j, I approximate the binomial distribution by a Poisson distribution (i.e. $B_i \to \infty$ and $p_j \to 0$):

$$P(n; \tilde{I}_{ij}(\vec{x})) = \frac{\tilde{I}_{ij}^n(\vec{x})}{n!} \exp(-\tilde{I}_{ij}(\vec{x}))$$

Here, I defined the average innervation $\tilde{I}_{ij}(\vec{x})$ from neuron i to neuron j in the voxel at $\vec{x}$:

$$\tilde{I}_{ij}(\vec{x}) := B_i(\vec{x}) \cdot p_j(\vec{x})$$

The connectivity statistics between any two neurons *(i,j)* can thus be described by the 3D scalar field $\tilde{I}_{ij}(\vec{x})$. The probability of finding a connection between any two neurons i and j within a specific voxel located at $\vec{x}$ is further given by:

$$p_{ij}(\vec{x}) = 1 - P(n = 0; \tilde{I}_{ij}(\vec{x})) = 1 - \exp(-\tilde{I}_{ij}(\vec{x}))$$

Because I assume that synapses in different voxels are formed independently of another, the total probability of finding a connection between two neurons i and j is:

$$\begin{aligned} p_{ij} = 1 - \prod_{\vec{x}} P(n = 0; \tilde{I}_{ij}(\vec{x})) &= 1 - \exp(-\sum_{\vec{x}} \tilde{I}_{ij}(\vec{x})) \\ &= 1 - \exp(-I_{ij}) \end{aligned}$$

Here, $I_{ij} := \sum_{\vec{x}} \tilde{I}_{ij}(\vec{x})$ is the total (i.e. summed over all overlapping voxels) average innervation from neuron i to neuron j. Intuitively, I_{ij} is the expected number of synapses connecting neuron i to neuron j.

2.4.4 Calculation of statistical synaptic innervation at cell type levels

Using the innervation matrix I_{ij} for all pairs of neurons in the network, analyses can be extended to the population level, allowing comparison with pairwise connectivity measurements performed in vitro/vivo. In silico, pairwise connectivity between two populations (pre: A and post: B) can be described by three experimentally accessible parameters: the convergence C_b, i.e. the fraction of the presynaptic population connected to a single postsynaptic neuron $b \in B$, the divergence D_a, i.e. the fraction of the postsynaptic population targeted by a single presynaptic neuron $a \in A$, and the connection probability P_{AB}, i.e. the probability that any two neurons $a \in A$, $b \in B$ are connected. These three quantities can now be defined in terms of the neuron-to-neuron connection probability $p_{ij} = 1 - \exp(-I_{ij})$ introduced above:

$$C_b = \langle p_{ab} \rangle_{a \in A}$$
$$D_a = \langle p_{ab} \rangle_{b \in B}$$
$$P_{AB} = \langle p_{ab} \rangle_{a \in A,\, b \in B}$$

Here, $\langle \cdots \rangle_{a \in A}$ is the ensemble average across all neurons a in population A etc. Additionally, the distribution of the number of synapses per connection n_{AB} between these two populations can be computed by averaging across the individual synapse number distributions $n_{ij} := P(n; I_{ij})$:

$$n_{AB} = \langle n_{ab} \rangle_{a \in A,\, b \in B} = \langle Poisson(I_{ab}) \rangle_{a \in A,\, b \in B}$$

2.4.5 Structural connectivity constraints on functional connectivity during simulations

These structural connectivity parameter distributions form the basis for network-embedded simulations of single neuron morphologies, as they provide limits on functional connectivity (i.e., which synapses are active at what time) between presynaptic cell types and the postsynaptic neuron. First, statistical connectivity from all presynaptic neurons in

the dense network model to the postsynaptic neuron can be calculated depending on the location of the postsynaptic neuron (limited by the resolution of the average reference frame of vS1), e.g., at the registered location of an individual neuron recorded in vivo. Second, the subcellular distribution of synapses $\tilde{I}_{ij}(\vec{x})$ influences how synaptic inputs are integrated by the postsynaptic neuron. The amplitude of postsynaptic potentials (PSPs) from synapses located far from the soma is strongly attenuated and has a slower time course compared to PSPs from synapse located closer to the soma [94]. Third, summation of I_{ij} over all presynaptic neurons of the same cell type gives the total number of expected inputs from one particular cell type to a single neuron, rendering an upper limit of how many synapses of each cell type can potentially be active on the postsynaptic neuron (i.e., proportional to the average functional connectivity). Fourth, the convergence C_b described above determines the variability of the functional connectivity: If the convergence is high, i.e., the postsynaptic neuron receives synapses from a large fraction of the presynaptic population, then this population can influence the postsynaptic neuron in each trial despite large heterogeneity and trial-to-trial variability of the responses of individual neurons in the presynaptic population (i.e., the postsynaptic neuron can "average" across the presynaptic population and the variability of functional connectivity across trials is small compared to the mean functional connectivity). On the other hand, if the convergence is low and the postsynaptic neuron only receives synapses from a small fraction of the presynaptic population, then the functional connectivity is influenced by the trial-to-trial variability of individual presynaptic neurons (i.e., the number of active synapses may be very different from one trial to the next and hence the variability of the functional connectivity is large compared to the mean functional connectivity). Finally, the synapse number distribution n_{ij} is related to the reliability of functional connectivity between two neurons: Release of neurotransmitters at individual cortical synapses is stochastic (i.e., not every action potential arriving at the presynaptic bouton results in release of neurotransmitters [95]). The reliability of a connection thus depends on the number of synapses between two neurons, i.e., if they are connected by more than one synapse, then the presynaptic neuron is more likely to influence the postsynaptic neuron every time it is active.

2.5 Network-embedded simulations of different cell types

In this section, I will describe a new strategy to perform network-embedded simulations of functionally realistic models of different excitatory cell types during different network states, e.g. ongoing (spontaneous) or sensory-evoked activity. Functional synaptic input to a single postsynaptic neuron, as well as the integration of this input, is modeled using mathematical descriptions of synapses and ion channels, and using the cable equation to model dendrites, soma and axon of the postsynaptic neuron. The parameters constraining these models are determined experimentally:

1. The location of the postsynaptic neuron is determined with $50\mu m$ precision (limited by the variability of the average reference frame of vS1).

2. The number and subcellular distribution of synapses from different presynaptic cell types is given as statistical distribution of connection probability and synapse numbers at a resolution of $50\mu m$ (as described above in section 2.4.3).

3. The number and timing of spikes in presynaptic neurons of different cell types is based on in vivo measurements of spontaneous and sensory-evoked activity, given as spiking probability as a function of time (as described above in sections 2.1 and 2.3).

4. The effect of synaptic inputs is given as distribution of amplitudes of unitary EPSPs/IPSPs (uEPSPs/uIPSPs) for different cell types, based on in vitro measurements between pairs of identified neurons.

5. The biophysical properties of the postsynaptic neuron (e.g. the density of ion channels in soma and axon) are determined based on in vivo and in vitro measurements of identified neurons.

These experimental constraints are regarded as statistical distributions and sampled stochastically.

In practice, first a neuron morphology that is representative for its morphological cell

type is selected, and, depending on its location, the number and subcellular distribution of synaptic inputs, as well as the presynaptic partner neurons are determined. Second, presynaptic neurons are turned into point neurons and activated based on cell type-specific response probabilities measured in vivo. Finally, the dendrites, soma and (if necessary) the axon of the neuron morphology are converted into a biophysically realistic compartmental model of this cell type. Spatial discretization (compartmentalization) is performed without simplification of the dendritic topology and dendritic branch lengths. Each sample from the distributions of experimental constraints thus results in a possible spatiotemporal synaptic input pattern (i.e., functional connectivity) onto the neuron. Because the distributions of experimental constraints represent the biological variability of the respective structural and functional parameters, all functional connectivity configurations allowed within these constraints can be interpreted as an individual trial. Each trial is then simulated by numerically solving the cable equation and, if voltage-dependent ion channels are present, Hodgkin-Huxley type equations to determine the membrane potential of the neuron in space and time. The simulated responses of many trials are then compared with in vivo measurements of the response of neurons of this cell type, e.g. after whisker deflection. I will demonstrate this approach on two examples: the subthreshold response of a L2py neuron to SuW deflection, and the spiking response of L5tt neurons to PW and SuW deflections.

2.5.1 L2 pyramidal neuron model

Note: This description has in part been adapted from Egger, Schmitt et al. 2015 [57].

The aim of this model is to investigate the contribution of excitatory synaptic inputs and inhibitory synaptic inputs from INs located in L1 to subthreshold responses of a L2py after SuW deflection.

Network embedding. In this model, D1 is chosen as the PW. Hence, for neurons located in the D1 column, this model represents a PW deflection. In order to model SuW deflections, I therefore additionally included the D2 column in the model. For neurons located in the D2 column, a D1 whisker deflection represents a SuW deflection. As a

representative model for the population of L2py in the D2 column I selected a L2py morphology located at a cortical depth of $215\mu m$. The distance to the D2 column center was $65\mu m$, and the distance to the D1 column center was $390\mu m$ (Figure 2.8).

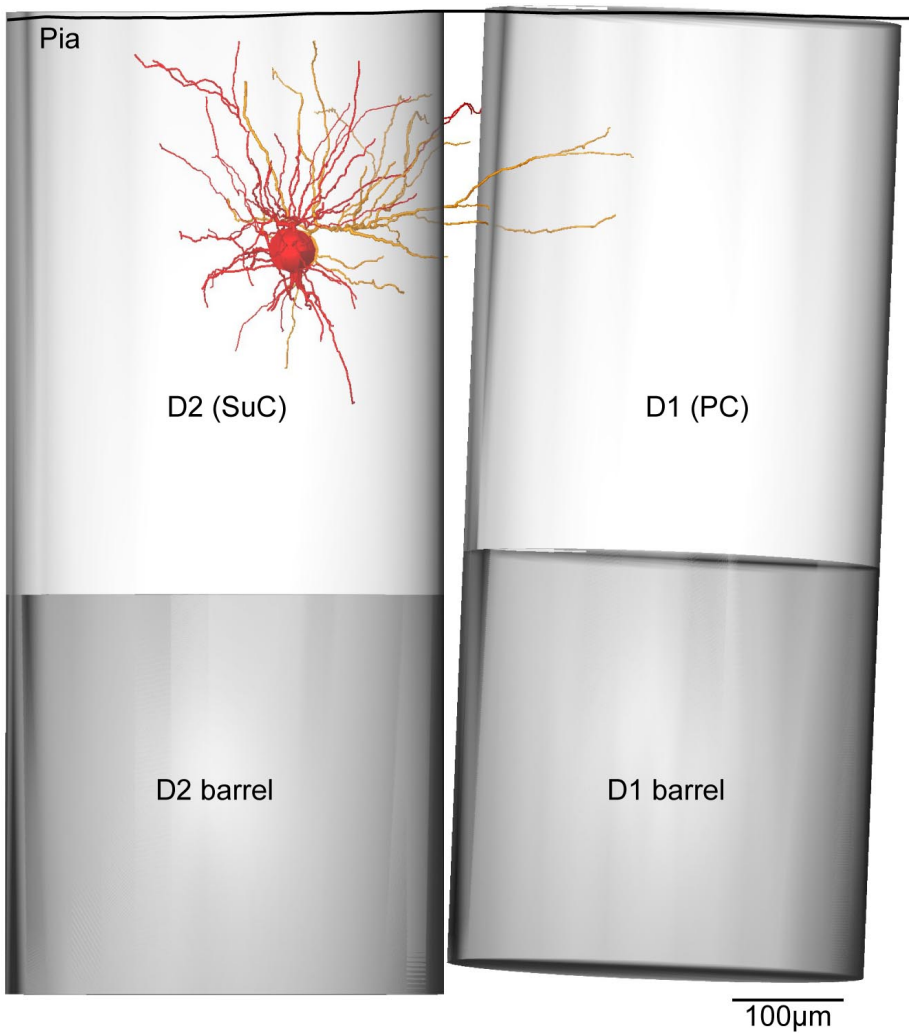

Figure 2.8: Soma and dendrite morphology of L2 neuron model in rat vS1. Red: Soma and basal dendrites, orange: apical dendrites. Soma and dendrite diameters increased for visualization.

The total length of the dendritic arbor of the L2py neuron model was $8,880\mu m$, close to the average dendrite length of this cell type ($8,580\mu m$) [31, 56]. Next, I determined the innervation of the L2py neuron model by seven excitatory and one inhibitory cell types (L2py, L3py, L4py, L4sp, L4ss, L5st, L5tt, and L1 INs) using the NeuroNet software, as described above (see section 2.4.3). The number and location of excitatory and inhibitory synapses was determined based on the innervation (i.e., Poisson approximation

Cell type	Synapses per connection PC	Synapses per connection SC
L1 IN	1-2**	–
L2py	1.4*	2.8
L3py	1.4*	2.8
L4py	2.25*	4.5*
L4sp	2.25*	4.5*
L4ss	2.25*	4.5
L5st	1.4*	2.8*
L5tt	1.4*	2.8*

Table 2.3: Anatomical constraints on connectivity between presynaptic cell types and L2py model neuron. Parameters are based on in vitro [96, 97] measurements, *extrapolated based on the measured values, or **based on connectivity measurements using the dense network model alone.

as described above) once and kept fixed for the remaining simulations. For excitatory connections to L2py, additional experimental constraints on the number of synapses per connection are available based on paired recordings and reconstructions of different cell types [96, 97], and these were therefore included in the model. L4py and L4sp neurons were assumed to connect to the L2py neuron with the same number of synapses per connection as L4ss neurons. L5st and L5tt pyramidal neurons were assumed to make the same number of synapses per connection as L2py/L3py neurons. Transcolumnar connections were assumed to have half the number of synapses per connections compared with intracolumnar connections (Table 2.3).

Additional constraints on the number of synapses per connection beyond the distributions resulting from the dense network model are not available for inhibitory connections from L1 INs. Within these constraints, I randomly created 50 samples from the space of possible connectivity patterns. Each sample varied in the number of connected presynaptic neurons, as well as the identity of the synapses connected to each presynaptic neuron. This allows investigating the influence of detailed wiring patterns on the observed model response.

Activity of presynaptic neurons from different cell types. All neurons in the dense network model that were presynaptic to the L2py neuron model were converted into point neurons while keeping their cell type identity and 3D soma location. These presynaptic neurons were then activated independently depending on the average ongo-

ing and sensory-evoked activity of the respective cell type after PW or SuW deflection. Ongoing and sensory-evoked activity of different cell types was determined by identifying the morphological cell type of neurons recorded and identified during in vivo experiments, as described in the Methods section 2.3 and the Results section 3.1.3. During simulated periods of ongoing activity, presynaptic neurons were modeled as Poisson spike sources with constant AP firing rates (Table 2.4). During simulated periods of evoked activity, additional sensory-evoked spikes were generated by the presynaptic neurons. Presynaptic neurons with soma location closest to the D1 column were activated based on the evoked response probability of the corresponding cell type after PW deflection (Table 2.4). The timing of excitatory cell types was determined based on a log-normal distribution with parameters $\mu = 1.61, \sigma = 1.5$, and an offset of 10ms after stimulus (corresponding to a median response time of 15ms after stimulus [26]), because latencies of excitatory cell types after whisker deflection, as well as the subcellular distribution of synaptic inputs from these cell types, were similar. Timing of whisker-evoked presynaptic responses of L1 INs were determined from a normal distribution with a mean of 15.2ms after stimulus and a standard deviation (SD) of 2.2ms (see section 3.1.3).

Presynaptic neurons with soma location closest to the D2 column were activated based on the evoked response probability of the corresponding cell type after SuW deflection (Table 2.4). The timing of excitatory cell types was determined from a uniform distribution between 10-50ms after the stimulus. As for PW deflections, latencies of different cell types were modeled as uniform because the subcellular distributions of synaptic inputs from these cell types were similar. L1 INs showed no increased activity after SuW deflections.

Additional delays of action potentials due to finite conduction velocity along the axon were not modeled, i.e., each synapse was activated at the same time as the corresponding presynaptic neuron.

Synapses from different presynaptic cell types. Conductance-based synapses were modeled with a double-exponential time course and use-dependent depression or facilitation [98]; i.e., after activation of the synapse, the conductance varied according to

Cell type	Spontaneous spiking (Hz)	Evoked spiking PW 0-50ms (AP/stim)	Evoked spiking SuW 0-50ms (AP/stim)
L1 IN	1.0	0.072	–
L2py	0.47	0.013	0.018
L3py	0.32	0.14	0.018
L4py	0.56	0.34	0.027
L4sp	0.32	0.37	0.027
L4ss	0.52	0.25	0.027
L5st	1.1	0.05	0.022
L5tt	3.53	0.33	0.173

Table 2.4: Functional constraints on activity of presynaptic cell types to L2py neuron model. Parameters are based on in vivo measurements [26, 31, 57].

the following formula:

$$g(t) = g_{max} \cdot N \cdot \alpha \cdot (\exp(-\frac{t}{\tau_{decay}}) - \exp(-\frac{t}{\tau_{rise}}))$$

Here, N is a normalization constant depending on τ_{rise} and τ_{decay} to ensure that the maximum value of $g(t)$ always is $g_{max} \cdot \alpha$. α is a facilitation/depression variable. If the synapse is modeled as facilitating, α is described by:

$$\frac{d\alpha}{dt} = \frac{1-\alpha}{\tau_f} + f_0 \sum_{t_s} \delta(t - t_s)$$

Here, τ_f is the facilitation time constant, f_0 is a constant facilitation variable ($f_0 > 0$), t_s refers to all synapse activation times, and δ is the Dirac delta function. If the synapse is modeled as depressing, α is described by:

$$\frac{d\alpha}{dt} = \frac{1-\alpha}{\tau_d} - (1 - d_0) \cdot \alpha \sum_{t_s} \delta(t - t_s)$$

Here, τ_d is the depression time constant, d_0 is a constant depression variable ($0 < d_0 < 1$), t_s refers to all synapse activation times, and δ is the Dirac delta function. Glutamatergic (i.e., excitatory) synapses were modeled with a fast α-amino-3-hydroxy-5-methyl-4-isoxazolepropionic acid receptor (AMPAR) conductance and a slow, voltage dependent N-methyl-D-aspartate receptor (NMDAR) conductance. AMPAR conductances had rise

and decay times of 0.1 and 2ms, respectively; NMDAR conductances had rise and decay times of 2 and 26ms, respectively [97]. Voltage dependence of the Mg block of NMDAR conductances was modeled by multiplying the conductance value with a factor $1/(1+\eta \cdot \exp(-\gamma \cdot V))$ [99], where $\eta = 0.25$, $\gamma = 0.08/mV$, and V is the membrane potential in millivolts [100]. AMPAR and NMDAR conductances had a depression variable d_0 of 0.5 and 0.6, respectively, and a depression time constant $\tau_d = 200ms$ [101]. Inhibitory synapses with a γ-Aminobutyric acid receptor ($GABA_A$) conductance had rise and decay times of 1 and 20ms, respectively [102]. $GABA_A$ conductances had a depression variable d_0 of 0.8 and a depression time constant $\tau_d = 200ms$ [101]. The reversal potential of glutamatergic synapses was set to 0mV, and the reversal potential of GABAergic synapses was set to -75mV.

Because during experiments whisker stimuli were delivered randomly with respect to up-/down-states, and transition periods between states, I modeled whisker-evoked input to the L2py neuron model during simulated up- and down-states by activating synapses according to the average ongoing activity of the respective presynaptic cell types, as described above. The maximum conductance and release probability during up- and down states were constrained by systematic variation of these parameters, and calculating the mean and standard deviation (SD) of the membrane potential at the soma, as well as the input resistance after current injection at the soma, resulting in a distribution of parameter sets of maximal conductance values and release probabilities of excitatory and inhibitory synapses. For modeling up and down states, parameter sets for synaptic conductances and release probabilities were chosen to match reported experimental values [103] of the mean membrane potential during up (exp.: $-58.9 \pm 1.2mV$; model: $-60.1mV$) and down ($-73.9 \pm 1.4mV$; $-72.5mV$) states, the SD of the membrane potential during up states ($2.5 \pm 0.1mV$; $2.4mV$), and the input resistance during up ($36.6 \pm 2.3M\Omega$; $40.3M\Omega$) and down ($29.2 \pm 2.0M\Omega$; $34.7M\Omega$) states (also see Figure 3.16 D in the results section for comparison with in vivo measurements). From all parameter sets within the experimental variability, I chose two parameter sets that did not differ in the conductance values of synapses, but only in the release probabilities of excitatory and inhibitory synapses during up and down states (Table 2.5). Ongoing activity preceding whisker-evoked input was modeled based on up-state parameters in 50% of simulation trials and

based on down-state parameters in the other 50% of simulation trials. Transitions between states were not modeled.

Next, for a realistic model of whisker-evoked input to the L2 neuron, I first determined the maximum conductance values of excitatory synapses by comparing the distribution of uEPSP amplitudes obtained by separate activation of all connected presynaptic neurons (i.e., one presynaptic neuron may activate one or more synapses) to measured distributions of uEPSP amplitudes for different cell types [96, 97]. I determined the mean, standard deviation and the maximum of the distribution of uEPSP amplitudes after successive activation of all presynaptic neurons for a fixed value of the peak conductance at each synapse. These parameters were obtained while systematically varying the peak conductance across a large range, and then fitted with a second-order polynomial (see example in Figure 2.9).

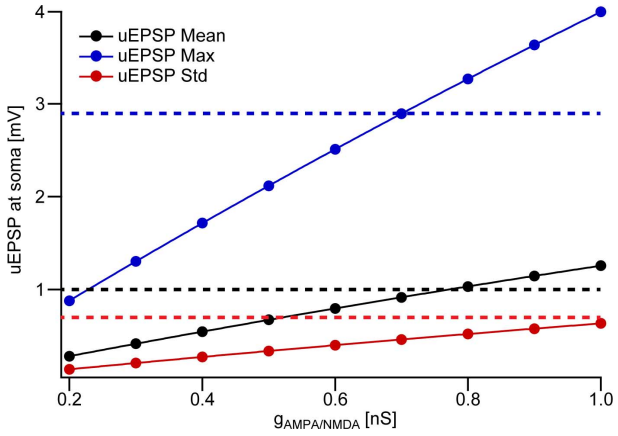

Figure 2.9: Constraining the conductance at synapses to the L2py neuron model. Mean, standard deviation (Std) and maximum value of the uEPSP amplitude distribution of contacts from all presynaptic L2py neurons to the L2py neuron model (i.e. at least one synapse per contact) for different values of the maximum conductance at AMPA and NMDA receptors. Solid lines are fit to the simulation values (dots). Dashed lines are the corresponding values of the experimentally determined uEPSP amplitude distribution from [96].

An optimal conductance was determined by finding the conductance value that resulted in a uEPSP amplitude distribution that was the most similar to the experimentally determined uEPSP amplitude distribution for the corresponding cell type. To do so, I minimized the squared difference between the fit results of mean, standard deviation and maximum to the experimentally measured values at the same time (mean and standard

Cell type	Ongoing g_{AMPA} (g_{GABA})/g_{NMDA} (nS)	Evoked g_{AMPA} (g_{GABA})/g_{NMDA} (nS)	Ongoing release prob. up/down	Evoked release prob. up/down
L1 IN	0.6/–	1.6/–	1.0/0.6	1.0/1.0
L2py	1.1 /1.1	0.73/0.73	0.5/0.1	0.2/0.9
L3py	1.1/1.1	0.57/0.57	0.5/0.1	0.2/0.9
L4py	1.1/1.1	0.33*/0.165*	0.5/0.1	0.2/0.9
L4sp	1.1/1.1	0.33*/0.165*	0.5/0.1	0.2/0.9
L4ss	1.1/1.1	0.33/0.165	0.5/0.1	0.2/0.9
L5st	1.1/1.1	0.57*/0.57*	0.5/0.1	0.2/0.9
L5tt	1.1/1.1	0.57*/0.57*	0.5/0.1	0.2/0.9

Table 2.5: Parameter values of excitatory and inhibitory synapses onto the L2py model neuron. Parameters are based on in vitro [96, 97] and in vivo [103] measurements or *extrapolated based on the measured values.

deviation were weighted double). Conductance values of synapses from L4py and L4sp were assumed to be equal to the conductance values of synapses from L4ss. Maximum conductance values were fitted separately for L2py and L3py synapses due to differences in their subcellular distributions, i.e., L2py synapses had a larger mean path length distance to the soma. Conductance values of synapses from L5st and L5tt were assumed to be equal to conductance values of synapses from L3py due to their similar subcellular distributions (Table 2.5). Reliable measurements of the connection strength of L1 IN synapses onto L2py are not available, and I therefore assumed a maximum conductance value of 1.6nS for the $GABA_A$ conductance. The release probability of excitatory synapses was determined by systematic variation independently for up- and down-states until the compound whisker-evoked PSP reached approximately the same absolute peak value [104] (Table 2.5). The release probability of inhibitory synapses was fixed at 1.

Biophysically realistic neuron model. I used a previously published model of the subthreshold behavior of L2 pyramidal neurons in rat vS1 [103]. I restricted the model to subthreshold responses because the spiking probability of L2py is very low under the present experimental conditions (i.e., in the anaesthetized state, after passive whisker deflection [46]). The dendrites and soma of this cell type contain voltage-dependent ion channels that lead to anomalous rectification of the membrane potential. When the membrane potential is depolarized (for example during an up state), then the input resistance of the neuron in response to current injection is higher compared to when the

membrane potential is hyperpolarized (for example during a down state). This effect is well-described by a phenomenological model that adds a nonlinear term to the I-V curve of the neuron [103]:

$$\Delta V = R_0 \Delta I + c_{AR} \Delta I^2$$

The length of individual compartments of each dendrite branch was determined by the electrotonic length constant of the branch to time-varying input. The membrane time constant of neurons is of the order of 10ms. I therefore determined the electrotonic length constant of each branch at a frequency of 100Hz and set the length of individual compartments in this branch to 10% of this length constant. The resulting length of individual compartments was on average $\sim 15\mu m$, but never larger than $\sim 40\mu m$. Specific membrane resistance was set to $5,000\Omega cm^2$, axial resistance to $150\Omega cm$, and the specific membrane capacitance was set to $1\mu F/cm^2$. Anomalous rectification in dendrites and the soma was adjusted to give a value of $c_{AR} = 18.2M\Omega/nA$ [103]. Spines were accounted for by scaling the surface area of dendritic segments by $\frac{1+A_{Spines}}{A_{Shaft}}$, where A_{Spines} was computed proportional to the length of the dendritic segment ($0.8\mu m^2/\mu m$), and A_{Shaft} was the surface area before adjustment [105]. The reversal potential of the leak conductance was set to -75mV. All numerical simulations were carried out using the NEURON package (NEURON 7.2 [106]).

Monte Carlo sampling from constrained parameter space. In the previous paragraphs, I described how to combine statistical connectivity (i.e., 50 different network embeddings of the same neuron), functional connectivity (i.e, spiking probabilities and timing of presynaptic neurons, as well as synaptic release probability) and physiological data (i.e., synaptic conductances and biophysical parameters of the soma and dendrites of the L2py neuron model) to create a fully constrained L2py neuron model. These constraints are still in the form of statistical distributions, representing the biological variability underlying structural and functional connectivity to L2py neurons. Hence, any sample from these distributions, which represents a spatiotemporal configuration of active synapses to the L2py neuron model during ongoing and SuW-evoked activity (i.e., which synapses are active at what time), as well as their physiological properties, can be

regarded as biologically realistic within the present constraints and is thus interpreted as an individual trial. Specifically, I sample 200ms of ongoing activity (50% of the samples during up and down states, respectively), followed by 50ms of SuW-evoked activity. For each of these trials, the membrane potential of the neuron in the dendrites and at the soma in response to the specific synaptic input pattern is numerically simulated. Because the model did not include a spiking mechanism, I excluded traces depolarized to more than -38mV at the soma [22]. The first 100ms of subthreshold activity are discarded to remove numerical artifacts. The parameters I will analyze subsequently are the number of active synapses during ongoing and SuW-evoked activity for each presynaptic cell type, the average PSP amplitude 10-50ms post-stimulus, and the average SD of the PSP 15-50ms post-stimulus. Drawing a finite number of samples from the constrained parameter space of functional connectivity configurations results in statistical error in these quantities. Therefore, I estimated how many trials are required to minimize this error sufficiently to allow investigating the influence of different parameters on the target quantities. A total of 2,000 simulation trials (1,000 for up- and down-states, respectively) were sufficient to minimize the statistical error to $2 \times 10^{-3} mV$ (Figure 2.10). Thus, the full model contained 100,000 samples (i.e., 50 different network embeddings with 2,000 samples of functional connectivity each).

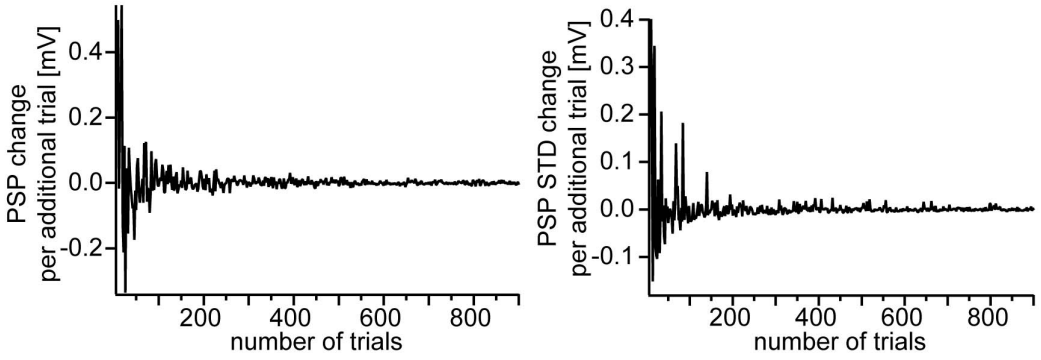

Figure 2.10: Estimate of sampling error during L2py neuron simulations. Change in average PSP amplitude (left) and PSP SD (right) after increasing the sample size by 1 to the new total sample size (bottom axis).

Finally, in order to determine the influence of the different parameter distributions on the target quantities (average PSP amplitude and average PSP SD), I generated samples

where all parameters/statistical distributions except for one were kept fixed.

1. To investigate the influence of sensory-evoked responses of L1 INs on the average PSP amplitude/PSP SD, I generated 100,000 samples excluding responses of L1 INs located in the D1 column.

2. To separate the effects of excitary functional connectivity and inhibitory functional connectivity on the average PSP amplitude/PSP SD, I first generated 100,000 samples including L1 INs located in the D1 column. Then, I simulated the response of the L2py neuron model to the same 100,000 samples excluding L1 INs located in the D1 column. Next, I generated 100,000 samples including L1 INs located in the D1 column, followed by an additional 100,000 samples which were identical for L1 INs, but newly sampled for excitatory functional connectivity.

3. To investigate the influence of the subcellular distribution of L1 IN synapses to the L2py neuron model on the average PSP amplitude/PSP SD, I generated a network embedding in which synapses from L1 INs located in the D1 column were spatially distributed in the same pattern as synapses from L4ss located in the D2 column, without changing the number of synapses from L1 INs. I then generated 2,000 samples of functional connectivity including/excluding responses of L1 INs located in the D1 column, while keeping functional connectivity of excitatory synapses fixed (i.e., using the same set of 2,000 samples for excitatory synapses).

4. To investigate the influence of possible specificity in the connectivity from L1 INs to the L2py neuron model beyond the statistical connectivity model, I kept connectivity from excitatory cell types fixed (i.e., I randomly picked one of 50 network embeddings) and generated 2,000 samples of functional connectivity including/excluding responses of L1 INs located in the D1 column under the constraint that L1 INs are connected to L2py neurons with 11 synapses on average.

5. I investigated the effect of different physiological and biophysical parameters on the average PSP amplitude/PSP SD. First, I created 100,000 samples including/excluding responses of L1 INs located in the D1 column, and sampled conductance values of excitatory synapses from a log-normal distribution [107] instead of a fixed value

at all synapses (the mean of the log-normal distribution was set to the fixed value used for each cell type in all other simulations). Second, I created 100,000 samples including/excluding responses of L1 INs located in the D1 column, and excluded the voltage-dependent NMDAR conductances at excitatory synapses. Third, I investigated possible effects of varying conductance values of L1 INs by keeping functional connectivity fixed (i.e., I randomly picked one of 50 network embeddings and generated 2,000 samples of functional connectivity) and only changing the maximum conductance value at L1 IN synapses. Finally, I investigated possible effects of the chloride reversal potential at L1 IN synapses by keeping functional connectivity from excitatory cell types fixed (i.e., I randomly picked one of 50 network embeddings) and generated 2,000 samples of functional connectivity including/excluding responses of L1 INs located in the D1 column, and set the reversal potential of L1 IN synapses to -85mV.

2.5.2 L5tt pyramidal neuron model

The goal of this model is to identify the mechanisms that underlie the broad whisker touch receptive field (RF) of L5tt neurons in rat vS1.

Network embedding. In this model, the C2 barrel column and C2 whisker were chosen as PC and PW, respectively. They are located at the center of rat vS1/the whisker pad. I am going to model the response of L5tt to PW and eight SuW deflections (PW: C2, SuW: B1-B3, C1, C3, D1-D3) and compare the simulated model responses to the average response of a population (n=9) of L5tt to the same whisker deflections recorded and identified in vivo. In order to create a model that is representative of the L5tt population in C2, I first selected a L5tt morphology comprising soma and dendrites that was representative of the L5tt population (Figure 2.11).

The distance of the soma to the pia surface was $1075\mu m$ (L5tt average: $1123 \pm 72\mu m$ [56]). The total dendrite length of the neuron was close to the average of all L5tt morphologies in the sample (model: $15343\mu m$; L5tt average: $14729 \pm 3391\mu m$). The same was true for the length of the apical ($8849\mu m$; $7946 \pm 1589\mu m$) and basal ($6494\mu m$; $6783 \pm 2451\mu m$) dendrites, as well as the number of branch points (77; 86 ± 23). Next, I

Figure 2.11: Soma and dendrite morphology of L5tt neuron model in rat vS1. Red: Soma and basal dendrites, orange: apical dendrites. Soma and dendrite diameters increased for visualization.

placed the L5tt morphology at nine different horizontal locations within the C2 column (Figure 2.12), with an average distance between locations of $\sim 100\mu m$. The locations were chosen such that the morphology at each location represents about 11% of the total population of L5tt located in the C2 column, and therefore captures location-specific differences in connectivity of the L5tt population.

Hence, the number and location of presynaptic neurons, as well as the number and subcellular distribution of synapses from all presynaptic cell types in the entire dense network model of rat vS1 and VPM to the L5tt morphology were determined for each

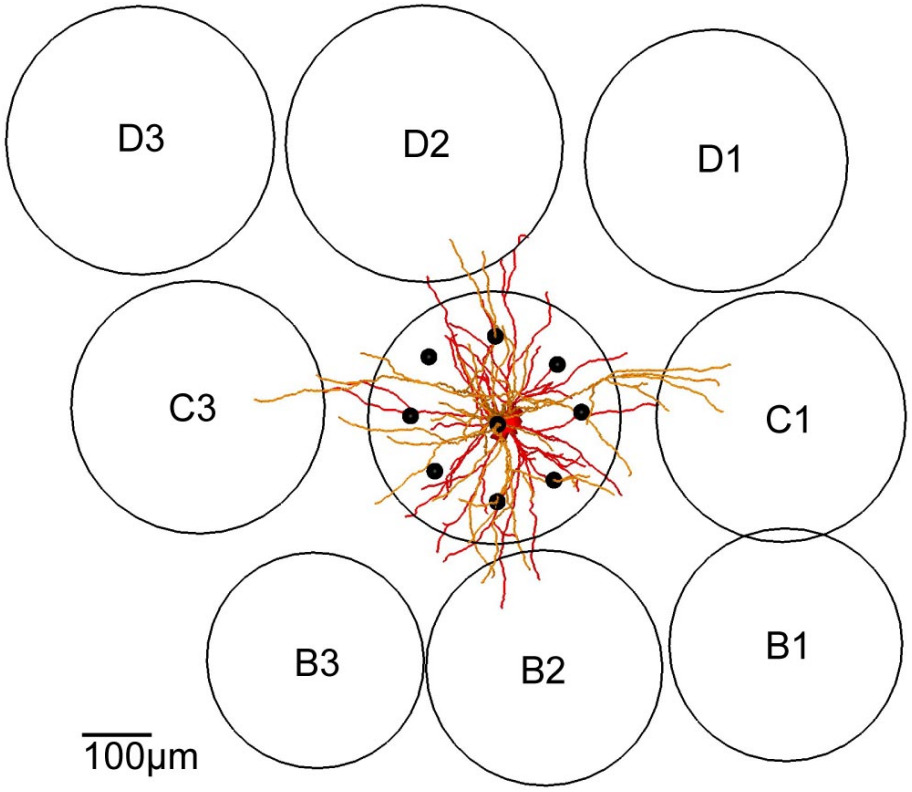

Figure 2.12: Locations of L5tt neuron model in network. Tangential view onto the nine different locations (black dots) within the C2 column used to perform network-embedding of the L5tt dendrite morphology (red: soma and basal dendrites, orange: apical dendrites). The spatial sampling approximately subdivides the C2 column into nine equally-sized horizontal areas.

of the nine locations separately. At each location, 50 network embedding realizations were generated based on the methods described in sections 2.4.3 and 2.4.4. The average and standard deviation of the number of synapses per presynaptic cell type across these 50 realizations was calculated. Then, the network embedding realization closest to the average for all presynaptic cell types was chosen as representative anatomical model for this particular location.

Activity of presynaptic neurons from different cell types. As described above for the L2py neuron model, presynaptic neurons were converted to point neurons, keeping cell type identity and 3D soma location, and activated based on ongoing and whisker-evoked response probabilitites and timings. In this model, I investigate the response of L5tt to PW and eight different SuW deflections, with the goal of identifying the pathways and mechanisms underlying whisker-evoked responses of this cell types. To do so, two

conditions have to be met: First, for all cell types, possible differences between cell types should be incorporated (in contrast to the L2py model described above, where the average SuW response was modeled). Second, in order to differentiate between contributions of different cell types to whisker-evoked responses of L5tt, differences in the response times of different cell types should be incorporated at millisecond resolution. To do so, I created millisecond-resolution poststimulus time histograms (PSTHs) for PW and eight SuW deflections for all excitatory cell types in rat vS1 by identifying the morphological cell type of neurons recorded and identified during in vivo experiments, as described in the Methods section 2.3 and the Results section 3.1.3. For each recorded neuron, the PC is determined after reconstruction and registration. Correspondingly, the principal whisker is defined as the whisker that is somatotopically aligned with the PC of the neuron. The PSTH of each cell of the 50ms following deflection of the PW and the eight SuW is computed across trials. Next, cell type-specific whisker-evoked PSTHs are computed by aligning the PSTHs of all cells of the same morphological type with respect to the PW, averaging the PSTH for each whisker relative to the PW across cells and subtracting the ongoing activity of this type. During simulations in the up-state, the amplitude of the PSTH is scaled by a factor of 0.4571 to reflect lower response probabilities of cortical neurons in the up-state [108]. The sum over the evoked PSTH in response to different whisker deflections is commonly referred to as the whisker-evoked RF of a cell type. Hence, cell type-specific RFs are shown centered on the PW and row/arc offset of the eight SuW, while cell type- and whisker-specific evoked PSTHs are shown as a function of time (Figure 2.13). For a detailed description of ongoing and whisker-evoked responses of all cell types, see section 3.1.3.

During simulations of whisker deflection, each presynaptic neuron is activated as a Poisson spike train [8] with a base rate given by the ongoing activity, and after whisker deflection, with a time-varying spike rate given by the sum of the ongoing activity and the PSTH. The PSTH used to model sensory-evoked activity of each presynaptic neuron is determined based on the cell type of the neuron and the location of the deflected whisker with respect to the PW and SuW receptive field of the neuron. For example, if the neuron is located in the D2 column and a D2 whisker deflection is simulated, then the neuron will be activated based on the PSTH corresponding to PW whisker deflection. However,

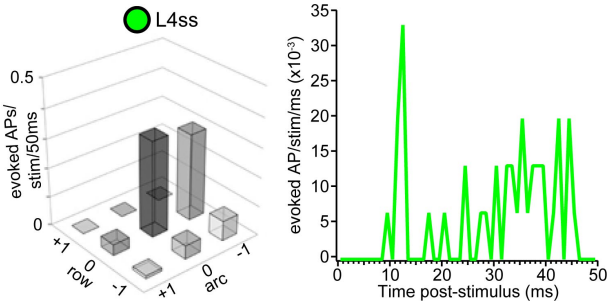

Figure 2.13: Example of cell type-specific whisker receptive field and PSTH. Left: Average whisker deflection-evoked RF of all identified L4ss neurons within 50ms post-stimulus. The RF is centered on the PW, and eight SuW are grouped according to their relative location to the PW on the whisker pad. Right: Average PSTH of all identified L4ss in response to PW deflection with 1ms resolution. The amplitude of the PW response in the left panel is equal to the sum over this PSTH.

if the neuron is located in the D2 column and a C2 whisker deflection is simulated, then the neuron will be activated based on the PSTH after deflections of the SuW in the same arc (here: 2), but in the more dorsal row (-1, here: C).

In vivo responses of inhibitory interneurons (except for L1 INs, see section 3.1.3) have not been measured in combination with identification of morphologies to allow correlation with morphological IN types used in this study. Therefore, I developed a simple model of the response of INs to PW and eight SuW deflections. The model is motivated by the assumption that PW and SuW responses of INs are caused by direct feed-forward thalamocortical input and additional recurrent intracortical input to all INs [109, 110]. The PSTH for each whisker deflection is constructed by picking the maximum value of the PSTHs of active excitatory cortical cell types (i.e., cell types with significantly increased response within 20ms after whisker deflection) and VPM for each 1ms time bin (Figure 2.14). In case of PW deflection, the PSTH is additionally shifted 1ms towards the deflection time (but no earlier than VPM activation), reflecting faster responses of INs compared to excitatory cell types after PW deflection [111]. The amplitude of these whisker-specific PSTHs was constrained by fixing the total ratio of spikes evoked after PW compared to SuW deflection at 2:1 [111]. This left the integral of the PW PSTH (i.e., the mean number of spikes in 50ms following whisker deflection) as the only parameter of the model. This parameter was determined by comparing the simulated response probability of the L5tt neuron model after PW deflection with the response probability

after PW deflection measured in vivo (Figure 2.14). Responses to SuW deflections were not separately adjusted, and therefore comparison of SuW amplitudes of the L5tt neuron model with responses measured in vivo remains valid. Ongoing activity of inhibitory neurons was assumed to be 7Hz [112], except for L1 INs (see Table 2.4).

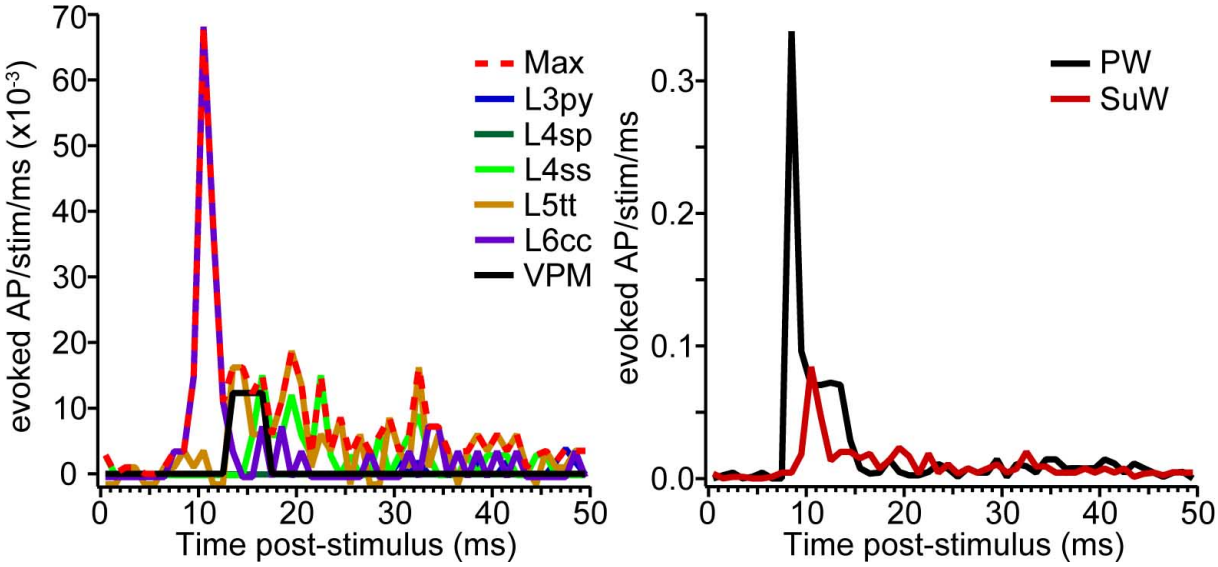

Figure 2.14: Example of PW and SuW PSTH of inhibitory interneurons. Left: Example calculation of one SuW (C1) PSTH of INs based on the maximum activity of active excitatory cell types in cortex and VPM. Right: Modeled PSTHs of INs after PW deflection (black trace) and one example SuW deflection (red trace, see left panel) after normalization to a total activity of 1.0 and 0.5 after a PW or SuW deflection, respectively.

Finally, I determined PW and SuW PSTHs of thalamocortical input from VPM. VPM neurons have been shown to fall into two functional groups: single whisker (SW) and multi whisker (MW) responsive neurons [87]. On the other hand, VPM neurons subdivide into different axonal projection patterns based on soma location within an individual barreloid [113, 114, 115]. In this thesis, I grouped all VPM neuron morphologies and neglected these differences. Hence, I also created average PSTHs of VPM neurons combining SW and MW responsive neurons.

Synapses from different presynaptic cell types. I used the same biophysical models of glutamatergic and GABAergic synapses as described for the L2py neuron model (section 2.5.1). AMPAR conductances had rise and decay times of 0.1 and 2ms, respectively; NMDAR conductances had rise and decay times of 2 and 26ms, respectively [97]. AMPAR and NMDAR conductances had a reversal potential of 0mV. Voltage dependence

of the Mg block of NMDAR conductances was modeled by multiplying the conductance value with a factor $1/(1 + \eta \cdot \exp(-\gamma \cdot V))$ [99], where $\eta = 0.25$, $\gamma = 0.08/mV$, and V is the membrane potential in millivolts [100]. AMPAR and NMDAR conductances of presynaptic L5tt inputs had a facilitation variable f_0 of 0.84, and a facilitation time constant $\tau_f = 16.5ms$ [116]. AMPAR and NMDAR conductances of presynaptic VPM inputs had a depression variable d_0 of 0.6, and a depression time constant $\tau_d = 108ms$ [45]. AMPAR and NMDAR conductances of all other presynaptic excitatory inputs had a depression variable d_0 of 0.8, and a depression time constant $\tau_d = 844ms$ [116]. $GABA_A$ conductances had rise and decay times of 1 and 20ms, respectively [102], a depression variable d_0 of 0.8 and a depression time constant $\tau_d = 298ms$ [117]. The reversal potential of $GABA_A$ conductances was set to -75mV. As described for the L2py neuron model, maximum conductance values of excitatory synapses were determined by comparing the distribution of uEPSP amplitudes obtained by separate activation of all connected presynaptic neurons to measured distributions of uEPSP amplitudes for different cell types (see example in Figure 2.15; Table 2.6).

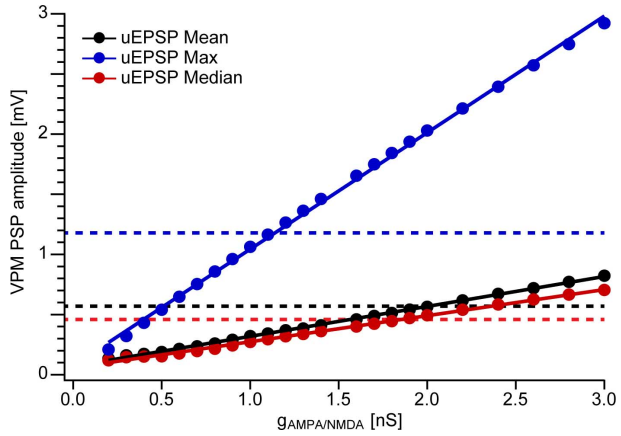

Figure 2.15: Constraining the conductance at synapses to the L5tt neuron model. Mean, median and maximum value of the uEPSP amplitude distribution of connections from individual VPM neurons (i.e. at least one synapse per contact) to the L5tt model neuron for different values at the maximum conductance of AMPA and NMDA receptors. Solid lines are fit to the simulation values (dots). Dashed lines are the corresponding values of the experimentally determined uEPSP amplitude distribution.

I determined the mean, standard deviation and the median of the distribution of uEPSP amplitudes after activation of all presynaptic neurons for a fixed value of the peak conductance at each synapse. uEPSPs with values smaller than 0.1mV (in case

Cell type	L2py	L3py	L4	L5st	L5tt	L6cc/inv	L6ct	VPM
Conductance (ns)	1.47	1.68	1.14	1.38	1.59	1.63	1.80	1.78

Table 2.6: Conductance values of excitatory synapses onto L5tt model neuron. AMPARs and NMDARs were assumed to have the same peak conductance. L4 cell types were assumed to have the the same peak conductance values. Parameters are based on in vitro [118] and in vivo [32] measurements.

of presynaptic intracortical cell types) or 0.15mV (in case of VPM synapses) were not included in the distribution, because they were below the experimental uncertainty in the studies used to constrain the uEPSP distributions [32, 118]. Including these small uEPSP amplitudes would systematically bias the resulting distributions towards smaller values, and thus lead to overestimation of the peak conductance. These parameters were obtained while systematically varying the peak conductance across a large range, and then fitted with a linear function. The optimal conductance was determined by finding the conductance value that minimized the squared difference between the fit results of mean, standard deviation and median to the experimentally measured values at the same time (Figure 2.15; mean and median were weighted double). Maximum conductance values of inhibitory synapses were fixed at 1nS [119]. Release probabilities of excitatory and inhibitory synapses were set to 0.6 and 0.25, respectively [117, 120].

Biophysically realistic neuron model. I used a previously published model of the sub- and suprathreshold behavior of L5tt neurons in rat S1 based on Hodgkin-Huxley type models of various ion channels [121]. This model describes the experimentally observed sub- and suprathreshold properties of this cell type in a biophysically realistic way. Most importantly, it supports two distinct action potential generation mechanisms (Figure 2.16).

First, current injection at the soma triggers a sodium channel-based AP at the soma and the axon. This AP further back-propagates (bAP) into the apical trunk dendrite [123]. Second, near-coincident current injection at the soma and the main bifurcation of the apical dendrite triggers three APs in quick succession, i.e. a burst [122]. The burst occurs when the bAP coincides with depolarization in the "hot zone" around the main bifurcation of the apical dendrite [124], which has a high density of voltage-dependent calcium channels. The additional depolarization due to the bAP triggers a calcium spike

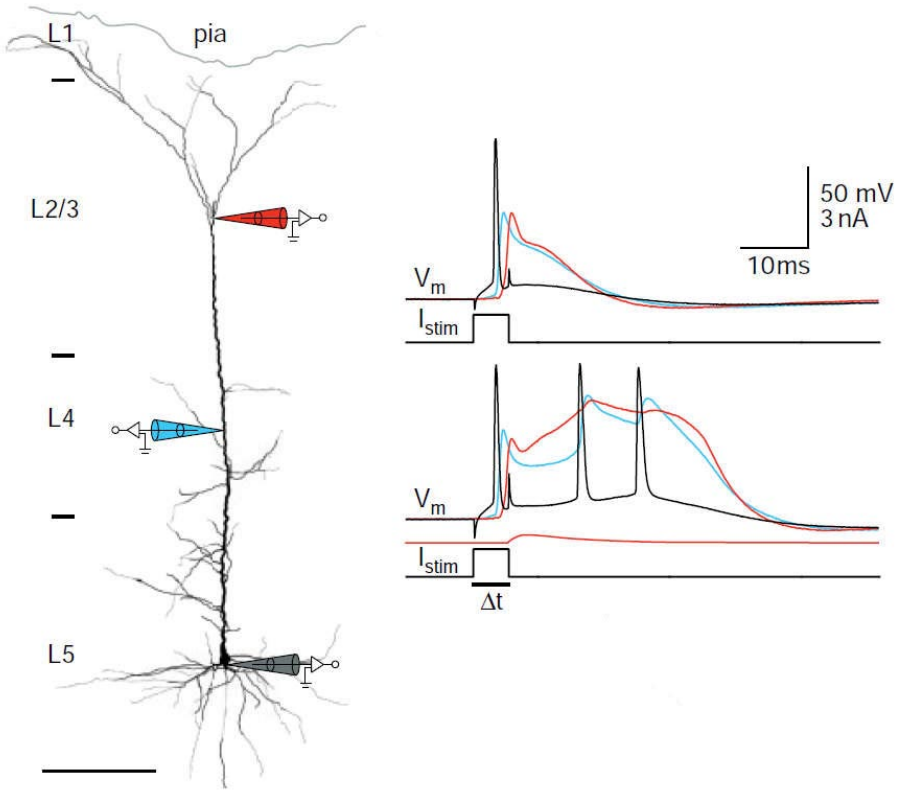

Figure 2.16: Coincidence detection in L5tt pyramidal neurons in vitro. Left: Experimental configuration with patch electrodes at the soma, apical trunk and apical tuft of a L5tt. Top right: After brief current injection at the soma (I_{stim}), a somatic AP is triggered (black voltage trace). This AP backpropagates (bAP) along the apical dendrite (blue and red voltage traces). Bottom right: After brief current injection at the soma followed by EPSP-like current injection at the apical tuft (black and red I_{stim} traces), the bAP and the current injection at the apical tuft trigger a Ca^{2+} spike in the apical dendrite, which in turn triggers two more APs at the soma. Figure adopted from [122].

in the apical dendrite, which in turn spreads to the soma and triggers two more APs (termed back-propagating action potential calcium spike (BAC) firing). The biophysical model is adapted to the morphology of the model neuron used here with an multi-objective optimization algorithm that determines an optimal set of the distribution of various ion channels that generate sub- and suprathreshold responses in agreement with experimental results ([125, 121]; kindly provided by Etay Hay and Idan Segev). A simplified axon morphology was attached to the reconstructed soma based on [126]. The axon consisted of an axon hillock with a diameter tapering from $3.5\mu m$ to $1\mu m$ over a length of $10\mu m$, an axon initial segment of length $10\mu m$ and diameter $1\mu m$, and 1mm of myelinated axon. The diameter of the reconstruction of the apical trunk and oblique dendrites was scaled

by a factor of 2.5 to allow for AP backpropagation and BAC firing to occur (i.e., after scaling the diameter of the apical trunk was $4.5\mu m$ at the soma, and $1.5\mu m$ at the main bifurcation located at a distance of $\sim 900\mu m$ from the soma). As described for the L2py neuron model, I determined the electrotonic length constant of each dendrite branch at a frequency of 100Hz and set the length of individual compartments in this branch to 10% of this length constant. The resulting length of individual compartments was on average $\sim 15\mu m$, but never larger than $50\mu m$. The length of axonal compartments was set to $10\mu m$. Fixed membrane parameters are the axial resistance ($100\Omega cm$ in all compartments), the membrane capacitance ($1\mu F$ at the soma and axon, $2\mu F$ in the apical and basal dendrites to account for increased surface area due to spines, and $0.04\mu F$ along the myelinated part of the model axon) and the passive membrane conductance along the myelinated part of the axon ($g_{pas} = 0.4\text{pS}/\mu m^2$, i.e. equivalent to a specific membrane resistance of $25000\Omega \cdot cm^2$). The reversal potential of the passive membrane conductance was set to -90mV. Conductance densities of the non-specific cation current I_h were fixed at $0.8\text{pS}/\mu m^2$ in the soma and axon, and $2\text{pS}/\mu m^2$ in the basal dendrites. In the apical dendrite, the conductance density of I_h increased exponentially with the distance to the soma: $-0.8696 + 2.087 \cdot \exp(d/d_{max})\text{pS}/\mu m^2$, where d is the distance to the soma, and d_{max} is the distance of the apical dendrite tip located the furthest from the soma. The parameters to be optimized are the peak conductance per unit membrane area for various voltage-dependent ion channels and the parameters of a phenomenological model of the calcium dynamics in different parts of the morphology (i.e. axon, soma, basal and apical dendrites; Table 2.7).

The target of the optimization are different features of the membrane potential in response to two stimuli, i.e. (i) brief current injection at the soma, triggering an AP at the soma and a bAP, and (ii) brief current injection at the soma, followed by current injection in the "hot zone" of the apical dendrite, triggering burst firing of three APs. The specific features are listed in Table 2.8 and were determined experimentally by Hay et al [121].

These features are combined into five objectives, which are then optimized simultaneously using an evolutionary algorithm [125]. Briefly, a set of 1000 models is generated with parameters drawn randomly from a physiologically plausible range. In every it-

Parameter	Soma	Axon	Apical	Basal
pas	0.326	0.256	0.882	0.631
Na_t	24300	880	252	–
Na_p	49.9	14.6	–	–
K_t	471	841	–	–
K_p	0	7730	–	–
SKv3.1	9830	9580	112	–
SK E2	492	0.577	34	–
Ca_{LVA}	46.2	85.8	1040	–
Ca_{HVA}	6.42	6.92	45.2	–
τ_{Ca}	770	507	133	–
γ_{Ca}	0.000616	0.0175	0.0005	–
I_m	–	–	1.79	–

Table 2.7: Optimized parameters of biophysical model of L5tt model neuron. These parameters were obtained using the multi-objective optimization algorithm described in the text. Units for different ion channel densitites are pS/μm^2. τ_{Ca} (ms) is the time constant of the calcium buffering model, and γ_{Ca} is a dimensionless parameter describing the calcium buffer affinity. pas: passive membrane conductance; Na_t: fast inactivating sodium current; Na_p: persistent sodium current; K_t: fast inactivating potassium current; K_p: slow inactivating potassium current; SKv3.1: fast non-inactivating potassium current; SK E2: calcium-acitvated potassium current; Ca_{LVA}: low voltage-activated calcium current; Ca_{HVA}: high voltage-activated calcium current; I_m: muscarinic potassium current.

Feature	Mean ± STD	Model	Difference (SD)
Ca^{2+} spike peak	6.73 ± 2.54mV	10.8mV	1.6
Ca^{2+} spike width	37.43 ± 1.27ms	36.5ms	0.7
BAC spike count	3 ± 0	3	0
Mean somatic AP ISI	9.9 ± 0.85ms	9.4ms	0.6
Somatic AHP depth	-65 ± 4mV	-66mV	0.3
Somatic AP peak	25 ± 5mV	34mV	1.8
Somatic AP half-width	2 ± 0.5ms	1.6ms	0.8
Spike count (somatic current injection only)	1 ± 0	1	0
bAP amplitude at $835\mu m$ from the soma	45 ± 10mV	14mV	3.1
bAP amplitude at $1015\mu m$ from the soma	46 ± 9.33mV	9mV	2.9

Table 2.8: Features of L5tt BAC firing used to constrain the biophysically realistic model. Experimental features adapted from [121]. ISI: inter-spike interval; AHP: after-hyperpolarization. Model features based on optimized parameters (see Table 2.7). Difference between model features and average experimental features given in units of SD of the experimental features. The recording locations for the bAP amplitude were adjusted to account for a longer apical trunk of the morphology used here.

eration, each model is then evaluated by simulating the response to the two stimuli, calculating the features and determining the error by calculating the difference between each simulated and measured feature in units of standard deviations of the experimental feature. After each model has been evaluated, a new set of 1000 models is generated from the previous set by stochastically transferring parameter values from "good" models (i.e. lower errors) to "worse" models (i.e. higher errors). Additionally, parameters values of all models are updated stochastically to avoid converging to local minima of the objective errors. This procedure is repeated for 500 iterations. From the final set of 1000 models, the model with the lowest variability in all five objective errors and lowest sum across all objective errors at the same time is chosen (Figure 2.17). All numerical simulations were carried out using the NEURON package (NEURON 7.2 [106]).

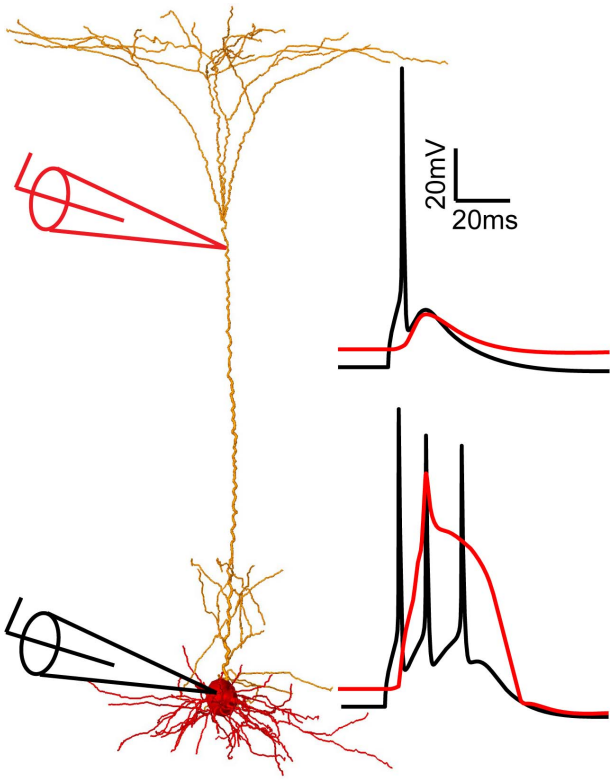

Figure 2.17: Biophysically realistic model of a L5tt neuron (see Table 2.7 for parameters). Top traces: response to brief current injection at the soma (1.9nA amplitude, 5ms duration), measured at the soma (black electrode/membrane potential trace) and at the Ca^{2+}-"hot zone" (red electrode/membrane potential trace). Bottom traces: response to brief current injection at the soma (1.9nA amplitude, 5ms duration), followed by an EPSP-like current injection at the "hot zone" (red electrode; 5ms delay after current injection at soma, amplitude 0.5nA, 0.5/5ms rise/decay time), measured at the same locations.

Monte Carlo sampling from constrained parameter space. As described previously for the L2py neuron model, I generate samples from the statistical distributions of anatomical, functional and physiological constraints to generate biologically realistic functional connectivity patterns to the L5tt neuron model during ongoing activity and after PW/SuW deflections. Each sample consists of 245ms of ongoing activity, followed by 50ms of whisker-evoked activity. Each of these samples is interpreted as an individual trial and the membrane potential in the dendrites, soma and axon of the L5tt morphology in response to the spatiotemporal synaptic input pattern of each trial is simulated. The first 100ms of ongoing activity are discarded to remove numerical artifacts. Ongoing activity is analyzed in a 100ms interval (i.e., from 120-220ms), following the protocol of [26]. The quantities I am going to analyze are the number, presynaptic cell type and activation time of synapses, the subthreshold membrane potential at the soma during ongoing activity, as well as the probability and timing of APs at the soma. I am going to compare APs at the soma during ongoing and sensory-evoked activity to measurements of the mean ongoing spike rate of L5tt, as well as the evoked response probability within 50ms after PW and eight SuW responses. Similar to the L2py neuron model, I estimated how many samples are required to minimize the statistical (sampling) error. After 200 trials, I estimated the statistical error of the ongoing activity as $\sim 5\%$ and the statistical error of the evoked RF per deflected whisker as $\sim 10\%$ (Figure 2.18). Thus, the full model consisted of 16,200 samples (i.e., 200 samples per PW and eight SuW deflections, for each of the L5tt neuron model at nine locations within the C2 column).

In order to determine the influence of the different parameter distributions on the target quantities (subthreshold membrane potential at the soma during ongoing activity, probability and timing of APs at the soma), I generated samples while keeping all but one of the distributions fixed.

1. To investigate the possible influence of location-specific connectivity on responses of L5tt, I analyzed the subthreshold and suprathreshold responses separately for each of the nine model locations in the C2 column.

2. To investigate the impact of different cell types on PW- and SuW-evoked AP responses, I generated 16,200 samples without sensory-evoked activity of L5tt (i.e.,

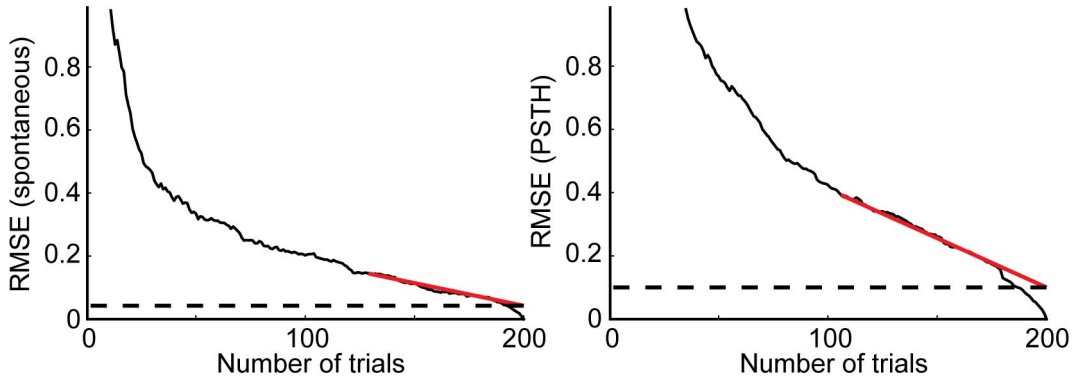

Figure 2.18: Estimate of sampling error during L5tt neuron simulations. Root mean square error (RMSE) of the mean ongoing activity (left) and the evoked PSTH of nine whiskers 50ms post-stimulus (right). The RMSE was calculated with respect to the value of these two quantities after 200 trials. Therefore, I extrapolated the RMSE from a linear region to the final estimated value after 200 trials.

the ongoing activity of L5tt remained unaffected), and 16,200 samples without sensory-evoked activity of L6cc (i.e., the ongoing activity of L6cc remained unaffected).

3. To investigate the possible influence of different biophysical properties of synapses from presynaptic L5tt, which display short-term facilitation, compared to all other presynaptic excitatory cell types displaying short-term depression, I generated 16,200 samples where synapses were simulated including facilitation/depression.

Chapter 3

Results

3.1 Anatomical model of rat vS1

In the following pages, I am going to describe the average model of neural networks in rat vS1, developed using the previously described methods. Across multiple spatial scales from the 3D geometry of rat vS1 to the 3D distribution of synapses, this model is used to provide constraints on the synaptic connectivity of single neurons depending on pre- and postsynaptic cell type, soma location and dendrite morphology of the postsynaptic neuron.
The most important results of the average anatomical model that impact the simulation results are:

- As previously described, the variability of anatomical parameters and 3D geometry of rat vS1 across animals is low. Here, I found that this can be used for precise registration of single neuron morphology to the average model of rat vS1 to determine the 3D location of a neuron in the brain and its subcellular distribution of synaptic inputs with high resolution.

- The 3D distribution of neuron somata is also preserved across animals, but the vertical (laminar) and horizontal organization are found to be whisker-specific (i.e., an "average column" at cellular resolution does not exist). Further, the vertical and horizontal organization is different for excitatory and inhibitory neurons.

- Excitatory cell types, classified using soma location and morphological and topological features of dendrites, display specific axon projection patterns, as well as specific ongoing and whisker-evoked activity.

- Inhibitory cell types can be classified using soma location and vertical axon projection patterns. These inhibitory projection types form the structural basis of sensory-evoked feed-forward inhibition used in simulations.

- The dense average network model of rat vS1 matches sparse experimental observations across multiple scales. However, in contrast to sparse experimental samples, the network model allows investigation of location-and cell type-specific connectivity at subcellular resolution, which will later be used in the models.

3.1.1 Precision of 3D registration

Note: This description is adapted from Egger et al. 2012 [54].

I have previously established that the anatomical parameters describing the geometry of individual barrel columns are column-specific, but preserved across different animals [68]. This allowed generating an average model of the geometry of rat vS1, which serves as the average reference frame, by registration of 12 3D reconstructions of pia and WM surfaces, as well as the 24 barrels and barrel columns representing the large facial whiskers to a common coordinate system and averaging the anatomical parameters of each individual column across reconstructions. The limit on 3D registration precision of individual experiments to the average reference frame of rat vS1 is determined by the across-animal variability of common landmarks used for registration (here: the 3D location and orientation of barrels and barrel columns), which I have previously shown to be remarkably small [68]. The average 3D variability of the location of individual barrels and barrel columns across different animals is $89\mu m$ (Figure 3.1). Further, I was able to show that the 3D layout of the barrels with respect to each other is also preserved. Based on these results, I will show in the following paragraphs that precise registration of single neuron morphologies into the average reference frame of rat vS1 and subsequent integration

into the dense network model based on 3D reconstruction of anatomical landmarks in individual experiments is possible.

Unfortunately, the high-contrast cytochrome-oxidase staining needed to automatically extract the barrel landmarks [68] prevents tracing biocytin-labeled [59] dendrite and in particular axon morphologies. In turn, the low-contrast cytochrome-oxidase staining needed to reliably trace neuron morphologies prevents automated extraction of the barrel landmarks. Thus, to assess how accurate 3D neuron tracings can be registered to the average reference frame by rigid transformations, systematic differences between manually and automatically extracted reference landmarks needed to be quantified. To do so, all visible anatomical landmarks for 94 reconstructed neuron morphologies with somata located within rat vS1 and at varying cortical depth between L2 and L6 (recording depth: $222 - 1727\mu m$ [26]) were traced manually. Using this set of morphologies, I developed a precise registration pipeline that automatically compensates for differences between manually and automatically extracted landmarks. The individual steps of the pipeline are exemplarily illustrated for one L5tt neuron [50] in Figure 3.2.

Global alignment of neuron location. The barrel center of the manually reconstructed PC (i.e., containing the neuron's soma) was aligned with the respective barrel center of the average reference frame of rat vS1. This is in contrast to the optimal global translation described before (section 2.2.2), where the center of mass of the manual reconstruction and the average reference frame are aligned. However, alignment of the center of the PC guarantees the highest possible registration accuracy of soma/dendrites/axon within the PC, at the cost of achieving less precision in surrounding columns. Then, the remaining BC locations were registered by using only rigid transformations (Figure 3.2 C, left panel). This step resulted in a rotation of the principal BC axis of 14.0 ± 7.6^o ($1.6 - 32.8^o$, Figure 3.2 C, top-right panel). Because the BC axis of the unregistered tracings was defined by the cutting plane of the vibratome, the rotation of the 'global orientation' of the neuron, compensated for systematic differences introduced by cutting the brain into sections. The orientation of the BC axis after the first registration step was on average more variable (SD: 7.6^o) than the 4.5^o deviation in column orientation determined for the average reference frame of rat vS1. This likely reflected the observation that the manually determined contours defining BT and BB were less precise than

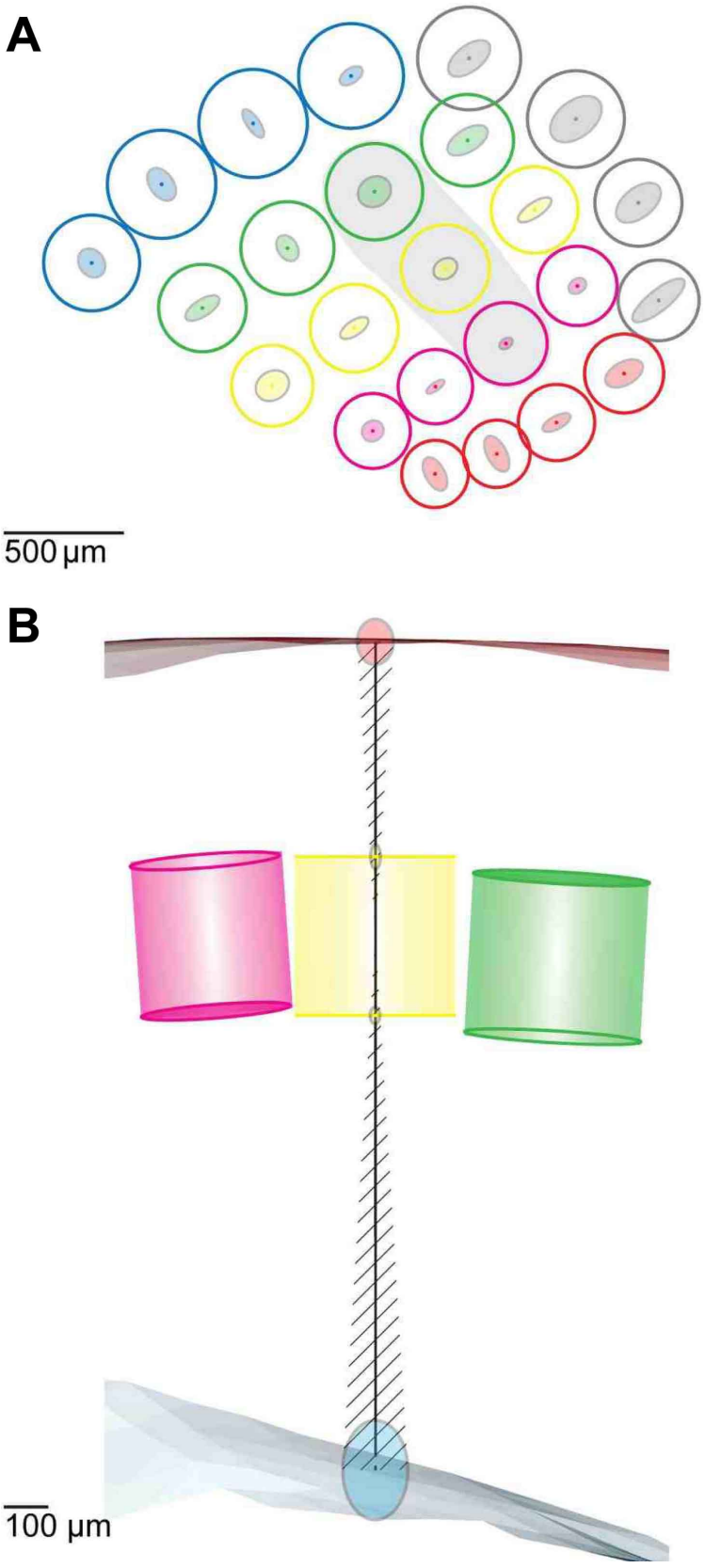
A
500 µm
B
100 µm

Figure 3.1 *(previous page)*: Variability of the average reference frame of rat vS1. (A) Variability of the registered BT points measured along rows/arcs. Barrels in shaded region are shown in the side view in (B). (B) Vertical axis of the error ellipses shows the variability of the registered BT, BB, pia and WM along the barrel column axis. Dashed region indicates horizontal variability due to variability of the orientation of the barrel column axis across animals. This error is smaller than the variability along rows and arcs between animals, and thus negligible at the BT and BB. Figure adopted from [54].

their automated counterparts.

Local alignment of neuron orientation. I thus introduced a second rotation step. The apical dendrite of pyramidal neurons in the cortex usually projects along an axis perpendicular to the pia surface and thus, parallel to the large blood vessels in its immediate surrounding [68]. The local blood vessel pattern can consequently be used to determine the vertical axis of a barrel column and hence of a reconstructed neuron. To do so, I reconstructed the blood vessels throughout vS1 and determined local vertical axes with $50\mu m$ precision (i.e., $50\mu m$ spacing between neighboring vertical axes, see section 2.2.1). Further, I determined the orientation corresponding to the first principal component of the apical dendrite and rotated the tracing until this 'dendrite orientation' matched the vertical axis closest to the respective soma. In cases where no clear apical dendrite was present (e.g., for L4ss [88]), the direction of the main axon leaving the soma in a straight direction towards the WM was defined as the neuron's orientation. The additional rotation of the 'neuron orientation' was small ($0.8 - 20.0^o$, 7.3 ± 4.5^o, Figure 3.2 C, bottom-right panel) compared to the global orientation step. In particular, the resultant variability in neuron orientation of 4.5^o matched the previously determined variability in BC axis orientation across animals.

Correction of systematic landmark deviations in lower-resolution reconstructions. After translations and rotations, the new BT, BB, pia and WM locations were systematically compared to their counterparts in the average reference frame of rat vS1. The average vertical locations of all landmarks deviated from the average reference frame (Figure 3.2 D, right panel). All parameters varied independently for different columns. For example, for the D2 column, the manual BB deviated on average $59\mu m$ from the respective reference landmark (manual: $947\mu m$ vs. reference: $888\mu m$ depth below the pia surface). The BT deviated on average by $68\mu m$ (manual: $594\mu m$ vs. reference: $526\mu m$)

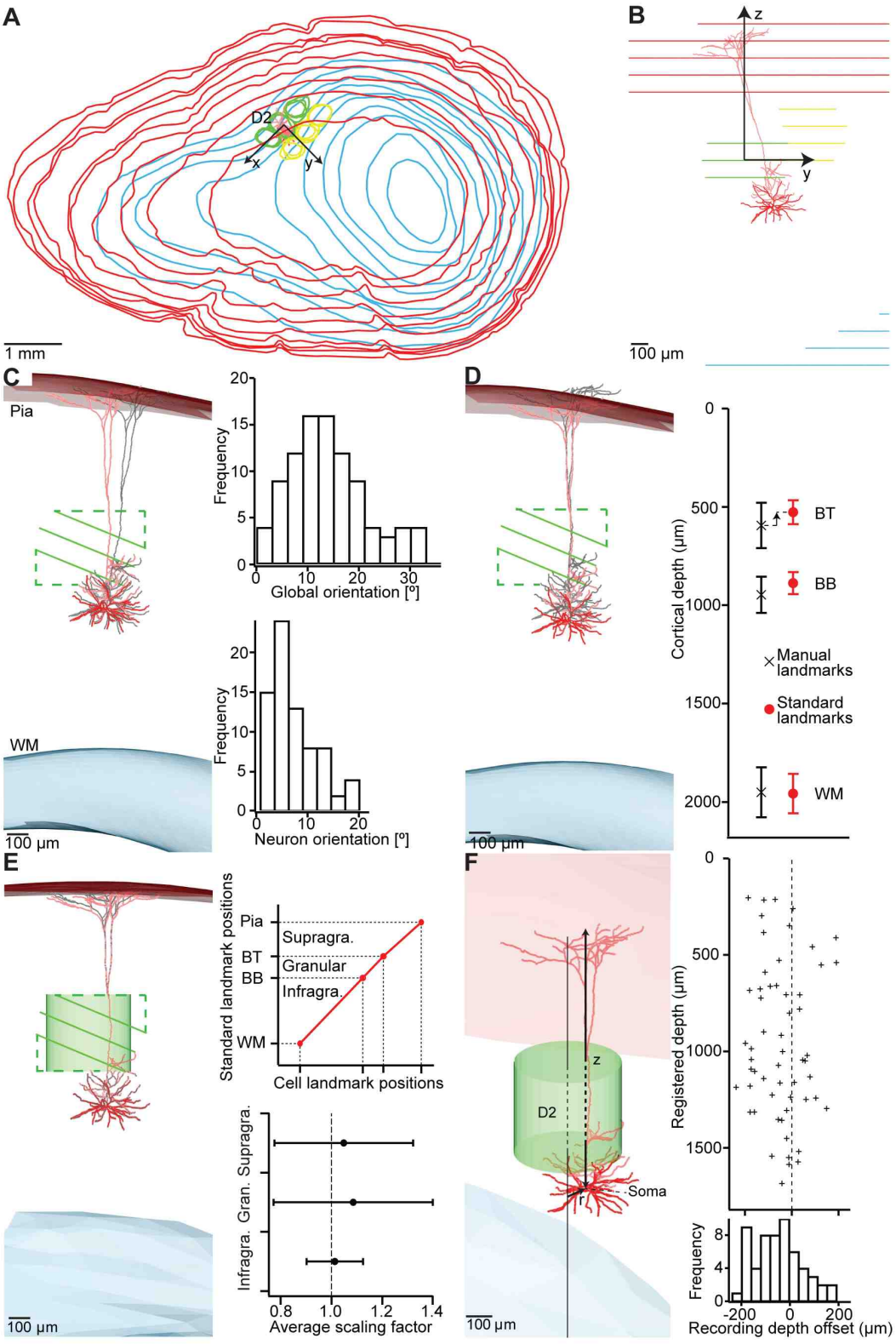
A
D2
x
y
1 mm
B
z
y
100 µm
C
Pia
WM
100 µm
Frequency
Global orientation [°]
Neuron orientation [°]
D
Cortical depth (µm)
BT
BB
Manual landmarks
Standard landmarks
WM
100 µm
E
Standard landmark positions
Pia
Supragra.
BT
Granular
BB
Infragra.
WM
Cell landmark positions
Infragra.
Gran.
Supragra.
Average scaling factor
100 µm
F
z
D2
Soma
100 µm
Registered depth (µm)
Frequency
Recording depth offset (µm)

Figure 3.2 *(previous page)*: Registration of 3D neuron morphologies to the average reference frame of rat vS1. (A) Example of a L5tt neuron reconstructed from $100\mu m$ thick sections. Outlines of pia, WM and barrels are added to the reconstruction in the coordinate system given by the slicing direction. (B) Side view of (A). The slicing direction does not match the orientation of the column containing the neuron soma. (C) Reconstruction of landmarks in 3D and registration of the barrels to the average reference frame. It may be necessary to correct the orientation of the neuron to match the direction of the local column axis (gray – before rotation, red – after rotation). The histograms show the rotation angle used to align the barrel field outlines with the average reference frame (global orientation) and the angle of the subsequent rotation aligning the neuron orientation with the local column orientation. (D) The barrel outlines in the reconstruction are of lower resolution along the slicing direction and thus show a systematic offset compared to the barrel landmarks in the average reference frame. This is corrected for by translation along the local column axis. (E) The variability between different reconstructions is minimized by scaling the supragranular, granular and infragranular structures such that the landmarks of the reconstructed neuron coincide with the landmarks in the average reference frame. The average scaling factors for the individual layers are very close to 1. (F) Registration of the neuron to the average reference frame of rat vS1 allows objective determination of anatomical parameters such as the soma location in 3D. Comparison of the registered depth of 56 neurons with the penetration depth of the pipette recorded during the experiment shows that this recording depth is on average $46\mu m$ lower than the registered depth, but varies in a range of up to $200\mu m$ around the registered depth. Figure adopted from [54].

and the depth location of the WM deviated on average by $7\mu m$ (manual: $1950\mu m$ vs. reference: $1957\mu m$) from the respective landmarks in the average model. Consequently, I shifted the contours of the principal column in each tracing by the respective differences between the mean values of the manual tracings and the average reference frame (Figure 3.2 D, left panel). Further, I measured the distance between the apical tuft endings and the reconstructed pia surface exemplarily for four neurons where the apical tufts reached the upper most part of L1 (i.e., true distance to the pia surface was zero). The average distance of the apical tuft endings to the reconstructed pia surfaces was $39 \pm 5\mu m$. Thus, I shifted all manually traced contours by $-39\mu m$ with respect to the neuron tracing. In addition, the thickness of the first vibratome section may deviate from the assumed $100\mu m$ thickness. I therefore compared the average distance to the pia for four neurons whose apical tufts ended within the first vibratome section and ten neurons with tufts already reaching the pia in deeper sections. The reconstructed pia of the first section was on average $20\mu m$ too high and I corrected the vertical pia location accordingly.

Stepwise linear scaling. In the final registration step, differences between the registered vertical locations of BT, BB, pia and WM of each individual neuron tracing were compared to the respective reference landmarks (Figure 3.2 E, top-right panel). BT, BB, pia and WM deviated independently from each other. Therefore, I chose a stepwise linear scaling to match the respective landmarks of each tracing with the counterparts in the average reference frame (Figure 3.2 E, left panel). Three scaling factors were determined between: (i) the pia and the BT (i.e., supragranular layers), (ii) the BT and BB (i.e., granular layer) and (iii) the BB and the WM (i.e., infragranular layers). The scaling factors were on average very close to 1 (i.e., 1.05 ± 0.27, 1.09 ± 0.31 and 1.01 ± 0.11 in supragranular, granular and infragranular layers, respectively).

Precision of neuron registration to the average vS1 model. In summary, by (i) coarse registration of BC locations, (ii) fine tuning of neuron orientation, (iii) shifting the vertical locations of BT, BB, pia and WM by their respective average differences between manually and automatically determined landmarks and (iv) stepwise linear scaling of the neuron along the vertical column axis, I found that the manually reconstructed vibrissal cortices could be matched to the average reference frame of rat vS1 as precisely as the automatically reconstructed versions. The precision of registering individual neurons to the average reference frame may thus be expressed as the standard error (SE) of the average BC location across animals, multiplied with the respective scaling values in supragranular, granular and infragranular layers, respectively. Specifically, the vertical precision of the supragranular layers can be determined as the SE of the BT locations, which was $15\mu m$, multiplied with the average scaling of 1.05, resulting in $SE_{z,supra} = 16\mu m$. The vertical precisions of the granular and infragranular layers can be determined accordingly by the SE in barrel and column heights (i.e., $SE_{z,granular} = 10\mu m$ and $SE_{z,infra} = 28\mu m$), respectively. Combined with the precisions along the row and arc ($SE_{row} = 19\mu m$, $SE_{arc} = 14\mu m$, see above), the 3D registration accuracy for neurons located in supragranular layers is $28\mu m$, in the granular layer it is $26\mu m$ and in infragranular layers it is $37\mu m$. Consequently, the 3D location of the soma, as well as dendrites and axons close to the PC, can on average be determined with $\sim 30\mu m$ accuracy. However, the registration was optimized to match the BC location of the PC. The registration accuracy of neuronal branches that project out of the PC (i.e., long-range projections into septa and SCs) was

hence not determined by the SE of the surrounding BC locations, but by their average SDs. The average 3D registration accuracy of neuronal (long-range) projections within SCs was thus $\sim 89\mu m$ (i.e. a cube with $50\mu m$ side length). At this stage it should be emphasized that the present registration precisions are to be considered with respect to the average dimensions of the vibrissal cortex, i.e., SE and SD of the barrel location describe the precision of registered local and long-range projections, respectively. However, since the 3D layout of an individual cortex may deviate more from the average model of rat vS1 than the average of the 12 cortices, the 'minimal' precision of registration may be given as the average RMSE of the BC locations determined by a 'leave-on-out' analysis, i.e., $146\mu m$. For a summary of the column-specific registration precisions see Table 3.1.

Precision of soma location without registration. As a first application of the registration method, I compared the vertical locations of the somata after registration with their respective recording depths (i.e., penetration depth of the pipette, Figure 3.2 F). In general, the recording depth slightly deviated from the registered depth. Some neurons were deeper within in the cortex than suggested by their recoding depths; others were closer to the pia. On average, the recording depth deviated by $-46 \pm 102\mu m$ from the registered soma depth (i.e., unregistered neurons appeared to be deeper within the cortex). The surprisingly small difference of, on average, $46\mu m$ between the registered depth of the soma and the penetration depth of the recording pipette suggest that tissue shrinkage due to perfusion, fixation and histology (see Methods), which can be up to 20% [65], is largely compensated by the present approach of generating an average reference frame of rat vS1. Consequently, the recording depth may be used as a predictor of a neuron's location within the present reference frame of vS1 with approximately $\pm 102\mu m$ precision. However, as I will show in the following section, without 3D reconstruction of anatomical landmarks and registration of neuron morphology, as presented here, this precision will likely be insufficient to draw conclusions about cell type or even laminar location.

Implications for network-embedded modeling. The precision of the registration method determines two key parameters used during model building. First, the precise 3D location of the neuron model may affect the input it receives from different presynaptic cell types [31]. Second, the subcellular distribution of synapses from different presynaptic

Barrel	SE (μm)	SD (μm)	RMSE (μm)
A1	27	95	179
A2	24	80	170
A3	27	89	166
A4	26	86	166
Alpha	40	138	211
B1	19	65	106
B2	14	48	101
B3	15	51	108
B4	19	65	131
Beta	36	124	158
C1	27	92	106
C2	20	69	104*
C3	22	75	102
C4	30	102	167
Gamma	42	139	176
D1	30	105	153
D2	28	98	121
D3	24	83	110
D4	27	95	150
Delta	33	114	203
E1	20	71	148
E2	23	81	136
E3	26	91	160
E4	24	85	168

Table 3.1: Precision of registration for each barrel column. The average precision of the soma/dendrites/axon location within the PC (i.e., containing the neuron's soma) is determined as the standard error of the barrel location (SE). The average precision of long-range projecting axons into columns surrounding the principal column is given by the standard deviation of the barrel location (SD). The minimal precision is derived from a leave-one-out analysis as the root mean squared error between the predicted and actual barrel location (RMSE) for 12 reconstructions of rat vS1. The RMSE of the C2 barrel (*) is computed as the average of C1 and C3, because the C2 BC is the origin of the coordinate system during parameterization. Table adopted from [54].

cell types in the dense network model can only be determined as accurately as neuron morphology can be registered to the average reference frame of rat vS1 [31]. During the description of the network-embedded simulation results, I will show how activity of the simulated neurons is affected by these parameters.

3.1.2 Across- and within-animal-variability of soma distributions

Note: This description is adapted from Meyer, Egger et al. 2013 [55]. Experiments to label and image neuron somata were carried out by Hanno Meyer (Max Planck Florida Institute for Neuroscience).

I measured the number of excitatory and inhibitory neurons within 24 barrel columns ($\alpha - \delta$, A1-E4) and the septa between them in four different rats (Figure 3.3; Table 3.2). The average total number of neurons in this large portion of the vibrissal cortex was $529,715 \pm 39,104$ (mean $\pm$ SD). 87% of the neurons in vibrissal cortex were excitatory, 13% inhibitory. Extrapolating L4 barrel boundaries toward the pia and WM, 81% of all neurons were located within barrel columns, 19% in the septa between them. The total volume of this part of the vibrissal cortex after perfusion and fixation [65] was $6.60 \pm 0.58 mm^3$, which is consistent with measurements of the cortex geometry using cytochrome-oxidase as a marker to reveal the barrels ($6.53 \pm 0.75 mm^3$ [54]). The across-animal-variability in total neuron numbers (SD of mean: 7.4%) and volume (8.8%) were similar. Consequently, the average neuron density across the entire vibrissal cortex was preserved ($80,419 \pm 3,688 mm^{-3}$). The same was true for the average density in columnar ($82,402 \pm 4,011 mm^{-3}$) and septal ($72,792 \pm 2,419 mm^{-3}$) regions, respectively. There was no difference between the neuron density in the septa between whisker rows ($67,078 \pm 4,751 mm^{-3}$) and in the dysgranular zone surrounding vS1 ($68,236 \pm 2,226 mm^{-3}$ anterior-medial to the E-row and $66,311 \pm 1,084 mm^{-3}$ posterior-lateral to the A-row). Labeling brain sections with GAD67 did not only reveal the columnar organization of rat vS1, as previously reported [53], but also showed the segregation of VPM thalamus into barreloids (also see Figure 2.3 in the methods section). Using the same methodology as

for vS1, I measured the number of excitatory and inhibitory neurons for the respective 24 barreloids in three different rats (Table 3.2). The average total number of neurons in this portion of vibrissal thalamus was $9,963 \pm 718$. As for vS1, the variability in neuron numbers across animals was small (7.2%). 100% of the neurons in VPM thalamus were excitatory (i.e., GAD67-negative). The total volume of this part of vibrissal thalamus (i.e., convex hull around 24 barreloids) was $0.19 \pm 0.03 mm^3$, resulting in an average neuron density across the entire VPM of $52,494 \pm 5,082 mm^{-3}$. Densities in VPM within and above/below barreloids ($51,507 \pm 4,422$ and $54,440 \pm 6,559 mm^{-3}$, respectively) were larger compared to the surrounding thalamic nuclei, with $49,680 \pm 1,097$ and $41,477 \pm 3,612 mm^{-3}$ in nucleus reticularis (RT) and posterior medial nucleus (POm), respectively.

Whisker-specific laminar organization. Each detected soma was assigned to its nearest barrel column or to the septum, respectively (Figure 3.3 A-B). The resultant column/septum-specific 3D distribution of excitatory (Figure 3.3 C) and inhibitory somata (Figure 3.3 D) could thus be analyzed with respect to previously defined cytoarchitectonic layers [31]. Cortical thickness (i.e., pia-WM distance along the respective vertical column axis) increased substantially across vS1, being thinnest at the barrel column corresponding to the α-whisker ($1,612 \pm 36 \mu m$) and thickest at the E3-whisker representation ($2,089 \pm 15 \mu m$).

The increase in cortical thickness was linear across whisker rows (linear regression: $R^2 = 0.99$, p=0.001). Consequently, the density distributions of individual barrel columns were 'stretched' along their respective vertical axis, resulting in column-specific depth locations and thicknesses of the respective cytoarchitectonic layers (Figure 3.3 E (dashed lines)). In contrast, the height of the L4 barrel increased sublinearly ($R^2 = 0.9$, p=0.10). Thus, the depth of granular L4 was more constant across vS1 than the respective cortical thickness. For example, cortical thickness increased from the A2- ($1,760 \pm 39 \mu m$) to the E2-column ($2,063 \pm 50 \mu m$) by $303 \mu m$, the depth of the L4 peak (Gaussian approximation) shifted by $116 \mu m$ (from $647 \mu m$ to $763 \mu m$ below the pia surface), whereas the L5/6 peak shifted ~ 2.4 times more, i.e., by $275 \mu m$ (from $1409 \mu m$ to $1684 \mu m$). The density of excitatory and inhibitory neurons within each of the respective layers was constant across vS1. The average neuron density was $61,603 \pm 3,721 mm^{-3}$ (SD of mean: 6.0%)

	Exc. neurons vS1	Inh. neurons vS1	Exc. neurons VPM
α	10,244 ± 2,235	1,536 ± 298	186 ± 30
β	13,161 ± 857	1,841 ± 640	199 ± 23
γ	17,270 ± 1,406	2,393 ± 857	282 ± 11
δ	19,155 ± 1,363	2,764 ± 849	246 ± 22
A1	9,346 ± 1,480	1,675 ± 486	196 ± 23
A2	9,424 ± 1,789	1,624 ± 370	198 ± 28
A3	8,066 ± 990	1,351 ± 160	132 ± 16
A4	8,228 ± 1,679	1,432 ± 655	89 ± 20
A row	8,766 ± 719	1,521 ± 154	154 ± 53
B1	12,520 ± 1,806	1,866 ± 402	295 ± 40
B2	11,953 ± 2,279	2,089 ± 392	306 ± 26
B3	10,292 ± 1,951	1,741 ± 346	227 ± 35
B4	10,726 ± 1,952	1,667 ± 242	149 ± 8
B row	11,373 ± 1,039	1,841 ± 185	244 ± 73
C1	15,459 ± 2,538	2,032 ± 551	329 ± 12
C2	17,195 ± 1,545	2,511 ± 661	350 ± 3
C3	15,273 ± 1,661	2,258 ± 435	253 ± 19
C4	13,028 ± 3,075	1,890 ± 278	218 ± 29
C row	15,239 ± 1,709	2,173 ± 272	287 ± 62
D1	17,588 ± 2,191	2,489 ± 895	286 ± 4
D2	20,377 ± 2,124	3,005 ± 844	311 ± 7
D3	19,776 ± 3,304	2,920 ± 535	296 ± 37
D4	18,862 ± 1,443	2,758 ± 686	270 ± 26
D row	19,151 ± 1,214	2,793 ± 227	291 ± 17
E1	22,183 ± 2,412	3,276 ± 836	298 ± 55
E2	25,813 ± 4,133	3,750 ± 897	346 ± 41
E3	24,391 ± 4,890	3,575 ± 698	403 ± 33
E4	21,587 ± 4,118	3,085 ± 395	361 ± 41
E row	23,493 ± 1,961	3,421 ± 298	352 ± 43
Mean	15,497 ± 5,266	2,314 ± 697	259 ± 78

Table 3.2: Whisker-specific cellular organization in rat vS1 and vibrissal thalamus (VPM). All numbers are mean ± SD (vS1: n=4; VPM: n=3). Table adopted from [55].

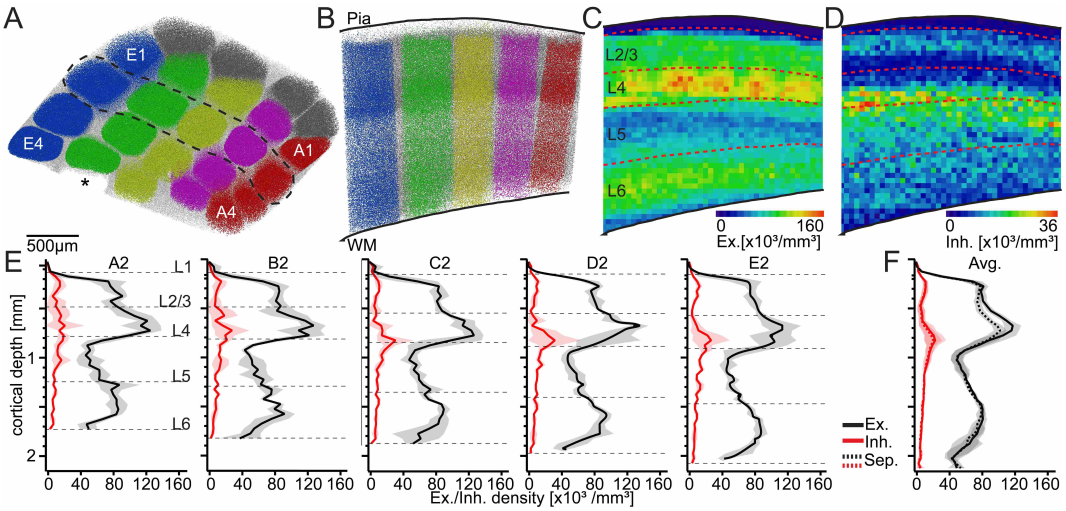

Figure 3.3: Whisker-specific laminar cellular organization of rat vS1. (A) Tangential view of all neuron somata in vS1 of one animal. Somata are assigned to their closest barrel column [row colors: A (red), B (pink), C (yellow), D (green), E (blue), Greek arc (gray)] or to the septum (white). *D5 barrel column excluded from analysis. (B) Semicoronal view of the somata within the dashed region in A. A 3D reconstruction of pia and WM surfaces allows for determining the position of all neuron somata with respect to cytoarchitectonic layer borders (20). (C) A 2D average projection of the 3D excitatory neuron density. L4 barrels are clearly visible as segregated spots of high neuron density (24). (D) A 2D average projection of the 3D inhibitory neuron density. Segregation between barrels and septa is not evident. L2 and upper L5 are separable as bands of high inhibitory neuron density, as reported previously (22). (E) Average distribution of excitatory and inhibitory neuron somata along the vertical column axis for columns in arc-2. Shaded regions are ±1 SD. Dashed lines represent column-specific layer borders. (F) Average distribution of excitatory/inhibitory somata across all barrel columns and septa. Figure adopted from [55].

within supragranular (s) L1-3, $122,931 \pm 6,204 mm^{-3}$ (5.1%) within granular (g) L4 and $79,092 \pm 5,383 mm^{-3}$ (6.8%) within infragranular (i) L5-6. The same was true for the average density in columnar (s: $63,878 \pm 4,329$; g: $126,145 \pm 6,298$; i: $79,424 \pm 5,441 mm^{-3}$) and septal (s: $56,061 \pm 2,301$; g: $111,293 \pm 7,558$; i: $77,090 \pm 5,040 mm^{-3}$) regions, respectively. Because neuron densities within a layer were constant, but layer depths and thicknesses changed across vS1, the numbers of excitatory and inhibitory neurons within cytoarchitectonic layers were highly whisker-specific. The relative proportions of neurons per layer were however virtually identical for all barrel columns. $24 \pm 1\%$ of all neurons within a barrel column were located within supragranular layers (L1: $0.5 \pm 0.1\%$; L2/3: $23.3 \pm 1.1\%$), $25.2 \pm 2.0\%$ in granular L4 and $51 \pm 2\%$ in infragranular layers (L5: $24.2 \pm 0.9\%$; L6: $26.8 \pm 1.2\%$). The proportion of neurons within the L4 barrel was in-

dependent of the respective cortical thickness (Pearson's correlation coefficient: r=0.02, two-tailed t-test: p=0.93) and significantly correlated with (i.e., predicted) the respective supragranular (r=-0.46, p=0.02) and infragranular (r=-0.77, $p < 10^{-4}$) proportions. In contrast, supra- and infragranular proportions were uncorrelated (r=0.24, p=0.26). Consequently, the largely preserved vertical extent and depth location of the L4 barrels caused the constant laminar neuronal composition of cortical barrel columns, despite substantial whisker-specific increases in neuron numbers and cortical thickness.

Whisker-specific horizontal organization. I calculated the direction of the gradient within the horizontal plane of vS1 (Figure 3.4 (arrows)) for the volume, neuron density, neuron number and fraction of inhibitory neurons per barrel column, respectively. The horizontal gradient in column volume revealed a 'rowish' organization of rat vS1 (see also [54]). Barrel columns within the same whisker row displayed almost identical volumes, whereas the column volume increased in an orderly manner from the A- towards the E-row by a factor of ~ 2.5 (Figure 3.4 A, $p < 10^{-15}$, 1-way ANOVA). In contrast, average neuron densities did not differ between columns, as indicated by the absence of a horizontal gradient across vS1 (Figure 3.4 C, p=0.49, two-tailed t-test).

Consequently, the average number of neurons per cortical barrel column followed the gradient in column volume, resulting in relatively constant neuron numbers for columns within the same whisker row (Table 3.2) and an orderly ~ 2.5-fold increase from the A- ($10,803 \pm 1,275$ neurons) toward the E-row ($26,914 \pm 2,256$ neurons) (Figure 3.4 B, $p < 10^{-15}$, 1-way ANOVA). Figure 3.4 C (bottom rectangle refers to the septum) indicates a significant drop in neuron density between barrel columns and septa. In contrast, the relative proportion of inhibitory neurons was independent of barrel column identity or septal location (Figure 3.4 D, p=0.65, two-tailed t-test). Moreover, the average 1D profiles in Figure 3.3 F (right panel) revealed that the density of inhibitory neurons was nearly identical between columns ($10,826 mm^{-3}$) and septa ($9,516 mm^{-3}$). The distribution of excitatory neurons differed between columns and septa, but differences were limited to L4. There, the density of excitatory cells dropped from barrels to the septum by up to 17%, reflecting a decrease from $\sim 120,000$ to $\sim 100,000$ neurons per mm^3. Figure 3.4 E -F further illustrates this finding for the distribution of excitatory and inhibitory neurons within supragranular, granular and infragranular layers, respectively. A

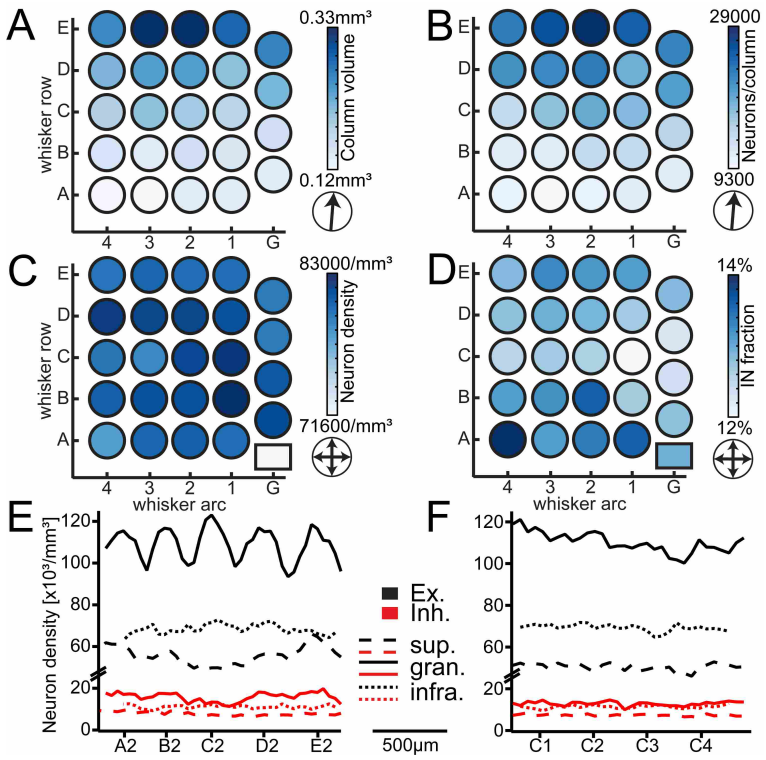

Figure 3.4: Whisker-specific horizontal cellular organization of rat vS1. (A) Average volume per barrel column based on the four vibrissal cortices analyzed, showing a significant increase from the A- to the E-row. (B) Average number of all neurons (excitatory and inhibitory) per barrel column, increasing from the A- to the E-row concomitantly with the column volume. (C) The average neuron density (excitatory and inhibitory) per barrel column is constant across the barrel field and larger than septal neuron density (box). (D) The average fraction of inhibitory neurons (IN) is similar across the barrel field and does not differ between columns and the septum (box). (E) The average distribution of excitatory/inhibitory neurons in different cortical layers, measured along arc-2 (from left to right: A2–E2), shows a clear separation into barrel columns and septa only in L4, where excitatory neurons delineate the barrels. (F) The average distribution of excitatory/inhibitory neurons in different cortical layers, measured along the C-row (from left to right: C1–C4), is not indicative of a separation between barrel columns and septa at the cellular level. Figure adopted from [55].

significant separation between columns and septa was only evident for the distribution of excitatory neurons within granular L4 along the whisker arc (i.e., between whisker rows). Consequently, outside the L4 barrel, the cellular organization of excitatory and inhibitory neurons was virtually identical in barrel columns, septa and the dysgranular zone surrounding vS1.

Organization between vibrissal thalamus and cortex. I also determined the neuron numbers, volumes and densities of each individual VPM barreloid (Table 3.2, Figure

3.5 A-C). The relationship between barreloid volume and neuron density differed from the vibrissal cortex.

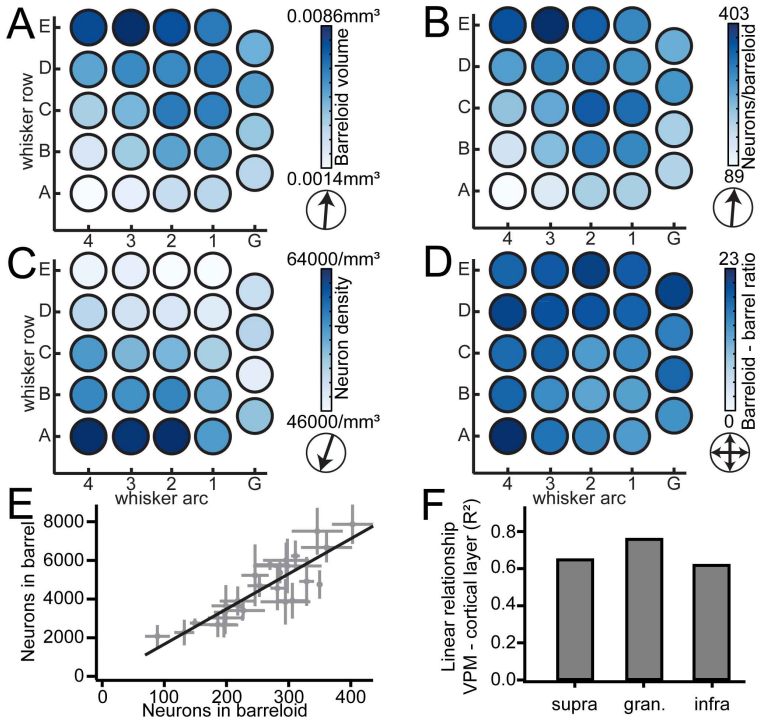

Figure 3.5: The ratio between whisker-specific cortical and thalamic neurons is constant. (A) The average volume per barreloid across VPM increases from the A- to the E-row, as in vS1. (B) The average number of neurons per barreloid also increases from the A- to the E-row. (C) The average neuron density per barreloid increases from the E- toward the A-row. (D) The average ratio between the number of neurons per barrel and corresponding barreloid is highly preserved. (E) Relationship between the number of neurons per barreloid in VPM and the number of neurons in the corresponding barrel is linear. Error bars are ±1 SD. (F) The linear relationship between neurons per barreloid and the respective number of target neurons in cortex is more pronounced for granular L4, compared with supra- and infragranular layers. Figure adopted from [55].

The neuron density was not constant across VPM, but increased from the E1 towards the A4 barreloid by about 50%. Conversely, barreloid volume increased in the opposite direction from the A4 towards the E3 barreloid. Consequently, the number of neurons per barreloid was, similar to barrel columns, approximately constant within a whisker row, increasing in an orderly manner by $\sim$ 2.5-fold from the A- (154 ± 53 neurons) towards the E-row (352 ± 43 neurons) ($p < 10^{-10}$). Thus, the ratio between the number of neurons per barrel column and the number of neurons within the respective barreloid was relatively constant (i.e., 68 ± 11). Because the depth locations and heights of the L4 barrels were

more preserved than cortical thickness, I calculated the ratios between barrel columns and barreloids for supragranular, granular and infragranular layers individually (Figure 3.5 D-F). The correlation between neuron numbers in the barreloid and the L4 barrel ($R^2 = 0.76$) exceeded the ones with the other layers ($R^2 = 0.68$ for supra- and $R^2 = 0.62$ for infragranular layers), reflecting a remarkably constant neuron ratio of 18 ± 3 between each barrel and the respective barreloid (i.e., no significant gradient in neuron ratios, p=0.14; two-tailed t-test).

Implications for network-embedded modeling. The precise 3D reconstruction of neuron somata distributions in rat vS1 and VPM thalamus revealed three features of the cellular organization that could impact the simulation results. First, the variability of the number and 3D distribution of neuron somata is small between different animals. Measured as the SD as percentage of the mean, the variability was 7% for the total number of neurons, and $\sim 10\%$ for the 3D distribution of neuron somata at $50\mu m$ resolution, as determined by the precision of the average model of rat vS1. Second, in contrast, the total number and laminar organization was different between individual barrel columns (i.e., whisker-specific). Further, because this organization follows a spatial pattern (increasing along whisker rows), modeled neurons will in general receive more synaptic input from barrel columns with a larger number of neurons compared to barrel columns with a smaller number of neurons (assuming that axon lengths of cortical cell types are not whisker-specific). Third, the laminar and horizontal organization of IN somata deviates from the organization of excitatory neuron somata. Hence, it is not valid to assume that INs account for a constant fraction of all cortical neurons when calculating statistical connectivity at the resolution of the average model of rat vS1. Instead, the 3D IN somata distribution is used to determine numbers of presynaptic INs.

3.1.3 Morphological and functional cell types in rat vS1

Note: This description is in part adapted from Narayanan, Egger et al. 2015 [56], and Egger, Schmitt et al. 2015 [57].

Robustness of cell type assignment. Excitatory as well as inhibitory neuron mor-

phologies were assigned to different cell types in a two-step process. First, all neurons are sorted in a multi-dimensional feature space (e.g., using the OPTICS algorithm as described in section 2.3) and manually grouped into cell types. However, the sorting may not allow unambiguous assignment of all neurons into cell types. Therefore, I developed a second step in which all neurons that could be assigned to a cell type, as well as neurons that could not unambiguously be assigned to any cell type, are assigned a probability of belonging to any cell type. This probability is calculated based on the features of each neuron and its proximity to the different cell types in feature space. Finally, each neuron is assigned to the cell type with the highest probability. Here, I evaluate the robustness of this final assignment of excitatory and inhibitory neuron morphologies into cell types. Supervised assignment of excitatory neuron morphologies resulted in unambiguous assignment of 126 out of 153 neurons. Based on assignment of these neurons to different cell types, a probability space was constructed, and the probability of each neuron belonging to any cell type calculated (see section 2.3). The average probability used to assign a neuron to its final cell type was $98 \pm 8\%$ (range: $55 - 100\%$).
Supervised assignment of inhibitory neuron morphologies resulted in unambiguous assignment of 158 out of 204 neurons. As described for excitatory cell types, a probability space based on unambiguously assigned neurons was constructed and used to calculate the probability of each neuron of belonging to a cell type. Here, the average probability used for cell type assignment was $98 \pm 7\%$ (range: $56 - 100\%$).

Excitatory cell types. Excitatory cell types were determined from a sample of 153 excitatory neurons across the entire cortical depth (i.e. from L2 to L6). Experiments to label neurons in vivo and reconstruct their morphology were carried out by Christiaan de Kock and Rajeev Narayanan. Additionally, a subset of previously published dendrite and axon morphologies [71] was kindly provided by Randy Bruno and Bert Sakmann. I used objective classification (as described in section 2.3) to subdivide the sample into ten axo-dendritic excitatory cell types (Figures 3.6 and 3.7; [56]).

Because morphologies were sampled in every $50\mu m$ bin of cortical depth and in every $50\mu m$ bin along the radial column dimension, the spatial sampling is regarded as representative for rat vS1 (i.e., sufficient to reveal possible location-specific differences in neuron morphology). Further, the ten excitatory cell types represent all morphologi-

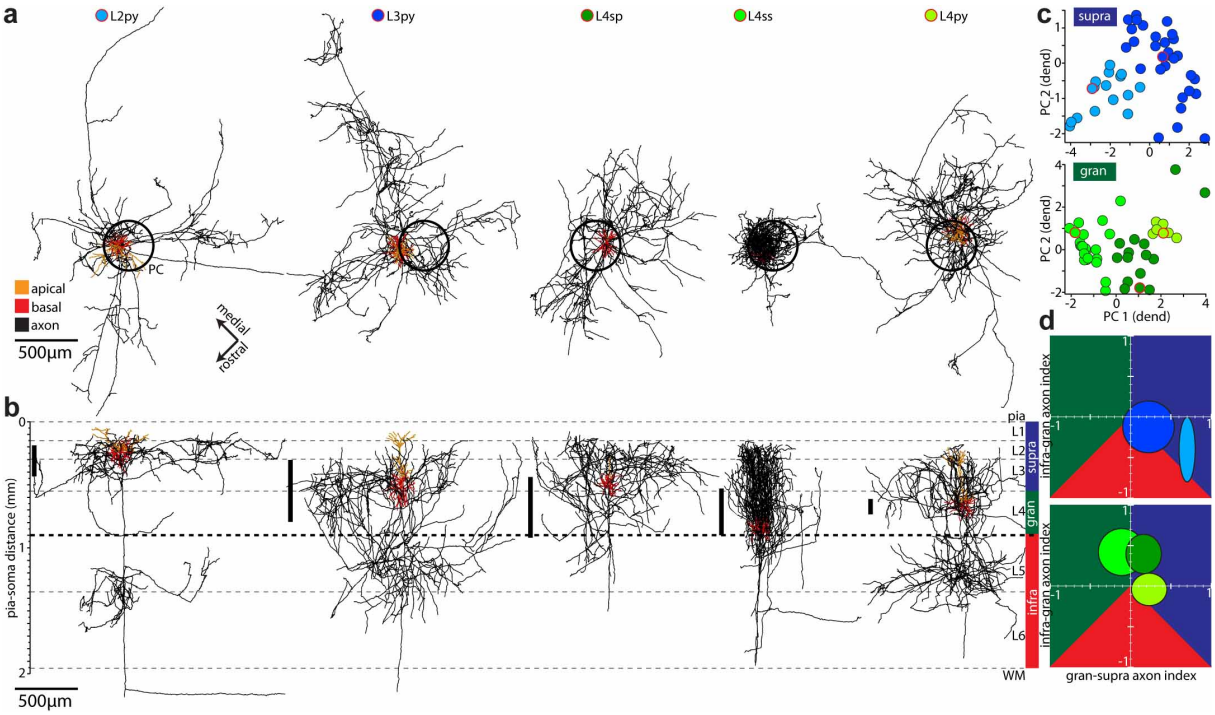

Figure 3.6: Excitatory axo-dendritic cell types in the supragranular and granular layers. (A) Top view onto exemplary morphologies of the 5 excitatory cell types located in L2–4. (B) Semi-coronal view along the arc of the morphologies shown in panel A. Bold dashed line represents the L4/5 border. Bold lines to the left of the exemplary morphologies indicate the range of soma locations of the different cell types. (C) Raster plots of the first 2 principal components (PCs) of soma- dendritic features that discriminated between [supra-]granular cell types. Red outlined circles represent the exemplary neurons in panel A,B. (D) Analyses of cell type-specific axonal features. The horizontal and vertical axes refer to the relative proportion of axon in granular/supragranular and infragranular/-granular layers, respectively. The gran-supra axon index (g-s) is -1 or +1 if all axon was within L4 or L1–3, respectively. The infra-gran axon index (i-g) is -1 or +1 if all axon was within L5–6 or L4, respectively. Ellipses represent mean ± SD of the respective 5 supragranular and granular soma-dendritic cell types. Background colors (as in panel B) indicate where most axon of a respective cell type was found. Ellipses were largely disjoint. Thus, neurons grouped by soma-dendritic features shared cell type-specific axonal morphologies. Figure adopted from [56].

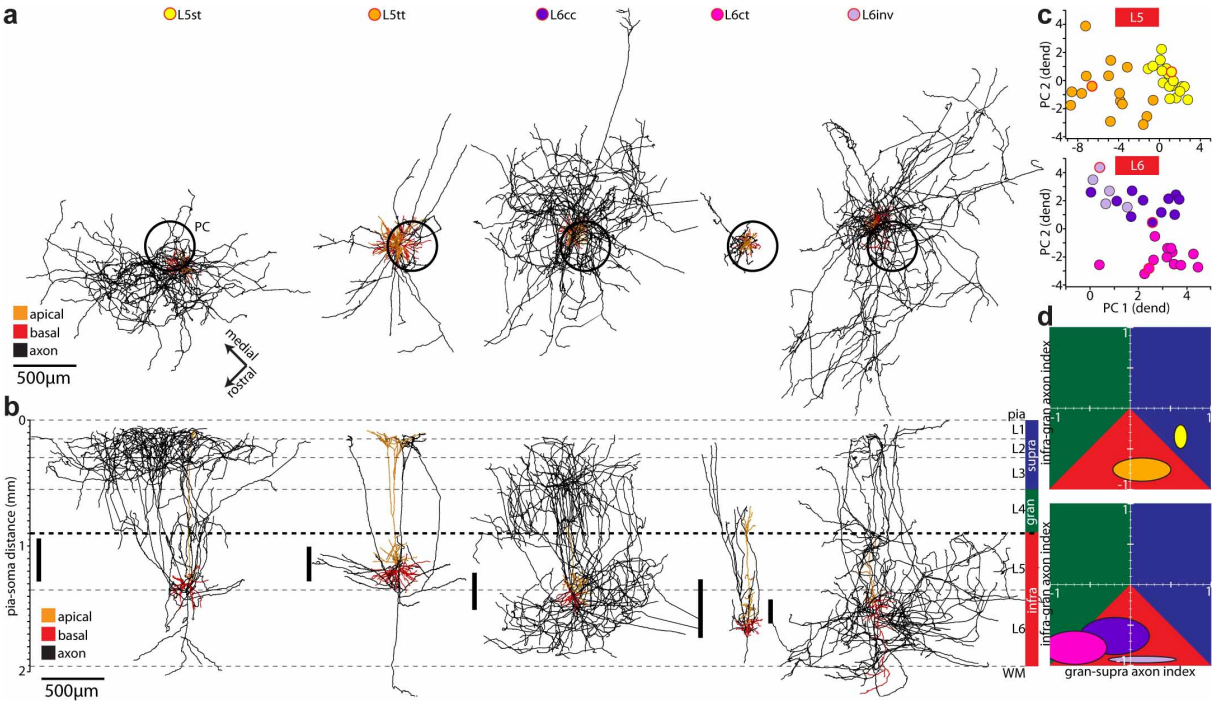

Figure 3.7: Excitatory axo-dendritic cell types in the infragranular layers. (A) Top view onto exemplary morphologies of the 5 excitatory cell types located in L5–6. (B) Semi-coronal view along the arc of the morphologies shown in panel A. Bold lines to the left of the exemplary morphologies indicate the range of soma locations of the different cell types. (C) Raster plots of the first 2 PCs of soma-dendritic features that discriminated between infragranular cell types. (D) Analyses of cell type-specific axonal features (as in Figure 3.6). As for the supragranular and granular cell types, ellipses were disjoint indicating that dendrite and axon morphologies were cell type-specific. Figure adopted from [56].

cal classes that have been reported to date for rat vS1: L2py (n=16) and L3py (n=30) [46, 127]; L4sp (n=15), L4ss (n=22) and L4py (n=7) [88]; L5st (n=18) and L5tt (n=16) [128, 129]; L6cc (n=11), L6ct (n=13) and L6inv (n=5) [130]. Consequently, sampling $\sim 1\%$ of all excitatory neurons located within a barrel column of rat vS1 is regarded as representative for all cell type-specific soma/dendrite/axon morphologies.

Analysis of the vertical soma locations revealed that somata of neurons from different cell types intermingled (Figures 3.6 B and 3.7 B [31]). Hence, laminar soma location alone is not predictive of the morphological cell type. Further, axonal parameters for each neuron were calculated and grouped by the respective soma-dendritic cell type (Figure 3.6 D and 3.7 D). One of several features that discriminated well between axonal cell types was the relative proportion of axon each neuron projected towards supragranular

(s), granular (g) and infragranular (i) layers. To visualize these measures, the respective relative proportions can be converted into into two axon indices (Figures 3.6 D and 3.7 D). For example, the gran-supra axon index is defined as (% axon supragranular - % axon granular) / (% axon supragranular + % axon granular). It has a range from -1 to +1, and it is +1 if 100% of the axon of a neuron is located within the supragranular layers, and -1 if 100% of the axon of a neuron is located within the granular layer. Plotting the mean and SDs of these indices for the respective soma-dendritic cell types illustrated that neurons displayed axonal projection patterns that were similar within, but significantly different between soma-dendritic cell types.

To determine if these axo-dendritic cell types also reflect functional cell types, I calculated the ongoing activity and evoked spiking activity of 57 identified neurons in response to PW and SuW deflections (i.e., the receptive field) in a 50ms window post-stimulus (Figure 3.8, [26]). As described previously, the ongoing activity was highly cell type-specific (Table 3.3).

Cell type	Ongoing activity (Hz)
L2	0.46 ± 0.69
L3	0.31 ± 0.44
L4py	0.64 ± 0.57
L4sp	0.30 ± 0.13
L4ss	0.53 ± 0.18
L5st	1.10 ± 0.43
L5tt	3.53 ± 1.59
L6cc	0.95 ± 0.32
L6inv	0.43*
L6ct	0.08 ± 0.08

Table 3.3: Ongoing activity of excitatory cell types in vS1. *Only one L6inv neuron was characterized functionally and subsequently identified. Table adopted from [31].

The average amplitude in response to PW and SuW whisker deflection, as well as the shape of the receptive field (i.e., the number and identity of responsive SuW) were specific for each morphological cell type. However, sensory-evoked responses of cortical neurons are highly variable. I therefore calculated the mean and SD of the average PW and SuW responses for each cell type (Figure 3.9).

Figure 3.9 shows the distribution of these two parameters for each cell type. In the

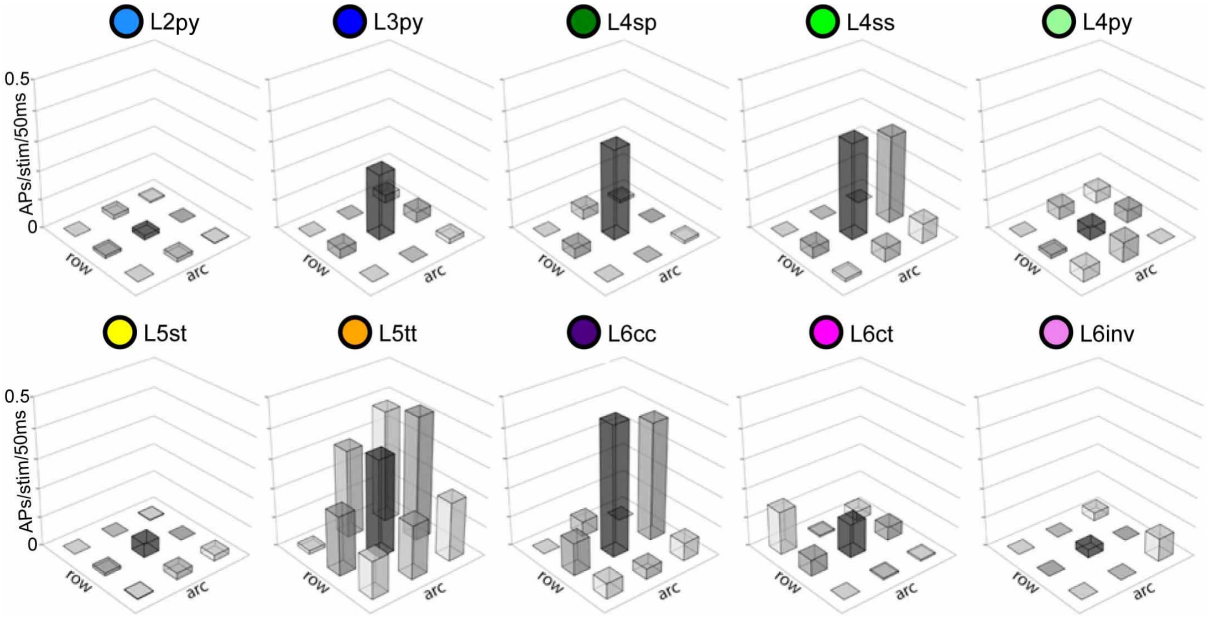

Figure 3.8: Average PW and SuW receptive fields of excitatory cell types. Whisker-specific receptive fields are aligned to the PW (center). Along the 'arc' axis, the arc relative to the PW is +1/0/-1 from left to right. Along the 'row' axis, the row relative to the PW is +1/0/-1 from left to right. Thus, the PW is at coordinates 0/0. Only one L6inv neuron was characterized functionally and subsequently identified.

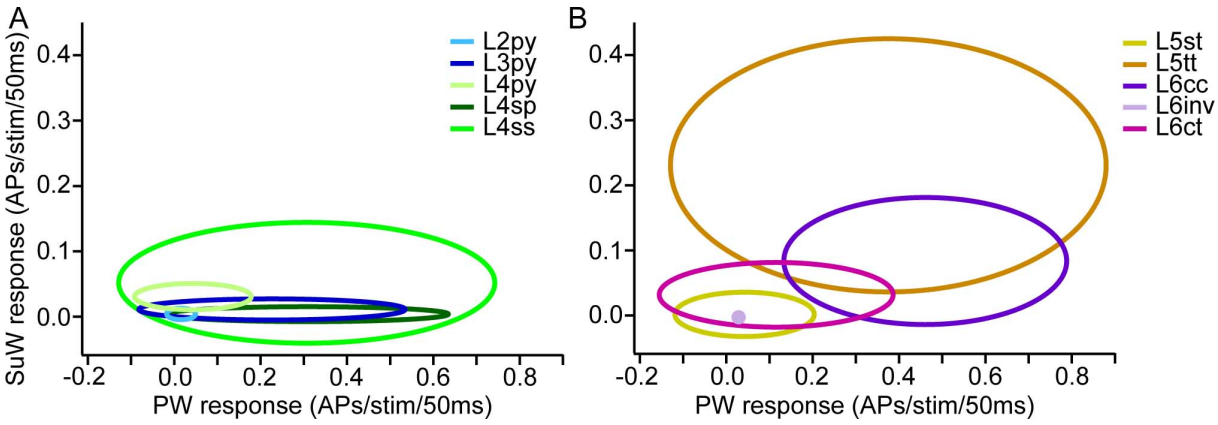

Figure 3.9: Variability of responses of excitatory cell types. (A) Distribution of PW response amplitude and PW response amplitude relative to SuW responses for excitatory cell types in supragranular and granular layers. Ellipses are centered on the mean of each cell type and represent ±1 SD. (B) Same as in A for excitatory cell types in infragranular layers. Functional data for L6inv was available only for one identified neuron (dot).

supragranular layers (Figure 3.9 A), L2py and L4py are mostly unresponsive and have equally low response probabilities after PW and SuW deflections. L3py and L4sp have similar distributions of PW and SuW response amplitudes (i.e., PW-specific), while L4ss have a distinct SuW response to deflection of the adjacent caudal whisker in the same row (compare Figure 3.8). In infragranular layers (Figure 3.9 B), only two cell types (L5tt and L6cc) show substantial PW responses. L6cc responses are more reliable across cells (lower SD) and more PW-specific than L5tt, but display a specific SuW response to deflections of the same adjacent caudal whisker as L4ss. In contrast to the other cell types, the average PW and SuW amplitude of L5tt correlated significantly ($r=0.81$, $p=0.008$). L5st and L6ct responses are low and unspecific across the population. Finally, I determined the PSTH of the average evoked response after PW and SuW deflections (Figure 3.10; the PSTH of VPM neurons is derived from [87]). The cell types with shortest latencies are L6cc (PW deflection: 9ms/SuW deflection: 10ms), L4ss (9ms/14ms), L5tt (11ms/12ms), L3 (12ms/19ms) and L4sp (13ms/14ms). For comparison, the latency of VPM neurons to PW and SuW deflections is 8ms and 13ms, respectively. This is in line with previous analysis of this data set where neurons were grouped based on laminar location [26]. Remarkably, the PW-evoked response of L6cc seems to be the earliest of all excitatory cortical cell types, and it is as synchronous as the thalamocortical input from VPM. For L6cc and L5tt, the response latency to SuW deflection is nearly identical to the latency after PW deflection. suggesting that SuW responses of these cell types do not originate from SuW responses of presynaptic thalamic neurons.

In summary, objective cell type assignment of excitatory neurons based on soma location and dendrite morphology revealed that neurons within a cell type also share common axonal projection patterns, as well as ongoing and sensory-evoked activity. Specific axon projections of different cell types can result in specific subcellular innervation patterns of postsynaptic neurons, in particular of the L5tt neuron model, which has a dendritic extent across nearly the entire cortical depth. Further, in every cortical layer, cell types with and without sensory-evoked responses intermingle. Therefore, 3D reconstruction and registration of neuron morphology is necessary in order to correctly combine location, axon projection patterns and ongoing and sensory-evoked responses of different presynaptic cell types into the model.

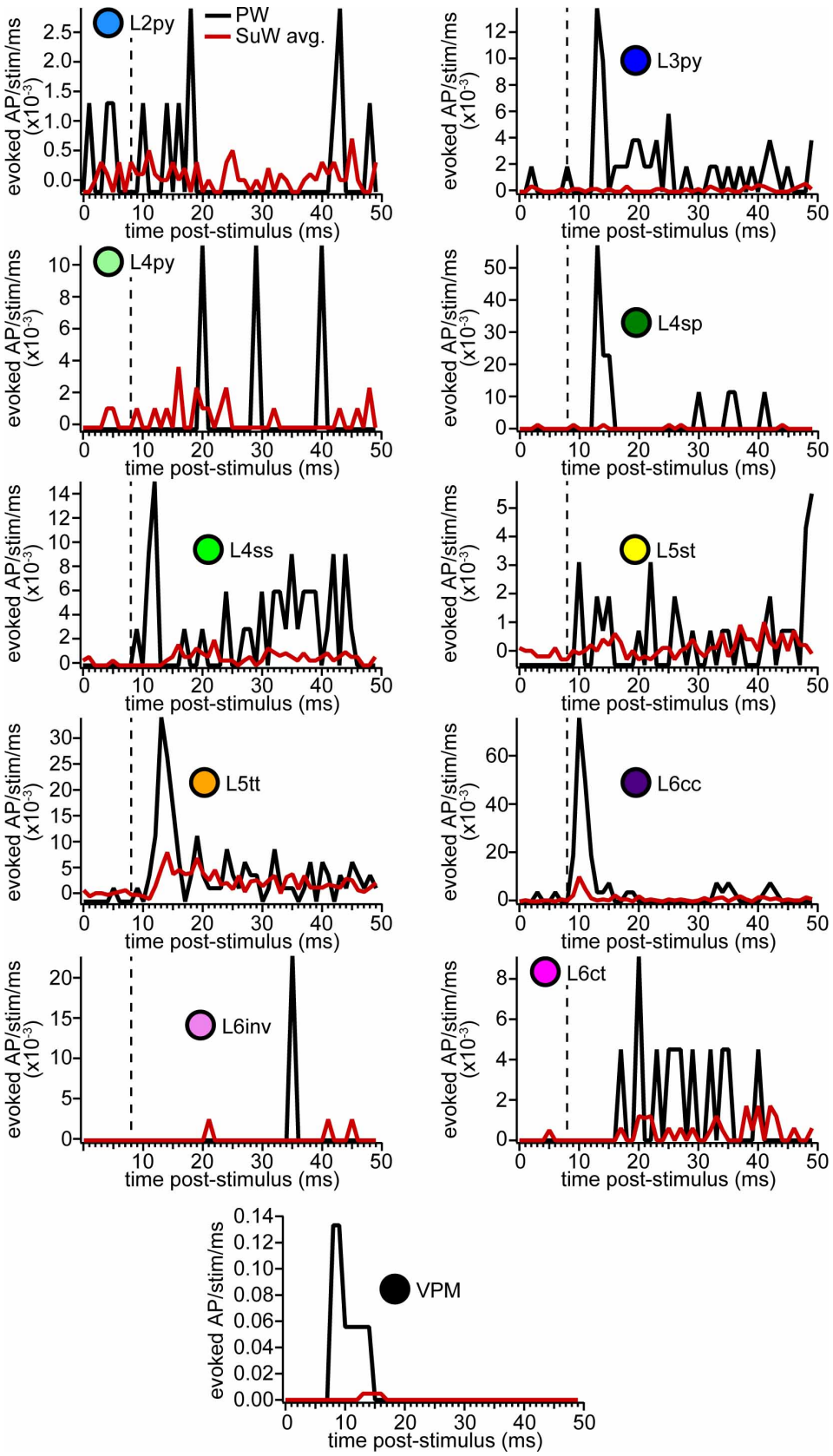
L2py
PW
SuW avg.
L3py
L4py
L4sp
L4ss
L5st
L5tt
L6cc
L6inv
L6ct
VPM
evoked AP/stim/ms (x10-3)
time post-stimulus (ms)

Figure 3.10 *(previous page)*: PSTH of PW and SuW responses of excitatory cell types. Evoked activity (i.e. total number of APs per stimulus per ms minus ongoing activity per ms) for ten excitatory cell types in vS1 and VPM. Black trace: Average PW response across all identified neurons of each cell type. Red trace: Average SuW response across eight SuW and all identified neurons of each cell type. Dashed line marks latency of VPM response after PW deflection (derived from the VPM evoked PSTH, see bottom panel).

Inhibitory cell types. Experiments to label and reconstruct INs in vitro/in vivo were carried out by Hanno Meyer, Marlene Arzt, Mike Hemberger and Arno Schmitt. Additionally, a set of previously published IN morphologies was kindly provided by Moritz Helmstaedter, Dirk Feldmeyer and Bert Sakmann. For objective classification, IN morphologies were not grouped by laminar soma location, as is commonly done (e.g. [131, 77]). Cortical layers are commonly defined based on the density of excitatory neuron somata [53]. However, as shown in section 3.1.2, the vertical organization of IN somata does not correspond to cortical layers. Therefore, IN morphologies across the cortical depth (i.e., from L2-6) were pooled and soma location and features of vertical (i.e., along the column axis) axon projection patterns analyzed independently of cortical layers. Classification of 204 in vitro labeled and reconstructed IN morphologies revealed five axonal projection types (Figure 3.11, Master thesis by Daniel Udvary under my supervision [79]). These five projection types fall into two broad classes: Local projecting INs, and non-local projecting INs. Each of these two classes makes up $\sim 50\%$ of the total IN population. Local projecting INs display $\geq 90\%$ of their axon projection patterns within $\pm 250 \mu m$ of their soma location, as measured along the vertical column axis. Non-local projecting INs display additional specific projection patterns along the vertical column axis. As observed for excitatory cell types, soma locations of IN projection types intermingle. Specifically, local projecting INs can be found across the entire cortical depth. Non-local projecting types are also present across the cortical depth, but specific projection types can be found at specific depths (Figure 3.11). Finally, there was no correlation between axon projection types and morphological features of dendrites within each cell type. This has been described previously for a subset of the IN morphologies [132], which additionally demonstrated that no correlation between current injection-evoked responses and axon projections of these INs exists.

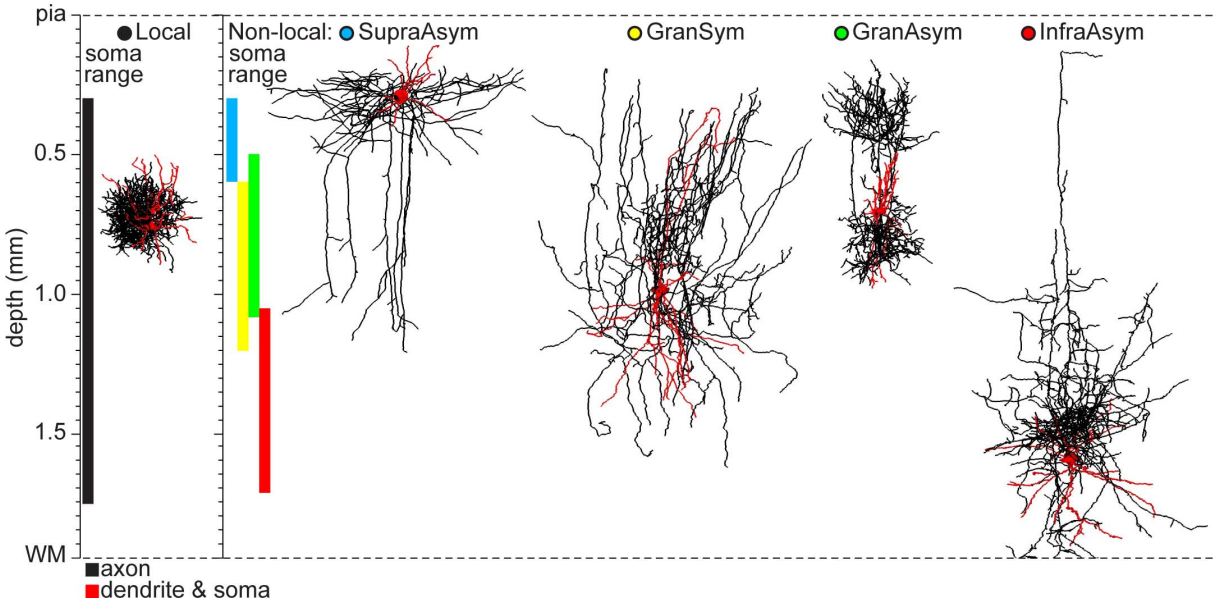

Figure 3.11: Inhibitory axon projection cell types. Axon projections of inhibitory cell types remained either local around the soma location of the neuron (Local, left) or displayed additional non-local projections (Non-Local, right). SupraAsym: Supragranular asymmetric projecting type; GranSym: granular symmetric projecting type; GranAsym: granular asymmetric projecting type; InfraAsym: infragranular asymmetric projecting type. Colored bars indicated range of soma locations of the different cell types. Figure adopted from Udvary et al., in preparation.

In contrast to previous IN classification approaches (e.g. [133]), here INs were subdivided based on their axonal projections because these form the structural basis of specific subcellular innervation of modeled neurons. Further specificity in terms of subcellular innervation of specific postsynaptic cell types from subsets of these projection types may exist (for example, chandelier cells are found among INs in supragranular layers and are known to specifically target the axon initial segment of pyramidal neurons [134]), but for simulations of sensory-evoked inhibition in this thesis I simplify inhibitory pathways to this first-order estimate based on axon projection patterns.

In contrast to the dataset of excitatory neurons, IN morphologies were obtained by recording/labeling in acute brain slices in vitro. Therefore, in vivo measured responses of these neurons to PW and SuW deflections are not available (a model of functional responses of INs used for simulations is given in section 2.5.1).

However, in collaboration with Arno Schmitt, Damian Wallace and Jason Kerr, I investigated structural properties and sensory-evoked responses of INs located in L1. Using

two-photon (2p) microscopy (Figure 3.12 A), L1 INs in vS1 in anesthetized rats were targeted for whole-cell recordings (n=29; soma depth from pia: $25 - 105\mu m$, mean $\pm$ SD: $59 \pm 24\mu m$). Current injections in vivo resulted in heterogeneous patterns of AP responses (Figure 3.12 B), which closely resembled those observed for INs in acute brains slices in vitro [135, 136, 102].

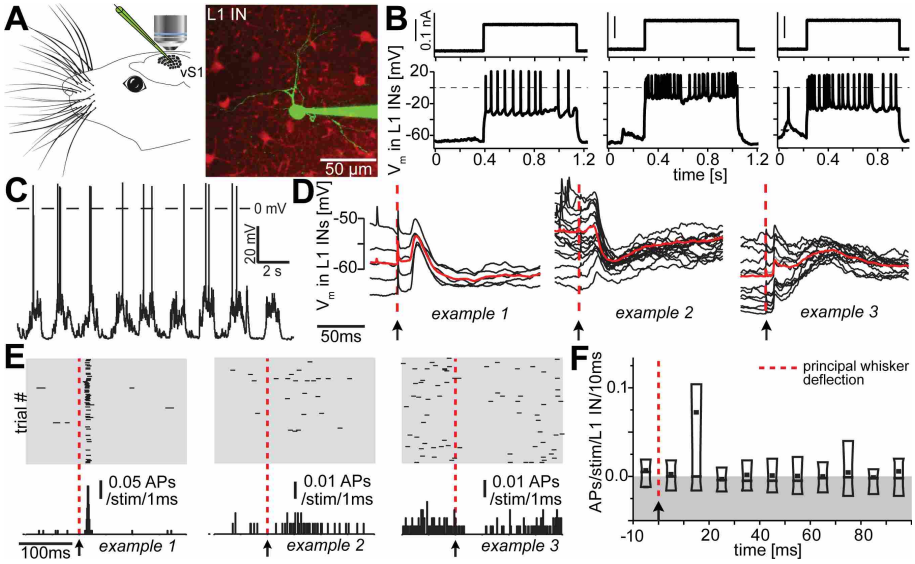

Figure 3.12: Functional characterization of L1 INs recorded in vivo. (A) Individual L1 INs in rat vS1 were targeted for whole-cell recordings using 2p microscopy. (B) Step current injection-evoked spiking responses (three exemplary neurons are shown). (C) Ongoing up- and down-state activity of exemplary L1 IN. (D) All recorded L1 INs had short latency subthreshold responses following whisker deflections (three exemplary neurons are shown). Red, average across trials. (E) Whisker-evoked spiking of the neurons shown in D. (F) Poststimulus time histogram at 10ms resolution of whisker-evoked spiking across all recorded L1 INs. Box, 10th–90th percentile; line, median; dot, mean. Figure adopted from [57].

Next, after identification of the respective PW using intrinsic optical imaging (IOI), spontaneous and whisker deflection-evoked sub- or suprathreshold responses were measured for each recorded L1 IN. Spontaneous AP frequency was $1.1 \pm 0.9Hz$ (Figure 3.12 C). All recorded L1 INs displayed reliable whisker-evoked subthreshold responses (Figure 3.12 D) with onset latencies ($9.8 \pm 2.2ms$ [137]) as short as those previously reported for excitatory cell types in L3–5 [46, 35, 48]. Fourteen of 29 L1 INs showed whisker-evoked APs. Although AP responses were heterogeneous (Figure 3.12 E), spiking occurred most strongly in the first 20ms after stimulus, and when averaged for all neurons, the time window of 10–20ms contained the majority of stimulus evoked APs. On average, AP

responses had returned to prestimulus rates in less than 20ms (average, $15.2 \pm 2.2ms$; Figure 3.12 F). Within the 10-20ms window, whisker-evoked activity across all L1 INs was 0.07 ± 0.23 APs per stimulus. Neither subthreshold nor AP responses were correlated with spontaneous AP frequencies.

L1 IN Axons Innervate L1 of All Surrounding Columns. Following the in vivo recording, L1 INs were labeled, 3D dendrite and axon morphologies as well as anatomical landmarks (pia, WM and barrel outlines) were reconstructed and registered to the average model of rat vS1 (Figure 3.13 A and B).

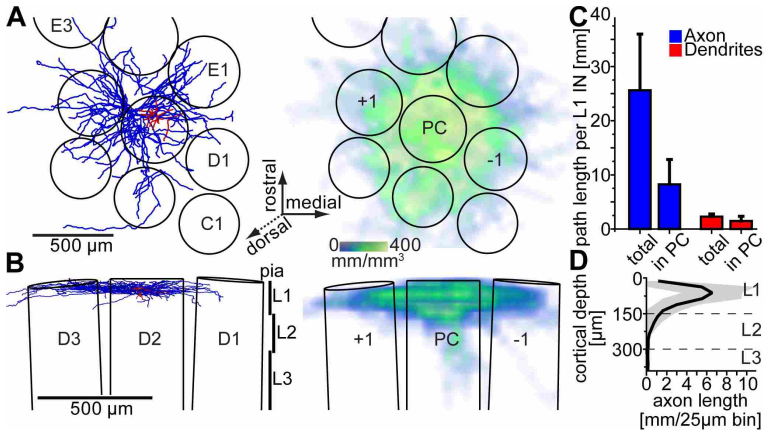

Figure 3.13: Morphological characterization of L1 INs labeled in vivo. (A) (Left) Exemplary reconstruction of L1 IN (red, dendrites; blue, axon) registered to the average model of rat vS1 (top view onto the cortical surface). (Right) 3D axon density averaged across all reconstructed and registered L1 INs. (B) Coronal views of A. Axonal projections remained either confined to L1 (Left) or displayed additional sparse branches descending into L2 (Right). (C) Average path lengths per L1 IN within and outside the PC. (D) 1D axon length profile along the vertical cortex axis averaged across all L1 INs (black, mean; gray, SD). Figure adopted from [57].

All reconstructed L1 INs (n=10) displayed comparable dendritic fields and 3D axon projection patterns. In the horizontal plane (tangential to vS1; Figure 3.13 A), axonal projections spread beyond the dimensions of the PC, innervating all surrounding barrel columns (Figure 3.13 C). In the coronal plane, axons were confined to L1, with a subset of cells displaying additional sparse branches descending into L2/3 of the PC (Figure 3.13 D). Similar laminar axon patterns were observed in vitro and were used to subdivide L1 INs into axonal cell types (e.g., neurogliaform (NGF)-like INs [136]). However, criteria to distinguish between morphological types are ambiguous [135]. Moreover, whether morphological properties correlate with electrophysiological responses remains controversial

[135, 102]. In this data set, current injection-evoked responses in vivo were heterogeneous and did not correlate with dendritic and/or axonal properties. Similarly, spontaneous AP frequencies and whisker-evoked responses across INs with axons confined to L1 were not significantly different from those that projected additional sparse branches to L2/3. Consequently, all L1 INs were grouped as one cell type.

Implications for network-embedded modeling. Objective classification of soma and dendrite morphologies of excitatory neurons revealed that these cell types display specific axon projection patterns and ongoing and sensory-evoked responses after PW and SuW deflections. Together, these features form the basis for specific subcellular functional connectivity patterns to the postsynaptic neuron during network-embedded simulations. IN cell types were determined based on axon projection patterns along the vertical column axis, forming the structural basis for feed-forward inhibition after whisker deflections. Apart from L1 INs, which display short-latency evoked spiking after PW deflection, INs were grouped as one functional cell type (see also the Methods section 2.5.2) for simulation purposes. Specific subcellular functional connectivity of INs thus results from projection type-specific innervation.

3.1.4 Dense network model of rat vS1

Note: This description is adapted from Egger, Dercksen et al. 2014 [66].

Dense average network model of rat vS1. Based on the anatomical input data specified in the Methods section (section 2.4.2; Figure 2.5), I generated an average dense model of entire rat vS1 (Figure 2.6). The model consists of 10 excitatory and 6 inhibitory axo-dendritic cell types in 24 barrel columns of rat vS1, and thalamocortical axons from the corresponding 24 barreloids in VPM. The total volume of the vS1 model was $6.4 mm^3$ [54]. First, the average 3D distributions of excitatory and inhibitory somata were registered to the reference frame and somata were placed and assigned to cell types (Figure 2.6 B) and anatomical substructures as described in the Methods section (i.e. each soma contains four labels: the nearest barrel column, whether the soma is inside the column or within the septum, the cell type, and whether it is excitatory or inhibitory). The

total number of neurons within the model was 529,926, with 462,436 being excitatory and 67,490 being inhibitory. As described in the Methods section, placement of somata within $50\mu m$ voxels and cell type assignment is implemented stochastically. The resulting variability was estimated by generating 10 network realizations of the C2 barrel column and calculating mean and standard deviation of the number of neurons per cell type across these realizations. Measuring the SD as percentage of the mean, the variability per cell type was on average 3% (range: $0.7 - 7.5\%$), which is less than the variability of the number of somata across animals (SD as percentage of the mean: 7%). Next, each soma was replaced by an appropriate 3D soma/dendrite/axon morphology, using the up-scaling routines specified in the Method section (section 2.4.2 and Figure 2.6 C-E). On average, dendrite morphologies were moved $29 \pm 20\mu m$ along the vertical column axis during the up-scaling process. Thus, the spatial coverage of the sparse morphological sample was sufficient to allow selection of a dendrite morphology of the corresponding cell type within $50\mu m$ of nearly all somata. Additionally, axon morphologies for 6225 thalamocortical projection neurons from VPM were placed in the model (i.e., up-scaled from n=14 VPM axon reconstructions), innervating all 24 barrel columns [31, 73]. The somata and dendrites of each neuron were converted into 3D PST surface densities, reflecting the respective surface areas multiplied with connection-specific PST distributions. Likewise, dendrites of excitatory neurons and axons of all neurons were converted into 3D PST spine and bouton distributions, respectively (see Tables 2.2 and 2.1 for all values).

The resultant total soma/dendrite surface area (i.e., of all neurons in rat vS1) was $1.9 \times 10^{10}\mu m^2$. The total number of spines was 5.2×10^9, and the total number of boutons was 6.4×10^9. The average bouton (synapse) density across entire rat vS1 was 1 bouton per μm^3, which matches previous measurements (0.94 ± 0.12 synapses per μm^3) of synapse densities using electron-microscopic tomography on small tissue volumes ($\sim 200\mu m^3$) of rat vS1 [138]. Hence, the up-scaled model of entire rat vS1 resembles the average structural organization of this brain region at mesoscopic (geometry within $50\mu m$ inter-animal variability), microscopic (cellular distributions within 7% inter-animal variability) and nanoscopic (bouton densities) scales. Consequently, within the margins specified by the respective inter-animal variability (SDs of geometry, soma distribution, cell type-specific dendrite/axon projections, and spine/bouton densities), the dense 3D

model of rat vS1 can be considered as a precise average representation of this particular piece of neuronal tissue.

With respect to the network-embedded simulations, this model includes the complete thalamocortical part of the lemniscal pathway, i.e., all thalamocortical and intrinsic cortical pathways involved in signaling passive whisker touch. It therefore allows to statistically estimate the number and subcellular distribution of synapses from all cell types involved in whisker touch-evoked signal flow in rat vS1 to the postsynaptic neuron models.

Statistical connectivity constraints within the dense network model of rat vS1. Within the dense network model of rat vS1, I can now determine structural overlap of PSTs and presynaptic boutons between all pairs of neurons, always taking all neurons present in the respective overlap volumes into account. Figure 3.14 illustrates this process on the example of one L4ss neuron (j) being innervated by one thalamocortical axon (i) originating in VPM (see also Figure 2.6 C-E). First, the bounding box (BB) around the dendrites of the postsynaptic neuron is determined (Figure 3.14 A left) and the number of PSTs for each $50\mu m$ voxel within the BB is calculated. In case of VPM neurons innervating L4ss (i.e. excitatory cell types), PSTs are limited to spines [90] as specified in the meta-connectivity input file (see Table 2.2). The exemplary L4ss neuron comprises a total of 4,640 spines, with a maximum of 523 spines per voxel (Figure 3.14 A right).

Second, the number of presynaptic boutons in any voxel of the BB is calculated. For the present example, the particular VPM axon has a total of 2,964 boutons in the BB, with up to 94 boutons per voxel. However, within the BB, dendritic spines originating from other excitatory neurons are present as well, rendering as equally likely contact sites for the VPM boutons in each voxel as the spines of the exemplary L4ss neuron. The total number of spines within the BB was 2.1×10^7, with a maximum of 130,000 spines per voxel. Furthermore, VPM axons could also target somata and/or dendritic shafts of inhibitory interneurons ([91], as specified in the meta-connectivity input file), where a total of 1.8×10^6 PSTs on inhibitory surfaces are present within the BB, with a maximum of 13,500 surface PSTs per voxel. Consequently, the 3D innervation field $I_{ij}(\vec{x})$ between the dendrites of the L4ss neuron (j) and the axon of the VPM neuron (i), was determined with respect to all other potential PSTs (i.e., excitatory and inhibitory) present in each

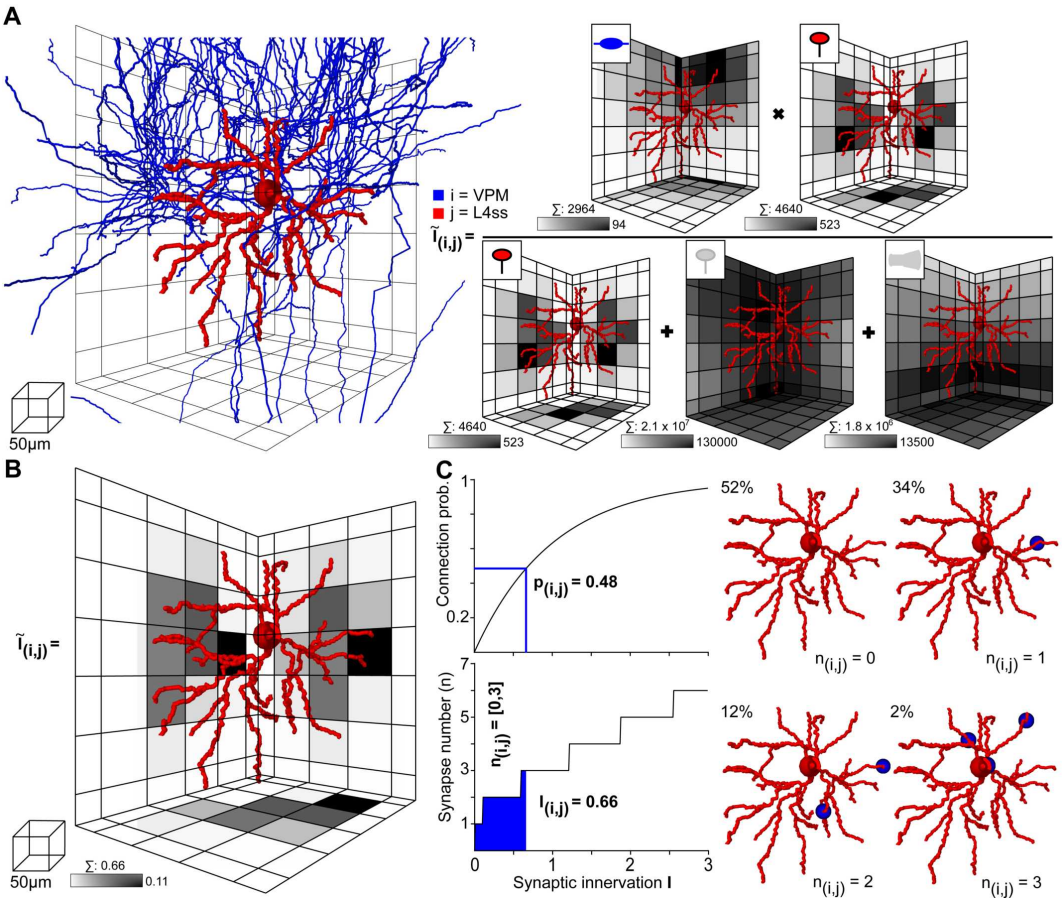

Figure 3.14: Computation of statistical innervation between neurons in dense networks. (A) Left: VPM axon (blue) and L4ss dendrite (red) from Figures 2.6 C–E. The grid used for computing bouton, spine and dendrite surface densities is shown for scale. Right: Calculation of the 3D innervation density $\tilde{I}_{ij}(\vec{x})$ from the VPM axon to the L4ss dendrite. The gray-colored squares in the grid represent the maximum projection of the respective pre/postsynaptic quantity. Scale bar shows maximum value of the respective pre/postsynaptic quantity in the grid. Above each scale bar, the total number of pre/postsynaptic elements in the grid is shown. (B) Resulting subcellular 3D innervation density $\tilde{I}_{ij}(\vec{x})$. (C) Left top: Connection probability from neuron i to neuron j as a function of the total innervation I_{ij}. Bottom: Possible range of the number of synapses from neuron i to neuron j, n_{ij} (95th percentile for $n > 0$) as a function of the total innervation I_{ij}. Right: Four possible synapse distributions and their probability of occurrence for the innervation from the VPM axon to the L4ss dendrite, computed from the 3D innervation density in (B). Figure adopted from [66].

voxel. In addition, the number of all available target sites (2.3×10^7) was four orders of magnitude larger than the number of spines/boutons from the individual neurons, justifying the approximation of the binomial connection probability by a Poisson distribution. The resultant 3D innervation field $I_{ij}(\vec{x})$ between the two exemplary neurons is shown in Figure 3.14 B. Summing across all voxels results in the total innervation $I_{ij} = 0.66$, with a maximal innervation of 0.11 per voxel. Using the Poisson approximation (i.e., independent synapse formation, see Methods section 2.4.3), this innervation number corresponds to a pairwise connection probability of $p_{ij} = 0.48$, and to a range of putative synapses between i and j of $n_{ij} = 0 - 3$ (Figure 3.14 C left). These numbers form the statistical constraints for network embedding of single neuron morphologies as described in the Methods section 2.4.3. In case of the present example, the probability that the two neurons were unconnected was 52%, that they were connected by a single synapse was 34%, and by two or three synapses was 12% and 2%, respectively (Figure 3.14 C right). Specifically, when generating 50 network embedding realizations (as was done for the simulations), in 26 of these realizations, these two neurons would be unconnected, in 17 realizations, they would be connected by one synapse, in 6 realizations by two synapses, and in one realization they would be connected by three synapses. Further, the subcellular location of these synapses is constrained by the 3D innervation field $I_{ij}(\vec{x})$ (Figure 3.14 B, C).

Thus, even though the axonal arbor of the example VPM neuron displays substantial overlap with the dendritic arbor of the example L4ss neuron (2,964 VPM boutons and 4,640 L4ss spines, respectively), the probability of these two neurons being connected according to this quantitative implementation of Peters' rule (see section 2.4) is less than 50%. This method of calculating statistical connectivity between neurons based on 3D distribution of presynaptic boutons and PSTs, and at the same time taking the entire "background" of PSTs from other neurons in the overlap volume into account, is fundamentally different from other approaches to estimated connectivity based on overlap of dendrites and axons. Because there are on the order of 1000 other potential postsynaptic target neurons projecting dendrites into the overlap region, approaches that calculate connectivity from structural overlap without normalization by the total number of PSTs (e.g. [82]) will result in gross overestimation of connection probabilities, or require many

additional ad-hoc assumptions to prune contact sites between dendrites and axons until realistic synapses numbers are reached [139]. In consequence, structural axo-dendritic overlap should never be calculated from sparse morphological data alone and connectivity measurements by Peters' rule should not be presented in a binary fashion (i.e. overlap equals connectivity, no overlap equals no connectivity). Instead, structural overlap in the present form results in innervation measurements at subcellular (reference frame) resolution, which can be converted into pairwise connection probabilities and a range of putative synapse numbers. These can then be used as constraints to create network embedding realizations of single neurons for simulations, as described above.

Comparison of network model connectivity measurements with experimental results. In the following, I compare measurements of pairwise connection probabilities and putative synaptic contact sites using the dense network model with previously reported measurements in rat vS1 using (i) paired recording/reconstruction between L4ss neurons in vitro [140, 141], (ii) dual recordings and correlation analysis between VPM and L4, L5A, L5B and L6 neurons in vivo [45, 32], and (iii) electron-microscopic reconstructions of synaptic contact sites between VPM and individual L4ss neurons [90]. For comparison, I restricted in silico connectivity measurements between the respective cell types to neurons located within a single barrel column (D2, (Figure 3.15 A-C)) and averaged connectivity measurements across all neurons of the respective D2 populations. The D2 column model comprised 17,810 excitatory neurons including 4,657 neurons of L4 cell types (2,480 L4ss; 1,707 L4sp; 470 L4py), 1,386 L5st, 1,103 L5tt, 1,391 L6cc, 767 L6inv and 4,048 L6ct neurons. Further, the D2 column model contained 2,545 INs and 311 thalamocortical axons originating in the D2 barreloid of the VPM [55].

Computing the innervation I_{ij} for all pairs of VPM and L4, L5st, L5tt and L6 neurons, respectively, as well as for all pairs of L4ss neurons, allowed calculating the respective neuron-to-neuron connection probabilities p_{ij} and the average distribution of the number of synapses per connection n_{AB} (Figure 3.15 D). Further, I computed the cell type averages of (i) convergence between L4ss neurons, as well as between VPM and L4, L5st, L5tt and L6 neurons in our D2 column model, and (ii) the 99th percentile of the number of putative synapses, and compared these numbers to experimental results (Figure 3.15 E). The in silico L4ss-to-L4ss convergence measurements yielded a value of 0.31 ± 0.10, com-

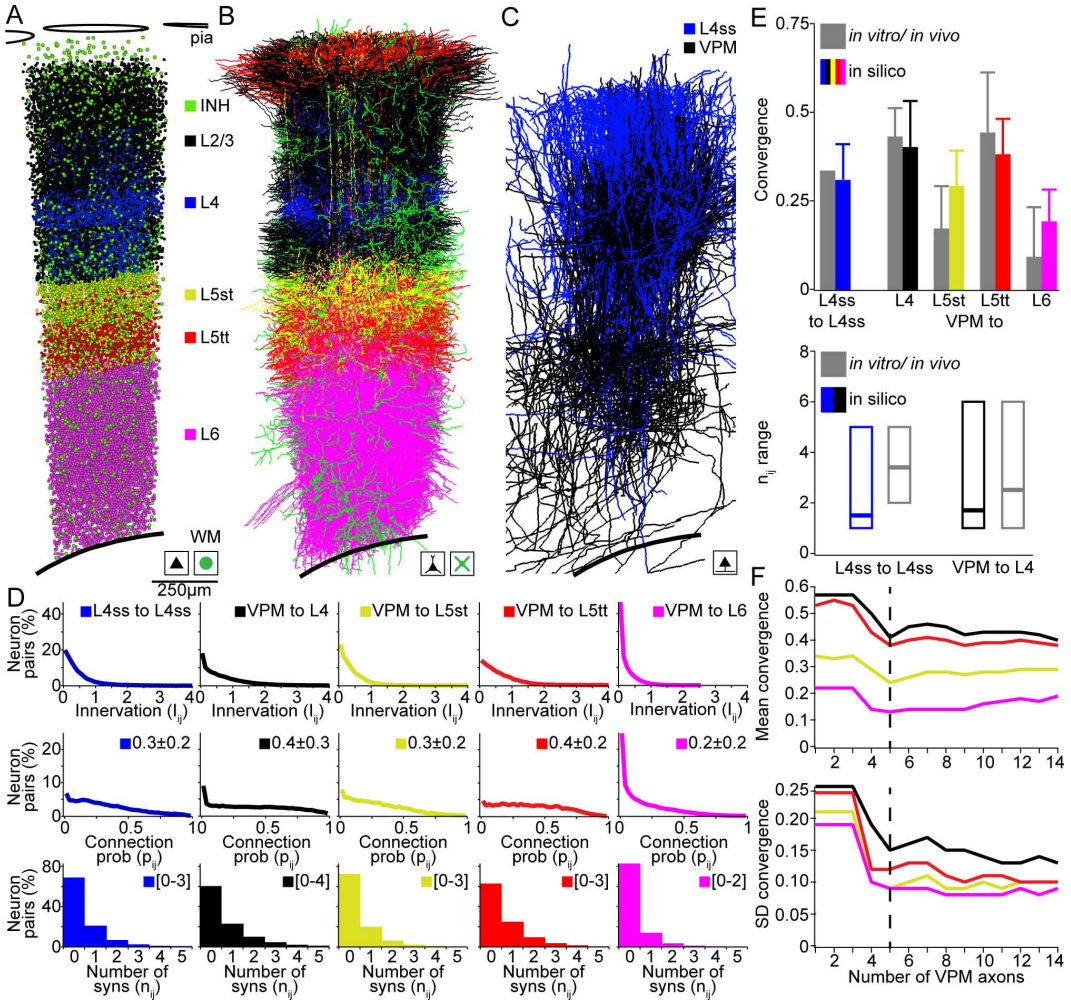

Figure 3.15: Validation of the rat vS1 statistical connectome. (A) Cell type-specific distribution of neuron somata in the model D2 column. (B) Cell type-specific distribution of dendrites in the model D2 column from (A). Note that large basal dendrites of L3py neurons located in the septum around the L4 barrel obscure dendrites of L4ss located inside the barrel. (C) Distribution of L4ss axons (blue) and VPM axons (black) in the model D2 column from (A). (D) Distribution of neuron-to-neuron innervation I_{ij} , the neuron-to-neuron connection probability p_{ij} and the average distribution of the number of synapses per connection n_{ij} for the four postsynaptic cell types in (B) and the two presynaptic cell types in (C). (E) Comparison of pair-wise connectivity statistics in the model D2 column (in silico) and experimental results from physiological and anatomical measurements in vitro and in vivo. Top: convergence of intra-barrel connectivity and thalamocortical connectivity from VPM. Bottom: Observed and calculated range of number of synapses per connection (in silico: 99% cumulative range of the average distribution of n_{ij}). (F) Effect of the size of the sparse morphological sample on connectivity measurements. Top: Mean convergence of thalamocortical input from VPM to four cell types in the model D2 column (see E for color-code) as a function of the VPM axon sample size. Bottom: Standard deviation of the convergence of thalamocortical input to these four cell types as a function of the VPM axon sample size. Figure adopted from [66].

pared to 0.31-0.36 as measured in vitro [140, 141]. VPM-to-L4 convergence was 0.40 ± 0.13 (in silico), compared to 0.43 ± 0.08 (in vivo). VPM-to-L5st convergence was 0.29 ± 0.10 (in silico), compared to 0.17 ± 0.12 (in vivo). VPM-to-L5tt convergence was 0.38 ± 0.10 (in silico), compared to 0.44 ± 0.17 (in vivo) and VPM-to-L6 convergence was 0.19 ± 0.09 (in silico), compared to 0.09 ± 0.14 (in vivo) [45, 32]. The in silico measurements of pair-wise connection probabilities matched the previously reported cell type-specific values within one SD. However, while the error bar of the experimental measurements reflects the statistical error due to a limited sample size, the error bar of the in silico measurements represents the variability of the convergence within a cell type. This variability reflects location-specific differences in connectivity (e.g. VPM innervation decreases with radial distance to the column axis [31, 142, 90]), as well as morphological variability within a cell type (e.g. neurons with shorter dendrites receive fewer synapses [90]).

Further, even though somata of the different cell types intermingled within and across cortical layers, the model predicted cell type-specific differences in synaptic connectivity within layers (e.g. VPM to L5st vs. L5tt). These findings are in line with previous reports that revealed that synaptic connectivity is in general cell type- and not layer-specific [143, 82].

To further evaluate how the sample size of morphological reconstructions affects the connectivity estimates, I repeated these measurements and progressively increased the number of VPM axons used for up-scaling from 1 to 14. Increasing the sample size beyond ~ 5 VPM axons did not change the results (Figure 3.15 F), indicating that at least 5 axon reconstructions are required to capture the variability of projection patterns (at $50 \mu m$ resolution) within a cell type.

Finally, the range of putative synapses per connection for L4ss-to-L4ss connections was 1-5 (in silico), compared to 2-5 (in vitro, [140]). For VPM-to-L4 connections, the range was 1-6 (in silico), compared to 1-6 (in vivo, [90]). Whereas the in silico ranges of putative synapses per connection matched the previous in vitro/vivo results, the model predictions showed that the most likely scenario for interconnected L4ss should be that they share only a single synaptic connection. However, reconstructions from paired-recordings revealed a more bimodal distribution, i.e. pairs of L4ss share either no contacts, or if they are connected, they share more than one contact [140]. This potential discrepancy could

arise from limitations to identify weakly connected L4ss (i.e. just one synaptic contact) using paired-recordings, or could indicate that the assumption of independent synapse formation is not justified for L4ss.

Implications for network-embedded modeling. The present dense average model of neural networks in rat vS1 provides anatomical constraints on average connectivity between neurons in rat vS1, as well as its variability. First, the model provides complete input distributions from the thalamocortical part of the lemniscal pathway, i.e., thalamocortical and intracortical cell types involved in passive whisker touch-evoked signal flow, as studied in the L2py and L5tt models. Second, the dense statistical connectivity model matches (sparse) experimental measurements from synapse to cell type levels (e.g., synapse densities, numbers of synapses per connection, and connection probabilities between cell types). Third, this complete, dense statistical connectivity model allows generating network embedding realizations obeying these connectivity constraints, as well as variability in connectivity, for example depending on the soma location of the postsynaptic neuron (as in the L5tt neuron model).

3.2 Simulation results

The resulting network embedding realizations of postsynaptic neurons can now be combined with cell type-specific activity patterns to simulate sensory-evoked signal flow. Based on combination of anatomical and functional constraints, I performed network-embedded simulations of two different excitatory cell types in the average model of rat vS1.

- Simulation of anatomically and functionally constrained network-embedded models yielded results that agree with all previous measurements of the target quantities without further optimization of the models.

- The strategy for sensitivity analyses (i.e., sampling from one distribution, while keeping other constraints fixed) allowed to dissect the contribution of different parameters to simulated responses.

- These functionally realistic models allow to make predictions using specific manipulations of the network that are experimentally testable in vivo.

3.2.1 Modeling whisker deflection-evoked responses of L2py neurons

Note: The description of the L2py model results is adapted from Egger, Schmitt et al. 2015 [57].

Because of its location close to the cortical surface, responses of this cell type to PW and SuW deflections have been widely investigated in vivo using a variety of experimental techniques, from whole-cell or cell-attached recordings, 2p imaging of calcium activity in somata, to 2p imaging of Ca^{2+} hotspots on dendrites (i.e., putative spines) [46, 47, 26, 43]. The observed spiking probability in response to whisker deflections is very low (on the order of 1%, see also Figure 3.8), and therefore I restricted the model to subthreshold responses. These have previously been shown to be similar for PW and SuW deflections [46]; however, the underlying pathways have been shown to be only partially shared [43].
The goal of this model is to identify synaptic inputs underlying subthreshold SuW responses of L2py neurons, and to investigate how excitatory and inhibitory synapses (specifically from L1 INs) interact to shape these responses.

3.2.2 Constraints of the L2py neuron model

As described in the Methods section 2.5.1, I selected one representative L2py neuron morphology, converted its soma and dendrites into a full-compartmental biophysical model [103], and determined the number and subcellular distribution of synaptic contacts it receives from seven excitatory cell types and L1 INs, respectively (Figure 3.16 A, Table 3.4). The total number of putative synapses in this model was 7,411, of which 7,063 were excitatory und 348 inhibitory; 1,810 and 5,601 synapses originated from neurons located in the PC and SC, respectively. L1 IN inputs were located on distal apical dendrites and largely separated from those of excitatory cell types in L2-5 (Figure 3.16 B). This proce-

dure was repeated 50 times by varying the presynaptic partner neurons assigned to each (or multiple) synaptic contacts, reflecting different configurations of anatomical connectivity in the model network within the statistical distributions of connectivity parameters as described in the anatomical model (section 3.1.4). Combining these network embedding realizations with spiking probabilities and timings of excitatory cell types and L1 INs during ongoing activity and after whisker deflection (see also Methods section 2.5.1 and Results section 3.1.3), I generated 100,000 samples of biologically realistic functional connectivity realizations (Figure 3.16 C).

This procedure estimated that the model neuron received on average 3 ± 1 excitatory synaptic inputs per millisecond during simulated periods of ongoing activity (i.e., up states). Previously, the same number of active synaptic contacts was estimated by tuning activity of presynaptic neurons until voltage traces simulated within a full-compartmental model met those obtained by whole-cell recordings during up states in vivo [103]. The present data further suggest that excitatory inputs after SuW deflection originate from a highly heterogeneous mix of excitatory cell types located throughout all cortical layers of the PC and SC (Figure 3.16 C). Consequently, these results contradict the classical view of the cortical circuitry, which postulated L4 as the primary source of feed-forward excitation in L2/3. This view had been challenged previously, where high-resolution 2p imaging of Ca^{2+} hotspots on dendrites of L2py neurons in mouse vS1 [43] revealed that the majority of spines responded to deflections of the PW and SWs. In line with these in vivo imaging results, I estimate that $\sim 50\%$ of the excitatory inputs (primarily from L5) to L2py can be activated by the PW and SuW, 30% and 20% (primarily from L2–4) exclusively by the PW or by a SuW, respectively.

3.2.3 Simulation of fully constrained synaptic input patterns to L2py neuron model

By combining these functional connectivity configurations with the constrained biophysical models of synapses and dendrites, I simulated dendritic integration of these spatiotemporal synaptic input patterns and measured the resulting membrane potential at

Cell type	Neurons PC	Neurons SC	Synapses PC	Synapses SC	Distance synapses PC to soma (μm)	Distance synapses SC to soma (μm)
L1 IN	105	163	44	304	270 ± 75	188 ± 83
L2py	1513	1966	334	2292	155 ± 120	105 ± 60
L3py	1583	1955	186	812	206 ± 103	107 ± 63
L4py	475	592	25	256	75 ± 93	91 ± 71
L4sp	2357	2854	46	253	101 ± 29	124 ± 78
L4ss	2535	3168	150	712	115 ± 84	95 ± 39
L5st	1112	1368	1020	646	122 ± 87	135 ± 74
L5tt	1593	2128	5	326	297 ± 76	88 ± 61

Table 3.4: Anatomical model of PC-SC network and number of synapses from the two barrel columns onto the L2py model neuron. Table adopted from [57].

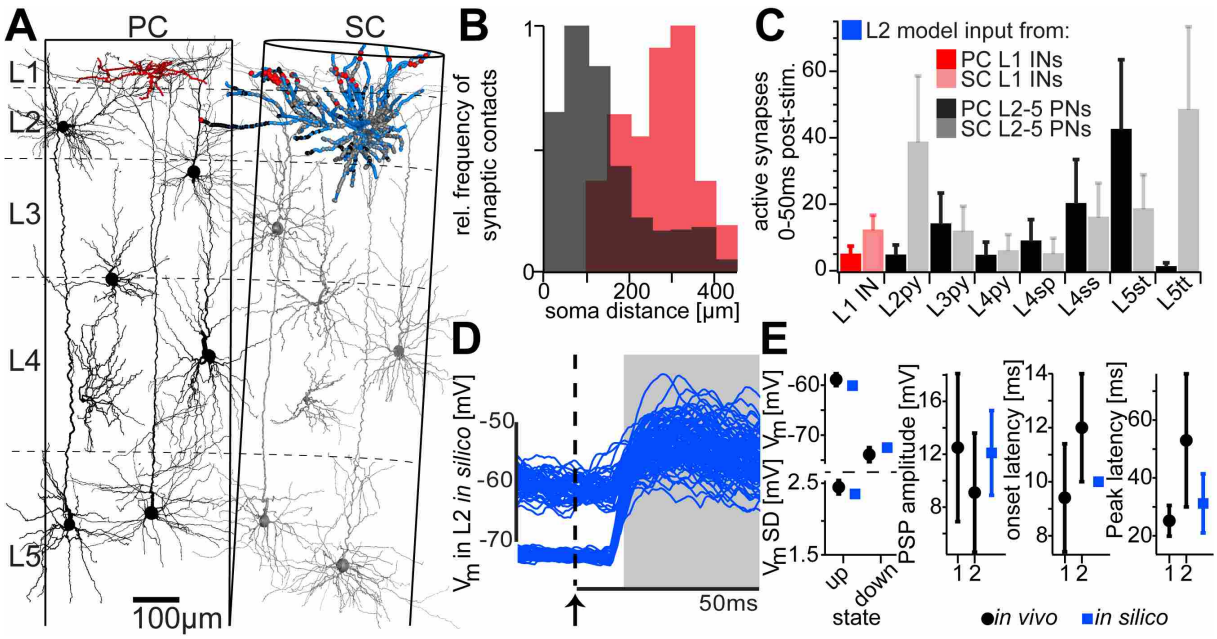

Figure 3.16: Whisker-evoked responses of a L2py neuron in silico. (A) Full-compartmental model of an in vivo-labeled L2py (blue), embedded into an anatomically well-constrained el of the average vS1 circuitry (exemplary in vivo-labeled dendrites are shown for each excitatory pyramidal neuron (PN) cell type). The number and subcellular distribution of synaptic contacts impinging onto the L2py model were determined statistically (1% of the synaptic contacts for one of 50 models are shown). (B) Path length distances between synaptic contacts from excitatory cell types ((black) and L1 INs (red) and the soma of the L2py model. (C) Cell type-specific number of active synaptic contacts during a period of 50ms following whisker deflection. (D) Simulation of 200 trials of ongoing and whisker-evoked synaptic activity using the model configuration shown in A (15ms of ongoing activity before and 50ms of evoked activity after the whisker deflection stimulus are shown). (E) Comparison between simulated (in silico) and in vivo measured ongoing (8) or whisker-evoked PSPs. 1 and 2 refer to L2py PSP measurements in our (Figure 3.20) and a previous study [46], respectively. Figure adopted from [57].

the soma (Figure 3.16 D). The somatic membrane potential in silico during ongoing up- and down-state activity was in agreement with previous in vivo measurements [103]. Remarkably, without refinement of the biophysical model, or tuning/optimization of the anatomical parameters, the shape of the postsynaptic potentials (PSPs) in silico (i.e. peak amplitude, onset and peak latencies) were in line with our ([57], Figure 3.20) and previous [46] in vivo measurements (Figure 3.16 E). Because the shape of the PSP response to whisker deflections, as well as the number of synapses during ongoing activity, as well as the type of synapses activated after SuW deflection, all match previous experimental measurements in vivo, the present model can be regarded as functionally realistic. This means, it is a realistic representation of the functional connectivity and resulting membrane potential of L2py neurons during ongoing and sensory-evoked activity in vivo. Therefore, this model can be used to investigate the influence of various constraints on the simulated responses, such as the contribution of L1 INs to the PSP shape, and to make predictions of specific manipulations that are testable in vivo.

3.2.4 Influence of different constraints on simulated responses of L2py

To test the impact of distal L1-to-L2 synaptic inputs onto the whisker-evoked PSP, I repeated the simulations, but deactivated the L1 INs in the PC (Figure 3.17 A). The variability of whisker-evoked PSPs (SD of membrane depolarization 15-50ms post stimulus across trials) increased significantly (Figure 3.17 B), whereas the shape of the mean PSP remained largely unchanged (i.e. amplitude, onset and peak latencies, (Figure 3.18 A)). To determine a possible mechanism underlying this in silico prediction, I performed sensitivity analyses as described in the Methods section 2.5.1. I generated new samples by systematically varying one of the anatomical, functional and biophysical parameters within the measured constraints, while keeping the other parameters unchanged (Figure 3.17 C, Figure 3.18).

Varying functional connectivity of excitatory cell types, but leaving functional L1-to-L2 connections unchanged, did not influence average trial-to-trial variability. In contrast, leaving functional configurations of excitatory cell types unchanged and deactivating L1

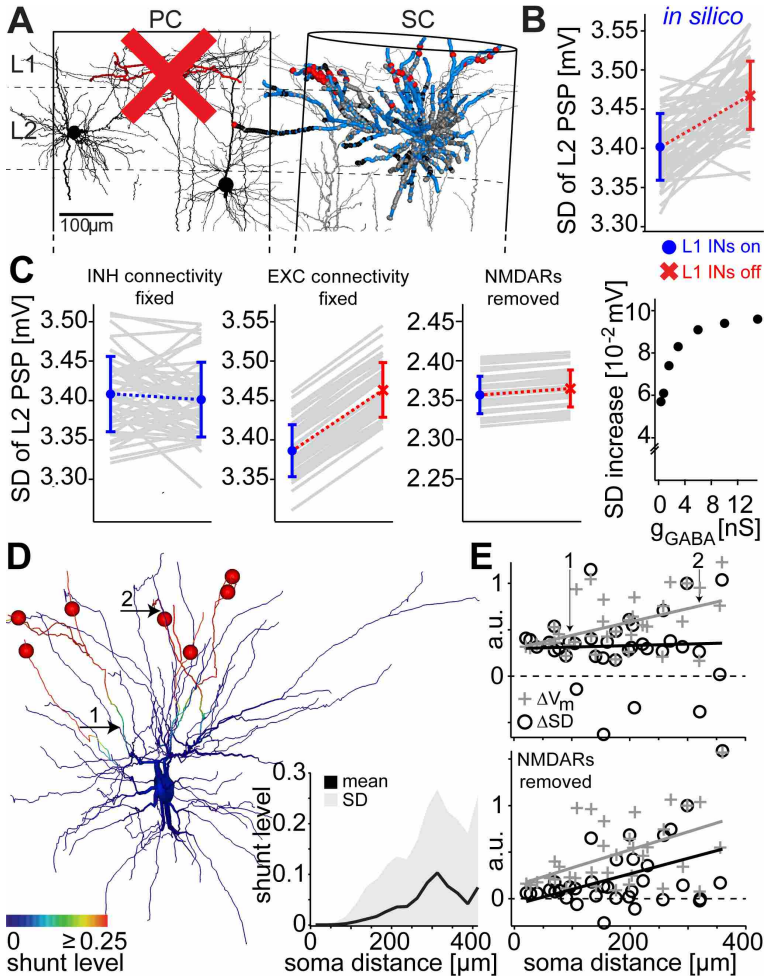

Figure 3.17: Deactivation of L1 INs in silico predicts increase of L2py PSP variability. (A) The same model configuration as in Figure 3.16, but without L1 INs in the PC. (B) Comparison of whisker-evoked PSP variability between models with (Left) and without (Right) PC L1 INs (each gray line refers to one of the 50 anatomical models). (C) Sensitivity analyses from left to right: varying functional connectivity of PN synaptic contacts; keeping PN functional connectivity fixed and deactivating PC L1 INs; removing NMDARs from PN synapses; varying L1 IN synapse strengths around the value used in all simulations (1.6 nS). (D) L1 IN inputs shunt dendritic branches as quantified by the shunt level (SL). The average (across trials) SL decreases monotonically toward proximal dendrites, reaching zero $\sim 100\mu m$ from the soma. (E) Change (with vs. without L1 INs) of the average (across trials) membrane potential (ΔV_m) and its variability (ΔSD), calculated at multiple dendritic locations in the presence (Upper) and absence (Lower) of NMDARs in the model. Figure adopted from [57].

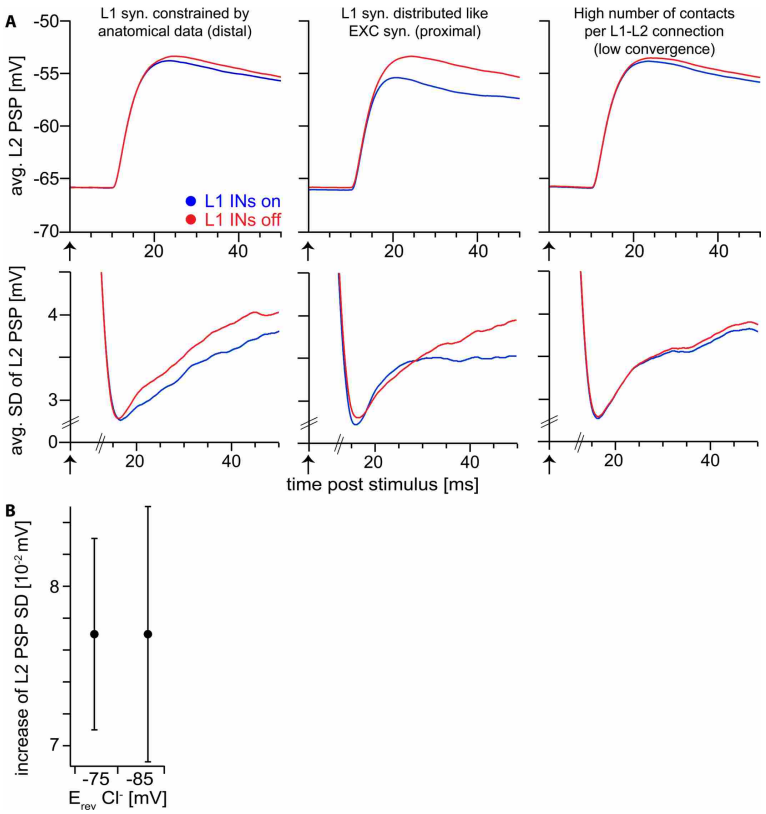

Figure 3.18: Sensitivity analysis of the computational model. (A) Top row: whisker-evoked PSP of L2py model averaged across 100,000 simulation trials. Bottom row: SD of whisker-evoked PSP across 100,000 simulation trials. (Left) Spatial distribution of L1 IN synapses on L2py constrained by anatomical data (Figure 3.16). (Center) L1 IN synapses on L2py distributed spatially overlapping with excitatory synapses of PNs (i.e., located on proximal dendrites; mean distance to soma along dendrites $97 \pm 45 \mu m$). In this scenario, L1 INs affect both PSP amplitude and SD at the soma. (Right) To test the assumption of high convergence of L1 IN inputs onto the L2py neuron model (i.e., L1 IN synapses originate from a large fraction of the presynaptic population), I generated network configurations with high specificity (i.e., low convergence) of distal L1 IN to L2py contacts (here: 11 synapses per connection). A high number of synapses per connection are equivalent to a low number of connected presynaptic L1 INs. In combination with the low spiking probability of L1 INs, this results in a small number of trials in which inhibitory synapses are activated. Therefore, the effect of L1 INs (reduction of PSP SD) is largely abolished. (B) A hyperpolarized chloride reversal potential (-85mV) has no effect on the reduction of the PSP SD by L1 IN synapses. The absolute value of the PSP SD is largely unaffected (control: $3.39 \pm 0.04 mV$, hyperpolarized: $3.34 \pm 0.04 mV$). Figure adopted from [57].

INs, the simulations resulted in identical increases of trial-to-trial variability for each of the 50 anatomical connectivity configurations. Changing the subcellular distribution of L1 IN inputs from the anatomically constrained configuration to overlap with excitatory synaptic inputs resulted in reduction of both PSP amplitude and PSP SD by L1 INs (Figure 3.18 A, center). Assuming high specificity in L1 IN - L2py connectivity (i.e., high number of synapses per connection, or equivalently a low convergence) largely abolishes the effect of L1 INs on the PSP SD (Figure 3.18 A, right). Next, hyperpolarizing the chloride reversal potential (Figure 3.18 B) or increasing the strength of the L1 IN synapses beyond the value used for all simulations did not change the effect on trial-to-trial variability. The latter is in line with a previous study, which showed that changes in input resistance saturate for large conductance values [144]. Assuming that the conductance of excitatory synapses is not uniform, but instead follows a log-normal distribution, did not change the average PSP amplitude (uniform conductance values: -51.38 ± 0.09mV, log-normal conductance values: -51.40 ± 0.30mV; here, SD is calculated across 50 network embeddings). The overall PSP SD was slightly increased, and L1 INs still reduced the PSP SD (with L1 INs: 3.86 ± 0.11mV, without L1 INs: 3.92 ± 0.10mV). Finally, by removing the NMDAR conductances, the increase in trial-to-trial variability was largely abolished. Taken together, these sensitivity analyses revealed that the observed change in trial-to-trial variability critically depends on the location (not strength) and high convergence of L1 IN inputs and the presence of NMDAR conductances at excitatory synapses.

3.2.5 Theoretical explanation of mechanism underlying PSP SD reduction

These results are reminiscent of theoretical work [145], which suggested that IN inputs can affect NMDAR conductances locally and/or globally, depending on their relative location to each other (Figure 3.19 A-B). First, IN input hyperpolarizes the membrane potential, which results in shunting of the adjacent (i.e. as determined by the passive membrane properties) dendritic compartments. Activation of NMDAR conductances within the shunted compartments will thus generate smaller depolarization, compared to non-shunted dendrites ('local' effect). Second, the local shunting also suppresses NMDAR-

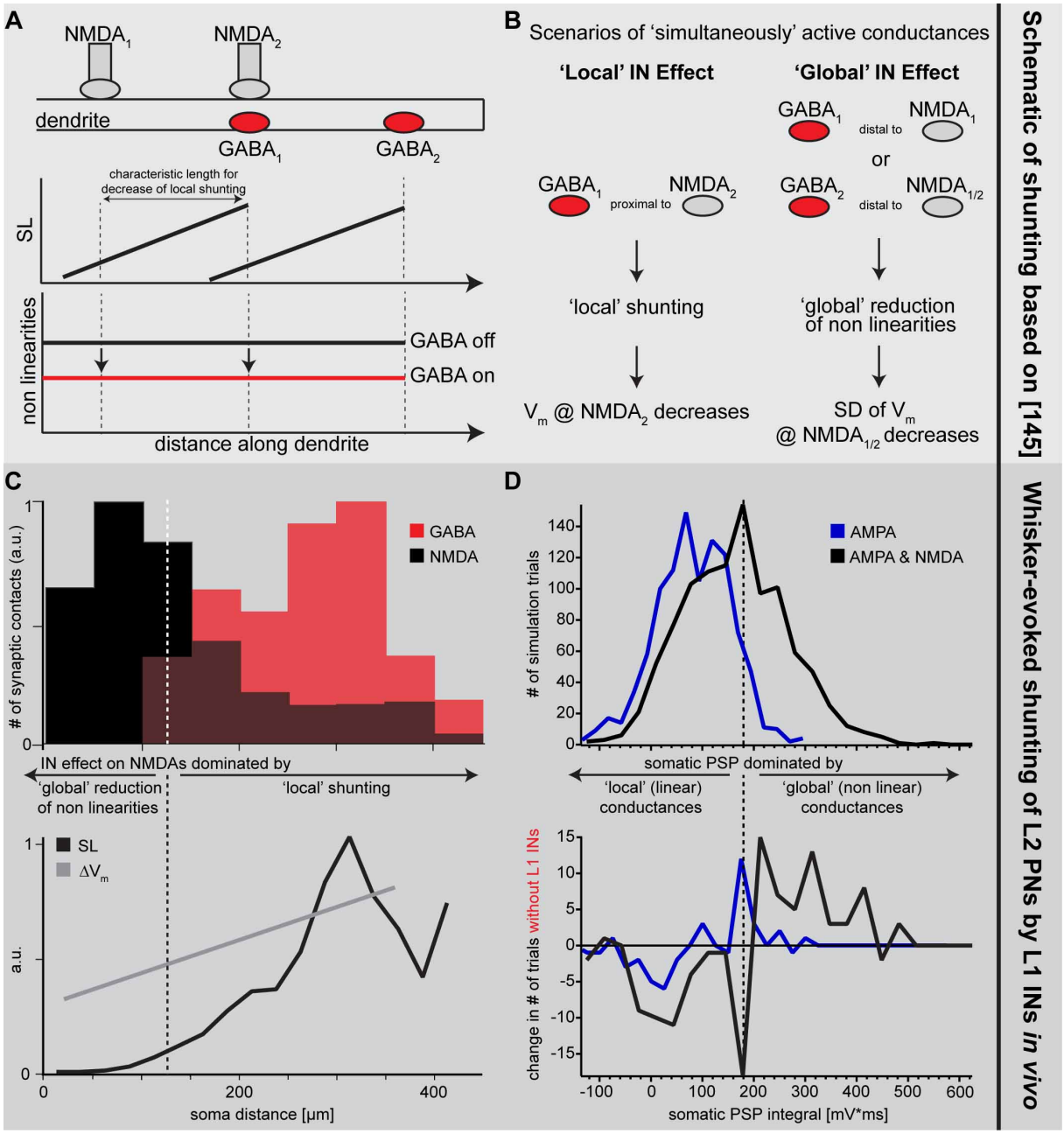
A
NMDA1
NMDA2
dendrite
GABA1
GABA2
characteristic length for decrease of local shunting
SL
non linearities
GABA off
GABA on
distance along dendrite
B
Scenarios of 'simultaneously' active conductances
'Local' IN Effect
'Global' IN Effect
GABA1 proximal to NMDA2
GABA1 distal to NMDA1
or
GABA2 distal to NMDA1/2
'local' shunting
'global' reduction of non linearities
Vm @ NMDA2 decreases
SD of Vm @ NMDA1/2 decreases
C
# of synaptic contacts (a.u.)
GABA
NMDA
IN effect on NMDAs dominated by
'global' reduction of non linearities
'local' shunting
SL
ΔVm
a.u.
soma distance [µm]
D
# of simulation trials
AMPA
AMPA & NMDA
somatic PSP dominated by
'local' (linear) conductances
'global' (non linear) conductances
change in # of trials without L1 INs
somatic PSP integral [mV*ms]
Schematic of shunting based on [145]
Whisker-evoked shunting of L2 PNs by L1 INs in vivo

Figure 3.19 *(previous page)*: Principles underlying dendritic inhibition in vivo. (A) (Top) Schematic model of proximal excitatory inputs (nonlinear NMDARs) and distal inhibitory inputs (GABAA receptors). Note that GABA1 is located distally with respect to NMDA1, but colocalized (proximal) relative to NMDA2, whereas GABA2 is located distally with respect to both NMDA1 and NMDA2. (Middle) Spread of shunt level (SL, a measure of the spatial efficacy of an inhibitory input along the dendrite) [145] from inhibitory synapses to more proximal locations. (Bottom) Nonlinearities throughout the dendrite mediated by NMDARs are reduced by the spread of SL from distal inhibitory synapses to more proximal NMDARs. (B) Effect of active inhibitory inputs depends on their location relative to active excitatory inputs. Locally, inhibitory inputs decrease the membrane potential (local shunting) [145]. In contrast, if the active inhibitory input is located distally with respect to the excitatory input, it can control/reduce NMDAR-dependent nonlinearities (global reduction) [145] and thus reduce the membrane potential noise (i.e., SD) that is amplified by the nonlinearities. (C) (Upper) Spatial distribution of excitatory (NMDAR) and inhibitory (GABA) synaptic inputs along the dendrites of the L2py neuron model (Figure 3.16). Excitatory synapses located within $\sim 100\mu m$ of the soma are not shunted by the more distal inhibitory synapses and are thus primarily influenced by global reductions of nonlinearities. Excitatory synapses located further away from the soma are both colocalized with inhibitory synapses (proximal) and affected by more distal inhibitory synapses. They are therefore mostly affected by local inhibitory shunting but also by global reductions of nonlinearities. (Lower) Average SL and effect of inhibitory inputs on local membrane potential (ΔV_m; Figure 3.17), confirming the local shunting of membrane potential in more distal parts of the dendrites where inhibitory synapses are proximal to excitatory synapses. Average SL and ΔV_m decrease toward the soma, explaining the observation that the average PSP at the soma is largely unaffected by distal inhibition. (D) Global nonlinearities observed at the soma. Figure adopted from [57].

mediated non-linearities, which effectively decreases regenerative dendritic events, also at locations that are not directly affected by the shunting ('global' effect). Thus, in case IN inputs are activated simultaneously with PN inputs (e.g. after whisker deflection), the average (i.e. across trials) evoked membrane potential within shunted dendritic compartments should be smaller compared to situations with no IN input (ΔV_m). At the same time, NMDAR-mediated non-linearities should be reduced throughout the entire dendritic tree, which can be quantified as the change (with vs. without IN input) of the trial-to-trial variability (ΔSD) of the membrane potential. I quantified the two effects for whisker-evoked L1 IN inputs impinging onto L2 PNs, by calculating the 'shunt level' (SL [145]) along the dendrites of our neuron model (Figure 3.17 D). The SL decreased monotonically from the distal location of highest IN input density, reaching zero $\sim 100\mu m$

from the soma (i.e., IPSPs of distal L1 IN synapses have little effect at the soma). As predicted by the theory, ΔV_m was proportional to the SL (Pearson correlation coefficient R=0.62, p=0.02), and hence decreased monotonically towards the soma (Figure 3.17 E). In contrast, ΔSD was independent of the dendritic location and the respective SL (R=-0.02, p=0.95). To confirm that the decoupling between ΔSD and the SL was indeed caused by suppression of regenerative non-linear events, I removed the NMDAR conductances from the model. As expected, ΔV_m and ΔSD then decreased both monotonically towards the soma (i.e. proportional to the SL (Figure 3.17 E)).

This model also explains the observation that proximal L1 IN synapses affect both PSP amplitude and PSP SD (Figure 3.18 A, center). Proximal inhibitory synapses affect NMDAR-mediated nonlinearities. At the same time, the SL in this configuration extends to the soma and affects the membrane potential at the soma, in contrast to the anatomically constrained configuration (i.e., IPSPs of proximal L1 INs are visible at the soma). Finally, I performed 2,000 simulation trials with AMPARs at excitatory synapses and 2,000 simulation trials with AMPARs and NMDARs at excitatory synapses to quantify NMDAR-mediated nonlinearities in the model. I computed the respective histograms of the whisker-evoked PSP integrals at the soma during 10-50ms following whisker stimulation [101, 119] (Figure 3.19 D). Because AMPARs have a linear (independent of membrane potential) conductance, I used the distribution of PSP integrals from these simulations to define the range of linear PSPs (dashed line; mean + 1.5 SD). The distribution of PSP integrals in simulations with NMDARs was broader and contained more nonlinear events (Figure 3.19 D, upper panel). After removing the L1 INs, the number of nonlinear events increased by $\sim$ 15% in simulations with AMPARs and NMDARs (Figure 3.19 D, lower panel).

3.2.6 In vivo pharmacology confirms in silico predictions

To summarize, the in silico predictions about the effect of L1 INs on SuW-evoked subthreshold responses of L2py are that the PSP SD between 15-50ms should increase without L1 INs, while PSP amplitude and peak latency should remain largely unaffected. This could further be related to specific subcellular organization (i.e., located in distal

dendrites) as well as unspecific connectivity (i.e., high convergence) of L1 IN synapses. In vivo experiments that closely resembled the conditions of the model were performed by Arno Schmitt (Figure 3.20 A). Injection of an AMPAR-specific antagonist (GYKI-53655 (Ivax, Budapest)) locally into L1 of the PC prevented L1 INs from AP firing (Figure 3.20 B), similar to inactivation of PC L1 INs in the model. To validate that this pharmacological manipulation remained specific to L1 INs, somatic calcium transients in populations of L2/3 neurons – right below the injection site – were imaged before and during the injection of GYKI. Neither the average whisker-evoked population response in L2/3 (n=42 neurons from 3 animals, p=0.79, p=0.17, p=0.29), nor its variability were significantly changed (Figure 3.20 C).

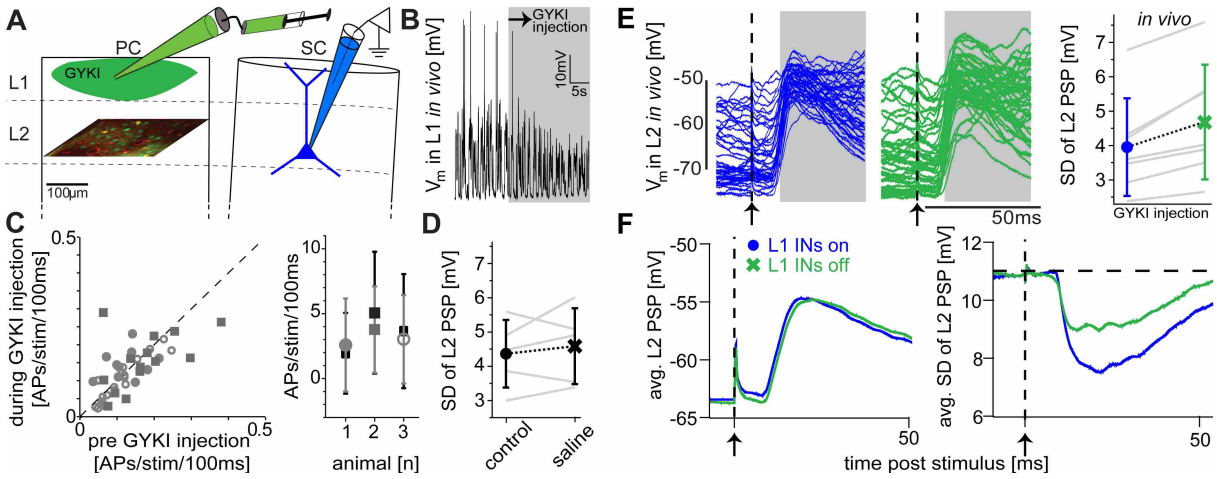

Figure 3.20: Pharmacological deactivation of L1 INs in vivo confirms in silico predictions. (A) Experimental setting to match in vivo conditions with the in silico scenario shown in Figure 3.17. Whole-cell patch clamp recordings were performed on L2 neurons located in a SC during deflections of the PW before and during injection of GYKI locally into L1 of the PC to prevent spiking in L1 INs. (B) Whole-cell recording showing ongoing activity of exemplary L1 IN located within the PC before and during GYKI injection. (C) Left: whisker-evoked response probabilities of L2 neurons within the PC, as revealed by 2p calcium imaging, before and during the injection of GYKI. Right: whisker-evoked APs in PC L2 neurons in the same animal before (black) and during (grey) GYKI injections. (D) PC L1 injections of saline had no systematic effect on SC L2 PSP variability. (E) Ongoing and whisker-evoked subthreshold activity of exemplary SC L2 neuron before (left) and during (center) pharmacological blockage of PC L1 INs. Right: variability across whisker deflection trials of PSP response increased for every recorded L2py neuron. (F) Left: average (across trials) PSPs of SC L2 neuron before (blue) and during (green) GYKI injections. Right: trial-to-trial variability of SC L2 PSPs was significantly increased during GYKI injections. Figure adopted from [57].

Moreover, to validate that the injection procedure itself did not alter the subthreshold whisker-evoked responses of L2py, whole-cell recordings before and during injection of saline into L1 were made and L2 PSPs in response to PW deflection were measured (n=5, p=0.63, Figure 3.20 D). Based on these control experiments, it was possible to investigate how the absence of L1 INs affects whisker deflection-evoked PSPs in L2py in vivo. To do so, whole-cell recordings on L2 PNs (located within a SC) were made before and during the injection of GYKI into L1 of the PC and PSPs in response to PW deflection were measured. Remarkably, every L2 neuron recorded under these experimental settings (n=7) showed an increase in trial-to-trial variability ($4.0\pm1.4mV$ vs. $4.7\pm1.7mV$, p=0.02, Figure 3.20 E). In contrast, the shape of the PSP response remained unchanged, with neither membrane potentials at peak amplitudes ($-51.9 \pm 6.1mV$ vs. $-51.8 \pm 7.1mV$, p=1), nor peak latencies ($25.2 \pm 5.3ms$ vs. $26.6 \pm 5.9ms$, p=0.16) being significantly altered (Figure 3.20 F).

Remarkably, these in vivo measurements agree with the model predictions. In particular, the scenario that both PSP amplitude and PSP SD were affected was not observed in the in vivo experiments, suggesting that distal inhibition of L2py by L1 INs is a general organizational principle of this circuit. Additionally, reduction of PSP SD was observed in every L2 neuron recorded in vivo (Figure 3.20 E), suggesting that the assumption of high convergence/low specificity of the L1 IN–L2py connection is justified.

3.2.7 Modeling passive whisker touch receptive fields of L5tt neurons

Using the model of L2py subthreshold SuW responses, I have successfully demonstrated the feasibility of creating a functionally realistic model of an excitatory cell type using fully constrained network-embedded simulations. Now, I want to apply this approach to a more complex question. I want to develop a realistic model of AP responses of L5tt neurons to passive whisker touch and identify cell type-specific pathways and synaptic mechanisms underlying these responses. L5tt provide output from cortex to various subcortical structures, such as thalamus, superior colliculus or brainstem [146, 147]. Additionally, they display the highest activity of excitatory cortical cell types spontaneously

as well as after deflections of the PW and the adjacent SuW. Hence, not only is it important to understant their output signal because it represents the output of cortex to other brain regions, but also because it allows to study the general question of how broad RFs arise in cortex (e.g. [26, 148]).

3.2.8 Constraints of the L5tt neuron model

Structural connectivity. As described in detail in the Methods section 2.5.2, I selected a representative L5tt soma and dendrite morphology and created nine representative network embedding realizations at equally spaced locations within the C2 column (see also Figure 2.12). In Figure 3.21, the L5tt morphology and all somata of presynaptic excitatory and inhibitory neurons to the L5tt neuron in rat vS1 and VPM of one of these network embedding realizations are shown with respect to different cortical layers, barrel columns and VPM barreloids.

The L5tt neuron model has presynaptic neurons located not only across the entire cortical depth, but also horizontally across entire rat vS1. Averaged across all nine network embedding realizations (i.e., across locations in the C2 column), the L5tt neuron model has $19,396 \pm 635$ presynaptic partner neurons. Of those, $17,757 \pm 639$ (or 92%) are excitatory, and $1,639 \pm 37$ (or 8%) are inhibitory. About 1/3 of all presynaptic excitatory neurons are located in the PC ($5,936 \pm 378$). In contrast, nearly 1/2 of all presynaptic INs are located in the PC (749 ± 56). In thalamus, most presynaptic neurons are located in the barreloid that is somatotopically aligned to the PC of the L5tt (137 ± 17 of 224 ± 29 total). Virtually all other presynaptic neurons are located in adjacent barreloids (78 ± 32). This heterogeneity in the columnar origin of presynaptic cortical neurons was consistent across all nine neuron models and was reflected in the average number of synapses originating from different cell types and columns (and barreloids in VPM; Figure 3.22).

The total number of synapses from neurons in rat vS1 and VPM to the L5tt neuron models is $24,161 \pm 785$ (mean and SD across nine locations in the network). Of those, $21,859 \pm 782$ (about 90% of all synapses) are excitatory and $2,302 \pm 74$ (about 10%) are inhibitory synapses. $9,313 \pm 670$ (i.e., about 39%) of all synapses originate from the PC, i.e. most of the synapses originate from neurons located in SuCs. However, this is highly

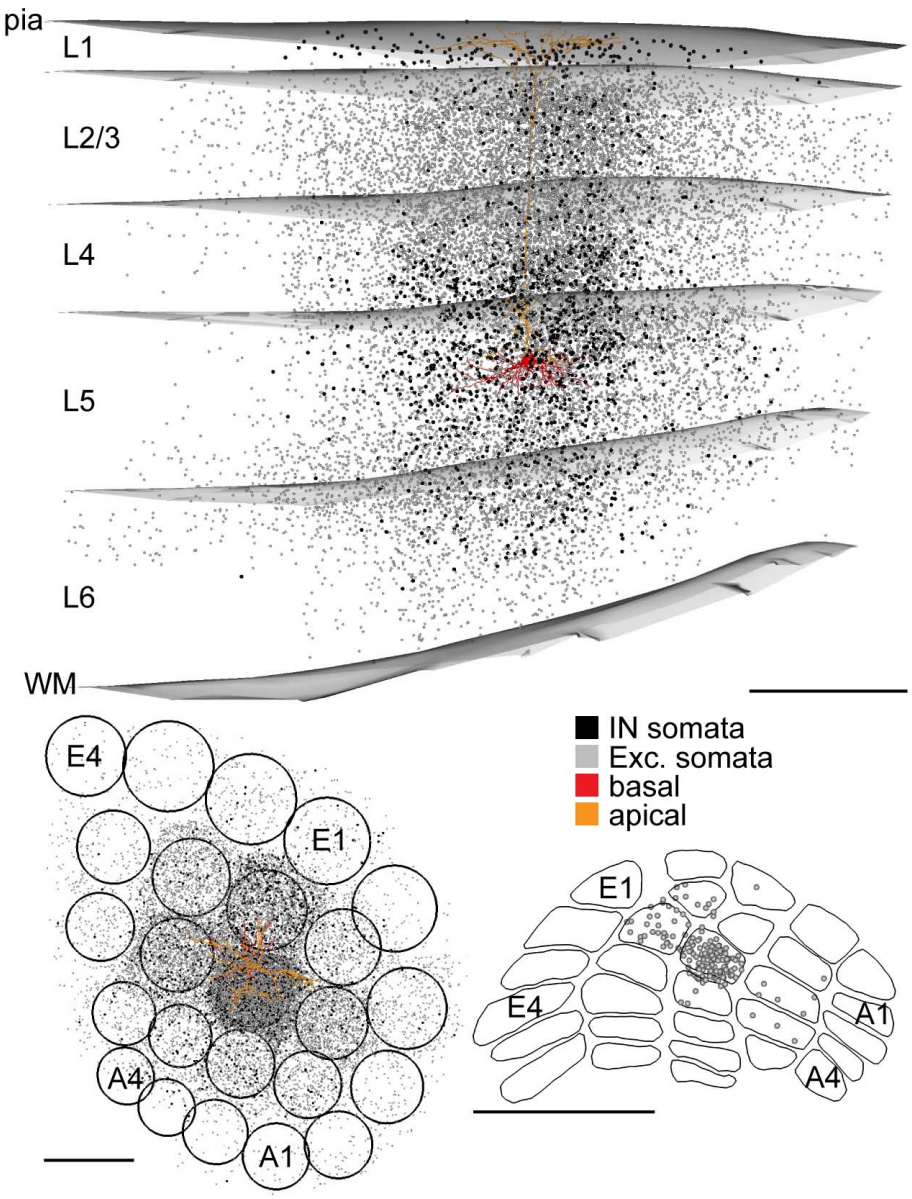

Figure 3.21: Presynaptic neurons of L5tt neuron model. Top: Semi-coronal view of the dendrites and soma of one L5tt neuron model embedded into the network model of rat vS1. Surfaces represent the curved pia, WM and layer boundaries. Orange: apical dendrite, red: basal dendrites and soma, grey: soma locations of presynaptic excitatory neurons, black: soma locations of presynaptic inhibitory neurons. Bottom left: Tangential view of the dendrites and soma of one L5tt neuron model embedded into the network model of rat vS1. Circles represent the barrel column outlines in L4. Bottom right: soma locations of presynaptic excitatory neurons in VPM. Contours represent the outlines of barreloids in VPM. Scale bar in all panels: $500\mu m$.

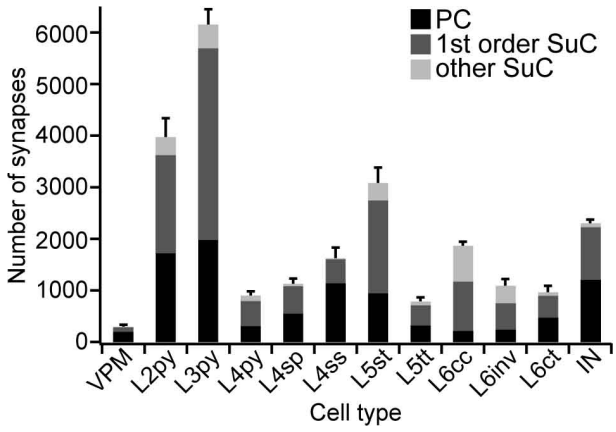

Figure 3.22: Cell type-specific number of synapses to L5tt neuron model. 1st order SuC refers to the eight SuCs adjacent to the PC. Error bars represent standard deviation of the total number of synapses per cell type across nine different model locations in the network. Shading indicates column in which somata of presynaptic neurons are located.

dependent on the presynaptic cell type. Synapses from VPM (67% from the PC), L4sp (49%), L4ss (70%), L6ct (49%) and inhibitory neurons (52%) are mostly PC-specific. On the other hand, synapses from L6cc (12% from the PC) and L6inv (22%) originate mostly from neurons outside of the PC.

The variability of the total number of synapses across all locations is surprisingly small: Measuring the SD as percentage of the mean, the variability of the total number of inputs across locations is only 3%. However, the location-specific variability of connections from different presynaptic cell types with different soma locations is substantially larger. For example, the average number of synapses from L4ss located in the PC to the models at all locations is $1,140 \pm 292$ (i.e., location-specific variability of 26%). The location-specific variability of L4ss synapses from adjacent SCs is 86% (58 ± 50 synapses). This is also the case for thalamocortical input from VPM: The location-specific variability of VPM synapses from the aligned barreloid is 17% (199 ± 34 synapses), and from adjacent surround barrleloids is 88% (11 ± 10 synapses). The mean location-specific variability across cell types measured in this way is 20% for synapses originating from neurons in the PC, 68% for synapses originating from neurons in the adjacent SCs and 123% for synapses originating from neurons located in other columns.

Finally, I determined the subcellular distribution of synapses from these different cell types (Figure 3.23). All presynaptic cell types innervated the basal dendrites (i.e.

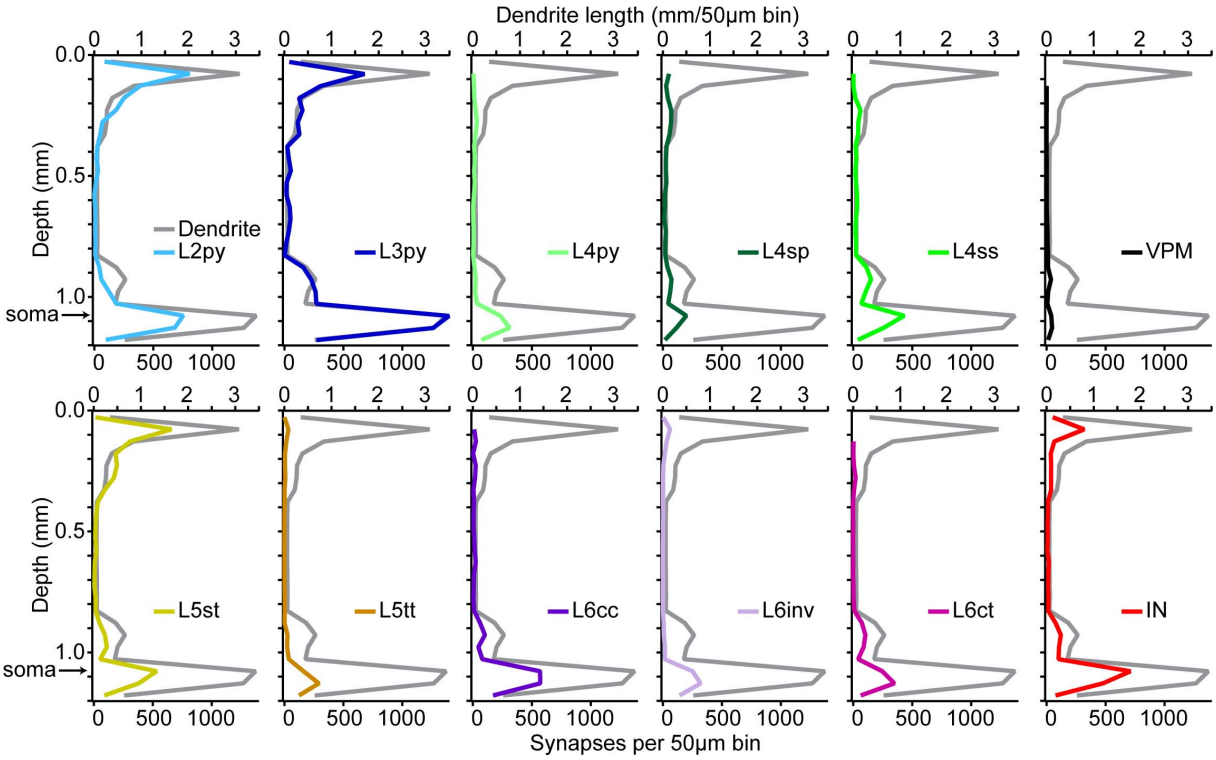

Figure 3.23: Subcellular distribution of synapses from different cell types to L5tt neuron model. Each panel shows the distribution of dendrites (grey, scale at top) of the L5tt morphology along the vertical column axis (scale at left) and the distribution of synapses from one presynaptic cell type onto this neuron (color, scale at bottom) along the vertical column axis.

between 1.0-1.2mm cortical depth). The apical tuft dendrites (i.e. between 0-0.2mm cortical depth) were mostly innervated by neurons in the supragranular layers (i.e., L2py and L3py), L5st and INs. L4 neurons did not innervate the apical tuft despite extensive axonal projections into the supragranular layers (see Figure 3.6). The apical oblique dendrites (visible as a peak in the dendrite length profile around 0.9mm) were also innervated by a specific subset of presynaptic cell types from each layer. For example, L3py, but not L2py neurons from the supragranular layers innervated the apical oblique dendrites. Of all L4 cell types, only L4ss innervated these oblique dendrites. In infragranular layers, L5tt and L6inv did not innervate the apical oblique dendrites. Synapses from VPM were numerically small compared to synapses to from cell types in vS1, and were found mostly in the basal and apical oblique dendrites. The location-specific variability of the subcellular distribution of synapses at the level of different presynaptic cell types (i.e., no taking different locations of presynaptic neurons into account) is on average about

57% (measured as the percentage of the SD of the mean at a resolution of $50\mu m$, i.e., corresponding to the resolution of the average model of rat vS1). This suggests that the precise location of the L5tt neuron model within the network at scales as small as $100\mu m$ is a major determinant of the specific synaptic innervation pattern by different presynaptic cell types.

The anatomical connectivity constraints presented here revealed that while the overall number of synapses to the L5tt neuron model is largely independent of its location within the C2 column, this is not the case when grouping synaptic inputs by the cell type of the corresponding presynaptic neuron. At a resolution of $\sim 100\mu m$ (i.e., the distance between locations used for network-embedding of the L5tt neuron model), the number of synapses originating from different cell types located in different barrel columns varies more than the typical across-animal variability of anatomical parameters (e.g. the 3D soma distribution has a variability of $\sim 10\%$ at a resolution of $50\mu m$). This reflects highly cell type-specific axon projection patterns within rat vS1 (see section 3.1.3). These axon projection patterns further lead to very specific subcellular innervation patterns of the postsynaptic L5tt neuron, even for presynaptic cell types located in the same layer.

Functional connectivity. Based on the number and subcellular distribution of synapses from different presynaptic cell types and the measured activity of these cell types, I generated 16,200 samples representing biologically realistic functional connectivity configurations (i.e., 200 samples for each of nine whisker deflections and nine model locations). Each sample consisted of 295ms of ongoing acitivity during the up state. The first 100ms were discarded after simulations to remove numerical artifacts. The remaining 195ms contained ongoing activity, as well as 50ms of whisker-evoked activity between 245-295ms. During ongoing activity, on average 12 ± 3 synapses are activated per ms (Figure 3.24) and give rise to the simulated subthreshold and suprathreshold responses. Of those, 9 ± 3 are excitatory synapses, and 4 ± 2 are inhibitory synapses.

A PW deflection was represented on average by 1552 ± 69 synapses in 50ms following the stimulus onset (Figure 3.25). Of those, 64% were excitatory and 36% inhibitory synapses. In contrast, a SuW deflection was represented by 1065 ± 120 synapses. The ratio of excitatory to inhibitory synapses was similar to a PW deflection. To account for spontaneously occuring spikes in the presynaptic population, I subtracted the aver-

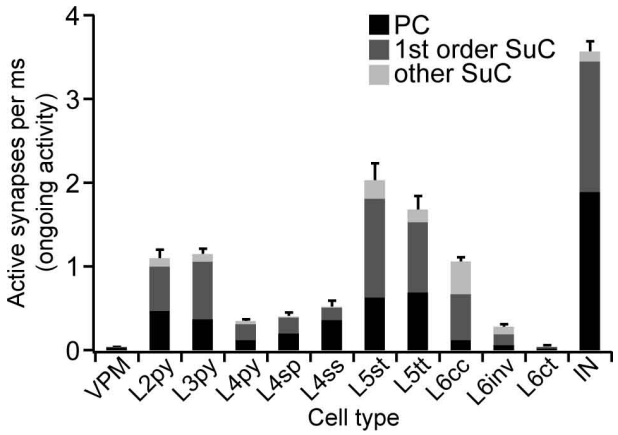

Figure 3.24: Cell type-specific number of active synapses during ongoing activity (per ms). 1st order SuC refers to the eight SuCs adjacent to the PC. Error bars represent standard deviation across nine different model locations in the network. Shading indicates column in which somata of presynaptic neurons are located.

age number of active synapses during an equally long interval of ongoing activity. The resultant number of activated synapses that can be attributed to the sensory stimulus is 943 ± 69 after a PW deflection (60% excitatory/ 40% inhibitory synapses) and 456 ± 120 after a SuW deflection (54% excitatory/ 46% inhibitory synapses).

In the previous paragraphs, the SD reflects the variability of the number of active synapses across different trials. In case of PW deflections, this variability reflects the Poisson distribution used to model activation of presynaptic neurons (SD of 39 synapses), as well as the variability across different locations in the C2 column (SD of 56 synapses). SuW deflections are represented by a lower number of synapses, but with nearly two-fold variability of the number of active synapses across trials. The increased variability can be attributed largely to two sources: First, different SuW deflections evoked different numbers of synapses on average, and thus grouping all SuW increases the trial-to-trial variability of the number of active synapses. For example, deflection of the B1 whisker was represented by 1022 ± 83 synapses on average, while deflection of the D3 whisker was represented by 950 ± 68 synapses. Second, location-specific variability after SuW deflections was larger than after PW deflection. For example, analyzing the number of active synapses representing a B1 whisker deflection at each of the nine locations in the C2 column separately revealed that the remaining variability (36 synapses) reflects the Poisson distribution underlying activation of presynaptic neurons. Hence, the variability

of the number of synapses across different locations of the L5tt model in the C2 column is ~ 114 synapses (i.e., about twice as large as the variability across locations after PW deflection). This reflects the heterogeneity of synaptic connectivity from presynaptic neurons located in SCs (as described above), which are primarily activated after SuW deflections.

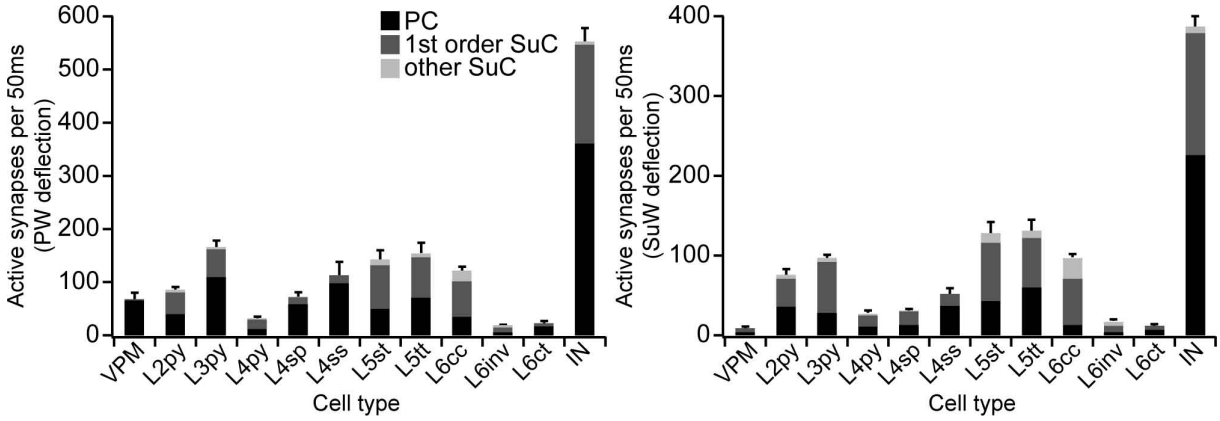

Figure 3.25: Cell type-specific number of active synapses during sensory-evoked activity. Left: average number of active synapses from different presynaptic cell types in a 50ms window following PW deflection. Right: average number of active synapses from different presynaptic cell types in a 50ms window following SuW deflection. 1st order SuC refers to the eight SuCs adjacent to the PC. Error bars represent standard deviation across nine different model locations in the network. Shading indicates column in which somata of presynaptic neurons are located.

3.2.9 Functionally realistic simulated responses of L5tt model

As shown in the previous paragraphs, the total number of active synapses following whisker deflection is relatively robust (SD as percentage of the mean $\sim 5\%$), but the specific response in individual trials additionally depends on the cell type of the presynaptic neuron to each synapse and specific timing of synapses (e.g., excitatory vs. inhibitory synapses). Therefore, I numerically simulated the response of the L5tt neuron model to the sampled spatiotemporal synaptic input patterns. During periods of ongoing activity, these synaptic inputs result in a tonic depolarization of the membrane potential and spontaneous AP firing (Figure 3.26).

Subthreshold membrane potential was on average $-65.4 \pm 4.1mV$. This was well

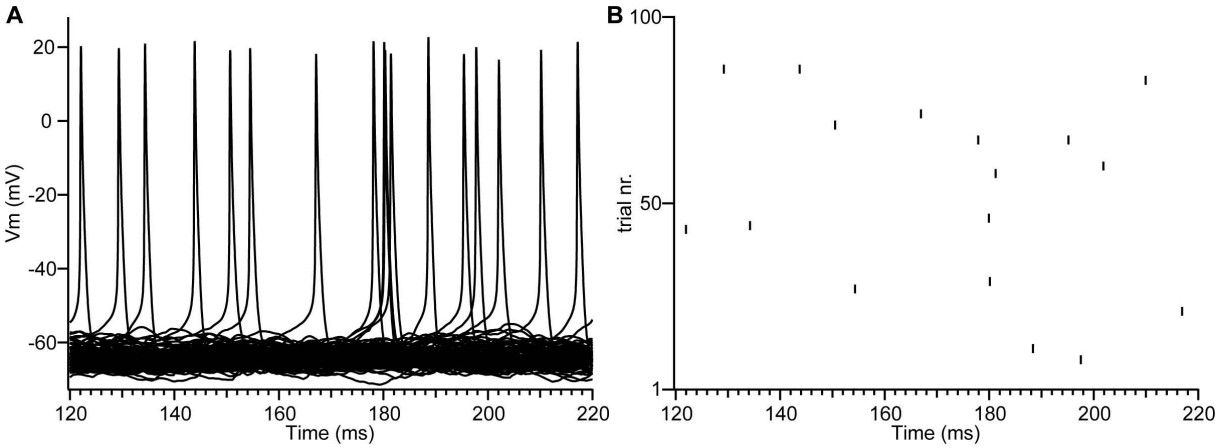

Figure 3.26: Sub- and suprathreshold activity of L5tt neuron model during simulated up-state. (A) Simulated membrane potential measured at the soma of the L5tt model located at the B3 border (see Figure 2.12) during 100 trials of 100ms of simulated ongoing activity. (B) Spike raster plot derived from the 100 membrane potential traces in (A). Spontaneous spiking frequency based on these example trials is 1.7Hz.

within the range reported previously for this cell type during up states using in vivo whole cell recordings (mean: -63mV, range between experiments: -73 to -55mV [149]). The resulting ongoing spiking activity was $1.6 \pm 1.4Hz$ (average and SD across nine different model locations). This was on the lower end of the experimentally determined distribution of ongoing activity of this cell type ($3.5 \pm 1.6Hz$, range: 1.6-6.3Hz [31]).
Next, I investigated the responses of the L5tt models to whisker deflections by simulating synaptic input patterns after deflection of the PW and eight SuW (see Figure 3.25). Trials with and without spiking responses could be observed after deflection of the PW and each of the eight SuW.

However, the number of trials which showed a response was different for each individual whisker. In order to compare these differences to measurements of the in vivo response of L5tt, I calculated the cumulative PSTH in 50ms following the whisker deflection onset and subtracted the average spontaneous activity determined previously (i.e., I calculated the whisker RF). Then, I correlated the resultant evoked spike probability of each whisker with the corresponding evoked spike probability of L5tt measured in vivo (Figure 3.28; r=0.88, p=0.002).

Finally, I compared the time course of the simulated response with the in vivo measurements ([26], Figure 3.29). The PSTH of in vivo measured responses displays two

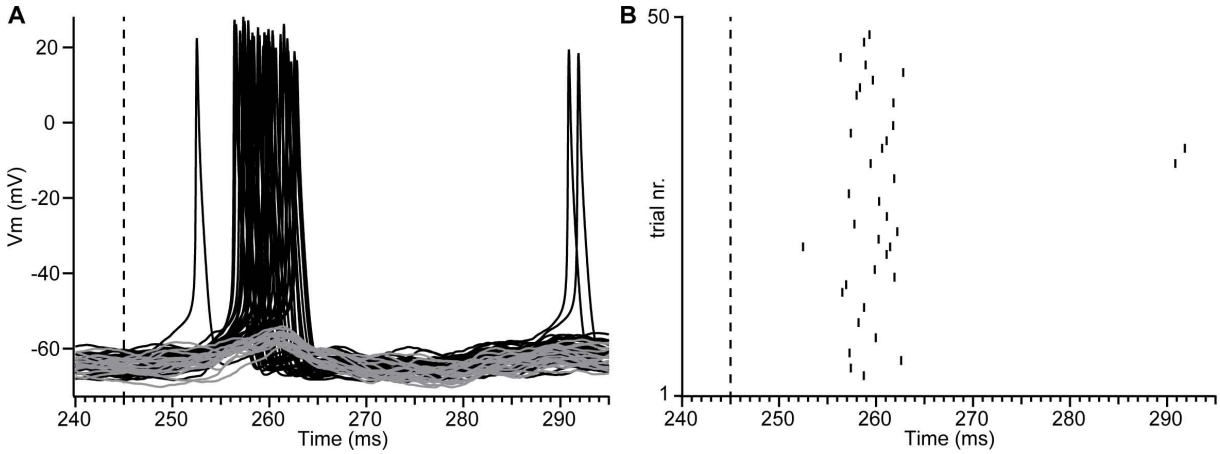

Figure 3.27: Sub- and suprathreshold activity of L5tt neuron model during simulated PW-evoked activity. (A) Simulated membrane potential measured at the soma of the L5tt model located at the B3 border (see Figure 2.12) during 50 trials of 5ms of simulated ongoing activity, followed by 50ms of simulated PW deflection-evoked activity. Whisker deflection occurs at 245ms (dashed line), and leads to responses that remain subthreshold (grey traces) and responses with APs (black traces) in 50ms following whisker deflection. (B) Spike raster plot derived from the 50 membrane potential traces in (A).

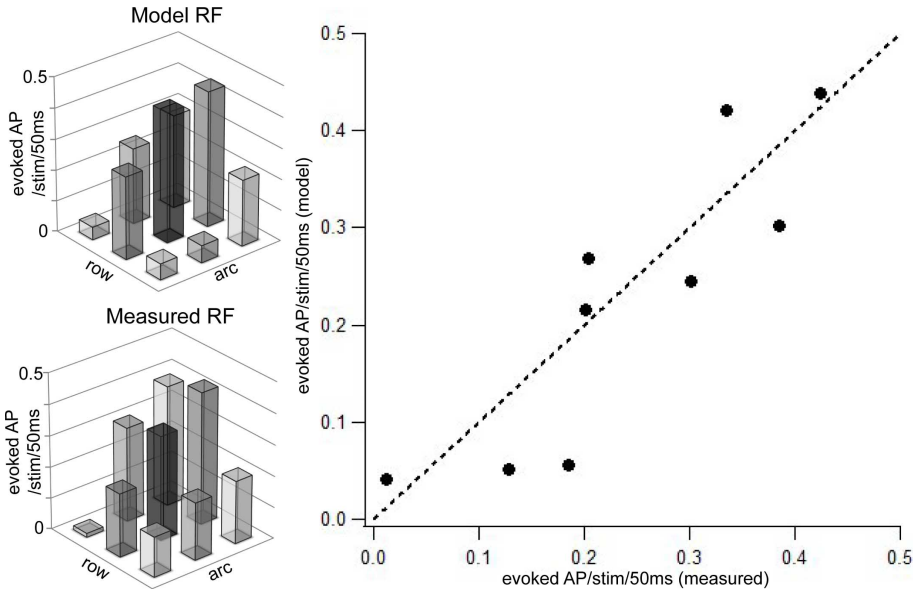

Figure 3.28: Sensory-evoked AP responses of L5tt model match in vivo measurements. Left: Whisker deflection RF averaged across the L5tt neuron model at all nine locations in the C2 column (top) and averaged across all recorded and identified L5tt (bottom). Right: Quantitative comparison of the evoked response in 50ms following whisker deflection. Each dot represents response to the deflection of a specific whisker in vivo (bottom) and in the model (left). Dashed line is the identity line.

phases. The early phase ($0-25$ms) displays a peak of activity in response to PW and all SuW deflections (except for deflections of the B3 whisker). The late phase ($25-50$ms) consists of low sustained activity that is largely independent of the identity of the deflected whisker. In addition to comparing the amplitude of the evoked response (Figure 3.28), I calculated the "average spike time" (i.e., the center of mass of the PSTH) during the early phase for the in vivo measured as well as the simulated PSTH of each whisker. Average spike times for each whisker during the early phase differed between in vivo measurements and simulations by 1.4 ± 1.3ms (range: 0-4ms). The simulated responses lack a substantial sustained activity in the late phase (but see the response to C1 whisker deflection). This is probably due to the simplified model of IN responses (see section 2.5.2). The approximation that all IN projection types respond equally to whisker deflections is sufficient to explain early responses of L5tt, but not the response during the late phase.

Hence, within the given constraints, the simulated PW- and SuW-evoked responses can be regarded as functionally realistic in terms of spiking probability as well as spike timing during the early phase ($0-25$ms post-stimulus) with millisecond accuracy.

3.2.10 Influence of different constraints on simulated responses of L5tt

The present functionally realistic model of ongoing as well as PW- and SuW-evoked activity allows to investigate the influence of various constraints on the simulated responses. Specifically, I am going to investigate (1) how including cell type-specific short-term depression and facilitation of synaptic inputs impacts the responses, (2) what the effect of location-dependent variability of synaptic inputs, as described above in section 3.2.8, on ongoing and whisker-evoked responses is, and (3) how PW- and SuW-evoked spiking occurs within the given constraints of cell type-specific synapse numbers and activation times (i.e., what are the mechanisms and pathways underlying these responses).

Synaptic depression and facilitation. I generated 16,200 samples of ongoing and whisker-evoked functional connectivity as described above, and simulated the response of the L5tt neuron model including cell type-specific facilitation and depression at in-

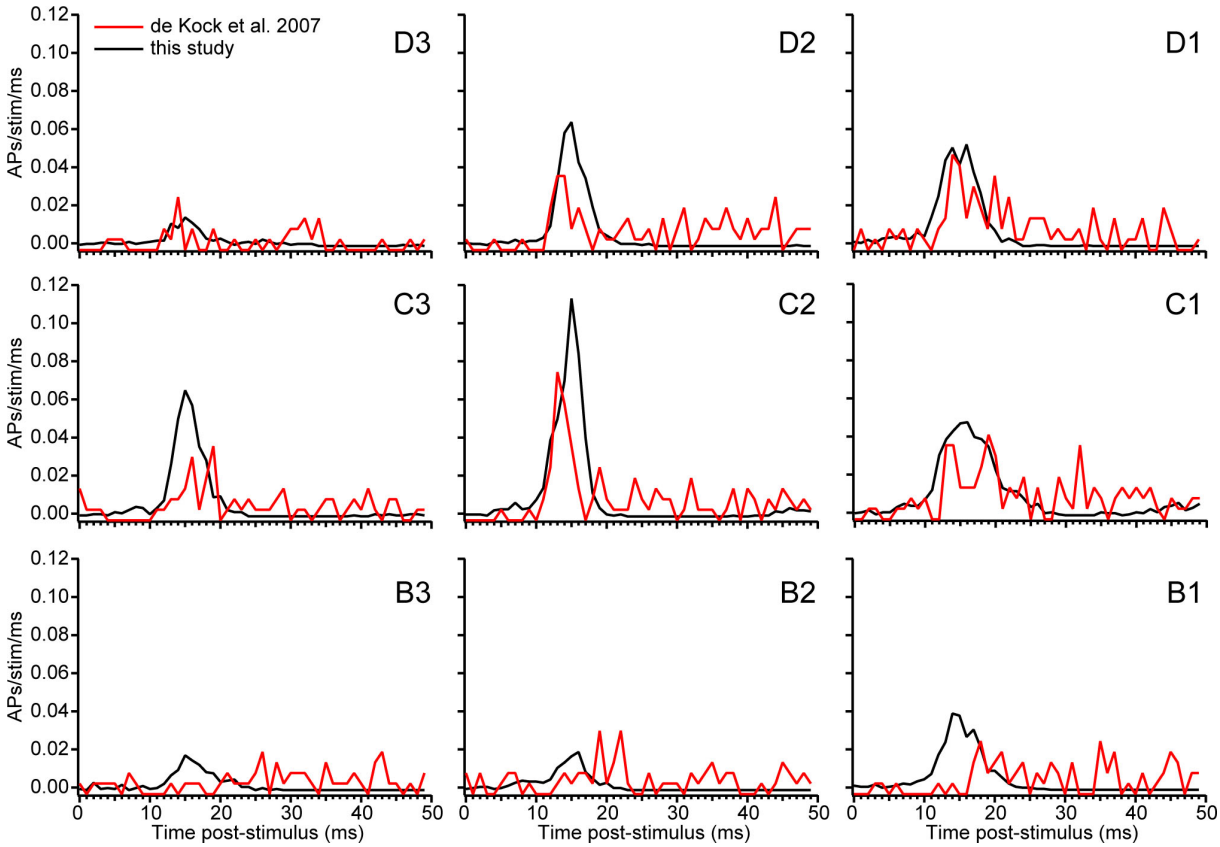

Figure 3.29: Time course of measured and simulated sensory-evoked AP responses of L5tt. Average PSTH of nine anatomical models with 1ms resolution for deflection of PW (C2) and eight SuW. Black traces are average across 1800 simulation trials each, red traces are averaged across measurements from 180 whisker stimulation trials (20 trials per whisker for n=9 recorded and identified L5tt, [26]).

tracortical and thalamocortical synapses (see also the Methods section 2.5.2 for detailed parameters). In general, simulated ongoing and sensory activity was higher (e.g. ongoing: $2.3 \pm 1.9Hz$, range: 0.4-5.6Hz), largely because the average inter-spike interval (ISI) of presynaptic INs was on the same time scale as the depression time constant of inhibitory synapses (average ISI: 143ms, depression time constant: 298ms), and therefore IN synapse conductances were tonically reduced. However, the effect was purely multiplicative, i.e. the ongoing activity of each of the nine models was scaled by a common factor compared to simulations without synaptic dynamics (r=0.99, $p < 10^{-4}$). The same was true when comparing the response after PW and SuW deflections. Evoked response amplitude of each individual whisker was on average higher by 46% and correlated significantly with the previous set of simulations (r=0.99, $p < 10^{-4}$).

Location-dependence of ongoing and sensory-evoked activity. To investigate location-specific differences in ongoing and sensory-evoked activity, I re-analyzed the 16,200 simulation trials described in the previous section 3.2.9 about functionally realistic responses of the L5tt model, but grouped them according to the location of the neuron model in the C2 column (i.e., 1,800 simulation trials per location).

The average subthreshold membrane potential during ongoing activity between the nine different model locations range from -66.3 to -64.3mV. Although these differences between models at different locations were small, they could predict the differences in ongoing spiking activity between these locations (range: 0.25-3.95Hz; r=0.96, $p < 10^{-4}$). Because the morphology and biophysical model of the L5tt neuron at all locations was identical, these differences have to originate from location-specific differences in excitatory and/or inhibitory synaptic input. Hence, I calculated the ratio of the mean number of active excitatory and inhibitory synapses per ms (E/I ratio) separately for each location. The E/I ratio was on average 2.42 ± 0.12 (range: 2.24-2.63) and correlated significantly with the average subthreshold membrane potential (r=0.92, $p < 10^{-3}$) and the average ongoing spike rate (r=0.86, $p < 0.01$) at each respective location.

I further investigated the location-dependence of PW and SuW-evoked responses. First, I compared the whisker-evoked response strength as measured by the evoked PSTH during 50ms following PW deflection at each location with the ongoing spiking activity of the model at the same location. These responses were not related (r=0.39, p=0.3), indicating that different synaptic inputs give rise to ongoing and whisker-deflection evoked responses. Second, I asked if the response of the individual models at nine different locations correlated similarly with the average in vivo response of L5tt as the average model response (i.e., averaging the response to each whisker deflection across all nine locations in the C2 column, see Figure 3.28). All models responded to deflections of SuW, but correlations with the average in vivo response were lower (mean correlation coefficient r=0.67; range: 0.14 to 0.87). This suggests that the nine L5tt neuron models at different locations within the C2 column combined can be viewed as a comparable sample of the population responses of L5tt as the in vivo recorded sample.

Finally, I asked how the precise location in the network and the specific dendrite morphology of the L5tt neuron reconstruction used for simulations contribute to its response

properties. I determined the anatomical model that was closest to the actual registered location of the in vivo recorded and reconstructed neuron morphology used for simulations. This was the model located at the border of the C2 column towards the D3 column (Figure 2.12). The distance between the model at the C2-D3 border and the registered location of the neuron was $27\mu m$, i.e. below the resolution limit of the reference frame. Next, I compared the PW and SuW responses (i.e., evoked activity within 50ms) of the model at the C2-D3 border and of the models at the other eight locations with the actual responses of this neuron to PW and SuW deflections measured in vivo. The correlation between in vivo measured responses and simulated responses was highest for the model at the C2-D3 border (i.e., where the neuron actually was located in the brain; r=0.80, p=0.01). Correlation coefficients between the models at the other locations and the in vivo measured responses were lower (average: r=0.59, range: 0.19-0.79). Thus, the integration of the dendrite morphology of the neuron at its precise location in the network model, and activation of resultant synaptic inputs based on measured response probabilities, explained 64% of its response variability to PW and SuW deflections, even though the model was never optimized or tuned with respect to the specific in vivo responses of this neuron.

Synaptic inputs underlying whisker-evoked responses of L5tt. In order to understand the mechanism underlying spiking responses in the early phase, I investigated the synaptic input patterns impinging onto proximal dendrites (i.e., including all synapses with a path length distance from the synapse location to the soma of less than $500\mu m$). First, I determined the average number of evoked synapses from excitatory and inhibitory cell types after deflection of the PW and each SuW. Evoked synapses were defined as the total number of active synapses in the interval 0-25ms minus the expected number of active synapses in a 25ms interval of spontaneous activity. The ratio of evoked excitatory to inhibitory synapses after a specific whisker deflection correlated strongly with the average response probability after deflection of the respective whisker (r=0.90, $p < 10^{-3}$), suggesting that a sufficient number of excitatory synapses have to overcome inhibitory synapses within a "window of opportunity" (i.e., a time window within which all synaptic inputs have to be integrated) to trigger spiking output. This is thought to be the basic mechanism of how feed-forward excitation from thalamus can activate cortical neurons

despite a small number of synapses compared to intracortical cell types, and in presence of strong feed-forward inhibition [45, 110, 44]. However, it is not clear if such a window of opportunity exists in the present situation, what time window it should correspond to, and what presynaptic cell types are active within this window. Therefore, I developed an objective method to identify such a window of opportunity based on comparison of functional connectivity realizations that give rise to spikes with functional connectivity realizations that do not lead to spiking responses. I sorted all trials into two groups (i.e. trials with spike and trials without spike in the early phase after whisker deflection). Then, I calculated the average number of active excitatory and inhibitory synapses in each group with 1ms resolution (Figure 3.30).

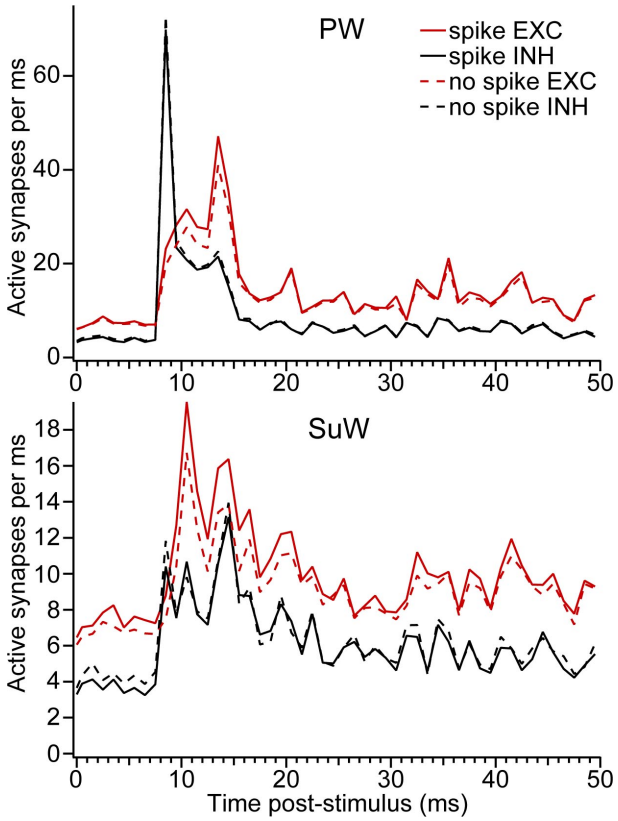

Figure 3.30: Active excitatory and inhibitory synapses after whisker deflection. Average number of active excitatory (red) and inhibitory (black) synapses per trial after PW deflection (top) or SuW deflection (bottom, average across eight SuW). Solid lines are averaged across all trials with spike in the early phase (0-25ms after whisker deflection), and dashed lines are averaged across all trials without spike in the early phase.

On average, more excitatory synapses are active in trials with spikes in the early phase than in trials without spikes in the early phase, both after PW and SuW deflection. In

contrast, the number of active inhibitory synapses is slightly lower in trials with spikes compared to trials without spikes. I therefore decided to investigate how well the difference in the number of active excitatory and inhibitory synapses could be used to predict the occurence of a spike in the early phase on the basis of individual trials (Figure 3.31).

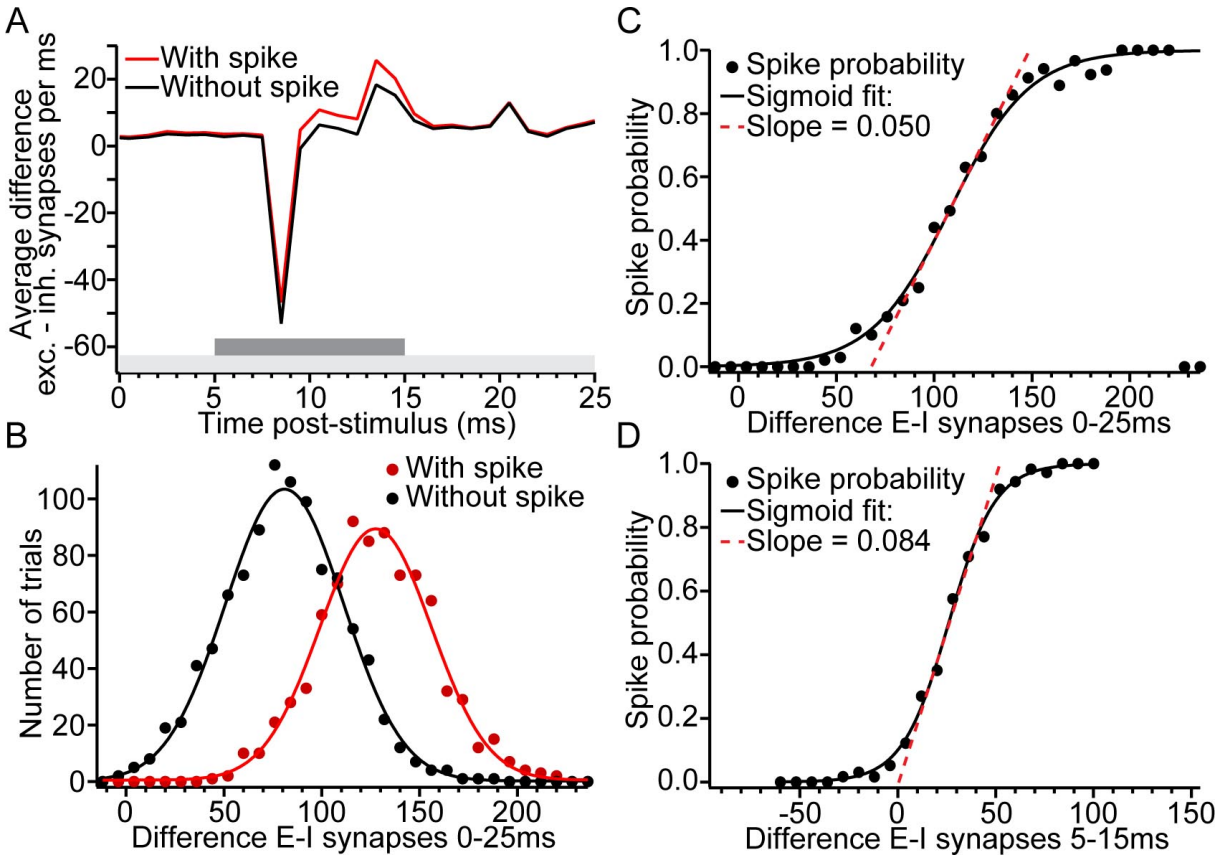

Figure 3.31: Calculation of predictive power of active synapses. (A) Average difference between the number of active excitatory and inhibitory synapses per trial after PW deflection in trials with (red) or without (black) spike in the early phase. Light gray line: window of opportunity 0-25ms post-stimulus; dark gray line: window of opportunity 5-15ms post-stimulus. (B) Distribution of difference between the total number of active excitatory and inhibitory synapses in the window of opportunity of 0-25ms (light gray line in A) across all PW deflection trials. Dots: Histogram of trials; solid lines: gaussian fit. (C) Spike probability as a function of the difference between the total number of active excitatory and inhibitory synapses in the window of opportunity of 0-25ms. Calculated from the histograms in (B). (D) Spike probability as a function of the difference between the total number of active excitatory and inhibitory synapses in the window of opportunity of 5-15ms (dark gray line in A).

To do so, I first calculated the difference in the number of active excitatory and inhibitory synapses in individual trials at 1ms resolution (Figure 3.31 A). Next, I integrated this difference (i.e., calculated the total difference) across a window of opportunity, e.g.

0-25ms after whisker deflection. Then, I again grouped all trials into two groups (trial/no trial in early phase) and calculated the histogram of the total difference in the window of opportunity for these two groups (Figure 3.31 B). From these histograms, I calculated the empirical spike probability as a function of the total difference in the window of opportunity (Figure 3.31 C). I then fitted a sigmoidal curve to this distribution. The inverse width (or slope) of the fitted sigmoidal curve can be interpreted as a measure for the predictive power of the total difference of active excitatory and inhibitory synapes in the window of opportunity for spiking responses: a high value of the slope indicates that the sigmoidal curve approaches a step function, which can be regarded as the perfect predictor. For example, choosing a window of opportunity between 5-15ms (dark gray line in Figure 3.31 A) results in a higher slope of the sigmoid fit to the spiking probability (Figure 3.31 D). This indicates that the number of active synapses in this time window is a better predictor of spiking activity than the number of active synapses in the entire interval from 0-25ms. To determine the window of opportunity that best predicts the spiking response of the L5tt neuron model in the early phase, I systematically varied the width and beginning time point of the window of opportunity for all possible time points in the early phase (i.e. 0-25ms). All trials were analyzed separately for the PW and each SuW (Figure 3.32).

Each point in these two-dimensional plots corresponds to a window of opportunity of a certain width between 1-25ms (horizontal axis) and beginning at a certain time after stimulus onset (window offset, vertical axis). The upper right half of these two-dimensional plots represents windows of opportunity past the early phase. Because I am only analyzing spiking responses and synaptic inputs in the early phase (0-25ms post-stimulus), these are therefore set to 0 and ignored during this analysis. Each valid window of opportunity is then colored according to the value of the slope of the sigmoid fit to the spike probability, as determined by the total difference between the number of active excitatory and inhibitory synapses in this window. The two example calculations in Figure 3.31 C (window of opportunity: 0-25ms) and D (window of opportunity: 5-15ms) are highlighted in green in the center panel. The structure of these plots can be understood at the example of the C2 deflection trials (center panel in Figure 3.32). Windows in the lower and upper left corner are poor predictors of spiking. In the lower left corner,

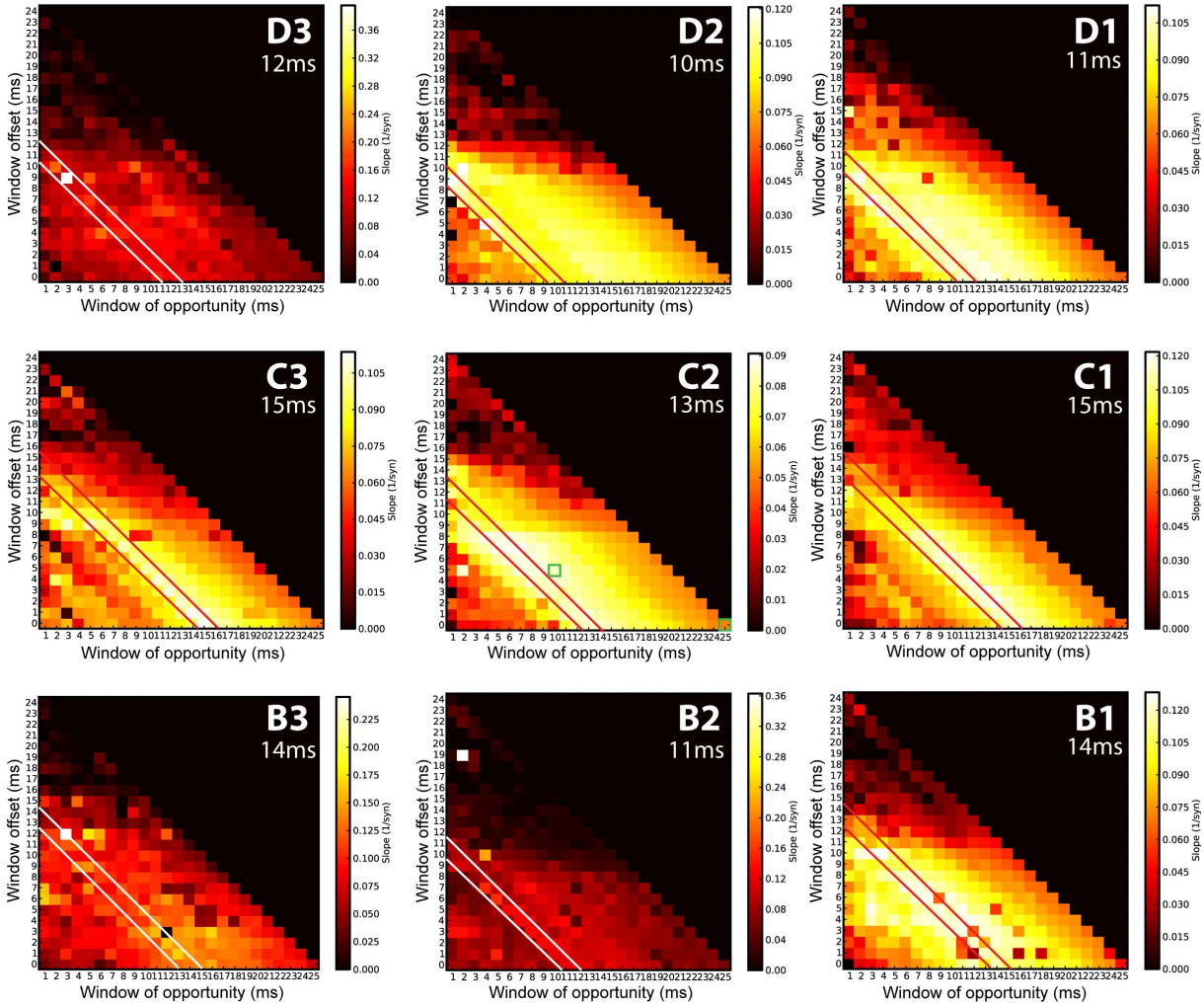

Figure 3.32: Determination of most predictive window of opportunity. Slope of sigmoid fit to spike probability as a function of difference in total number of active excitatory and inhibitory synapses for deflection of the PW (C2) and eight SuW. Each square represents a different window of opportunity between 0-25ms post-stimulus. Horizontal axis: width of the window of opportunity. Vertical axis: Offset (i.e. beginning) of the window of opportunity. Diagonal bars highlight windows of opportunity with highest average slope and ending at the same time (shown in upper right corner). Green squares in the C2 whisker deflection panel mark the windows used in the example calculations in Figure 3.31.

this includes windows of all widths, but not ending later than 8ms post-stimulus. This corresponds to the latency of thalamocortical synapses from VPM. Therefore, windows ending 8ms post-stimulus and earlier contain only synaptic activity due to spontaneous activity of presynaptic neurons, and are therefore unrelated to sensory-evoked spiking activity of the L5tt neuron models. In the upper left corner, windows beginning around 15ms or later contain synaptic activity that occurs after the average spike time of L5tt in the early phase (compare Figure 3.29), and is therefore not causally related to these spikes. Finally, windows of opportunity with high slope values are oriented in a diagonal direction. These diagonals represent windows that end at the same time (i.e., width of window + window offset = window end). I therefore calculated the average value of all windows of opportunity along these diagonals (i.e., ending at the same time) and determined the ending point with the highest average value. For C2 whisker deflections, the windows of opportunity ending after 13ms post-stimulus had the highest average slope value (0.082). The predictive power (i.e., the slope value) of these windows of opportunity is largely determined by the time at which they end, instead of the total width. For example, after C2 whisker deflection, the window from 8-13ms has a slope value similar to the window from 0-13ms. This suggests that active synapses between 0-8ms do not contribute to spiking in the early phase. As described above, active synapses from 0-8ms reflect ongoing and not sensory-evoked activity of presynaptic neurons. Therefore, the number of evoked synapses within the window of opportunity (i.e., total number of active synapses minus number of active synapses due to spontaneous activity) present the main contribution to spiking in the early phase. Hence, I am going to restrict the subsequent analyses to the *number of evoked synapses within the window of opportunity*.

Contribution of different cell types to activity in window of opportunity. Within the windows of opportunity identified above for each individual whisker deflection (Figure 3.32), I counted the number of evoked synapses of all excitatory cell types in all trials with and without spikes in the early phase.

Figure 3.33 A shows the contribution of all 10 excitatory intracortical cell types and thalamic input from VPM to the number of evoked synapses after PW deflection. The total number of evoked excitatory synapses was about 21% higher in trials with spikes than in trials without spikes in the early phase (122 ± 18 synapses in trials with spike/

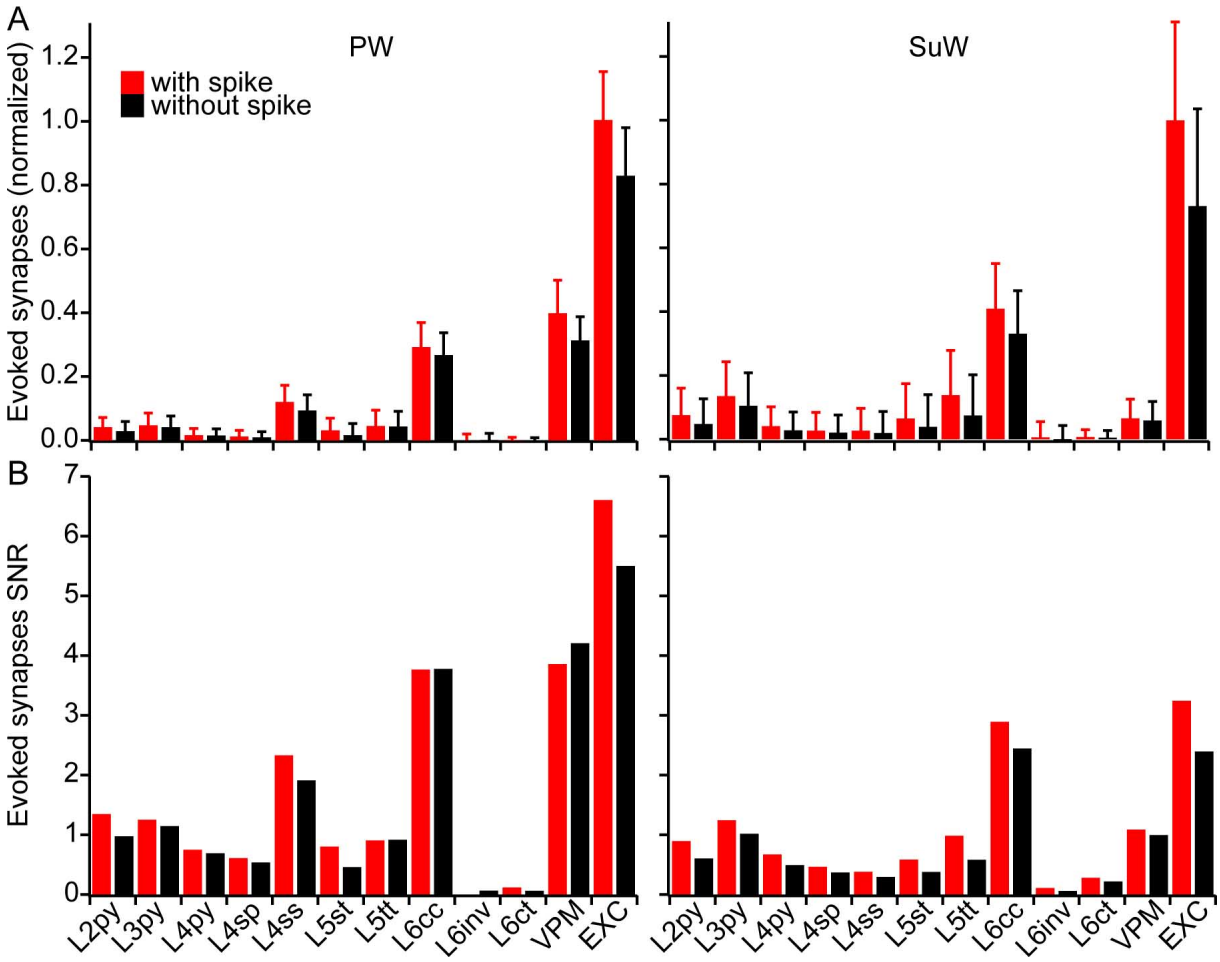

Figure 3.33: Evoked synapses in optimal window of opportunity. (A) Relative contribution of all presynaptic excitatory cell types to the number of evoked synapses in PW deflection trials with (red) and without (black) spikes in the early phase. Error bars are SD across trials. (B) Signal-to-noise ratio (SNR; i.e. mean/SD) of the evoked synapses in A. (C) As in A, averaged across all SuW deflection trials. Error bars are SD across trials and different whisker deflections. (D) SNR of the evoked synapses in C.

101 ± 18 synapses in trials without spike). The cell types with the largest number of evoked excitatory synapses were VPM (48 ± 13 in trials with spikes, 38 ± 9 in trials without spikes), followed by L6cc (35 ± 9 with/ 32 ± 9 without spikes) and L4ss (15 ± 6 with/ 11 ± 6 without spikes). In order to compare how reliable these contributions were across trials, I computed the signal-to-noise ratio (SNR) of each cell type (Figure 3.33 B). An SNR around 1 or lower indicates unreliable contribution of this cell type across trials. In turn, a high SNR indicates that despite statistical variations across trials as determined by the anatomical and functional constraints, a specific population of presynaptic neurons reliably provides input to the L5tt neuron model. The most reliable

presynaptic cell types were VPM, L6cc and L4ss. This suggests that spikes in the early phase after PW deflection are mainly driven by excitatory input from VPM and L6cc, and to a lesser degree by L4ss. After SuW deflections, the number of evoked excitatory synapses was about 37% higher in trials with spikes compared to trials without spikes in the early phase (51 ± 15 synapses in trials with spike/ 38 ± 14 synapses in trials without spike). Contributions of different excitatory cell types to spiking were more heterogeneous (Figure 3.33 C). The largest share of evoked excitatory synapses originated from L6cc (21 ± 6 with/ 17 ± 6 without spikes), followed by L3py (7 ± 5 with/ 5 ± 5 without spikes) and L5tt (7 ± 6 with/ 4 ± 6 without spikes). However, when measuring the contribution of different cell types to evoked synapses across deflections of all SuW and across trials by the SNR, only L6cc contributed reliably (Figure 3.33 D).

Together, VPM and L6cc accounted for 69% of all evoked excitatory synapses in the window of opportunity after PW deflection, and the very reliable L6cc accounted for 40% of all evoked excitatory synapses in the window of opportunity after SuW deflections. However, these numbers are still lower than the average number of excitatory synapses in trials without spikes, suggesting that the number and reliability of active excitatory synapses alone are insufficient to fully explain all early spiking responses after PW and SuW deflections. Therefore, I investigated the relative contribution and reliability of evoked synapses from excitatory cell types depending on the time of evoked spikes.

First, all PW and SuW deflection trials with spikes between 8-25ms post-stimulus (i.e., after activation of VPM) were sorted into 1ms bins (Figure 3.34 A). Next, for each trial the number of evoked synapses from all presynaptic excitatory cell types between 8ms and the time of the evoked spike (i.e., the cumulative number of synapses leading up to the spike) was determined. For all trials with spike times in the same 1ms bin, the average and SD of the evoked number of synapses of each cell type was calculated (Figure 3.34 B). Finally, the SNR of each cell type in each 1ms bin was calculated from the mean and SD (Figure 3.34 C). This analysis revealed distinct patterns of evoked synapses underlying sensory-evoked spikes in the early phase depending on the precise spike time. Specifically, in the first 5ms after activation of the thalamus (8-13ms post-stimulus), evoked synapses mainly originate from VPM, followed by L6cc with a delay of about 2ms. Spikes that occur later (13-20ms post-stimulus) are driven by much more

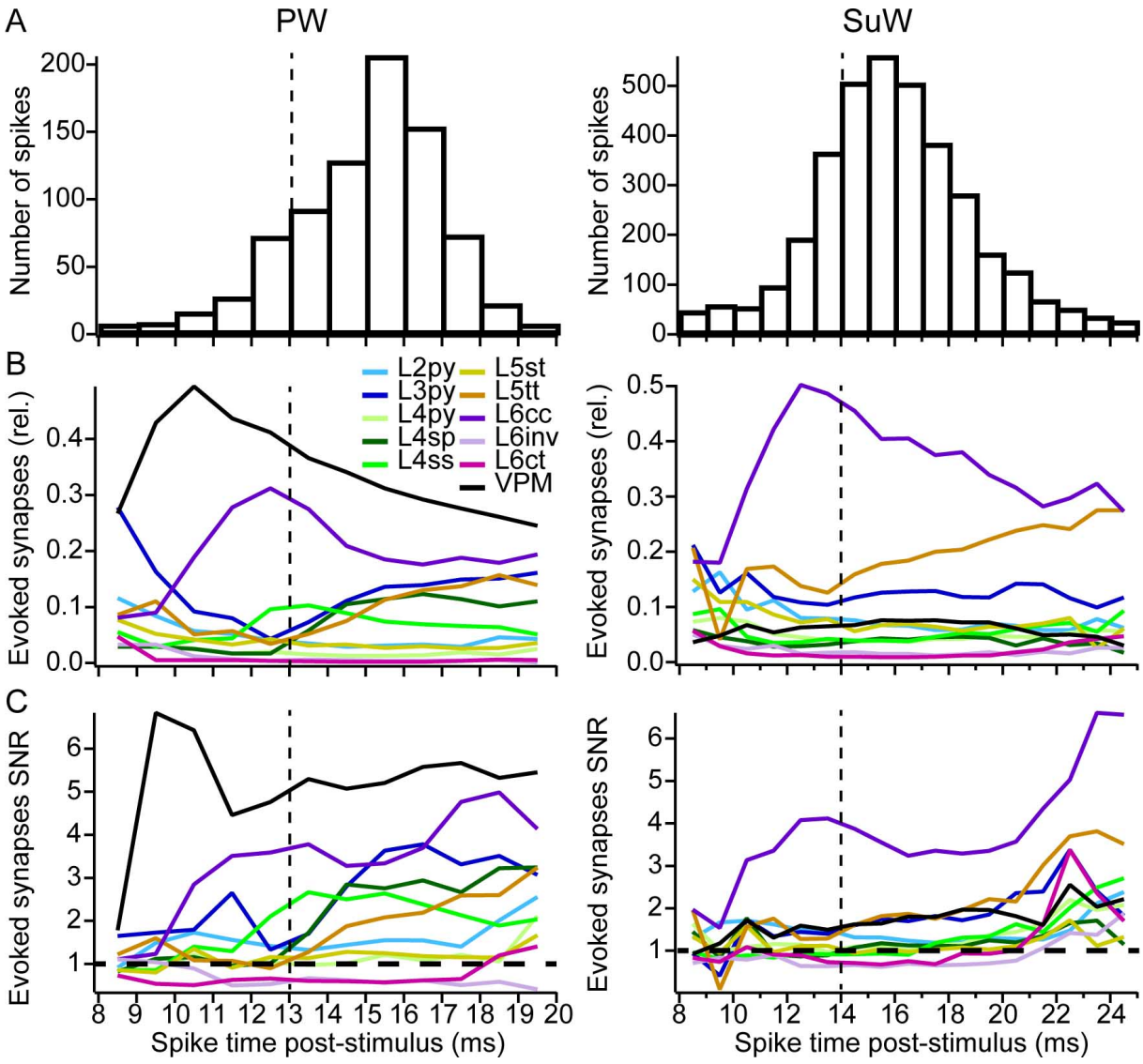

Figure 3.34: Reverse correlation of active synapses. (A) Number of trials with spikes in 1ms time bins after PW deflection (left) and deflection of eight SuW (right). Bins between 20-25ms after PW deflection contained only one spike and were excluded from statistical analysis. (B) Relative contribution of different cell types to the total number of evoked excitatory synapses as a function of spike time. The number of evoked synapses of each cell type is accumulated up to the spike time and averaged across trials. (C) SNR of evoked synapses of different cell types as a function of spike time. SNR is calculated as mean/SD across trials and whiskers of the accumulated number of evoked synapses per trial. Horizontal dashed line indicates SNR of 1, i.e. values around and below this line are unreliable across trials and whiskers. Vertical dashed lines indicate time periods with almost exclusive synaptic input from VPM and L6cc, and time periods with additional synaptic input from other excitatory cell types.

heterogeneous presynaptic populations including L3py and L4 cell types, and other L5tt (Figure 3.34 B, left). This is reflected in the SNR of different excitatory cell types at different spike times (Figure 3.34 C, left). VPM synapses are very reliable across the entire early phase, followed by L6cc. The other intracortical cell types only contribute reliably to the number of evoked synapses between 13-20ms post-stimulus. After SuW deflection, a qualitatively similar picture emerges. The number as well as the reliability of evoked synapses is dominated by L6cc up to 14ms post-stimulus. In the later phase, the contribution of other L5tt increases, followed by evoked synapses from L3py and VPM. These are less numerous, but equally reliable as L5tt synapses (Figure 3.34 B and C, right).

This analysis suggests that the earliest spikes in response to PW deflection (i.e., up to 13ms post-stimulus) are evoked by synapses from VPM and L6cc, while the earliest spikes after SuW deflection (i.e., up to 14ms post-stimulus) are evoked by synapses from L6cc. To test this hypothesis, I repeated the simulations of PW and SuW deflections using a model in which the evoked response of L6cc was inactivated, and a model in which the evoked response of L5tt was inactivated (Figure 3.35).

Inactivation of the evoked response of L5tt (purple trace) revealed that the early response (i.e., latency and amplitude of the PSTH up to the dashed line) after deflection of the PW and all SuW was largely unaffected. In contrast, inactivation of the evoked response of L6cc (orange trace) nearly completely abolished the early response after PW and SuW deflection. Specifically, the response latency after deflection of the PW (C2) and two SuW (C1 and D1) was longer, and the amplitude was reduced. The response after deflection of the remaining six SuW was completely abolished.

3.2.11 Explanation of mechanism underlying PW and SuW responses of L5tt

In the previous section, I showed statistically that after PW and SuW deflections, specific presynaptic cell types are reliably providing excitatory synaptic input to L5tt across trials within a window of opportunity that is whisker-specific, but around 10-15ms post-stimulus. In case of PW deflection, these were thalamic inputs from VPM, followed by

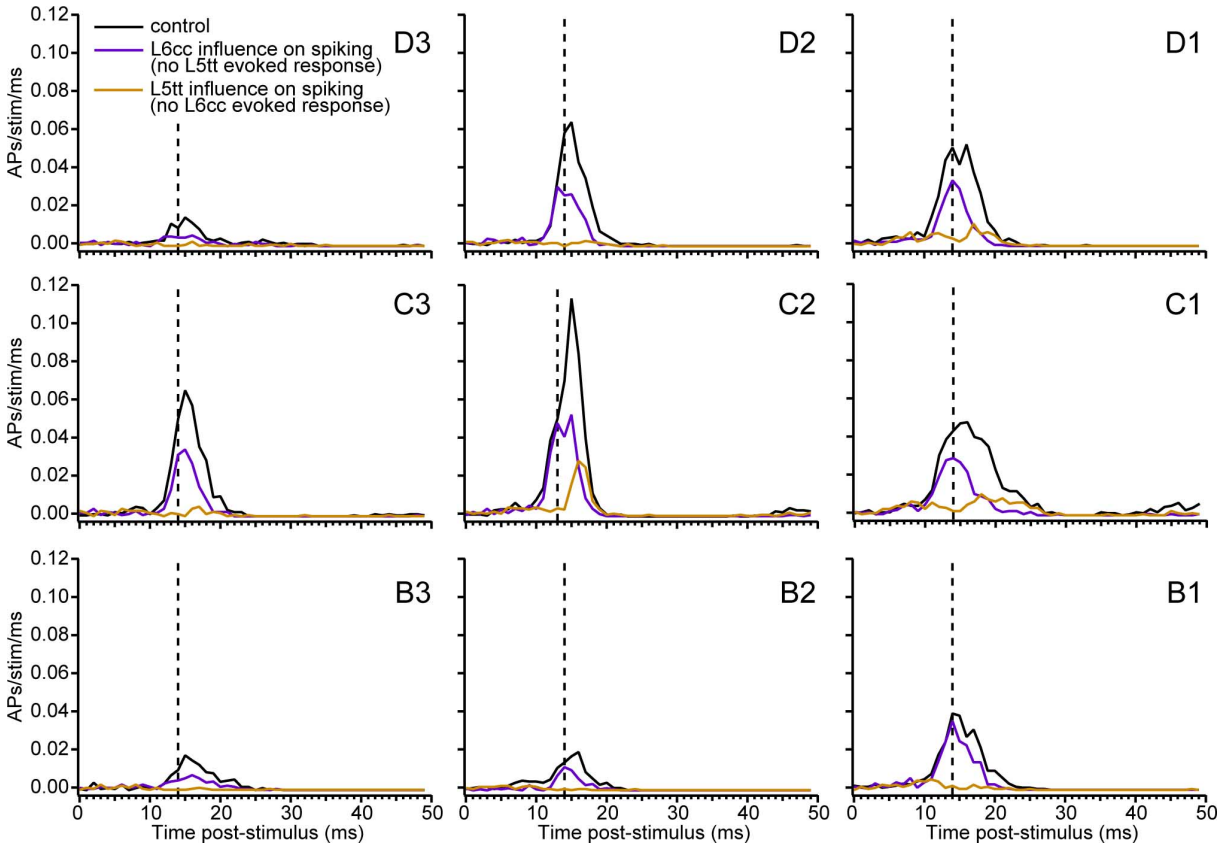

Figure 3.35: Influence of L6cc and L5tt on amplitude and time course of L5tt whisker-evoked responses. Average PSTH of nine anatomical models with 1ms resolution for deflection of PW (C2) and eight SuW. Black traces are average across 1800 simulation trials each (see Figure 3.29). Purple trace: average across 1800 simulation trials each, evoked response of presynaptic L5tt inactivated. Orange trace: average across 1800 simulation trials each, evoked response of presynaptic L6cc inactivated. Dashed line: Separation between two phases of evoked synaptic input patters from Figure 3.34.

L6cc and L4ss. In case of SuW deflections, the only cell type providing reliable excitatory synaptic inputs were L6cc. Direct thalamic input from VPM to L5tt after PW deflections has been demonstrated previously [32]. In contrast, the specific pathways and mechanisms underlying responses of L5tt after SuW deflections have so far not been identified. The present modeling and simulation results suggest the following synaptic mechanism: First, L6cc in all columns have largely PW-specific responses, i.e. they respond most strongly to deflections of the whisker aligned somatotopically with the barrel column that their soma is located in (see also Figure 3.8). Second, the temporal profile of the PW deflection response of L6cc to sensory-evoked input is highly synchronous and with short latency (i.e., $\sim 9 - 12$ms post-stimulus, Figure 3.10), most likely due to direct feed-forward

excitation from VPM [31]. Third, the intracortical axon projections of L6cc have a wide horizontal spread, i.e., they innervate nearly entire vS1 (Figure 3.7). Hence, L5tt in the PC receive synaptic input from L6cc in all surrounding barrel columns (see also Figure 3.22). After deflection of a SuW, L6cc in the somatotopically aligned barrel column (i.e., in a SC relative to the L5tt) are activated synchronously and with short latency. These L6cc then activate synapses on the basal dendrites of L5tt in the PC and cause short latency spiking responses.

3.2.12 Experimentally testable prediction of the SuW response mechanism

The identification of L6cc as the cell type underlying SuW responses of L5tt allows to make an experimentally testable prediction. I propose to measure the receptive field of L5tt after deflection of a second-order surround whisker (e.g. the response of a L5tt neuron located in the C2 column after deflection of the E2 whisker). The horizontal axonal extent of L6cc (but not L5tt) is large enough that L6cc located in the E2 column may innervate L5tt located in the C2 column (Figure 3.36 A). Specifically, the L5tt neuron models located in the C2 column receive on average 159 ± 69 excitatory synaptic inputs from neurons located in the E2 column. Of those, 116 ± 47 synapses originate from L6cc, 7 ± 9 from L3py, and none from VPM or L5tt. Hence, a simple estimate based on the response probability of L6cc to PW deflections suggests that there should be $\sim 13 \pm 5$ active synapses from L6cc located in E2 on the L5tt model after simulated deflection of the E2 whisker. Based on the previous analysis of the excitatory synaptic input required to trigger L5tt spiking, this should be sufficient to occasionally generate E2 whisker deflection-evoked spikes.

Simulation of E2 whisker deflection revealed that these L6cc synapses are indeed sufficient to increase the spiking output of the L5tt model (Figure 3.36 B). Specifically, the increase in spiking was 0.13 APs in 50ms post-stimulus. Inactivation of the sensory-evoked response of the L6cc population in the simulations completely abolished the increased spiking response. Thus, if one or several L5tt with responses to deflection of the E2 whisker can be identified, subsequent pharmacological deactivation of neurons in the

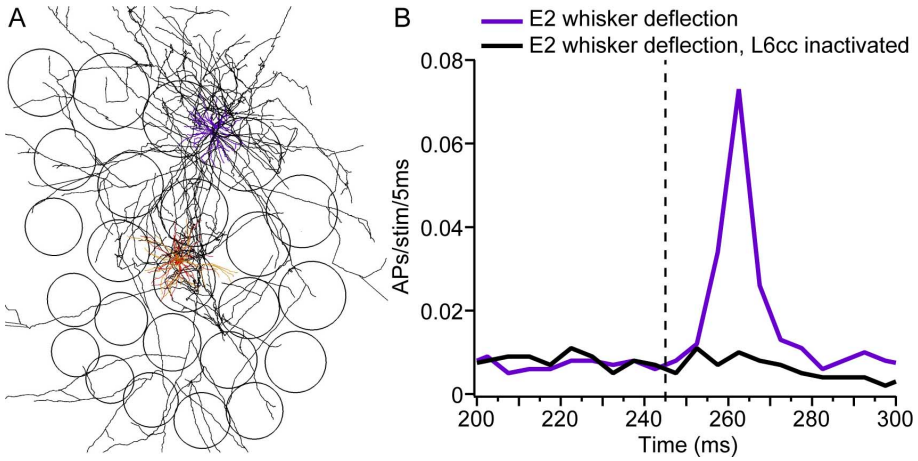

Figure 3.36: Experimentally testable prediction of L6cc synaptic drive underlying SuW responses of L5tt. (A) Tangential view of the barrel field (black circular contours outline individual barrel columns). L6cc located in the E2 column (purple: dendrites, black: axon) have an axonal extent that extends horizontally across the entire vibrissal cortex and can thus innervate L5tt located in the C2 column (center; red: soma and basal dendrites, orange: apical dendrite). (B) Simulated E2 whisker deflection leads to a measurable response in the L5tt model located in the C2 column. Inactivating the whisker-evoked response of L6cc in the model completely abolishes the response of the L5tt model to the same stimulus. Dashed line: whisker deflection.

infragranular layers of the E2 column should abolish these responses. Because L5tt located in the C2 column hardly receive other excitatory inputs than L6cc from the E2 column, this would confirm that indeed L6cc are the cell type providing the most important synaptic input underlying the SuW responses of L5tt.

Chapter 4

Discussion

In this thesis, I presented a new approach for simulations of sensory-evoked signal flow in models of cortical neurons that are fully constrained by experimental data. I developed the necessary tools that allow combining anatomical and functional data from different experiments. After objective classification using morphological properties, I was able to correlate structural and functional properties of different neuronal cell types. To reflect the variability within these hence defined cell types, the model constraints take the form of statistical distributions. During simulations, Monte-Carlo sampling from these distributions is used to explore the parameter space of possible functional connectivity patterns between cortical neurons. Each of these samples is interpreted as an individual trial, and the integration of the resultant spatiotemporal synaptic input patterns is simulated numerically in biophysically detailed neuron models. The simulation results can be compared with various in vivo measurements of functional responses, such as membrane potential or spike recordings at the soma, or calcium imaging of the activation of putative individual spines. Because the model parameters are fully constrained by experimental data and the simulation results match functional measurements in vivo, the model may be regarded as functionally realistic and thus allow to identify mechanisms underlying the resulting responses, followed by specific predictions that are testable in experiments. This approach allowed to my knowledge for the first time to determine the complete synaptic input pattern to cortical neurons during ongoing activity and sensory-evoked input. I determined the functional synaptic input patterns underlying subthreshold responses of L2py neurons, and the contribution of excitatory and inhibitory inputs to the

mean and variability of this response. Further, I was able to identify a specific pathway from L6cc neurons underlying SuW spiking responses of L5tt, resolving a general question about the origin of broad receptive fields of this cell type.

4.1 Anatomically realistic network model of rat vS1

One major prerequisite for development of these network-embedded models was to determine the structural connectivity patterns underlying signal flow after passive whisker touch in the anaesthetized animal (i.e., the thalamocortical and intracortical part of the lemniscal pathway of the vibrissal system). To do so, I developed an anatomically realistic statistical network model, based on detailed reconstruction of network geometry, cellular distributions, a sparse but representative sample of dendrite and axon morphologies, and a statistical model of synaptic connectivity between neurons in this network model. As a first prerequisite to building such an average network model, it is necessary to determine if the average network structure is actually well-defined, i.e., if geometry, cellular distribution and neuron morphology are reproducible across animals. Previously, I found that the 3D variability of cortex geometry in rat vS1 is $89\mu m$, i.e. a cube with side length of $\sim 50\mu m$ [68]. The observed variability of the distribution of neuron somata distributions at this resolution is $\sim 10\%$ (i.e. avg SD over the mean neuron density). Because the error of the automated neuron counting method has previously been determined to be 4% [70], the observed variability likely reflects the true inter-animal variability. Hence, the variations in organization of neuron somata along the column axis (Figure 3.3) and in the horizontal plane (Figure 3.4) reflect organizational principles of rat vS1. Finally, the set of all excitatory and inhibitory neuron morphologies contained reconstructions in all $50\mu m$ steps along the vertical barrel column axis, and in all $50\mu m$ steps along the radial coordinate to the barrel column axis. This revealed location-specific differences in neuron morphologies (e.g. the apical tuft dendrite of L3 pyramidal neurons always innervates L1, regardless of soma location) and the spatial distribution of different cell types (e.g. L4ss and L4sp are found inside the barrel column in the radial dimension, but not in the septum between barrel columns) in line with previous studies [71, 127].

Other approaches to reconstruction of neural network models. Suggestions for

reconstruction of such network models include dense reconstruction of synaptic connectivity at electron-microscopic (EM) resolution (e.g., [150, 83]), or extrapolation of connectivity measurements between many pairs of neurons, assuming uniform composition of cortical layers and columns (e.g., [1]).

EM reconstruction of neural circuitry is currently limited to tissue volumes with side lengths of few hundreds of micrometers [151]. In contrast, the "minimally required circuit" for simulation of passive whisker touch in rat vS1 includes all neurons immediately postsynaptic to thalamocortical input, as well as their postsynaptic targets. Spatially, this circuit can be defined by the volume of the axon projection patterns from a single barrel column (intracortical or IC-unit [56], Figure 4.1).

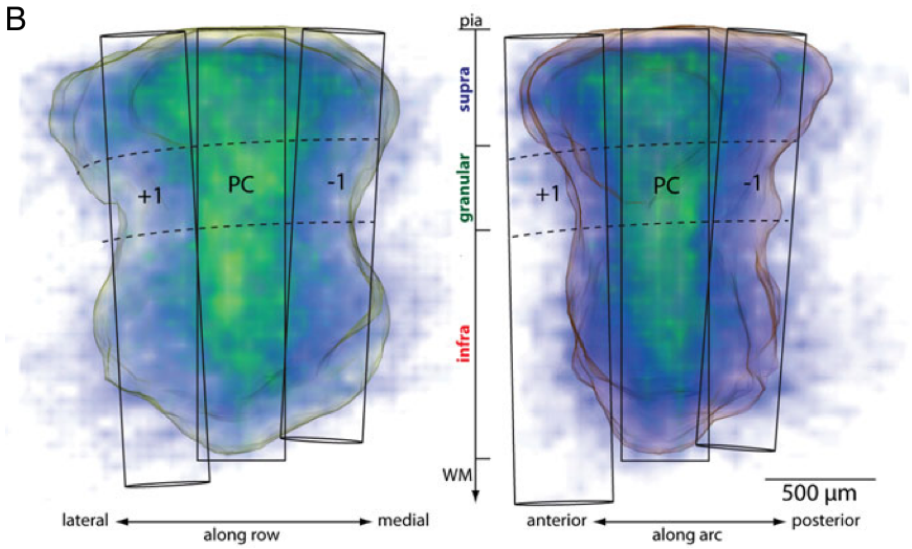

Figure 4.1: The IC-unit of vS1. 3D bouton density distribution from axons of all reconstructed excitatory neurons located within a cortical column, viewed along the row (left) and arc (right). The transparent surface area comprised the bouton distribution thresholded at 5% maximal density, revealing that IC axons from a single column activate a volume that comprises $\sim 3 \times 3$ columns and the septa between them. Figure adapted from [56].

Thus, the volume of interest is at least as big as an array of 3x3 barrel columns, i.e. on the order of $1mm^3$. Further, even assuming that a dense reconstruction of such a volume is available, it would have to be repeated several times to identify features of the circuitry that are common across animals, i.e., essentially again creating a statistical connectome. Finally, the in vivo spiking responses of the reconstructed neurons would remain unknown, requiring comparison with sparse samples of in vivo recorded and re-

constructed neurons, as presented here.

The second approach, as pursued for example by the Blue Brain Project [84], relies on the assumption that data from many different experiments can be combined and extrapolated by assuming that the basic cellular composition and circuitry of neocortex is stereotypical within and across brain areas. Based on the present results, for example regarding the non-uniform cellular organization even within a single brain region, I would argue that this assumption does not hold in general. Based on a very simple example, it is possible to show that the assumption of cellular uniformity alone leads to quantitatively different results from the detailed reconstruction presented here. Using NeuroNet, I estimated the average number of active synapses to the population of L5tt located in the C2 column after deflection of each SuW using the dense network model presented in section 3.1.4. As described in the Methods section 2.5.2, I determined the average functional connectivity to each L5tt located in the C2 column, and then calculated the average across the population of L5tt. The resultant average number of active excitatory synapses to the L5tt population after deflection of each SuW correlated significantly with the respective response probabilities ($r=0.73$, $p=0.04$). However, making the same estimate using the assumption that cortical columns are uniform structural units composed of the same number of neurons [1, 152], results in lower correlation ($r=0.57$, $p=0.14$). Although this is a very simple model, it seems unlikely that a biophysically detailed simulation based on these incorrect assumptions would result in functionally realistic responses as presented above. Therefore, an accurate and precise reconstruction of the anatomical circuitry as presented here was key to detecting the pathway and synaptic mechanism underlying SuW responses of L5tt.

Hence, the remaining questions about the validity of the present approach for building a dense statistical connectome are:

1. How representative is the sparse sample of neuron morphologies in terms of the biological variability of each cell type?

2. How does a statistical network model represent specific connectivity between cortical neurons?

3. Does this high precision reconstruction of network anatomy have functional conse-

quences?

1. Representative sample of neuron morphologies. I investigated the number of axon morphologies required to represent morphological variability within a cell type during the analysis of thalamocortical connectivity of the D2 barrel column (Figure 3.15 F). Systematic variation of the number of axon morphologies used to statistically measure network connectivity revealed that about 5 axon morphologies are required to capture the mean and variability of cell type-specific connectivity. For nearly all excitatory and inhibitory cell types, the sample of morphologies comprised at least 5 reconstructions (L4py: n=4, L6inv: n=4). To complement this analysis, I compared the set of reconstructed L5tt dendrite morphologies used in this study (n=16) with a set of L5tt dendrite morphologies (n=18) reconstructed in a different study (collaboration with Gerardo Rojas Piloni and Mike Guest, Max Planck Florida Institute). I performed a principal component analysis (PCA) of the combined set of L5tt dendrite morphologies using the 21 morphological and topological features used for assignment of excitatory cell types (Figure 4.2).

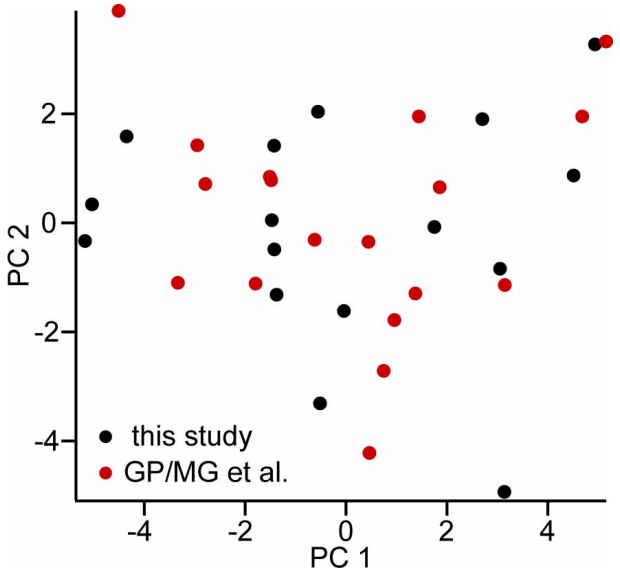

Figure 4.2: Morphological variability of L5tt in a limited sample. First two principal components (PC) of 21 morphological features of a combined data set of 34 in vivo labeled L5tt dendrite/soma reconstructions. In addition to all the L5tt soma and dendrite morphologies used in the present study (from [56]), doubling of the sample size does not increase the variability of the sample.

The two data sets (labeled in black and red, respectively) are completely overlapping in terms of mean and variability of the most important morphological features. Thus,

doubling the sample size for the cell type with the most complex dendrite morphology in rat vS1 had no effect on the statistical distribution of morphological features. This suggests that the sample sizes of the axon and dendrite morphologies of different cell types are sufficient to capture not only the average structure of networks in rat vS1, but also their biological variability.

2. Validity of statistical network model. As described in detail in section 2.4, I developed a quantitative version of "Peters' Rule" to determine synaptic connectivity between neurons based on structural overlap of axons and dendrites within the context of the dense network model. Intuitively, this method is based on determining all presynaptic boutons and all postsynaptic target sites on dendritic spines, dendritic shafts and neuron somata in entire rat vS1. Then, the 3D distribution of axons, dendrites and somata at the resolution of the dense network model of rat vS1 ($50\mu m$) is used as a constraint to determine which neurons can in principle connect to another. In the last step, the probability of synaptic connections between pairs of neurons is determined with respect to all other potential connections allowed in the same volume, assuming only independent synapse formation.

This quantitative version of Peters' Rule results in connectivity measurements that match (sparse) experimental measurements from the level of individual synapses to paired recordings. Further, the resulting connectivity is not random, but displays specific properties at various scales that so far have remained puzzling. For example, different spatially intermingling cell types in L5 receive different amounts of thalamocortical input from VPM ([32], see Figure 3.15), largely due to different morphology of their basal dendrites, which receive the majority of thalamocortical synapses [29, 31]. Conversely, L5tt neurons receive specific subcellular distributions of synaptic input from presynaptic neurons of different cell types, for example in their apical oblique and tuft dendrites (see Figure 3.23). Hence, the different axon projection patterns of excitatory cell types described in section 3.1.3 result in specific innervation patterns of postsynaptic neurons at a resolution of $50\mu m$ which is captured by the statistical network model described in this thesis. Further, the dense network model allows investigating variability of connectivity within cell types, for example depending on the specific soma location and/or dendrite morphology of the postsynaptic neuron [31]. Commonly, connectivity measurements in neural circuits

are expressed as a probability of connection between cell types (e.g., [153]). In contrast to sparse experimental measurements, the dense network model allows investigating the influence of the specific soma location and/or dendrite and axon morphology of pre- and postsynaptic neurons on connectivity, i.e. it is possible to describe connectivity beyond average connection probabilities [89]. For example, in collaboration with Itamar Landau and Haim Sompolinsky (Hebrew University, Jerusalem), I have been working on developing a simplified statistical description of connectivity and its variability within the dense network model. This allows analytical and numerical investigations of the effects of heterogenous connectivity patterns on network dynamics.

Nonetheless, a statistical network model as presented here cannot be used to discover specific connectivity based on principles beyond network geometry, cellular distribution and dendrite and axon morphologies. For example, certain inhibitory interneurons have been shown to exclusively target the axon initial segment of pyramidal neurons [134]. Further, paired recording and subsequent reconstruction of pairs of neurons in vitro has revealed that connections between nearby neurons (i.e., soma distances within $\sim 100\mu m$) in cortex usually consist of two or more synapses (e.g., [120, 140]), which may indicate underlying principles beyond independent synapse formation. However, these observations could in turn be used to investigate the resultant effect on cell type- and location-specific connectivity within the present dense network model. For example, given the same total number of synapses in the dense network model, the assumption of non-independent synapse formation (i.e., at least two synaptic contacts per connection) may result in lower cell type-specific connection probabilities than observed experimentally [84]. Hence, the present network model could be used to determine which previously suggested principles of intracortical connectivity are in line with other experimental observations.

3. Functional relevance of detailed anatomical network model. The simulation results revealed that it was in fact necessary to perform detailed 3D reconstruction and registration of neuron morphologies to the average network model.

First, when investigating the effect of L1 inhibitory synapses on the sensory-evoked responses of L2 pyramidal neurons, I discovered that their precise location at the distal apical tuft dendrites leads to shunting of dendrites without affecting the average membrane potential at the soma. If the subcellular resolution of the network assembly process

was not as high as $50\mu m$ (as determined by the biological variability of the geometry of rat vS1), but, for example, $150\mu m$, then it would not have been possible to detect that these inhibitory synapses are only located on dendrites more than $100\mu m$ away from the soma. In turn, during the network assembly process, L1 inhibitory synapses would have been placed more proximal to the soma. There, the shunting effect of these synapses would directly affect the membrane potential at the soma, and the simulation results would not have correctly predicted the effect measured experimentally (see also Figure 3.18).

Second, during analysis of the L5tt neuron model, I discovered that the simulated responses of the model closest to the location where the morphology used for simulations was located in the brain after registration matched the actual responses of this neuron recorded in vivo. This was especially remarkable because the model was never optimized with respect to these specific responses. Hence, understanding of the in vivo responses of individual neurons using the present method of network-embedded simulations may be possible, but requires both the complete reconstruction of the in vivo labeled dendrite morphology of the neuron, as well as knowledge of the precise location of the neuron in the network (e.g. using registration based on anatomical landmarks). This hypothesis could be tested by using the same network model to simulate the responses of other in vivo recorded neurons at their registered location in the network.

4.2 Identification of previously unknown cortical pathways

The combination of the dense network model with functional responses of different cell types to sensory-evoked input resulted in cell type- and stimulus-specific functional connectivity configurations, i.e. spatiotemporal synaptic input patterns, to the simulated postsynaptic neurons.

Simulation of these very heterogeneous input patterns to the L2py neuron model revealed that the subthreshold representation of SuW deflection is nonetheless robust across trials. Together with my collegues, I was able to show that this effect is at least in part due to

distal inhibition of apical tuft dendrites by L1 IN synapses. Despite recent interest in the function of L1 INs [102, 135, 136], why has this effect not been discovered before? Using sensitivity analyses of the network-embedded model of L2py, I was able to show that the effect (i.e., reduction of PSP SD across trials) is caused by on average 5 L1 IN synapses during each trial. Simulation of the model revealed that the effect further depends on the timing of L1 IN synapses with respect to excitatory inputs, the relative location of these synapses (i.e., inhibitory synapses should be located distally to excitatory synapses) and the absolute distance of L1 IN synapses to the soma - but not, for example, on the strength of inhibitory synapses. In the previously mentioned studies, connections between L1 INs and L2py neurons have been described, but their function remained unknown because they were studied in tissue slices, i.e., without simultaneous excitatory synaptic inputs to the dendrites of the L2py neurons. Thus, the effect of activating L1 IN synapses could only be revealed if in vivo-like synaptic input patterns of presynaptic excitatory and inhibitory cell types coincide, as for example in the present network-embedded model.

Using the same network-embedded modeling and simulation approach, I estimated the pattern of synaptic inputs impinging onto L5tt during up-states (i.e. ongoing activity) and after whisker deflection of the PW and eight SuW. The simulation results of whisker deflection-evoked responses of L5tt show that synaptic inputs from L6cc are a major determinant of the spiking response of this cell type both after PW and SuW responses. Why has this major pathway in cortex gone unnoticed so far? In fact, there is evidence in previous studies that L6cc display strong short-latency responses after whisker deflection and relay this information in horizontal directions. For example, de Kock et al. [26] describe that L6 neurons display the earliest response times of all excitatory cortical neurons. However, because all identified L6 neurons were grouped into one cell type, the strong response of L6cc was averaged with the non-responding L6ct. Further, Constantinople and Bruno [32] showed that L5tt respond to PW deflections even after pharmacological inactivation of the "canonical circuit" from thalamorecipient neurons in L4 to L3 and subsequently to L5tt. This is completely in line with the present simulation results, which suggest that synaptic inputs from neurons located in L3 and L4 modulate PW- and, to a lesser degree, SuW-evoked spiking responses after activation of L5tt by

L6cc. However, in contrast to the conclusion by the authors that thalamocortical input directly drives L5tt, the simulation results suggest that it is actually the combination of VPM and L6cc inputs that triggers the early spiking response of L5tt. In another recent study, Velez-Fort et al. [154] showed that L6cc in mouse primary visual cortex display short-latency sensory-evoked responses and wide horizontal axon projection patterns, suggesting that this pathway may be a general organizational feature of sensory cortices. Previous models of SuW responses of L5tt in rat vS1 had concluded that the synaptic origin is most likely from intracortical sources, but were not able to identify the precise origin. Work led by Kevin Fox [39] showed that broad pharmacological inactivation of cortical neurons, followed by local reactivation of neurons located in L5, largely abolishes SuW receptive fields, but leaves PW responses unaffected. The authors concluded that PW responses are most likely driven by thalamocortical inputs, while SuW responses are due to synaptic drive from L3 and L4 neurons. However, broad inactivation of cortex also affects L6cc. Hence, these results are in line with the present model of L6cc underlying SuW responses in L5tt. Finally, Kweygir-Afful et al. [37] manipulated input to thalamocortical projection neurons in VPM such that their SuW deflection responses were completely abolished, i.e., they only displayed PW deflection responses. However, SuW deflection responses of neurons located in the infragranular layers of the somatotopically aligned barrel column in vS1 remained unaffected, i.e., cortical neurons still responded to SuW deflections. This can also be explained by the present model: The L6cc synapses giving rise to the SuW responses of L5tt originate mostly from L6cc located in the corresponding SC, which in turn have largely PW-specific responses (see also Figure 3.10). These PW-specific responses likely derive from PW-specific thalamic inputs [31], and are therefore unaffected by manipulation of the SuW responses of VPM neurons.

4.3 Structural and functional pathways in sensory cortex

The identification of these new pathways using the present approach of network-embedded modeling raise the more general question about the relationship between structural con-

nectivity, functional connectivity and functional pathways in neural networks. For example, in the first 50ms following PW or SuW deflection, the number of active synaptic inputs onto the L5tt neuron model increases to $\sim$ 1500 and $\sim$ 1000, or about 5% of all synapses, respectively, which results in an increased output in the number of spikes of 0.4 and 0.2 spikes per trial, respectively. In contrast, typical estimates of the number of excitatory synaptic inputs required to trigger spiking in cortical L5tt neurons are on the order of 100-200 synapses [155]. The reason that this substantially larger number of synaptic inputs leads to increased spiking output in less than 50% of all trials is that strong and synchronous feed-forward inhibition has to be overcome by strong and synchronous excitatory inputs in a certain window of opportunity ([44], see also Figure 3.30). I found that within this window of opportunity, there were on average 21 additional excitatory inputs in trials with spikes after a PW deflection compared to trials without spikes, and 13 additional excitatory inputs in trials with spikes after a SuW deflection compared to trials without spikes.

However, because L5tt receive a highly heterogeneous pattern of synaptic inputs after a whisker deflection, which changes from one trial to the next, it is not possible to establish a direct causal relationships between individual synaptic inputs and the spiking output of the model. Instead, statistical analysis of functional connectivity configurations to L5tt revealed that thalamocortical neurons in VPM and L6cc provided reliable synaptic input across trials after PW deflections and L6cc after SuW deflections in the earliest phase after sensory input.

Similarly, as described above, the observed reduction of the PSP variability of L2py is caused by only a small number ($\sim$ 5) of L1 IN synapses, which are however reliably activated across trials. Further, the effect of these synapses on the PSP variability of L2py depends on their spatial location and temporal activation with respect to excitatory synapses.

Hence, a specific pathway (i.e., connection from a specific presynaptic cell type) underlying responses of any postsynaptic cell type should not be identified solely based on its connection strength, for example as measured by the number of synapses, or the synaptic efficacy measured at the soma, or in isolation from other excitatory and inhibitory synaptic inputs that are active at the same time. This criterion would have identified L3py

as the major pathway providing excitatory input to L5tt (i.e., the "canonical circuit" of neocortex [156], see also Figure 3.23), and would largely have underestimated the effect of L1 IN synapses on L2py, which relies on the interplay of excitatory and inhibitory inputs within the dendrites. Rather, the present approach of creating stimulus-specific functional connectivity configurations allows to investigate (1) whether the number of active synapses in a pathway increases before a spike and/or PSP response in the postsynaptic neurons, (2) whether synaptic inputs in this pathway are activated reliably across trials, and (3) what the effect of the interaction with other simultaneously active excitatory and inhibitory synapses is.

I would therefore argue to analyze cortical circuits (or neural networks in general) not in terms of serial pathway diagrams, where signals flow from one cell (or group of cells) to the next, but rather in terms of dynamically changing, stimulus-specific functional connectivity. Despite the resulting complexity and heterogeneity of functional connectivity patterns, it is possible to identify organizational principles underlying these patterns across trials. These robust organizational principles can then be regarded as functional pathways, for example underlying spiking responses of a certain cell type.

4.4 Outlook

The present thesis can be regarded as a proof-of-principle that across-scale modeling of sensory-evoked responses can lead to new insights about mechanisms underlying sensory-evoked signal flow. However, the results presented in this thesis are based on passive deflection of single whiskers in anaesthetized rats. The present anatomically realistic network model of rat vS1 presents a starting point to extend the approach of network-embedded modeling to different behavioral states and more complex stimuli, such as touch of an object by a rat that is actively moving its whiskers. Importantly, the structure of the network model (i.e., the number and distribution of synapses) most likely remains unaffected when considering the transition from the anaesthetized to the awake, whisking state. Instead, functional connectivity in the network model is influenced by additional long-range pathways to rat vS1.

First, whisker movement-related pathways, for example from vibrissal motor cortex [157]

or POm thalamus [158], may provide additional functional input to neurons in vS1. To integrate these pathways into the present model, the activity of neurons in POm and vibrissal motor cortex during whisker movement should be measured. The projection patterns of these long-range pathways could be reconstructed either by labeling and reconstruction of individual axon projections to vS1, followed by registration to the average model of rat vS1, as was done for thalamocortical input from VPM [73]. As an alternative, presynaptic populations could be labeled using virus injections to label all boutons of these populations [159, 30, 90], followed by registration of bouton distributions to the average model of rat vS1. Functional connectivity to different postsynaptic cell types can then be determined as described in this thesis.

Second, during awake states, activity of neurons in cortex is influenced by release of neuromodulators such as acetylcholine or epinephrine [160, 149, 161, 162]. These can act directly on the postsynaptic neurons, for example by binding to specific ligand-gated ion channels and changing the excitability of neurons and efficacy of synapses [160, 162], and/or indirectly by changing the activity of specific presynaptic populations, for example inhibitory interneurons [163]. The effects of neuromodulators acting directly on the simulated postsynaptic neurons have to be determined experimentally for each postsynaptic cell type, and can then be incorporated by modification of the biophysical models used during simulations [164].

The effect of neuromodulators on the activity of presynaptic neurons can be measured during different behavioral states of the animal. For example, the spontaneous activity of a subset of all reconstructed excitatory neurons (see section 3.1.3) has been measured after animals awoke from anaesthesia, and were either non-behaving or rhythmically moving their whiskers. A few cell types displayed increased spontaneous spiking activity in the awake state [31]. Additionally, when animals were awake and whisking, ongoing spiking activity of L5st was not only increased, but the timing of individual spikes was correlated to whisker movement [165]. These effects can be incorporated into the network-embedded modeling approach by activating presynaptic neurons based on activity measurements in the awake and/or whisking state, thus affecting only the functional connectivity between different presynaptic cell types and the simulated postsynaptic neuron.

Hence, by including neuromodulation of local circuits, as well as additional long-range

circuits from other cortical and subcortical regions, it may be possible to identify mechanisms underlying responses of cortical neurons to different stimuli during different behavioral states using the present approach of network-embedded simulations.

4.5 Conclusion

The major finding of this thesis was that it is possible to develop anatomically and functionally realistic models that allow predictive simulation of (simple) brain functions. A combination of biophysical models of signal transmission and integration between and within neurons, with experimental constraints on the morphology, connectivity and activity of different types of neurons, allowed simulations of activity that matched in vivo measurements. Because the models were fully constrained, this indicates that they were a realistic representation of signal flow within neurons in living animals, and allowed subsequent investigation of the interaction of cellular and network mechanism underlying the responses of these neurons.
In the course of this study, I found that the following requirements have to be met to allow for development of such models:

- *Identification of cell types.* This is the most important conceptual simplification in the model. Cell types have to be identified using objective criteria, for example morphological features, as used here. Further, these cell types have to allow correlation between structural and functional data from different experiments, e.g. measurements of sensory-evoked responses or properties of synaptic connections. This could be done by morphological identification of each functionally characterized neuron, as was done for the data presented in this thesis.

- *Precise anatomical model.* Reconstruction of synaptic connectivity within the studied system has to be performed at a resolution determined by the anatomical variability between different animals. This allows studying the organizational principles within a brain region, as well as sources of variability in connectivity. The key assumption at this point is that the average structure of these circuits does not change between animals, which I could show for the dense network model of rat

vS1. This has the following implications: (1) the model cannot be regarded as an actual brain, but only as a model representing common features of the cellular and synaptic organization of a brain region; (2) investigation of processes with dynamical changes in the structure of circuits (e.g. developmental or disease processes) require reconstruction of an average circuit model at each time point to be investigated; (3) small details in the structural organization lead to measurable functional differences, and hence the model is in general species- and brain region-specific and has to be constructed for each brain region investigated.

Based on the approach developed in this thesis, I was able to identify two novel mechanisms underlying widely investigated observations of signal flow in cortical circuits that have not been understood until now. While it might not have been impossible, it would certainly have been more difficult to dissect these mechanisms without precise predictions based on simulation results of the model. However, to get to this stage has required building on work started about 10 years ago. It remains to be seen if such an effort is easily repeatable and transferable to other systems and neuroscientific questions, but the necessary concepts and tools are now available, and therefore adaptation to new problems may proceed faster.

Appendix A

List of abbreviations

2p Two-photon

AHP After-hyperpolarization

AMPAR α-amino-3-hydroxy-5-methyl-4-isoxazolepropionic acid receptor

AP Action potential

BAC Backpropagating action potential calcium spike

bAP Backpropagating action potential

BB/BC/BT Barrel bottom/center/top

caudal towards the tail of the animal

dorsal towards the back of the animal (i.e., informally: upwards)

EPSP Excitatory postsynaptic potential

GABA γ-Aminobutyric acid

IN Inhibitory interneuron

In silico Computer-based numerical studies

In vitro "In glass", i.e., experiments performed in the laboratory

In vivo Experiments performed in the living organism

IOI Intrinsic optical imaging

IPSP Inhibitory postsynaptic potential

ISI Inter-spike interval

L1/2/3/4/5/6 Cortical layer 1/2/3/4/5/6

L2py/L3py/L4py L2 pyramidal neuron/L3 pyramidal neuron/L4 pyramidal neuron

L4sp/L4ss L4 star pyramidal neuron/L4 spiny stellate neuron

L5st/L5tt L5 slender-tufted pyramidal neuron/L5 thick-tufted pyramidal neuron

L6cc/L6inv/L6ct L6 cortico-cortical pyramidal neuron/L6 inverted pyramidal neuron/L6 cortico-thalamic neuron

lateral towards the side

medial towards the midline

NMDAR N-methyl-D-aspartate receptor

PC Principal column, i.e., barrel column containing a neuron's soma

PN Pyramidal neuron

POm Posterior medial subdivision of the thalamus

PSP Postsynaptic potential

PST Postsynaptic target site

PSTH Poststimulus time histogram

PW Principal whisker, i.e., the whisker that is somatotopically aligned to a neuron's PC

RF Receptive field

rostral towards the nose (i.e., informally: towards the front)

RT Thalamic reticular nucleus

S1/S2 Primary/secondary somatosensory cortex

SC/SuC Surround column, i.e., a column different than the PC

SD Standard deviation

SuW Surround whisker, i.e., a whisker different than the PW

uEPSP/uIPSP Unitary EPSP/IPSP

ventral towards the lower side (i.e., informally: towards the bottom)

VPM Ventral posterior medial nucleus of the thalamus

vS1 Vibrissal part of the primary somatosensory cortex

WM White matter tract

Bibliography

[1] Henry Markram. The blue brain project. *Nature Reviews Neuroscience*, 7(2):153–60, Feb 2006.

[2] Anna Devor, Peter A Bandettini, David A Boas, James M Bower, Richard B Buxton, Lawrence B Cohen, Anders M Dale, Gaute T Einevoll, Peter T Fox, Maria Angela Franceschini, Karl J Friston, James G Fujimoto, Mark A Geyer, Joel H Greenberg, Eric Halgren, Matti S Hämäläinen, Fritjof Helmchen, Bradley T Hyman, Alan Jasanoff, Terry L Jernigan, Lewis L Judd, Seong-Gi Kim, David Kleinfeld, Nancy J Kopell, Marta Kutas, Kenneth K Kwong, Matthew E Larkum, Eng H Lo, Pierre J Magistretti, Joseph B Mandeville, Eliezer Masliah, Partha P Mitra, William C Mobley, Michael A Moskowitz, Axel Nimmerjahn, John H Reynolds, Bruce R Rosen, Brian M Salzberg, Chris B Schaffer, Gabriel A Silva, Peter T C So, Nicholas C Spitzer, Roger B Tootell, David C Van Essen, Wim Vanduffel, Sergei A Vinogradov, Lawrence L Wald, Lihong V Wang, Bruno Weber, and Arjun G Yodh. The challenge of connecting the dots in the b.r.a.i.n. *Neuron*, 80(2):270–4, Oct 2013.

[3] Peters A and Jones EG, editors. *Cellular Components of the Cerebral Cortex*, volume 1. Plenum, New York, New York, 1984.

[4] C Koch. *Biophysics of computation: information processing in single neurons*. Oxford University Press, New York, New York, 1999.

[5] A Hodgkin and A Huxley. A quantitative description of membrane current and its application to conduction and excitation in nerve. *The Journal of Physiology*, Jan 1952.

[6] W RALL. Branching dendritic trees and motoneuron membrane resistivity. *Exp Neurol*, 1:491–527, Nov 1959.

[7] E Kandel, J Schwartz, and T Jessell, editors. *Principles of neural science*. McGraw-Hill, New York, New York, Jan 2000.

[8] C Koch and I Segev, editors. *Methods in neuronal modeling: from ions to networks*. MIT Press, Cambridge, MA, 1998.

[9] K A Hutson and R B Masterton. The sensory contribution of a single vibrissa's cortical barrel. *Journal of Neurophysiology*, 56(4):1196–223, Oct 1986.

[10] V B MOUNTCASTLE, P W DAVIES, and A L BERMAN. Response properties of neurons of cat's somatic sensory cortex to peripheral stimuli. *Journal of Neurophysiology*, 20(4):374–407, Jul 1957.

[11] DH Hubel and T Wiesel. Receptive fields, binocular interaction and functional architecture in the cat's visual cortex. *The Journal of Physiology*, 160:106–54, Jan 1962.

[12] D H HUBEL and T N WIESEL. Receptive fields and functional architecture of monkey striate cortex. *The Journal of Physiology*, 195(1):215–43, Mar 1968.

[13] M Helmstaedter, C P J de Kock, D Feldmeyer, R M Bruno, and B Sakmann. Reconstruction of an average cortical column in silico. *Brain Res Rev*, 55(2):193–203, Oct 2007.

[14] Dirk Feldmeyer, Michael Brecht, Fritjof Helmchen, Carl C H Petersen, James F A Poulet, Jochen F Staiger, Heiko J Luhmann, and Cornelius Schwarz. Barrel cortex function. *Progress in Neurobiology*, 103:3–27, Apr 2013.

[15] Dirk Feldmeyer. Excitatory neuronal connectivity in the barrel cortex. *Front Neuroanat*, 6:24, Jan 2012.

[16] D J Simons. Response properties of vibrissa units in rat si somatosensory neocortex. *Journal of Neurophysiology*, 41(3):798–820, May 1978.

[17] D J Simons. Temporal and spatial integration in the rat si vibrissa cortex. *Journal of Neurophysiology*, 54(3):615–35, Sep 1985.

[18] G E Carvell and D J Simons. Membrane potential changes in rat smi cortical neurons evoked by controlled stimulation of mystacial vibrissae. *Brain Res*, 448(1):186–91, May 1988.

[19] D J Simons, G E Carvell, A E Hershey, and D P Bryant. Responses of barrel cortex neurons in awake rats and effects of urethane anesthesia. *Exp Brain Res*, 91(2):259–72, Jan 1992.

[20] Roxanna M Webber and Garrett B Stanley. Nonlinear encoding of tactile patterns in the barrel cortex. *Journal of Neurophysiology*, 91(5):2010–22, May 2004.

[21] Maik C Stüttgen and Cornelius Schwarz. Psychophysical and neurometric detection performance under stimulus uncertainty. *Nature neuroscience*, 11(9):1091–9, Sep 2008.

[22] Sylvain Crochet, James F A Poulet, Yves Kremer, and Carl C H Petersen. Synaptic mechanisms underlying sparse coding of active touch. *Neuron*, 69(6):1160–75, Mar 2011.

[23] M Armstrong-James, K Fox, and A Das-Gupta. Flow of excitation within rat barrel cortex on striking a single vibrissa. *Journal of Neurophysiology*, 68(4):1345–58, Oct 1992.

[24] E Welker, M Armstrong-James, H Van der Loos, and R Kraftsik. The mode of activation of a barrel column: response properties of single units in the somatosensory cortex of the mouse upon whisker deflection. *Eur J Neurosci*, 5(6):691–712, Jun 1993.

[25] Tansu Celikel, Vanessa A Szostak, and Daniel E Feldman. Modulation of spike timing by sensory deprivation during induction of cortical map plasticity. *Nature neuroscience*, 7(5):534–41, May 2004.

[26] Christiaan P. J de Kock, Randy M Bruno, H Spors, and Bert Sakmann. Layer- and cell-type-specific suprathreshold stimulus representation in rat primary somatosensory cortex. *The Journal of Physiology*, 581(1):139–154, Feb 2007.

[27] C P J de Kock and B Sakmann. High frequency action potential bursts (¿or= 100 hz) in l2/3 and l5b thick tufted neurons in anaesthetized and awake rat primary somatosensory cortex. *The Journal of Physiology*, 586(14):3353–64, Jul 2008.

[28] E L White. Identified neurons in mouse sml cortex which are postsynaptic to thalamocortical axon terminals: a combined golgi-electron microscopic and degeneration study. *The Journal of Comparative Neurology*, 181(3):627–61, Oct 1978.

[29] Leopoldo Petreanu, Tianyi Mao, Scott M Sternson, and Karel Svoboda. The subcellular organization of neocortical excitatory connections. *Nature*, 457(7233):1142–1145, Sep 2009.

[30] Hanno S Meyer, Verena C Wimmer, Mike Hemberger, Randy M Bruno, Christiaan P. J de Kock, Andreas Frick, Bert Sakmann, and Moritz Helmstaedter. Cell type-specific thalamic innervation in a column of rat vibrissal cortex. *Cerebral cortex (New York, NY : 1991)*, Jun 2010.

[31] Marcel Oberlaender, Christiaan P. J de Kock, Randy M Bruno, Alejandro Ramirez, Hanno S Meyer, Vincent J Dercksen, Moritz Helmstaedter, and Bert Sakmann. Cell type-specific three-dimensional structure of thalamocortical circuits in a column of rat vibrissal cortex. *Cerebral cortex (New York, NY : 1991)*, 22(10):2375–2391, Oct 2012.

[32] Christine M Constantinople and Randy M Bruno. Deep cortical layers are activated directly by thalamus. *Science*, 340(6140):1591–4, Jun 2013.

[33] D J Simons and G E Carvell. Thalamocortical response transformation in the rat vibrissa/barrel system. *Journal of Neurophysiology*, 61(2):311–30, Feb 1989.

[34] D Goldreich, H T Kyriazi, and D J Simons. Functional independence of layer iv barrels in rodent somatosensory cortex. *Journal of Neurophysiology*, 82(3):1311–6, Sep 1999.

[35] Michael Brecht and Bert Sakmann. Dynamic representation of whisker deflection by synaptic potentials in spiny stellate and pyramidal cells in the barrels and septa of layer 4 rat somatosensory cortex. *The Journal of Physiology*, 543(Pt 1):49–70, Aug 2002.

[36] Kevin Fox, Nicholas Wright, Helen Wallace, and Stanislaw Glazewski. The origin of cortical surround receptive fields studied in the barrel cortex. *J Neurosci*, 23(23):8380–91, Sep 2003.

[37] Ernest E Kwegyir-Afful, Randy M Bruno, Daniel J Simons, and ASAF KELLER. The role of thalamic inputs in surround receptive fields of barrel neurons. *J Neurosci*, 25(25):5926–34, Jun 2005.

[38] Yonatan Katz, Jaime E Heiss, and Ilan Lampl. Cross-whisker adaptation of neurons in the rat barrel cortex. *J Neurosci*, 26(51):13363–72, Dec 2006.

[39] Nicholas Wright and Kevin Fox. Origins of cortical layer v surround receptive fields in the rat barrel cortex. *Journal of Neurophysiology*, 103(2):709–24, Feb 2010.

[40] C I Moore and S B Nelson. Spatio-temporal subthreshold receptive fields in the vibrissa representation of rat primary somatosensory cortex. *Journal of Neurophysiology*, 80(6):2882–92, Dec 1998.

[41] Bartlett W Mel. Synaptic integration in an excitable dendritic tree. *Journal of Neurophysiology*, 70(3):1086–1101, 1993.

[42] Hongbo Jia, Nathalie L Rochefort, Xiaowei Chen, and Arthur Konnerth. Dendritic organization of sensory input to cortical neurons in vivo. *Nature*, 464(7293):1307–12, Apr 2010.

[43] Zsuzsanna Varga, Hongbo Jia, Bert Sakmann, and Arthur Konnerth. Dendritic coding of multiple sensory inputs in single cortical neurons in vivo. *Proc Natl Acad Sci USA*, 108(37):15420–5, Sep 2011.

[44] Randy M Bruno. Synchrony in sensation. *Current opinion in neurobiology*, 21(5):701–8, Oct 2011.

[45] Randy M Bruno and Bert Sakmann. Cortex is driven by weak but synchronously active thalamocortical synapses. *Science*, 312(5780):1622–1627, Jun 2006.

[46] Michael Brecht, Arnd Roth, and Bert Sakmann. Dynamic receptive fields of reconstructed pyramidal cells in layers 3 and 2 of rat somatosensory barrel cortex. *The Journal of Physiology*, 553(Pt 1):243–65, Nov 2003.

[47] Jason N D Kerr, Christiaan P J de Kock, David S Greenberg, Randy M Bruno, Bert Sakmann, and Fritjof Helmchen. Spatial organization of neuronal population responses in layer 2/3 of rat barrel cortex. *J Neurosci*, 27(48):13316–28, Nov 2007.

[48] Ian D Manns, Bert Sakmann, and Michael Brecht. Sub- and suprathreshold receptive field properties of pyramidal neurones in layers 5a and 5b of rat somatosensory barrel cortex. *The Journal of Physiology*, 556(Pt 2):601–22, Apr 2004.

[49] Yuriy Mishchenko, Tao Hu, Josef Spacek, John Mendenhall, Kristen M Harris, and Dmitri B Chklovskii. Ultrastructural analysis of hippocampal neuropil from the connectomics perspective. *Neuron*, 67(6):1009–20, Sep 2010.

[50] Marcel Oberlaender, Zimbo S R M Boudewijns, Tatjana Kleele, Huibert D Mansvelder, Bert Sakmann, and Christiaan P. J de Kock. Three-dimensional axon morphologies of individual layer 5 neurons indicate cell type-specific intracortical pathways for whisker motion and touch. *Proc Natl Acad Sci USA*, 108(10):4188–93, Mar 2011.

[51] D Pinault. A novel single-cell staining procedure performed in vivo under electrophysiological control: morpho-functional features of juxtacellularly labeled thalamic cells and other central neurons with biocytin or neurobiotin. *Journal of Neuroscience Methods*, 65(2):113–36, Apr 1996.

[52] Rajeevan T Narayanan, Hemanth Mohan, Robin Broersen, Roel de Haan, Anton W Pieneman, and Christiaan P J de Kock. Juxtasomal biocytin labeling to study the structure-function relationship of individual cortical neurons. *J Vis Exp*, (84):e51359, Jan 2014.

[53] Hanno S Meyer, Verena C Wimmer, Marcel Oberlaender, Christiaan P. J de Kock, Bert Sakmann, and Moritz Helmstaedter. Number and laminar distribution of neurons in a thalamocortical projection column of rat vibrissal cortex. *Cerebral cortex (New York, NY : 1991)*, Jul 2010.

[54] Robert Egger, Rajeevan T Narayanan, Moritz Helmstaedter, Christiaan P. J de Kock, and Marcel Oberlaender. 3d reconstruction and standardization of the rat vibrissal cortex for precise registration of single neuron morphology. *PLoS Comput Biol*, 8(12):e1002837, Dec 2012.

[55] H. S Meyer, Robert Egger, J. M Guest, R Foerster, S Reissl, and M Oberlaender. Cellular organization of cortical barrel columns is whisker-specific. *Proceedings of the national academy of sciences*, 110(47):19113–19118, Oct 2013.

[56] Rajeevan T Narayanan, Robert Egger, Andrew S Johnson, Huibert D Mansvelder, Bert Sakmann, Christiaan P J de Kock, and Marcel Oberlaender. Beyond columnar organization: Cell type- and target layer-specific principles of horizontal axon projection patterns in rat vibrissal cortex. *Cerebral cortex (New York, NY : 1991)*, Apr 2015.

[57] Robert Egger, Arno C Schmitt, Damian J Wallace, Bert Sakmann, Marcel Oberlaender, and Jason N D Kerr. Robustness of sensory-evoked excitation is increased by inhibitory inputs to distal apical tuft dendrites. *Proc Natl Acad Sci USA*, 112(45):14072–7, Nov 2015.

[58] M T Wong-Riley. Changes in the visual system of monocularly sutured or enucleated cats demonstrable with cytochrome oxidase histochemistry. *Brain Res*, 171(1):11–28, Jul 1979.

[59] K Horikawa and W E Armstrong. A versatile means of intracellular labeling: injection of biocytin and its detection with avidin conjugates. *Journal of Neuroscience Methods*, 25(1):1–11, Aug 1988.

[60] S Haidarliu and E Ahissar. Size gradients of barreloids in the rat thalamus. *The Journal of Comparative Neurology*, 429(3):372–87, Jan 2001.

[61] J F Julien, P Samama, and J Mallet. Rat brain glutamic acid decarboxylase sequence deduced from a cloned cdna. *J Neurochem*, 54(2):703–5, Feb 1990.

[62] D L Kaufman, J F McGinnis, N R Krieger, and A J Tobin. Brain glutamate decarboxylase cloned in lambda gt-11: fusion protein produces gamma-aminobutyric acid. *Science*, 232(4754):1138–40, May 1986.

[63] Y Kobayashi, D L Kaufman, and A J Tobin. Glutamic acid decarboxylase cdna: nucleotide sequence encoding an enzymatically active fusion protein. *J Neurosci*, 7(9):2768–72, Sep 1987.

[64] R J Mullen, C R Buck, and A M Smith. Neun, a neuronal specific nuclear protein in vertebrates. *Development*, 116(1):201–11, Sep 1992.

[65] Hanno S Meyer, Daniel Schwarz, Verena C Wimmer, Arno C Schmitt, Jason N D Kerr, Bert Sakmann, and Moritz Helmstaedter. Inhibitory interneurons in a cortical column form hot zones of inhibition in layers 2 and 5a. *Proc Natl Acad Sci USA*, 108(40):16807–12, Oct 2011.

[66] Robert Egger, Vincent J Dercksen, Daniel Udvary, Hans-Christian Hege, and Marcel Oberlaender. Generation of dense statistical connectomes from sparse morphological data. *Frontiers in Neuroanatomy*, 8:129, Jan 2014.

[67] T A Woolsey and H Van der Loos. The structural organization of layer iv in the somatosensory region (si) of mouse cerebral cortex. the description of a cortical field composed of discrete cytoarchitectonic units. *Brain Res*, 17(2):205–42, Jan 1970.

[68] Robert Egger. 3d reconstruction and standardization of the barrel field in rat vibrissal cortex. Master's thesis, University of Heidelberg, Germany, Aug 2011.

[69] J Gower. Generalized procrustes analysis. *Psychometrika*, 40(1):33–51, Mar 1975.

[70] Marcel Oberlaender, Vincent J Dercksen, Robert Egger, Maria Gensel, Bert Sakmann, and Hans-Christian Hege. Automated three-dimensional detection and counting of neuron somata. *Journal of Neuroscience Methods*, pages 1–14, Mar 2009.

[71] Veronica Egger, Thomas Nevian, and Randy M Bruno. Subcolumnar dendritic and axonal organization of spiny stellate and star pyramid neurons within a barrel in rat somatosensory cortex. *Cerebral cortex (New York, NY : 1991)*, 18(4):876–89, Apr 2008.

[72] Randy M Bruno, Thomas T G Hahn, Damian J Wallace, Christiaan P J de Kock, and Bert Sakmann. Sensory experience alters specific branches of individual corticocortical axons during development. *J Neurosci*, 29(10):3172–81, Mar 2009.

[73] Marcel Oberlaender, Alejandro Ramirez, and Randy M Bruno. Sensory experience restructures thalamocortical axons during adulthood. *Neuron*, 74(4):648–655, May 2012.

[74] Marcel Oberlaender, Randy M Bruno, Bert Sakmann, and Philip J Broser. Transmitted light brightfield mosaic microscopy for three-dimensional tracing of single neuron morphology. *J Biomed Opt*, 12(6):064029, Jan 2007.

[75] Vincent J Dercksen, Hans-Christian Hege, and Marcel Oberlaender. The filament editor: an interactive software environment for visualization, proof-editing and analysis of 3d neuron morphology. *Neuroinformatics*, 12(2):325–39, Apr 2014.

[76] Moritz Helmstaedter, Bert Sakmann, and Dirk Feldmeyer. Neuronal correlates of local, lateral, and translaminar inhibition with reference to cortical columns. *Cerebral cortex (New York, NY : 1991)*, 19(4):926–37, Apr 2009.

[77] Christian Koelbl, Moritz Helmstaedter, Joachim Lübke, and Dirk Feldmeyer. A barrel-related interneuron in layer 4 of rat somatosensory cortex with a high intrabarrel connectivity. *Cerebral cortex (New York, NY : 1991)*, 25(3):713–25, Mar 2015.

[78] M Ankerst, M Breunig, H Kriegel, and J Sander. Optics: ordering points to identify the clustering structure. *ACM Sigmod Record*, Jan 1999.

[79] Daniel Udvary. Types of axonal inhibitory interneurons in rat vibrissal cortex. Master's thesis, University of Tuebingen, Germany, May 2014.

[80] E L White. Thalamocortical synaptic relations: a review with emphasis on the projections of specific thalamic nuclei to the primary sensory areas of the neocortex. *Brain Res*, 180(3):275–311, Dec 1979.

[81] Tom Binzegger, Rodney J Douglas, and Kevan A C Martin. A quantitative map of the circuit of cat primary visual cortex. *J Neurosci*, 24(39):8441–53, Sep 2004.

[82] Solange P Brown and Shaul Hestrin. Intracortical circuits of pyramidal neurons reflect their long-range axonal targets. *Nature*, 457(7233):1133–6, Feb 2009.

[83] Narayanan Kasthuri, Kenneth Jeffrey Hayworth, Daniel Raimund Berger, Richard Lee Schalek, José Angel Conchello, Seymour Knowles-Barley, Dongil Lee, Amelio Vázquez-Reina, Verena Kaynig, Thouis Raymond Jones, Mike Roberts, Josh Lyskowski Morgan, Juan Carlos Tapia, H Sebastian Seung, William Gray Roncal, Joshua Tzvi Vogelstein, Randal Burns, Daniel Lewis Sussman, Carey Eldin Priebe, Hanspeter Pfister, and Jeff William Lichtman. Saturated reconstruction of a volume of neocortex. *Cell*, 162(3):648–61, Jul 2015.

[84] Henry Markram, Eilif Muller, Srikanth Ramaswamy, Michael W Reimann, Marwan Abdellah, Carlos Aguado Sanchez, Anastasia Ailamaki, Lidia Alonso-Nanclares, Nicolas Antille, Selim Arsever, Guy Antoine Atenekeng Kahou, Thomas K Berger, Ahmet Bilgili, Nenad Buncic, Athanassia Chalimourda, Giuseppe Chindemi, Jean-Denis Courcol, Fabien Delalondre, Vincent Delattre, Shaul Druckmann, Raphael

Dumusc, James Dynes, Stefan Eilemann, Eyal Gal, Michael Emiel Gevaert, Jean-Pierre Ghobril, Albert Gidon, Joe W Graham, Anirudh Gupta, Valentin Haenel, Etay Hay, Thomas Heinis, Juan B Hernando, Michael Hines, Lida Kanari, Daniel Keller, John Kenyon, Georges Khazen, Yihwa Kim, James G King, Zoltan Kisvarday, Pramod Kumbhar, Sébastien Lasserre, Jean-Vincent Le Bé, Bruno R C Magalhães, Angel Merchán-Pérez, Julie Meystre, Benjamin Roy Morrice, Jeffrey Muller, Alberto Muñoz-Céspedes, Shruti Muralidhar, Keerthan Muthurasa, Daniel Nachbaur, Taylor H Newton, Max Nolte, Aleksandr Ovcharenko, Juan Palacios, Luis Pastor, Rodrigo Perin, Rajnish Ranjan, Imad Riachi, José-Rodrigo Rodríguez, Juan Luis Riquelme, Christian Rössert, Konstantinos Sfyrakis, Ying Shi, Julian C Shillcock, Gilad Silberberg, Ricardo Silva, Farhan Tauheed, Martin Telefont, Maria Toledo-Rodriguez, Thomas Tränkler, Werner Van Geit, Jafet Villafranca Díaz, Richard Walker, Yun Wang, Stefano M Zaninetta, Javier Defelipe, Sean L Hill, Idan Segev, and Felix Schürmann. Reconstruction and simulation of neocortical microcircuitry. *Cell*, 163(2):456–92, Oct 2015.

[85] Vincent J Dercksen, Robert Egger, Hans-Christian Hege, and Marcel Oberlaender. Synaptic connectivity in anatomically realistic neural networks: Modeling and visual analysis. In *Third Eurographics Workshop on Visual Computing for Biology and Medicine (VCBM 2012)*, pages 17–24, Goslar, Germany, 2012. Eurographics Association.

[86] P W Land, S A Buffer, and J D Yaskosky. Barreloids in adult rat thalamus: three-dimensional architecture and relationship to somatosensory cortical barrels. *The Journal of Comparative Neurology*, 355(4):573–88, May 1995.

[87] Michael Brecht and Bert Sakmann. Whisker maps of neuronal subclasses of the rat ventral posterior medial thalamus, identified by whole-cell voltage recording and morphological reconstruction. *The Journal of Physiology*, 538(Pt 2):495–515, Jan 2002.

[88] Jochen F Staiger, Iris Flagmeyer, Dirk Schubert, Karl Zilles, Rolf Kötter, and Heiko J Luhmann. Functional diversity of layer iv spiny neurons in rat somatosensory cortex: quantitative morphology of electrophysiologically characterized and biocytin labeled cells. *Cerebral cortex (New York, NY : 1991)*, 14(6):690–701, Jun 2004.

[89] Olaf Sporns and Rolf Kötter. Motifs in brain networks. *PLoS Biol*, 2(11):e369, Nov 2004.

[90] Carl E Schoonover, Juan-Carlos Tapia, Verena C Schilling, Verena Wimmer, Richard Blazeski, Wanying Zhang, Carol A Mason, and Randy M Bruno. Comparative strength and dendritic organization of thalamocortical and corticocortical synapses onto excitatory layer 4 neurons. *J Neurosci*, 34(20):6746–58, May 2014.

[91] J F Staiger, K Zilles, and T F Freund. Distribution of gabaergic elements postsynaptic to ventroposteromedial thalamic projections in layer iv of rat barrel cortex. *Eur J Neurosci*, 8(11):2273–85, Nov 1996.

[92] Henry Markram, Maria Toledo-Rodriguez, Yun Wang, Anirudh Gupta, Gilad Silberberg, and Caizhi Wu. Interneurons of the neocortical inhibitory system. *Nat Rev Neurosci*, 5(10):793–807, Oct 2004.

[93] A U Larkman. Dendritic morphology of pyramidal neurones of the visual cortex of the rat: Iii. spine distributions. *The Journal of Comparative Neurology*, 306(2):332–43, Apr 1991.

[94] W RALL. Distinguishing theoretical synaptic potentials computed for different soma-dendritic distributions of synaptic input. *Journal of Neurophysiology*, 30(5):1138–68, Sep 1967.

[95] R Angus Silver, Joachim Lubke, Bert Sakmann, and Dirk Feldmeyer. High-probability uniquantal transmission at excitatory synapses in barrel cortex. *Science*, 302(5652):1981–4, Dec 2003.

[96] Dirk Feldmeyer, Joachim Lübke, and Bert Sakmann. Efficacy and connectivity of intracolumnar pairs of layer 2/3 pyramidal cells in the barrel cortex of juvenile rats. *The Journal of Physiology*, 575(2):583–602, Aug 2006.

[97] Dirk Feldmeyer, Joachim Lübke, R Angus Silver, and Bert Sakmann. Synaptic connections between layer 4 spiny neurone-layer 2/3 pyramidal cell pairs in juvenile rat barrel cortex: physiology and anatomy of interlaminar signalling within a cortical column. *The Journal of Physiology*, 538(Pt 3):803–22, Feb 2002.

[98] J A Varela, K Sen, J Gibson, J Fost, L F Abbott, and S B Nelson. A quantitative description of short-term plasticity at excitatory synapses in layer 2/3 of rat primary visual cortex. *J Neurosci*, 17(20):7926–40, Oct 1997.

[99] C E Jahr and C F Stevens. Voltage dependence of nmda-activated macroscopic conductances predicted by single-channel kinetics. *J Neurosci*, 10(9):3178–82, Sep 1990.

[100] Matthew E Larkum, Thomas Nevian, Maya Sandler, Alon Polsky, and Jackie Schiller. Synaptic integration in tuft dendrites of layer 5 pyramidal neurons: a new unifying principle. *Science*, 325(5941):756–60, Aug 2009.

[101] Maria Lavzin, Sophia Rapoport, Alon Polsky, Liora Garion, and Jackie Schiller. Nonlinear dendritic processing determines angular tuning of barrel cortex neurons in vivo. *Nature*, pages 1–5, Sep 2012.

[102] Christian Wozny and Stephen R Williams. Specificity of synaptic connectivity between layer 1 inhibitory interneurons and layer 2/3 pyramidal neurons in the rat neocortex. *Cerebral cortex (New York, NY : 1991)*, 21(8):1818–26, Aug 2011.

[103] Jack Waters and Fritjof Helmchen. Background synaptic activity is sparse in neocortex. *J Neurosci*, 26(32):8267–77, Aug 2006.

[104] Robert N S Sachdev, Ford F Ebner, and Charles J Wilson. Effect of subthreshold up and down states on the whisker-evoked response in somatosensory cortex. *Journal of Neurophysiology*, 92(6):3511–21, Dec 2004.

[105] W R Holmes and W RALL. Electrotonic length estimates in neurons with dendritic tapering or somatic shunt. *Journal of Neurophysiology*, 68(4):1421–37, Oct 1992.

[106] M L Hines and N T Carnevale. The neuron simulation environment. *Neural Computation*, 9(6):1179–209, Aug 1997.

[107] Sen Song, Per Jesper Sjöström, Markus Reigl, Sacha Nelson, and Dmitri B Chklovskii. Highly nonrandom features of synaptic connectivity in local cortical circuits. *PLoS Biol*, 3(3):e68, Mar 2005.

[108] Carl C H Petersen, Thomas T G Hahn, Mayank Mehta, Amiram Grinvald, and Bert Sakmann. Interaction of sensory responses with spontaneous depolarization in layer 2/3 barrel cortex. *Proc Natl Acad Sci USA*, 100(23):13638–43, Nov 2003.

[109] Randy M Bruno, Vivek Khatri, Peter W Land, and Daniel J Simons. Thalamocortical angular tuning domains within individual barrels of rat somatosensory cortex. *J Neurosci*, 23(29):9565–74, Oct 2003.

[110] Qian-Quan Sun, John R Huguenard, and David A Prince. Barrel cortex microcircuits: thalamocortical feedforward inhibition in spiny stellate cells is mediated by a small number of fast-spiking interneurons. *J Neurosci*, 26(4):1219–30, Jan 2006.

[111] Vicente Reyes-Puerta, Jyh-Jang Sun, Suam Kim, Werner Kilb, and Heiko J Luhmann. Laminar and columnar structure of sensory-evoked multineuronal spike sequences in adult rat barrel cortex in vivo. *Cerebral cortex (New York, NY : 1991)*, 25(8):2001–21, Aug 2015.

[112] Luc J Gentet, Michael Avermann, Ferenc Matyas, Jochen F Staiger, and Carl C H Petersen. Membrane potential dynamics of gabaergic neurons in the barrel cortex of behaving mice. *Neuron*, 65(3):422–35, Feb 2010.

[113] T Pierret, P Lavallée, and M Deschênes. Parallel streams for the relay of vibrissal information through thalamic barreloids. *J Neurosci*, 20(19):7455–62, Oct 2000.

[114] Takahiro Furuta, Takeshi Kaneko, and Martin Deschênes. Septal neurons in barrel cortex derive their receptive field input from the lemniscal pathway. *J Neurosci*, 29(13):4089–95, Apr 2009.

[115] Takahiro Furuta, Martin Deschênes, and Takeshi Kaneko. Anisotropic distribution of thalamocortical boutons in barrels. *J Neurosci*, 31(17):6432–9, Apr 2011.

[116] Stephen R Williams and Susan E Atkinson. Pathway-specific use-dependent dynamics of excitatory synaptic transmission in rat intracortical circuits. *The Journal of Physiology*, 585(Pt 3):759–77, Dec 2007.

[117] A Gupta, Y Wang, and H Markram. Organizing principles for a diversity of gabaergic interneurons and synapses in the neocortex. *Science*, 287(5451):273–8, Jan 2000.

[118] Philipp Schnepel, Arvind Kumar, Mihael Zohar, Ad Aertsen, and Clemens Boucsein. Physiology and impact of horizontal connections in rat neocortex. *Cerebral cortex (New York, NY : 1991)*, 25(10):3818–35, Oct 2015.

[119] Etay Hay and Idan Segev. Dendritic excitability and gain control in recurrent cortical microcircuits. *Cerebral cortex (New York, NY : 1991)*, 25(10):3561–71, Oct 2015.

[120] H Markram, J Lübke, M Frotscher, A Roth, and B Sakmann. Physiology and anatomy of synaptic connections between thick tufted pyramidal neurones in the developing rat neocortex. *The Journal of Physiology*, 500 (Pt 2):409–40, Apr 1997.

[121] Etay Hay, Sean Hill, Felix Schürmann, Henry Markram, and Idan Segev. Models of neocortical layer 5b pyramidal cells capturing a wide range of dendritic and perisomatic active properties. *PLoS Comput Biol*, 7(7):e1002107, Jul 2011.

[122] M E Larkum, J J Zhu, and B Sakmann. A new cellular mechanism for coupling inputs arriving at different cortical layers. *Nature*, 398(6725):338–41, Mar 1999.

[123] G J Stuart and B Sakmann. Active propagation of somatic action potentials into neocortical pyramidal cell dendrites. *Nature*, 367(6458):69–72, Jan 1994.

[124] J Schiller, Y Schiller, G Stuart, and B Sakmann. Calcium action potentials restricted to distal apical dendrites of rat neocortical pyramidal neurons. *The Journal of Physiology*, 505 (Pt 3):605–16, Dec 1997.

[125] Shaul Druckmann, Yoav Banitt, Albert Gidon, Felix Schürmann, Henry Markram, and Idan Segev. A novel multiple objective optimization framework for constraining conductance-based neuron models by experimental data. *Frontiers in Neuroscience*, 1(1):7–18, Nov 2007.

[126] Z.F Mainen, J Joerges, J.R Huguenard, and T.J Sejnowski. A model of spike initiation in neocortical pyramidal neurons. *Neuron*, 15(6):1427–1439, 1995.

[127] Jochen F Staiger, Ingo Bojak, Stéphanie Miceli, and Dirk Schubert. A gradual depth-dependent change in connectivity features of supragranular pyramidal cells in rat barrel cortex. *Brain Struct Funct*, 220(3):1317–37, May 2015.

[128] L E Hallman, B R Schofield, and C S Lin. Dendritic morphology and axon collaterals of corticotectal, corticopontine, and callosal neurons in layer v of primary visual cortex of the hooded rat. *The Journal of Comparative Neurology*, 272(1):149–60, Jun 1988.

[129] A Larkman and A Mason. Correlations between morphology and electrophysiology of pyramidal neurons in slices of rat visual cortex. i. establishment of cell classes. *J Neurosci*, 10(5):1407–14, May 1990.

[130] Pratap Kumar and Ora Ohana. Inter- and intralaminar subcircuits of excitatory and inhibitory neurons in layer 6a of the rat barrel cortex. *Journal of Neurophysiology*, 100(4):1909–22, Oct 2008.

[131] Moritz Helmstaedter, Bert Sakmann, and Dirk Feldmeyer. L2/3 interneuron groups defined by multiparameter analysis of axonal projection, dendritic geometry, and electrical excitability. *Cerebral cortex (New York, NY : 1991)*, 19(4):951–62, Apr 2009.

[132] Moritz Helmstaedter, Bert Sakmann, and Dirk Feldmeyer. The relation between dendritic geometry, electrical excitability, and axonal projections of l2/3 interneurons in rat barrel cortex. *Cerebral cortex (New York, NY : 1991)*, 19(4):938–50, Apr 2009.

[133] Petilla Interneuron Nomenclature Group, Giorgio A Ascoli, Lidia Alonso-Nanclares, Stewart A Anderson, German Barrionuevo, Ruth Benavides-Piccione, Andreas Burkhalter, György Buzsáki, Bruno Cauli, Javier Defelipe, Alfonso Fairén, Dirk Feldmeyer, Gord Fishell, Yves Fregnac, Tamas F Freund, Daniel Gardner, Esther P Gardner, Jesse H Goldberg, Moritz Helmstaedter, Shaul Hestrin, Fuyuki Karube, Zoltán F Kisvárday, Bertrand Lambolez, David A Lewis, Oscar Marin, Henry Markram, Alberto Muñoz, Adam Packer, Carl C H Petersen, Kathleen S Rockland, Jean Rossier, Bernardo Rudy, Peter Somogyi, Jochen F Staiger, Gabor Tamas, Alex M Thomson, Maria Toledo-Rodriguez, Yun Wang, David C West, and Rafael Yuste. Petilla terminology: nomenclature of features of gabaergic interneurons of the cerebral cortex. *Nat Rev Neurosci*, 9(7):557–68, Jul 2008.

[134] P Somogyi. A specific 'axo-axonal' interneuron in the visual cortex of the rat. *Brain Res*, 136(2):345–50, Nov 1977.

[135] Shruti Muralidhar, Yun Wang, and Henry Markram. Synaptic and cellular organization of layer 1 of the developing rat somatosensory cortex. *Frontiers in Neuroanatomy*, 7:52, Jan 2013.

[136] Xiaolong Jiang, Guangfu Wang, Alice J Lee, Ruth L Stornetta, and J Julius Zhu. The organization of two new cortical interneuronal circuits. *Nature neuroscience*, 16(2):210–8, Feb 2013.

[137] Yinghua Zhu and J Julius Zhu. Rapid arrival and integration of ascending sensory information in layer 1 nonpyramidal neurons and tuft dendrites of layer 5 pyramidal neurons of the neocortex. *J Neurosci*, 24(6):1272–9, Feb 2004.

[138] Angel Merchán-Pérez, José-Rodrigo Rodríguez, Santiago González, Víctor Robles, Javier Defelipe, Pedro Larrañaga, and Concha Bielza. Three-dimensional spatial distribution of synapses in the neocortex: a dual-beam electron microscopy study. *Cerebral cortex (New York, NY : 1991)*, 24(6):1579–88, Jun 2014.

[139] Michael W Reimann, James G King, Eilif B Muller, Srikanth Ramaswamy, and Henry Markram. An algorithm to predict the connectome of neural microcircuits. *Front Comput Neurosci*, 9:120, Jan 2015.

[140] D Feldmeyer, V Egger, J Lubke, and B Sakmann. Reliable synaptic connections between pairs of excitatory layer 4 neurones within a single 'barrel' of developing rat somatosensory cortex. *The Journal of Physiology*, 521 Pt 1:169–90, Nov 1999.

[141] C C Petersen and B Sakmann. The excitatory neuronal network of rat layer 4 barrel cortex. *J Neurosci*, 20(20):7579–86, Oct 2000.

[142] Stefan Lang, Panos Drouvelis, Enkelejda Tafaj, Peter Bastian, and Bert Sakmann. Fast extraction of neuron morphologies from large-scale sbfsem image stacks. *Journal of Computational Neuroscience*, 31(3):533–45, Nov 2011.

[143] Gordon M G Shepherd, Armen Stepanyants, Ingrid Bureau, Dmitri Chklovskii, and Karel Svoboda. Geometric and functional organization of cortical circuits. *Nature neuroscience*, 8(6):782–90, Jun 2005.

[144] C Koch, R Douglas, and U Wehmeier. Visibility of synaptically induced conductance changes: theory and simulations of anatomically characterized cortical pyramidal cells. *J Neurosci*, 10(6):1728–44, Jun 1990.

[145] Albert Gidon and Idan Segev. Principles governing the operation of synaptic inhibition in dendrites. *Neuron*, 75(2):330–41, Jul 2012.

[146] Kevin D Alloway. Information processing streams in rodent barrel cortex: the differential functions of barrel and septal circuits. *Cerebral cortex (New York, NY : 1991)*, 18(5):979–89, May 2008.

[147] Alexander Groh, Christiaan P J de Kock, Verena C Wimmer, Bert Sakmann, and Thomas Kuner. Driver or coincidence detector: modal switch of a corticothalamic giant synapse controlled by spontaneous activity and short-term depression. *J Neurosci*, 28(39):9652–63, Sep 2008.

[148] A G Leventhal and H V Hirsch. Receptive-field properties of neurons in different laminae of visual cortex of the cat. *Journal of Neurophysiology*, 41(4):948–62, Jul 1978.

[149] Christine M Constantinople and Randy M Bruno. Effects and mechanisms of wakefulness on local cortical networks. *Neuron*, 69(6):1061–1068, Mar 2011.

[150] Kevin L Briggman, Moritz Helmstaedter, and Winfried Denk. Wiring specificity in the direction-selectivity circuit of the retina. *Nature*, 471(7337):183–8, Mar 2011.

[151] Moritz Helmstaedter. Cellular-resolution connectomics: challenges of dense neural circuit reconstruction. *Nat Methods*, 10(6):501–7, Jun 2013.

[152] C Nikoosh Carlo and Charles F Stevens. Structural uniformity of neocortex, revisited. *Proc Natl Acad Sci USA*, 110(4):1488–93, Jan 2013.

[153] Sandrine Lefort, Christian Tomm, J-C Floyd Sarria, and Carl C H Petersen. The excitatory neuronal network of the c2 barrel column in mouse primary somatosensory cortex. *Neuron*, 61(2):301–16, Jan 2009.

[154] Mateo Vélez-Fort, Charly V Rousseau, Christian J Niedworok, Ian R Wickersham, Ede A Rancz, Alexander P Y Brown, Molly Strom, and Troy W Margrie. The stimulus selectivity and connectivity of layer six principal cells reveals cortical microcircuits underlying visual processing. *Neuron*, 83(6):1431–43, Sep 2014.

[155] O Bernander, R J Douglas, K A Martin, and C Koch. Synaptic background activity influences spatiotemporal integration in single pyramidal cells. *Proc Natl Acad Sci USA*, 88(24):11569–73, Dec 1991.

[156] Rodney J Douglas and Kevan A C Martin. Neuronal circuits of the neocortex. *Annu Rev Neurosci*, 27:419–51, Jan 2004.

[157] Ning long Xu, Mark T Harnett, Stephen R Williams, Daniel Huber, Daniel H O'Connor, Karel Svoboda, and Jeffrey C Magee. Nonlinear dendritic integration of sensory and motor input during an active sensing task. *Nature*, 492(7428):247–51, Dec 2012.

[158] Chunxiu Yu, Dori Derdikman, Sebastian Haidarliu, and Ehud Ahissar. Parallel thalamic pathways for whisking and touch signals in the rat. *PLoS Biol*, 4(5):e124, May 2006.

[159] Verena C Wimmer, Randy M Bruno, Christiaan P. J de Kock, Thomas Kuner, and Bert Sakmann. Dimensions of a projection column and architecture of vpm and pom axons in rat vibrissal cortex. *Cerebral cortex (New York, NY : 1991)*, 20(10):2265–76, Oct 2010.

[160] Eve Marder and Vatsala Thirumalai. Cellular, synaptic and network effects of neuromodulation. *Neural Netw*, 15(4-6):479–93, Jan 2002.

[161] Lucas Pinto, Michael J Goard, Daniel Estandian, Min Xu, Alex C Kwan, Seung-Hee Lee, Thomas C Harrison, Guoping Feng, and Yang Dan. Fast modulation of visual perception by basal forebrain cholinergic neurons. *Nature neuroscience*, 16(12):1857–63, Dec 2013.

[162] Tristan Hedrick and Jack Waters. Acetylcholine excites neocortical pyramidal neurons via nicotinic receptors. *Journal of Neurophysiology*, 113(7):2195–209, Apr 2015.

[163] Rogier B Poorthuis, Leona Enke, and Johannes J Letzkus. Cholinergic circuit modulation through differential recruitment of neocortical interneuron types during behaviour. *The Journal of Physiology*, 592(Pt 19):4155–64, Oct 2014.

[164] A Destexhe, Z.F Mainen, and T.J Sejnowski. Synthesis of models for excitable membranes, synaptic transmission and neuromodulation using a common kinetic formalism. *Journal of Computational Neuroscience*, 1(3):195–230, 1994.

[165] Christiaan P. J de Kock and Bert Sakmann. Spiking in primary somatosensory cortex during natural whisking in awake head-restrained rats is cell-type specific. *Proceedings of the national academy of sciences*, 106(38):16446–16450, 2009.